

CR-72882

NREC 1159-1



**THE DESIGN OF AN ADVANCED TURBINE
FOR BRAYTON ROTATING
UNIT APPLICATION**

by
Andreas M. Kirschner
Colin F. Robertson
Anthony F. Carter

Northern Research and Engineering Corporation
Cambridge, Massachusetts 02139

July, 1971

prepared for
National Aeronautics and Space Administration

NASA Lewis Research Center
Contract NAS3-13492
Milton G. Kofskey, Project Manager
Fluid System Components Division



N71-37372	(ACCESSION NUMBER)	3	(THRU)
142	(PAGES)	28	(CODE)
CR-72882	(NASA CR OR TMX OR AD NUMBER)		(CATEGORY)

FACILITY FORM 602

1. Report No. NASA CR-72888	2. Government Accession No.	3. Recipient's Catalog No.	
4. Title and Subtitle THE DESIGN OF AN ADVANCED TURBINE FOR BRAYTON ROTATING UNIT APPLICATION (U)		5. Report Date July 1971	
		6. Performing Organization Code	
7. Author(s) Andreas M. Kirschner, Colin F. Robertson, Anthony F. Carter		8. Performing Organization Report No.	
9. Performing Organization Name and Address Northern Research and Engineering Corporation 219 Vassar Street Cambridge, Massachusetts 02139		10. Work Unit No.	
		11. Contract or Grant No. NAS3-13492	
12. Sponsoring Agency Name and Address National Aeronautics and Space Administration Washington, D. C. 20546		13. Type of Report and Period Covered Contractor Report	
		14. Sponsoring Agency Code	
15. Supplementary Notes Project Manager, Milton G. Kofskey, Fluid System Components Division, NASA Lewis Research Center, Cleveland, Ohio			
16. Abstract (U) A complete radial inflow turbine stage comprising an inlet scroll, nozzle row, rotor, and exhaust diffuser has been designed as an alternative to an existing stage of a Brayton cycle turbo-alternator-compressor unit. The design standard results from an optimization of efficiency at the design-point pressure ratio, and hence power output. The relatively low tip speed of the rotor and the operating temperature level permitted an aerodynamic standard for the rotor which is not significantly compromised by mechanical constraints. The selected rotor features a tandem blade row configuration with nonradial blading and backsweep of the rotor inlet blade angle. The nozzle row makes use of a contraction of the axial width across the row to reduce nozzle losses. The design-point efficiency of the stage is expected to be at least 2 percentage points, and possibly 4 percentage points, greater than that of the existing conventional stage; the uncertainty in the prediction results principally from the assessment of losses in the novel nozzle row configuration. The stage will be tested by NASA-Lewis Research Center personnel.			
17. Key Words (Suggested by Author(s)) radial inflow turbine, tandem blades, nozzle row, inlet scroll, exhaust diffuser, total pressure loss correlations, boundary-layer analysis, aerodynamic design analysis, mechanical design analysis		18. Distribution Statement U. S. Government and Contractors Only Publicly Available M. G. Kofskey, Lewis DRA 7/1/71	
19. Security Classif. (of this report) Unclassified	20. Security Classif. (of this page) Unclassified	21. No. of Pages 162	22. Price*

TABLE OF CONTENTS

SUMMARY	1
INTRODUCTION	3
Problem Statement	3
Technical Approach	4
Report Arrangement	5
PRELIMINARY DESIGN ANALYSIS	6
Objectives and Approach	6
Preliminary Aerodynamic Analysis Procedure	6
Preliminary Mechanical Analysis Procedure	11
Parametric Investigation	13
Preliminary Design Selection	16
AERODYNAMIC DESIGN	20
Rotor Design	20
Nozzle Design	24
Exhaust Diffuser Design	25
Inlet Scroll Design	26
Boundary-Layer Analysis	26
Design-Point Efficiency Estimate	28
MECHANICAL DESIGN	30
Introduction	30
Turbine Scroll and Nozzle Design	31
Rotor Mechanical Design	32
Flexural Vibrations	36
Shaft Attachment Methods	37
Bearing Analysis	37
Diffuser Design	40
Final Assembly and Installation	40
CONCLUSIONS AND RECOMMENDATIONS	41
Conclusions	41
Recommendations	42
REFERENCES	44
TABLES	47

FIGURES 68

NOMENCLATURE 122

APPENDICES 125

 I: AERODYNAMIC DESIGN PROCEDURES 126

 II: MECHANICAL DESIGN PROCEDURES 135

 III: REPRODUCTIONS OF THE MANUFACTURING DRAWINGS 145

DISTRIBUTION LIST 163

LIST OF TABLES

Table I:	Major Design Geometric Values for Datum Turbines Used in the Parametric Investigation	48
Table II:	Summary of Stage Performance and Operating Conditions	49
Table III:	Preliminary Design-Point Performance and Flow Field Details	50
Table IV:	Meridional Flow Path Specification of the BRU Rotor . .	55
Table V:	First Blade Row Definition Along the Streamtube Centers	56
Table VI:	Second Blade Row Definition Along the Streamtube Centers	57
Table VII:	Nozzle Vane Geometry Specification	58
Table VIII:	Diffuser Specification	59
Table IX:	Turbine Inlet Scroll Geometry Specification	60
Table X:	Rotor Adiabatic Wall Temperature and Biot Number Distribution Assumed for Rotor Temperature and Stress Calculations	61
Table XI:	Physical Properties of High Temperature Alloys	62
Table XII:	Summary of Disk Stresses and Deflections	65
Table XIII:	Summary of Blade Frequency and Vibratory Stress Results	66
Table XIV:	Turbine Research Package Assembly and Tool List	67

LIST OF FIGURES

Figure 1:	Schematic Picture of Radial Inflow Turbine Stage	69
Figure 2:	Static Efficiency Variation with Nozzle Inlet Diameters for Three Datum Designs and Variation of Static Efficiency, Disk, and Bending Stresses with Rotor Inlet Diameters for Datum 1 Design	70
Figure 3:	Variation of Static Efficiency with Outer Diameter and Mean Diameter at Rotor Discharge	71
Figure 4:	Variation of Static Efficiency with Passage Width at Nozzle Inlet and Rotor Inlet	72
Figure 5:	Variation of Static Efficiency with Rotor Blade Number and Stator Vane Number	73
Figure 6:	Variation of Static Efficiency with Rotor Axial Length and Vaneless Space Diameter Ratio	74
Figure 7:	Design Velocity Diagrams for the Vaned Nozzle and the Rotor Inlet Station	75
Figure 8:	Design Velocity Diagrams at the Rotor Discharge Station	76
Figure 9:	The Blade Loading Objective for the Outer Casing Streamtube of the Redesigned Turbine (16 Blades in Each Row of a Tandem Row Configuration)	77
Figure 10:	Final Meridional Flow Path of the BRU Turbine Rotor . . .	78
Figure 11:	Comparison of the Original and Redesigned Turbine Meridional Flow Paths	79
Figure 12:	First Blade Row Surface Velocity Distribution (Casing Streamtube)	80
Figure 13:	First Blade Row Surface Velocity Distribution (Hub Streamtube)	81
Figure 14:	Second Blade Row Surface Mach Number Distribution and Corresponding Blade Shape at a Radius of 1.70 Inches (Near the Outer Contour)	82
Figure 15:	Second Blade Row Surface Mach Number Distribution and Corresponding Blade Shape at a Radius of 1.125 Inches (Near the Hub)	83
Figure 16:	Second Blade Row Surface Velocity Distribution (Casing Streamtube)	84
Figure 17:	Second Blade Row Surface Velocity Distribution (Hub Streamtube)	85

Figure 18:	Blade Angle Variation Along the Streamline Near the Outer Casing (Casing Streamtube Centers)	86
Figure 19:	Meridional Flow Path of the Nozzle	87
Figure 20:	Surface Velocity Distribution of the Nozzle Vane	88
Figure 21:	Nozzle Vane Geometry Selected for the Final Design	89
Figure 22:	Turbine Inlet Scroll Geometry	90
Figure 23:	Two-Dimensional Boundary-Layer Parameters and Secondary Flow Parameter C_p of the First Blade Row (Casing Streamtube)	91
Figure 24:	Two-Dimensional Boundary-Layer Parameters and Secondary Flow Parameter C_p of the First Blade Row (Hub Streamtube)	92
Figure 25:	Two-Dimensional Boundary-Layer Parameters and Secondary Flow Parameter Σ from Hub to Casing of the First Blade Row (Suction Surface)	93
Figure 26:	Two-Dimensional Boundary-Layer Parameters and Secondary Flow Parameter Σ from Hub to Casing of the First Blade Row (Pressure Surface)	94
Figure 27:	Two-Dimensional Boundary-Layer Parameters and Secondary Flow Parameter C_p of the Second Blade Row (Casing Streamtube)	95
Figure 28:	Two-Dimensional Boundary-Layer Parameters and Secondary Flow Parameter C_p of the Second Blade Row (Hub Streamtube)	96
Figure 29:	Two-Dimensional Boundary-Layer Parameters and Secondary Flow Parameter Σ from Hub to Casing of the Second Blade Row (Suction Surface)	97
Figure 30:	Two-Dimensional Boundary-Layer Parameters and Secondary Flow Parameter Σ from Hub to Casing of the Second Blade Row (Pressure Surface)	98
Figure 31:	Two-Dimensional Boundary-Layer Parameters and Secondary Flow Parameter C_p from Pressure to the Suction Surface of the Nozzle Vane	99
Figure 32:	Two-Dimensional Boundary-Layer Parameters and Secondary Flow Parameter Σ from Casing to Hub Along the Suction Surface of the Nozzle Vane	100
Figure 33:	Two-Dimensional Boundary-Layer Parameters and Secondary Flow Parameter Σ from Casing to Hub Along the Pressure Surface of the Nozzle Vane	101
Figure 34:	Variation in Cross Section of the Turbine Inlet Scroll Transition Piece (from Scroll Inlet Flange to Zero Degrees Azimuthal Angle)	102

Figure 35:	Meridional View of Rotor Showing Heat Transfer Areas, Blade Panels, and Reference Surface	103
Figure 36:	Rotor Temperature Distribution at 100 Per Cent Speed . .	104
Figure 37:	Radial Variation of the Disk Stresses at Design Temperature Operating at 100 Per Cent Speed	105
Figure 38:	Radial Variation of Disk Stresses at Design Temperature Operating at 120 Per Cent Speed	106
Figure 39:	Radial Variation of Disk Stresses at Design Temperature Operating at 140 Per Cent Speed	107
Figure 40:	Radial Stress Distribution at Design Temperature Operating at 100 Per Cent Speed	108
Figure 41:	Tangential Stress Distribution at Design Temperature Operating at 100 Per Cent Speed	109
Figure 42:	Radial Variation of Equivalent Stress at Design Temperature Operating at 120 Per Cent Speed	110
Figure 43:	Radial Variation of Axial Deflection at Design and Room Temperatures (Reference at $z = 0$)	111
Figure 44:	Variation of Radial Elongation with Radius at Design and Room Temperatures	112
Figure 45:	Normal Thickness Distribution Along the Hub and Outer Contour (First Blade Row)	113
Figure 46:	Normal Thickness Distribution Along the Hub and Outer Contour (Second Blade Row)	114
Figure 47:	Blade Root Bending and Tensile Stresses at 120 Per Cent Speed (First Blade Row)	115
Figure 48:	Blade Root Bending and Tensile Stresses at 120 Per Cent Speed (Second Blade Row)	116
Figure 49:	Campbell Diagram for the Rotor	117
Figure 50:	Goodman Diagram for the Rotor	118
Figure 51:	Turbine Rotor System Characteristics	119
Figure 52:	Variation of Critical Speed with Bearing Stiffness . . .	120
Figure 53:	Radial Variation of Frontal and Back Pressures on the Turbine Wheel	121

SUMMARY

This report documents the aerodynamic and mechanical design of a radial inflow turbine stage for a Brayton rotating unit application. The work was performed under NASA Contract No. NAS3-13492. The new turbine is an alternative to one previously designed and tested.

Since the single-stage turbine in a turbo-alternator-compressor unit supplies both alternator and compressor drive power and the power requirements of the latter are significantly greater than that of the former, a one-percentage-point change in turbine efficiency will produce a relatively large change in the useful power output of the unit. In this particular turbine application, the combination of stress levels and operating temperature are such that the primary design emphasis could be placed on achieving an aerodynamic optimum within the over-all constraint of the life requirement of the turbine.

The work reported consists of three phases; the preliminary aerodynamic and mechanical design, the final aerodynamic design, and the final mechanical design including the production of manufacturing drawings.

The selected stage configuration differs from the previously tested stage in a number of respects. The rotor design features back-slope blading at rotor inlet and a tandem blade row design, the meridional flow path through the nozzle row is flared, the downstream diffuser section was designed for a linear static pressure rise, and the inlet scroll over-all dimensions were reduced compared with the original. Compared with the existing design, the efficiency of the stage is predicted to be between 2 and 4 percentage points higher at the design-point over-all total-to-static pressure ratio. The relatively large band of uncertainty assigned to the predicted efficiency is directly associated with the current deficiencies of loss prediction procedures for radial inflow turbines in general and their application to the nozzle row and rotor configurations of the new design.

The mechanical design of the rotor was undertaken for the BRU application. However, the stationary parts were designed for cold flow

testing on the NASA test stand. Drawings for all new parts for the turbine stage test have been reduced and reproduced for inclusion in this design report.

INTRODUCTION

Problem Statement

The basic objective of this program was to design a radial in-flow turbine that surpasses the performance of an existing unit (Refs 1 and 2) and which could replace the original with a minimum of modifications both in an actual BRU and the NASA turbine test stand.

The turbine drives a centrifugal compressor and an alternator in a closed Xe-He Brayton cycle. Since the compressor absorbs most of the turbine power output, a one-point improvement in the turbine efficiency will produce an approximate 3 per cent improvement in cycle efficiency. The principal objective was to achieve the highest possible stage efficiency for the over-all design-point total-to-static pressure ratio; the stage comprises an inlet scroll, a nozzle row, the rotor, and an exhaust diffuser.

Design Requirements

The design requirements for the turbine are as follows:

Working Fluid, Helium-Xenon Mixture

Turbine Inlet Total Temperature	2060 deg R (1144 deg K)
---------------------------------	-------------------------

Turbine Inlet Total Pressure	25.0 psia (172 kN/m ² abs)
------------------------------	---------------------------------------

Specific Heat at Constant Pressure	0.05925, Btu/lb/deg R (248 J/kg deg K)
------------------------------------	---

Ratio of Specific Heats	1.667
-------------------------	-------

Molecular Weight	83.8
------------------	------

Turbine Rotative Speed	36,000 rpm
------------------------	------------

Direction of Rotation	Clockwise Looking Upstream at Rotor Exit
-----------------------	--

Weight Flow	0.7484 lbm/sec (0.3395 kg/sec)
-------------	-----------------------------------

Turbine Inlet Total-to-Diffuser Exit Static Pressure Ratio	1.763
--	-------

Turbine Inlet Total-to- 1.749 or Greater
Diffuser Exit Total
Pressure Ratio

Technical Approach

The over-all technical approach to this problem was outlined by NASA personnel initially and further developed by NREC during the preliminary design effort. Considerable flexibility in the rotor design was permitted by the moderate wheel speed and the relatively low operating temperature of the closed-cycle rare gas turbine. Suggested rotor design modifications implied performance gains in both the vaned nozzle and the diffuser.

For the rotor the initially recommended design change was an increase in outer diameter over the previous design, which at constant rotative speed corresponds to increased tip speed. The consequent reduction in the absolute tangential inlet velocity would result in the use of backward swept blades which, in turn, would permit a more uniform loading distribution along the blade surfaces when compared to radial blades. A reduction in the number of rotor blades was also considered desirable in order to obtain the optimum balance between friction and diffusion losses. For this reason, alternate blading concepts to the conventional splitter configuration were also considered worthy of evaluation. In addition, the other dimensions of the rotor such as inlet passage width, passage length, and outer diameters at inlet and exit were considered variables in the design optimization.

The nozzle ring would benefit from an increase in discharge radius corresponding to that of the rotor, due to the reduced discharge velocity level. Here again, the remaining major nozzle dimensions (inlet radius, passage width) and vane number were to be selected in such a manner that the combined effect of loading, friction, and secondary flow losses would be minimized. Initial NASA design recommendations were shorter vane chords and flared nozzle walls.

Significant performance improvement was expected from a redesigned diffuser, since the experimental evaluation of the previous component (Ref 1) had indicated substandard performance. Diffuser

effectiveness as a function of diffusion is clearly related to mean rotor discharge conditions and as such are involved in the stage design optimization. Beyond that, however, the detailed design of the diffuser should include concepts that would reduce the adverse effects of the unsettled flow field emerging from the rotor.

Report Arrangement

The systematic design of the subject turbine evolved from preliminary aerodynamic and mechanical analyses to the detailed aerodynamic design and mechanical analyses. The report follows this order in the main part. There are three appendices; the first and second document the design and analysis procedures for the aerodynamic and mechanical design, respectively, while the third contains reproductions of the drawing reduced in size for report purposes.

PRELIMINARY DESIGN ANALYSIS

Objectives and Approach

The purpose of the preliminary analysis is to determine the principal dimensions and flow conditions (vector diagrams) at the inlet and discharge stations of each component as shown in Figure 1. The evaluation must consider aerodynamic performance and mechanical feasibility as a function of these dimensions and flow conditions and establish a basis for their final selection, the relevant criterion being optimum stage efficiency within specified mechanical constraints.

To achieve this purpose it is necessary to identify the significant geometric variables, to define the relevant stress criteria, and to formulate the relationship between geometry, flow field, and pressure losses on the one hand, and that between geometry and stresses on the other. The aerodynamic relationships were established by means of simplified flow field representation and suitable expressions for distinct loss mechanisms associated with friction, diffusion, dissipation, and nonuniformity of the flow field (loading), henceforth summarily termed the loss system. The mechanical relationships were similarly found from simplified expressions for rotor disk and blade root bending stresses and for blade natural frequency and vibratory stresses. Hence, a parametric analysis of performance and stress could be used to provide a rational approach to a preliminary design selection.

Preliminary Aerodynamic Analysis Procedure

A review of recent literature related to radial inflow turbines showed that the main contributions to radial turbine technology since the completion of NREC's major turbine program (Refs 3 and 4) are the reports on the turbine which was being redesigned and the various reports on internal blade row flow analysis procedures of Katsanis (for example, Ref 5). No improved loss correlations have been recently developed, and data on which to base improved correlations are very limited. Further analysis was therefore based on the methods presented in References 3 and 4.

Flow Analysis Procedure

The flow analysis consists principally of satisfying continuity and work requirements for the given design flow, pressure ratio, and specified geometry, taking into account the losses that occur across each component. Since the losses depend on the flow quantities to be calculated, the solution of the final flow quantities is arrived at by an iterative procedure. The iteration terminates when the change in efficiency from one iteration to the next iteration is within a prescribed limit. For the first iteration quantities which are not known are either assumed or approximated. In the succeeding iterations, the unknown quantities are taken to be those calculated in the previous iteration.

As part of the stage efficiency calculation, continuity is satisfied at inlet and exit stations of the rotor and nozzle vanes. At these stations either the tangential velocity or flow angle is known. From the given area, design flow and the estimated total pressure and temperature continuity is solved iteratively to calculate the flow quantities.

As a first step in the efficiency iteration loop, the exit total temperature is calculated from the specified pressure ratio and the efficiency calculated in the previous iteration. The diffuser exit static pressure is obtained from the given inlet total-to-exit static pressure ratio and inlet total pressure. Since the design flow is specified and the annulus area is known from the dimensions, the diffuser exit flow conditions are calculated assuming no discharge swirl.

The diffuser inlet total pressure is calculated from the diffuser loss formulation for the known area ratio, prescribed velocity gradient at the diffuser inlet, and the inlet blockage estimated from the average wall momentum thickness at the rotor exit. Since the absolute flow angle at the rotor exit is specified, the flow conditions are obtained by continuity iterations.

The rotor losses are calculated as the sum of the clearance loss and the combined friction and diffusion losses. The rotor inlet total pressure is obtained from the work and the calculated losses. The absolute inlet tangential velocity is calculated from the work, the exit

tangential velocity, and the blade speed. The remaining rotor inlet flow conditions are then calculated by continuity iterations.

The nozzle vane exit total pressure and tangential velocity are calculated from the vaneless space loss and conservation of momentum. The continuity iteration is then employed to calculate the remaining flow conditions at the exit of the nozzle vanes. The nozzle vane inlet total pressure is calculated from nozzle vane losses. Since the absolute flow angle at the nozzle vane inlet is prescribed, the flow conditions are obtained by continuity iterations.

The scroll or the turbine inlet total pressure is then obtained from the calculated scroll losses. The turbine efficiency is estimated based on the calculated inlet total pressure. The efficiency is then compared with the efficiency of the previous iteration. If the efficiency difference is greater than certain prescribed amounts, the new efficiency is assumed and the iteration procedure repeated with the given pressure ratio until the efficiency difference falls within the prescribed limit.

Loss System

During an initial evaluation of alternative loss systems, it was shown that the axial turbine loss correlation of Reference 6 could be modified to accurately predict the design-point efficiency of the existing BRU turbine as reported in Reference 1. However, while the over-all performance was accurately predicted, the individual component losses were less accurately predicted. Hence, although the initially proposed correlation is well suited to a parametric analysis, it was considered necessary to further refine the loss system in order that valid predictions of modification to the existing design geometry would be obtained. The measured static pressure in the stator-rotor gap was used to obtain estimates of the stator and rotor performance. Even though the calculation of a stator loss coefficient by means of static pressure data is subject to possible inaccuracy, it was clear that neither the axial-turbine-based loss correlation of Reference 6 (NREC Report 1125-1) nor the radial turbine stator correlation of Reference 3 (NREC Report 1067-1) would predict the stator loss of the existing turbine; the "1067" prediction gave too low a loss,

and the "1125" prediction gave too high a value. A more recent correlation, obtained from planar cascade tests of low-aspect-ratio axial turbine blade sections, was therefore considered. This correlation is based on an NREC program for USAAVLABS reported in Reference 7 (NREC Report 1137-1). (The report will be issued as AVLABS Report No. 70-14.) In applying this third correlation, the stator system loss was considered to have three components, a scroll loss, the stator blade row loss, and the vaneless space loss. From the following tabulation it will be seen that the "1137" and "1067" prediction produces the best agreement with the value derived from test data.

Loss Coefficient Derived from Experimental Data	= 0.082
Predicted Loss Coefficients	$\left\{ \begin{array}{l} \text{"1067"} = 0.036 \\ \text{"1125"} = 0.148 \\ \text{"1137"} + \text{"1067"} = 0.122 \end{array} \right.$

It appeared that a logical modification of the axial turbine blade row correlation to include the effect of the radius change through the stator blade row produced good agreement between the predicted total pressure loss and that derived from the experimental data of Reference 1.

The selected nozzle row total pressure loss coefficient is as follows:

$$\frac{\Delta P_o}{P_{o2} - P_2} = \left\{ \frac{t \tan \alpha_1 - \frac{D_2}{D_1} t \tan \alpha_2}{0.6 + 0.8 \cos \alpha_2} \right\} \left\{ 0.007 + 0.044 \frac{V_1}{V_2} \right\} \left\{ 1 + \frac{1}{1.6 AR} \right\} \left\{ 0.914 + 1.9 \left(\frac{t_e}{s} \right) + 5.7 \left(\frac{t_e}{s} \right)^2 \right\} \left\{ \frac{Re_{ref}}{Re} \right\}^{0.2} \quad (1)$$

Equation 1 is a modified version of that obtained for axial turbine cascades in Reference 6. The modification introduced for the radial nozzle is the diameter ratio $\frac{D_2}{D_1}$; it was reasoned that the conservation of angular momentum in a radial space should be taken into account when calculating the row loss due to tangential loading. The four remaining terms of Equation 1 introduce loss level correction for row acceleration, V_1/V_2 , passage aspect ratio, AR , trailing edge blockage, t_e/s , and Reynolds number.

Introduction of the above loss formulation into the radial turbine prediction program produced acceptably close agreement between test and prediction. The total pressure loss coefficient predicted for the scroll, nozzle vanes, and vaneless space is 0.0745 compared with the 0.082 value derived from the experimental data. In view of the possible inaccuracy associated with deriving a total pressure loss coefficient from measured static, the agreement was considered satisfactory.

In the case of the rotor losses, the initially selected loss correlations, based on Reference 3, considerably underestimated the rotor losses as deduced from the stage tests. At this point, a number of possible explanations were sought rather than some arbitrarily selected "correction" factor introduced. Two basic deficiencies of the original loss system were identified. One, the loss system did not take splitters into account other than by replacing blade and splitter numbers by an equivalent number of full blades. Two, since the loss formulation assumed a linear variation of relative velocity from inlet to exit, it could not account for a major loss associated with a deceleration along the hub line (which is inherent to most radial inflow turbines). Accordingly, a loss formulation was developed which introduced an intermediate station (Station 31, see Fig 1) between rotor inlet and rotor exit (Stations 3 and 4, respectively). Velocities calculated at the intermediate station are used in designs both with and without splitters. For the existing design, which employs splitters, two sets of velocity calculations are performed at Station 31 with and without the blockage of the splitter. The calculation station in which the splitter blockage is included is named 331 (and is used to calculate losses from 3 to 31). The station immediately downstream of the splitter is identified as Station 314 (and is used to calculate losses in the section between 31 and 4).

The calculation is based on a combined friction and diffusion loss. Velocity distribution calculations are used to calculate diffusion ratios which are then related to boundary-layer displacement thickness and, hence, a rotor total pressure loss coefficient. For the purpose of the calculation, the rotor flow is divided into inner and outer flows. Conditions for the inner flow are assumed to be the average of the mean

line and hub flow conditions. Similarly, the outer portion of the flow is represented by the average of the mean and outer streamline flow conditions. For the full blade, four components of diffusion are identified; that is,

$$D_w = \left(1 - \frac{W_{331,w}}{W_{3,w}}\right) + \left(1 - \frac{W_{314,w}}{W_{331,w}}\right) + \left(1 - \frac{W_{4,w}}{W_{314,w}}\right) + \left(1 - \frac{W_{4,av}}{W_{4,w}}\right) \quad (2)$$

where W_3 , W_{331} , W_{314} , and W_4 are relative velocities at the four calculation stations. The subscripts w and av denote wall and average values, respectively. Four values of D_w corresponding to the inner and outer, pressure, and suction surfaces are calculated. Only relative velocity ratios less than unity are used in the calculation. Each of the four values of D_w is used to calculate a displacement thickness, δ_2 , where

$$\delta_2 = \frac{l C_f}{1 + 1.7 \ln(1 - D_w)}, \quad 0 \leq D_w \leq 0.4$$

$$\delta_2 = \frac{l C_f}{(1 - D_w)^{4.5}}, \quad D_w > 0.4 \quad (3)$$

The four δ_2 values are used to obtain an average value $\bar{\delta}_2$, which in turn is used to calculate the loss coefficient, $\Delta P_o / (P_{04} - P_4)$, given by

$$\frac{\Delta P_o}{P_{04} - P_4} = 4 K \frac{\bar{\delta}_2}{D_R} \quad (4)$$

where K is a secondary flow factor and D_R is the hydraulic diameter for the rotor exit flow area.

The above loss formulation was used in the parametric analysis.

Preliminary Mechanical Analysis Procedure

Procedures used in the mechanical phase of the program are

fully documented in Appendix II. The following topics represent areas of primary concern in the preliminary design analysis of alternative rotors:

1. Blade root bending and tensile stresses.
2. Centrifugally loaded disk stresses.
3. Blade natural frequencies.

Each of these topics is briefly discussed below.

Blade Root Stresses

Experience has shown that where blades with any significant degree of backslope are used, the blade root bending moment at the disk periphery represents the stress limiting situation. If there is lean on the axial portion of the blade, however, the bending stresses produced in this section could very quickly become limiting. Tensile stresses are very rarely limiting.

Values of stress, when obtained, are compared with the appropriate strength value, usually yield strength, of the material to be used.

Disk Centrifugal Stresses

In many instances, the disk is not the limiting item in stress considerations. In addition, considerable improvement in both stress and deformation patterns may be affected by proper shaping of the impeller backface. The equations used in the preliminary analysis consider the two important stresses. These are the basic disk maximum stress and the stress induced by the moment exerted on the disk by backward sloped blades. The former was generally the more important, and it is determined entirely by the impeller tip speed and the material properties.

A conservative solution is represented by a solid homogeneous circular disk of uniform thickness. For a solid circular disk or cylinder, the maximum radial and tangential stress occurs at the center of the disk. Formulas for stress calculations are those of Reference 8.

Blade Natural Frequencies

Blade natural frequencies were predicted using the methods and equations of Reference 9. The primary consideration in the preliminary

design stage was that any blade design likely to be selected as an aerodynamic optimum would not have a calculated natural frequency less than 1.3 times the highest fundamental frequency. The highest fundamental frequency was assumed to be the number of rotor or stator blades, dependent on which was the highest number, times the design rotational speed.

Parametric Investigation

The parametric study consisted of selecting three datum designs and systematically varying the previously identified design geometric parameters. The latter datum designs were selected from the parametric investigation of the previous datum designs and only the parameters which showed improvement in turbine efficiency were used for parametric analysis of the latter datum designs. The major parameters of the three datum designs are listed in Table I.

Eleven design parameters were initially identified for parametric investigation. They consist of five diameters, three passage widths, a number of nozzle vanes, a number of rotor blades, and the axial length of the rotor. The five diameters correspond to the nozzle vane inlet and exit, rotor inlet, and rotor exit hub and shroud. The three widths are at the nozzle vane inlet and exit and rotor inlet. For the main portion of the parametric study, the number of independent variables was reduced to nine.

The vaneless space is provided mainly for the vane wakes to mix out before entering the rotor. Any large space would introduce additional frictional loss. Since the diameter ratio (vane exit to rotor inlet) for well-designed nozzle vanes is approximately 1.04 (Ref 3) and the reference turbine (Ref 1) has a diameter ratio of 1.03, the diameter ratio for the parametric study was assumed to be 1.03 for the three datum designs*. Hence, the nozzle exit diameter, D_2 , was eliminated as an independent variable for the initial parametric analysis*. Since the

* The influence of the ratio D_2/D_3 on stage performance was investigated for the final selection of stage geometric variables.

length of the vaneless space is small compared to the length of the nozzle vanes, the nozzle vane exit passage width, b_2 , was assumed to be the same as rotor inlet width, b_3 . Hence, the width b_2 was removed from the independent variables.

The first datum turbine (Datum 1) was selected with a 3 per cent increase in nozzle vane inlet diameter, D_1 , and a 4 per cent increase in both rotor inlet diameter, D_3 , and nozzle vane inlet width, b_1 , compared with the reference turbine. Datum 1 turbine was investigated for designs both with and without splitters. For the case without the splitters, the number of blades was taken to be the equivalent number based on meridional length. The efficiency of the Datum 1 turbine without the splitter was found to be about 0.6 per cent less than that of Datum 1 with the splitters. Therefore, splitters were assumed in all designs during the major portion of the parametric analysis.

In the parametric study all the variables except the rotor exit hub diameter and the number of blades were varied ± 4 per cent from the values of the datum designs. The rotor exit hub diameter was increased with the shroud diameter such that the exit area remained constant (the product of the mean diameter and the blade height being held constant).

The results of the parametric investigation are shown in Figures 2 through 6. In all but one case the variation in over-all total-to-static efficiency is shown as a function of the particular parameter. Each figure presents results for the first datum design, while some also contain data for Datum Designs 2 or 2 and 3, depending upon the relative importance of the parameters. Since the stress data are principally dependent on the tip diameter (or rotor tip speed), these have only been included with the fluid dynamic efficiency results of Figure 2 where the results of varying D_3 as an independent parameter are shown.

Considering the five figures in more detail, the effects of change in nozzle vane inlet diameter, D_1 , and rotor inlet diameter, D_3 , are shown in Figure 2. An increase in D_1 increases the efficiency as a result of changes in reaction and the Reynolds number of the nozzle vanes. Similar trends are exhibited for Datum 1, 2, and 3 turbine designs, but the increase in η_{S5} of 0.2 per cent in the case of Datum 1 decreases to

0.16 per cent for Datum 3 when D_1 is increased by 4 per cent from the datum values. This reflects the reduced level of stator loss for Datum 3 turbine compared to the Datum 1 stator loss. The effect of change in D_3 is also shown in Figure 2. The efficiency drops when D_3 is decreased as a result of the predominant increase in rotor diffusion. For an increase in D_3 , the decrease in rotor diffusion loss is small compared to the increase in rotor friction and nozzle vane loss, the latter of which is the result of higher nozzle vane exit diameter, D_2 . Therefore, an increase or decrease of 4 per cent in D_3 reduces the turbine efficiency. The efficiency attains a maximum at a diameter ratio slightly under 1.02. The stress levels are within preset limits for this diameter ratio. Therefore, for the other two datum turbines the diameter, D_3 , was chosen to be 1.02 times the Datum 1 value and held constant.

The variation of efficiency with rotor exit shroud diameter, D_{s4} , as well as with the mean diameter, D_{M4} , for constant exit annulus area is shown in Figure 3. A decrease of 4 per cent in D_{s4} decreases diffusion losses in rotor by approximately 15 per cent. The higher diffusion imposed on the diffuser results in a diffuser loss which is more than double that of the Datum 1 turbine. The net effect is a drop of 1.4 per cent in turbine efficiency. If, on the other hand, the diameter, D_{s4} , is increased, the increase in rotor diffusion loss predominates over the decrease in diffuser loss and brings down the turbine efficiency by 0.3 per cent. The turbine efficiency is predicted to steadily drop when the rotor exit mean diameter is increased as a result of increased rotor diffusion loss. This effect is opposed by the beneficial effect due to reduced upstream diffusion anticipated at the rotor hub. A review of the data shown in Figure 3 led to the conclusion that the trade-offs involved in changes of the exit dimensions of the rotor would only be established as a result of a detailed design analysis rather than by parametric analyses involving the geometries of the rotor exit.

The change in turbine efficiency with variation of nozzle vane inlet width, b_1 , is presented in Figure 4. For all three datum turbines the efficiency increases with increase in b_1 reflecting the increase in reaction across the nozzle vanes. The effect of change in rotor inlet

passage width on η_{s5} is also included in Figure 4. It can be seen from the figure that the efficiency increases with increase in b_3 , but the relative change is small especially for the Datum 2 design. This increase is the net result of increased losses in nozzle vanes caused by lower reaction and decreased rotor losses as a result of higher reaction and lower average relative velocity levels.

Figure 5 presents the effect of change in the number of both nozzle vanes and rotor blades. When the number of nozzle vanes is increased, the aspect ratio losses come down while the trailing edge losses go up, resulting in a net increase in η_{s5} . The rate of increase in efficiency becomes negligible at higher number of nozzle vanes. In the case of rotor blades the efficiency decreases for both increase and decrease in the number of blades. When the number of rotor blades is increased or decreased, the decrease or increase in clearance loss approximately compensates the increase or decrease in friction loss. The total diffusion loss increases for lower numbers of blades; the total diffusion loss shows a slight increase even though the diffusion loss per blade is decreased.

The efficiency decreases with increase in axial length, as shown in Figure 6. This decrease results from higher friction and diffusion losses. The clearance loss remains practically constant with rotor axial distance. The effect of vaneless space ratio (nozzle vane exit and rotor inlet) was investigated for the final selected design only. When the vaneless space diameter ratio (D_2/D_3) was increased, the nozzle vane diameter ratio (D_1/D_2) was kept constant. As shown in Figure 6, the efficiency decreases with increase in D_2/D_3 as a result of increased losses in the vaneless space. The nozzle vane and scroll losses remain essentially constant.

Preliminary Design Selection

The following summary presents the selection of the principal design variables and the basis of the selection. With the exception of the rotor blade number the parameters selected following the parametric analysis were retained for the detailed design. However, the rotor blade number and rotor configuration were reevaluated during the detailed design

of the rotor using computed boundary-layer characteristics. As a result of a more detailed evaluation of alternatives, a tandem blade row configuration with 12 blades per row was selected based on a further improvement in rotor efficiency. Table II presents a comparison of the previously tested design and the selected redesign in terms of various efficiency expressions and power output. Table III is a reproduction of the computer output of the program used to predict the design-point characteristic of the selected design; the output is considered to be self-explanatory. The vector diagrams for the row inlet or exit design stations are presented in Figures 7 and 8.

The 11 initially identified independent variables were reduced to 9 by the introduction of two ratios, D_2/D_3 and b_2/b_3 , which were treated as fixed values. Subsequently, the ratio D_2/D_3 was varied for the near-final design standard. Each of the variables is briefly discussed below using the design of Reference 1 as the reference turbine in the comparisons.

1. Nozzle Row Inlet Diameter, D_1 . Compared with the existing turbine, this geometric variable was increased by 15 per cent. While the selected prediction method indicated still further increases in efficiency with diameter, the rate of increase was relatively small at the selected value. The increasing frictional loss was considered sufficiently large that the choice of an optimum solidity for the nozzle row would become more critical. Hence, the nozzle inlet diameter was not increased to the value indicated by the stage optimization which implicitly assumes that an optimum solidity could be selected.
2. Rotor Inlet Diameter, D_3 . The diameter was increased by 6 per cent. The aerodynamic optimum, that is maximum overall total-to-static efficiency, was predicted to occur at the 6 per cent greater value of D_3 . The diameter increase implies the use of backslope blading; the actual value of rotor blade inlet angle was to be obtained during the detailed design phase. The stress level increases associated with the change were acceptable.

3. Nozzle Row Inlet Axial Width, b_1 . This width was increased by 45 per cent. The increase leads to a greater increase in velocity across the row. Although the prediction procedures indicated still further small increases with increase of width, the final value was selected after a review of possible row inlet blockage effects which could be expected to be more significant as the inlet flow angle increased still further beyond 55 degrees.
4. Nozzle Row Inlet and Rotor Row Inlet Axial Widths, b_2 and b_3 . These widths, which were assumed to be equal in the preliminary design analysis were increased by 4 per cent. The new values were predicted to be optimum with increases in nozzle row losses offsetting decreases or rotor losses with any further increase in the flow path width.
5. Rotor Row Exit Outer Diameter, D_{s4} . This value is unchanged from the reference turbine, since it corresponds to a near optimum with rotor and diffuser losses changing at approximately equal but opposite rates in the vicinity of the unchanged value of D_{s4} .
6. Rotor Row Exit Inner Diameter, D_{r4} . This value was also unchanged. When investigated keeping the rotor exit annulus area constant by also varying the outer diameter, the original value was concluded to be near optimum.
7. Number of Nozzle Row Blades, Z_n . The selected number of nozzle blades was 15 with this number predicted to correspond to an optimum solidity. (In the final evaluation of the efficiency of the redesign, one of the alternative prediction procedures indicated that this number of blades may correspond to a solidity in excess of an optimum.)
8. Number of Rotor Blades, Z_r . The initial recommendation of the NREC investigators was for 10 full blades and 10 splitters. However, the NASA personnel's evaluation of the selection resulted in a change to a tandem row configuration which was also approved by NREC on the basis that the turbine

was to be rig tested and a tandem row configuration might result in advances in turbine technology. While the prediction procedures had indicated a small reduction in rotor losses for a tandem row configuration with an appropriate number of blades per row, the lack of experimental data to confirm the choice of such a configuration was regarded as a relatively high risk approach; performance data for a tandem row rotor, however, were agreed to be of considerable interest.

9. Rotor Axial Length, L_z . The rotor axial length was reduced by 12 per cent. While not shown to be particularly significant in terms of rotor performance in the preliminary analysis, any further reduction of length could have resulted in increased blade lean in the vicinity of the maximum centrifugal root stress.
10. Vaneless Space Ratio, D_2/D_3 . This value was unchanged at 1.03. While a reduction was predicted to be marginally beneficial to stage performance as a result of vaneless space losses, the ratio was maintained at the value selected for the reference turbine to avoid possible effects associated with nozzle and rotor interaction with any closer spacing of the nozzle row and the rotor.

AERODYNAMIC DESIGN

Rotor Design

Objectives and Approach

The principal objective of the aerodynamic design is to define the meridional flow path and blading geometries of a tandem row rotor. Based on an evaluation of the results of flow analyses, the geometric specification of the rotor must, of course, be consistent with the overall design intent of designing a high performance stage.

The preliminary design analysis had established the principal dimensions of the rotor together with the inlet and exit flow conditions. The detailed design phase consisted of an iterative procedure making use of the computerized design methods outlined in Appendix I. Although the preliminary design analysis had led to the selection of 12 blades in each row, during the detailed design it was established that either more blades or a greater axial length would be required. Of the two alternatives, the former was selected and the number of blades increased to 16 in each row. The basic reason for the change was that the loading over the rearward portion of the first row had to be reduced below that originally targetted in order to avoid flow separation from the suction surface of the first blade row; any substantial separation might be expected to offset any other advantage associated with a tandem row design. The loss in loading associated with satisfying the blade end condition of equal velocities on both suction and pressure surfaces for the first row while maintaining an acceptable diffusion rate on the suction surface had been underestimated in the preliminary design analysis comparison of tandem row and full blade configurations.

For the revised number of blades, the design objective in terms of the surface velocity distribution is shown in Figure 9; the velocities shown are for an outer casing streamtube. The finally selected meridional flow path through the rotor was based initially on an analysis in which 12 blades were assumed. The objective loading for 12 blades is not illustrated herein. However, to a good approximation it was that which would

be obtained by loading the first blade row so that the composite loading would approach that of a single blade. The rapid unloading near the trailing edge of the first row was subsequently determined to be unachievable without a massive separation of the flow. Since the mean relative and absolute velocities for the design would not be greatly influenced by the change in the number of blades, the meridional flow path geometry was not redefined following the increase from 12 to 16 blades per row.

Rotor Meridional Flow Path

The selected rotor flow path is shown in Figure 10. The rotor tip diameter, the inlet axial width, the annulus diameters at rotor exit, and the axial length of the rotor are as determined by the preliminary analysis. The figure shows the axial location of the split between first and second rows. The hub line of the rotor is a spline curve which matches the slope of stator wall at rotor inlet. Figure 11 shows a comparison between the redesigned and the original stages. It will be seen that only the rotor exit annulus dimensions are unchanged and that the major rotor flow path changes are in the diameter of the rotor, axial length, and in the details of the inner and outer contours. It can be seen that the redesigned flow path has reduced curvatures along the inner and outer contours.

The specifications for the rotor flow path are given in Table IV. This table contains the r , z coordinates of the hub and the outer contour of the rotor; actual stationary casing dimensions are obtained by the addition of clearance to the rotor. The pairs of hub and outer contour points given in the table correspond to the ends of straight-line elements of the blading.

First Blade Row

While the blade camber line definition for a streamline near the outer casing could be computed from the meridional velocity data of preceding flow analyses and the targetted loading distribution, the loading along the hub streamline was constrained by mechanical design considerations. The orientations of the straight-line blade elements defining the

blade were constrained to produce a mechanically acceptable blading standard; the first row trailing edge line is approximately radial. As a result of the constraint, the split of loading between the rows along the hub line was initially a variable in the design iteration. The major portion of the flow path was derived using the ANALS computer program as the design tool. Blade inlet and exit regions, however, were finalized using Program BL2BL as the flow analysis tool.

The finally selected blade geometry is defined in Table V. This table is reproduced from computer output; points of corresponding number define straight-line elements through the mean camber line of inner and outer streamlines with the thickness distribution defined by cones having the specified thickness at the inner and outer contour end points. Blade inlet and exit angles are implicit in the specification of the blade camber. The calculated blade inlet angle varies from approximately -10 degrees at the hub to -13 degrees at the outer contour; thus, the amount of backslope in the rotor inlet is relatively small with the rotor operating in the range of -20 to -17 degrees of incidence at the design point. The calculated deviations at first row exit are relatively small as a result of the specification of relatively lightly loaded trailing edge regions.

The calculated velocity distributions for two streamlines near the outer contour and near the hub are shown in Figures 12 and 13. These plots of blade surface velocities as a function of meridional distance combine data from Programs BL2BL and ANALS with the former used for the inlet and exit regions and the latter for the major portion of the flow field where the assumptions related to a channeled flow are considered valid. The figures demonstrate that diffusion of suction surface velocities has been controlled and that pressure surface diffusions have been restricted to the immediate vicinity of the leading edge.

Second (or Tandem) Blade Row

From Figure 10 it can be seen that the second row can be considered as axial blading to a good approximation. Although row inlet and exit annulus dimensions correspond to their being part of a radial inflow turbine, the radial components of velocity at both stations are relatively minor compared to the axial and tangential components of velocity. Hence,

if a satisfactory distribution of loading and surface velocity distribution could be obtained ignoring the radial components, it is reasonable to expect an acceptable distribution when the resultant geometry was subjected to standard three-dimensional flow analysis.

The program used to obtain the geometric specifications of two constant radius sections (one near the casing and one near the hub) is an NREC computer program based on the Stanitz prescribed velocity distribution method of Reference 10. To select the prescribed distributions of the datum section, the following guide lines were established:

1. The inlet flow angles were those corresponding to the axial and tangential components of velocity at the first row exit at the appropriate radii.
2. The exit angles and Mach numbers were as previously established from the preliminary design results.
3. The velocity distributions were basically those previously established as objectives.
4. The leading edge loading would be such that there would be a negligible effect on the upstream flow angles which would be established by the first row.
5. The loading distribution over the rearward portion of the aerofoils would be such as to avoid any separation. Hence, the deviation of the flow would be predictable by potential flow methods.
6. The stack of the sections together with the area taper ratio should be consistent with the over-all mechanical requirements.

Profiles meeting the above requirements were obtained; the profiles together with the prescribed Mach number distributions used to generate them are shown in Figures 14 and 15. Using these basic profiles and assuming straight-line generation of the complete second blade row, the flow field analysis was completed using Programs ANALS and BL2BL. The calculated blade surface velocity distributions for two streamtubes near the casing and near the hub are shown in Figures 16 and 17; these velocity distributions indicate that the design intent was achieved.

The geometric specification of the second blade row is presented in Table VI. The geometric data are given for two streamlines with corresponding camber line points defining straight-line elements and normal thickness defining conical tapers.

In the table of angular coordinates, the reference angle for the second row is arbitrary; for the final design specification contained in the rotor drawing the leading edge of the second row is located approximately midway between the trailing edges of the first row.

Although the two blade rows were designed independently in terms of the blade-to-blade flow field calculations, the design approach to the rearward portion of the first row and the leading edge region of the second row was such that there is reason to believe the calculated surface velocity distributions are acceptably accurate. The blading, when viewed in terms of the streamline blade angles, $\beta = \tan^{-1} \frac{r_{de}}{dm}$, shows acceptable continuity between the rows; this can be interpreted as having designed blading with small flow deviation from the first row and small incidence at the second row. Figure 18 presents a blade angle plot for both rows for a streamline near the outer casing.

Nozzle Design

The detailed definition of nozzle vanes and meridional flow path geometries and the calculation of free stream velocity distributions were accomplished using the approach described in Appendix I. An initial vane geometry design was generated from a prescribed distribution of loading. Using this same specification and the meridional flow path shown in Figure 19 as input to the flow analysis program ANALS, acceptable distributions of surface velocities were obtained.

The surface velocity distributions shown in Figure 20 for the nozzle vanes were obtained using the more rigorous method of Program BL2BL. Both suction and pressure surfaces show continuous acceleration of the flow from inlet to exit. The calculated deviation at the trailing edge is 0.4 degrees, and the average flow angle at the leading edge of the rotor was calculated to exactly equal the required value of 74.1 degrees.

The selected nozzle geometry is illustrated in Figure 21; the profile consists of a 6 per cent thick NACA-63 airfoil superimposed on a camber line computed from the preselected vane loading distribution. The geometric specification of the vanes is given in Table VII; the vane blading is of constant section in the axial direction.

Exhaust Diffuser Design

Since the dimensions of the turbine rotor exit annulus are unchanged (the exhaust diffuser was constrained to match the testing delivery system) and the total length of the existing diffuser was considered adequately near optimum, the design of the exhaust diffuser consisted primarily of the calculation of flow area as a function of distance from the rotor.

NASA test data of Reference 11 have shown a diffuser designed for a linear static pressure rise to improve the performance of the existing BRU stage. Hence, the diffuser of the subject turbine has also been designed for a linear static pressure rise over the major portion of its length. A constant diameter was selected for the diffuser center body since any residual swirl will adversely affect the performance of an annulus diffuser having a reducing value of inside diameter. Hence, the diffuser aerodynamic design effort consisted of the calculation of the outside diameter for assumed values of total and static pressure as a function of axial length. Since the available length exceeded that necessary for the generally accepted optimum diffusion angle, an initial section of 1.25 in (3.175 cm) was designed for a constant static pressure, and the final exit section of 1.0 in (2.54 cm) was selected to provide a smooth transition to the existing delivery ducting. Over the linear static pressure portion of the diffuser the static pressure was assumed to vary between the diffuser inlet and exit static pressure values determined during the preliminary design analysis (see Table III). Similarly, the linear drop of total pressure through the diffuser is between the total pressure values established during the preliminary design.

The geometric specification of the diffuser is given in Table VIII.

Inlet Scroll Design

The scroll was designed to match an existing 5 in diameter inlet duct. The design procedure used is that detailed in Appendix I with the type of scroll geometry illustrated in Figure 22. Since the nozzle row inlet dimensions have been changed considerably in the redesign turbine compared with those of the reference turbine, a major change in the scroll detail was required. It was decided to design for a more compact scroll. As a result of the more compact design the tangential distance between the center line of the inlet ducting and the axis of the turbine was reduced. This change can be readily accommodated on the turbine test stand.

Even though the pressure loss in the inlet scroll is predicted to have little effect on the over-all performance of the stage, the previously computed loss was included in the calculation of scroll areas. The area and mean radius schedules for the scroll were calculated to be consistent with the design intent of a circumferentially uniform distribution of static pressure and radial component of velocity at nozzle row inlet.

The geometric specification of the inlet scroll is given in Table IX.

Boundary-Layer Analysis

Two-dimensional boundary-layer calculations were undertaken for representative surfaces of the rotor and the nozzle row. The procedure used was that outlined in Appendix I; the computer program used was Program BIANCA of Reference 12. For the rotor, eight surface elements were analyzed corresponding to pressure and suction surfaces of hub and casing streamtubes for both blade rows. For the nozzle row, two stream surfaces corresponding to the pressure and suction surface were analyzed.

These boundary-layer calculations ignore the effect of cross flows; that is, the migration of low momentum boundary layers in directions other than the free stream direction of the inviscid flow field. However, two secondary flow parameters, C_p and Σ , were also calculated to provide a qualitative indication of the magnitude of secondary flow

effects. The first of these parameters serves as an index for end wall flow and, in the case of the rotor, tip leakage. The second serves as an index for boundary-layer flow migration on blade surfaces.

Rotor Data

Figures 23, 24, 25, and 26 present the results of the boundary-layer analysis for the first row of rotor blading. Each figure contains two sets of normalized momentum thickness and shape factor together with the relevant secondary flow parameter for the flow region considered. Figures 27, 28, 29, and 30 present corresponding data for the second row. In only one case was separation predicted, this being for the suction surface of the first blade row at the hub streamtube. However, since the secondary flow will be away from this region of the blade, separation may not in fact occur. Conversely, the flow of low momentum fluid to adjacent streamtubes could cause the separation region to extend. In either event flow separation is not likely to result in any large efficiency penalty since the rearward portion of the first row was intentionally lightly loaded.

While the data presented in Figures 23 through 30 serve principally to illustrate the behavior of the boundary layers in the rotor, the data have been used for the design-point performance prediction discussed later. One tentative conclusion which can be drawn from the boundary-layer analysis is that the rotor design still does not constitute an optimum configuration even though it is expected to outperform the reference rotor. Based on a comparison of data from the first and second rows, it would appear probable that a configuration using more blades in the first row and fewer blades in the second row would result in lower rotor losses. Thus, a tandem row design in which the number of blades in the first row is twice that of the second row is recommended for any further investigation of tandem row radial inflow turbine rotors.

Nozzle Row Data

Figures 31, 32, and 33 present results of boundary-layer analyses for the nozzle row. In the case of the nozzle row the data are expected

to be approximately equal for the forward and rearward end walls. As was to be expected from the previously discussed surface velocity distributions, relatively low values of normalized momentum thickness and shape factor are predicted for the surfaces of the nozzle row. However, the data have been used to calculate a row total pressure loss from which it is inferred that the selected solidity of the nozzle row is in excess of an optimum value.

Design-Point Efficiency Estimate

Following the completion of the aerodynamic design of the nozzle and rotor rows and the boundary-layer analyses discussed above, a reevaluation of design-point performance is possible. Total pressure loss coefficients for the nozzle row and the rotor were obtained using the procedure presented in Reference 13. In turn, these losses can be expressed as efficiency decrements for comparison with the values obtained at the completion of the preliminary design phase. The following tabulation presents the comparison and also includes the diffuser decrements which were not reevaluated.

<u>Component</u>	<u>Efficiency Decrement</u>	
	<u>Preliminary Design</u>	<u>Final Design</u>
Stator	0.0161	0.0341
Rotor	0.0402	0.0440
Diffuser	<u>0.0137</u>	<u>0.0137</u>
Total	0.0700	0.0918

The stator comprises the inlet scroll, the nozzle row, and the vaneless space between the nozzle row exit and the rotor inlet. The above total decrements yield efficiencies based on over-all scroll inlet total pressure to diffuser exit static pressure of 93 and 90.82 per cent, respectively. If it is assumed that the more rigorous loss analysis undertaken following the completion of the detailed aerodynamic design is a more reliable estimate of loss than that undertaken during the final design, the performance improvement compared with the existing design will be 2 rather than 4 percentage points. While the higher loss in the rotor can be traced

to the increase in the number of rotor blades, the more significant change is that in the prediction of the stator system (and in particular the nozzle row) loss and is less readily explained. Which of the two alternative prediction procedures will predict most accurately the total pressure loss in the nozzle row will have to be determined from turbine rig tests. It should be noted that both prediction methods are the result of adapting existing methods for other turbomachinery components to the nozzle row of a radial inflow turbine and the particular case of a row across which there is a significant reduction in blade height. While the prediction procedure used in the preliminary design indicated that 15 blades was an optimum for the nozzle row, the loss derived from boundary-layer analysis can be interpreted as an indication that this number exceeds the optimum.

MECHANICAL DESIGN

Introduction

The detailed mechanical design was carried out such that the research parts are consistent with the existing bearing housing and stand and will meet the package and interface requirements of the BRU, as defined in Reference 2. The various procedures adopted in the mechanical design analyses are documented in Appendix II.

The turbine research parts were designed for ease of assembly so that alteration and/or replacement of the rotor, stator blade row, and exit diffuser are facilitated. An outline drawing, showing interface locations and useful over-all dimensions, is provided in reduced size form in Appendix III, which also contains reproductions of all drawings referred to below. The stress analysis of the rotor was performed to establish an adequate overspeed safety margin under hot design conditions.

A critical speed and bearing load analysis of the rotor system was performed to insure that critical speeds are out of the 10,000 to 35,000 rpm range for performance testing and that the bend shaft critical occurs above 120 per cent of the maximum operating speed. The burst speed of the impeller disk at design temperature was verified to be above 140 per cent of design speed. Peak steady-state dynamic rotor stresses at 120 per cent of design speed were calculated to be below the 0.2 per cent yield strength for the rotor disk material, including the equivalent stresses in the blade attachment areas. Extreme operating conditions were evaluated to assure that blade tip clearance, stress, and balance conditions are acceptable.

Blade stresses due to rotation, aerodynamic loading, and temperature were evaluated and a Goodman diagram plotted to determine the margin of safety for alternating stress. A Campbell diagram was plotted to confirm nonresonant operation from 40 to 120 per cent of design speed.

The design was provided with all instrumentation required with locations consistent with the specified requirements.

Turbine Scroll and Nozzle Design

The turbine scroll and nozzle ring were designed to meet the test operating conditions specified for component testing which included turbine inlet temperature up to 150 deg F (338 deg K) and an inlet pressure range from 10 microns of mercury to 60 psia (414 kN/m^2). The inlet flange was designed to interface with the stub-end flange as specified in AiResearch Drawing No. 699770. Calculations of both maximum stress and axial deflection were performed, and results indicated values to be well within acceptable limits for the materials selected.

Hastelloy X was selected as the material and a welded sheet metal design was established in order to minimize tooling changes and maintain compatibility with requirements for the BRU as defined in Reference 2. Minor changes in the inlet line location were coordinated with the NASA Project Manager in order to incorporate a scroll design which minimizes the vaneless annular space upstream of the nozzle vane inlet and hence has a smaller maximum diameter than that shown in Reference 2. The revised location of the scroll inlet flange is defined in the research turbine assembly outline (Drawing No. 1159-R-003).

The turbine scroll inlet section between the inlet flange and the scroll entrance station was carefully designed to provide a smooth area transition from the 5 in (12.7 cm) diameter circular inlet area to the initial typical cross-sectional area at the 0 degree scroll entrance station as shown in Figure 34. Details of the transition can be seen in the scroll fabrication assembly drawing (Drawing No. 1159-R-006).

Primary emphasis was placed on ease of assembly and alteration or replacement of component parts as can be seen in the cross-section provided in the research turbine package assembly drawing (Drawing No. 1159-R-002). The scroll is bolted directly to the bearing housing with a shim ground to size and placed under the scroll mounting flange to establish the rotor operating clearance of 0.009 to 0.011 in (0.0229 to 0.0279 cm). Provisions were made such that the turbine rotor, turbine nozzle ring, and turbine exhaust stationary shroud, including the diffuser section can all be installed or removed without disturbing the scroll assembly.

Rotor Mechanical Design

Rotor Steady-State Heat Transfer Coefficients

Rotor steady-state heat transfer coefficients, Biot number, and adiabatic wall temperatures are required to calculate rotor metal surface temperatures which are used, in turn, to predict the temperature distributing within the rotor. For analysis purposes, the rotor is subdivided into discrete surface areas, as indicated in Figure 35, and heat transfer coefficients are calculated based upon known and/or assumed boundary conditions. For the disk surfaces, such as BC, CD, and EF in Figure 35, the heat transfer coefficient depends upon the Reynolds and Prandtl number and is calculated by means of equations derived empirically for high velocity flow, the general expression for which is as follows:

$$h_{eff} = \left[0.0195 K \left(\frac{\rho W}{\mu} \right)^{0.8} \right] r^{0.6} \times Pr = \frac{A_{eff}}{A_{disk}} \times h_c \quad (5)$$

where K is fluid conductivity

ρ is density

W is relative velocity

μ is viscosity

r is radius

Pr is Prandtl number

A_{eff} is effective heat transfer area

A_{disk} is surface area of disk

and h_c is standard heat transfer coefficient.

For the areas where blades exist, such as surface DE in Figure 35, the surface is treated as a finned surface and the additional heat transfer is accounted for by a correction to the standard heat transfer coefficient based upon the appropriate area ratio as indicated in the above equations.

In the rotor attachment area, AB in Figure 35, the heat transfer coefficient is assumed to be simply the ratio of metal conductivity, K_{met} , divided by the length of the attachment surface or heat transfer

path, L , and the heat flux is calculated in this area from the boundary temperature conditions, one of which is assumed to be the temperature of the shaft at the bearing location.

After the heat transfer coefficient has been computed, the heat transfer between the fluid and the solid body is further described in the appropriate areas of Figure 35 by the standard dimensionless grouping of variables further identified as the Biot number and defined as

$$Bi = \frac{h_{eff} r_p}{K_{met}} \quad (6)$$

where h_{eff} is effective heat transfer coefficient

r_p is outside radius of disk

and K_{met} is metal conductivity.

Finally, adiabatic wall temperature is reevaluated from the general equations

$$T_{aw} = T_{\infty} + f_r \frac{W^2}{2gJc_p} \quad (7)$$

where

$$f_r = (Pr)^{1/2}$$

The adiabatic wall temperature, T_{aw} , is based upon the temperature assumed by an insulated plate when exposed to a high velocity hot gas stream. The recovery factor, f_r , assumes a turbulent boundary layer associated with high velocity flow and is based upon Prandtl numbers in the range between 0.5 and 2.0. The variables in the above equation are local static temperature, T_{∞} , local relative velocity, W , fluid specific heat at constant pressure, c_p , and Prandtl number, Pr .

For the blades portion of the disk, DE, relative velocity and static temperatures are evaluated at points along the mid-streamline of the blade passage. Relative velocity on the back, or unbladed portion of the disk, BC, is assumed to be one half of the local disk tangential velocity.

A summary of the results of these calculations is provided in Table X, which lists the Biot number and adiabatic wall temperature as a function of radius for the various surface areas of the turbine rotor.

Calculation of Temperature Distribution in Rotor

The rotor adiabatic wall temperature and Biot number data were used to determine the temperature distribution both on the surface and internal temperatures of the rotor. The results of this analysis are plotted in Figure 36, which shows constant temperature lines plotted on a cross-section of the rotor disk. The analysis was performed using Program THERMAL STRESS of Reference 4.

Thermal and Mechanical Disk Stress

An analysis of disk stresses and deflections was also performed with the use of Program THERMAL STRESS, which produces results based upon the geometry, operating speed, and temperature conditions provided. Both radial and tangential stresses were calculated and these are shown as a function of radius in Figures 37, 38, and 39 for 100 per cent, 120 per cent, and 140 per cent speed, respectively. Radial and tangential stress distributions are also shown in Figures 40 and 41, respectively, for the 100 per cent speed condition. All of the above information is provided at design operating temperatures of the BRU rather than the turbine stage re-search package.

The selected material for the rotor is Inconel Alloy 713LC; this was the material selection for the original turbine also. Before making the decision to retain the material specification of Reference 2, other materials were also evaluated. Table XI lists the properties of the materials considered. Reference to the properties of 713LC shown in Table XI and the stress data in Figures 37 through 41 will show that there are no advantages associated with a change in the rotor material nor is a change necessary to meet the turbine life objective. It is evident that the rotor design easily satisfies the requirements that the

maximum steady-state dynamic design stress at 120 per cent be less than the 0.2 per cent yield strength and that the burst speed of the rotor testing, based upon material ultimate strength, shall be above 140 per cent of the design speed. Equivalent stress, as usually defined, is shown in Figure 42 as a function of radius for both the front and back faces of the disk at 120 per cent speed and design operating temperature.

Calculated values of average tangential stress are provided in Table XII for 100, 120, and 140 per cent operating speeds for design operating temperature conditions. Also shown in the table are calculated values for average tangential stress at room temperature for a disk of alloy 713LC material at 120 per cent speed and aluminum alloy 7079-T6 at 100 per cent speed. Axial and radial disk tip deflections calculated for the five cases above are also included in Table XII.

Axial and radial deflection, as a function of radius, are provided in Figures 43 and 44, respectively, for the 120 per cent speed condition at operating temperature. These figures also include data for equivalent deflections at the lower level to be used in turbine rig tests.

Based on cost and delivery estimates assuming three or less rotors would be procured, a machined rotor is recommended.

Blade Root Stresses

Blade root stresses due to centrifugal loading were calculated using Program BLDR0T of Reference 14. The blade geometry is considered as a series of beams of rectangular cross section, pinned at the shroud line to adjacent beams but otherwise unrestrained except at hub; relatively conservative values of computed stress are expected from this approach. Blade thickness distributions used at the hub and shroud of the first and second blade rows, respectively, are shown in Figures 45 and 46. Calculated blade root bending and tensile stresses at 120 per cent speed are presented in Figures 47 and 48 for the first and second blade rows, respectively.

Blade Natural Frequency

Blade leading and trailing edge frequencies were calculated based upon plate theory. The plate model was assumed clamped on two sides, representing its attachment to the rotor hub and to the adjacent blade section or panel. Results are summarized in Table XIII; the lowest frequency was, as expected, calculated to be that for the second blade row trailing edge. A Campbell or interference diagram is plotted in Figure 49; the blade natural frequencies are shown relative to multiples of the rotor "once-per-revolution" frequency, f in cps.

Blade Vibratory Stress Levels

For the purpose of calculating blade vibratory stress, blade aerodynamic loading was calculated from the blade static pressures at hub and shroud and assuming a linear pressure distribution between these two points. An amplification factor based on the method of Trumpler and Owens (Ref 15) was used, with an appropriate stress concentration factor and the blade aerodynamic bending stress, to obtain a design value for the blade vibratory stress. The calculated results are shown in Table XIII and on the Goodman diagram provided as Figure 50. While predicted vibratory stress levels in the second row are not insignificant, they are nevertheless acceptably low.

Flexural Vibrations

A shaft flexural vibration analysis was performed on the rotor system illustrated in Figure 51. The system consists of the turbine, the rotor shaft mounted in two bearings, and half the aluminum disk coupling mounted on the output end of the shaft. The critical speed analysis was performed using an NREC computer program, Program HOLZER, which is based on standard procedures presented in Reference 16 and outlined in Appendix II. The analysis was completed for a range of turbine end bearing stiffness while maintaining a rear bearing stiffness of 2.5×10^5 lbf per in (4.38×10^5 N/cm) (as assumed in Ref 2). The results of the calculations are shown in Figure 52 which illustrates that there are no critical

speeds in the operating range from 10,000 to 43,200 rpm for an assumed turbine end bearing stiffness of 3×10^4 lbf per in (5.25×10^4 N/cm) (the stiffness assumed in Ref 2).

An analysis was also performed of a similar rotor system but assuming an aluminum turbine disk. As can be seen in Figure 52, the first rotor critical speed now occurs at 14,000 rpm, which is within the specified operating range and hence unsatisfactory. An aluminum alloy rotor was considered for the research package because stress and temperature levels would permit its use, reduce manufacturing costs, and facilitate manufacture.

Shaft Attachment Methods

The rotor will be attached to the shaft by means of a heavy shrink fit, as indicated in turbine wheel assembly Drawing No. 1159-E-005. Based on considerable experimental evidence, the heavy interference fit has more than adequate torque capacity and axial holding stability for the research application planned and will be used without radial pins of any kind to avoid the installation and operating problems which may accompany such devices. The stress concentrations resulting from radial holes in the highly stressed attachment area are also avoided.

Bearing Analysis

The adequacy of the existing bearing of the turbine research package was investigated. It was concluded that the bearing will meet the design objective of a time between overhaul (TBO) of 300 hours minimum. This conclusion is based on the calculated value of the expected minimum B_{10} life of the bearing.

The bearing used in the turbine research package is described in Reference 2. The description consists of the major characteristics of the bearing and a source control drawing. Simply stated, it is a Type 7104 angular contact ball bearing. As such, its B_{10} life should be obtained using the method established by the Anti-Friction Bearing Manufacturers Association (AFBMA). This method requires the calculation of

the thrust load and the radial load acting on the bearing. The details of the calculations are given below.

Thrust Calculation

The calculation of the net thrust on the wheel is based on considerations of the wheel as an open system. The axial forces acting on the wheel arise from the frontal and back pressures of the fluid and the change in axial momentum of the fluid. Hence,

$$\text{THRUST} = \int_0^{r_2} (P_f - P_b) 2\pi r dr + \frac{\dot{m} C_{m4}}{g_0} \quad (8)$$

where P_f is the frontal pressure

P_b is the back pressure of the fluid

r_2 is the tip radius of the wheel

\dot{m} is the mass flow

and C_{m4} is the axial velocity at the turbine exit.

A net thrust in the direction of the exit flow of 74.9 lbf (333.2 N) was obtained for the fluid properties and the design flow conditions. More specifically, a mass flow of 0.748 lbm per sec (0.3395 kg/sec), an exit axial velocity of 241 fps (73.5 m/sec), and the pressures shown in Figure 53 were used to evaluate the thrust. The frontal pressure in Figure 53 corresponds to static pressure at the shroud for $1.730 \text{ in} \leq r \leq 2.634 \text{ in}$ ($4.394 \text{ cm} \leq r \leq 6.690 \text{ cm}$), a linear variation between the hub and shroud values of the exit states pressure for $0.911 \text{ in} \leq r \leq 1.730 \text{ in}$ ($2.314 \text{ cm} \leq r \leq 4.394 \text{ cm}$), and the exit static pressure at the hub for $0 \leq r \leq 0.911 \text{ in}$ (2.314 cm). The back pressure, on the other hand, corresponds to a variation from the rotor inlet static pressure defined by

$$\frac{dp}{dr} = \frac{\rho W^2}{g_0 r} \quad (9)$$

where ρ is the fluid density and W is the relative velocity. Assuming that the fluid in back of the wheel rotates at one half of the wheel speed, ω , the pressure variation may be rewritten as

$$\frac{dp}{dr} = \frac{1}{4} \frac{\rho \omega^2 r}{g_0} \quad (10)$$

The density is evaluated at the turbine inlet conditions.

Radial Load Calculation

The radial load exerted on the bearing is obtained using the "2g" approximation. That is, the reaction of the bearing to the dynamic radial load is assumed to be less than or equal to the reaction to twice the static load. The reaction of the thrust bearing, R_1 , can be obtained from a summation of the forces and moments.

A reaction of 11.1 lbf (49.4 N) was obtained based on a weight of the turbine wheel, W_T , of 3.868 lb (1.75 kg), a distance between the centers of gravity of the wheel, and the thrust bearing of 2.371 in (6.022 cm), and a distance between the centers of gravity of the bearings of 4.006 in (10.175 cm). Distributing twice the weight of the shaft evenly between the bearings results in additional reaction of 2.1 lbf (9.34 N) or a total radial load of 13.2 lbf (58.72 N) for the thrust bearing.

Expected Minimum B_{10} Life

The AFMBA method of calculating B_{10} life states that

$$\text{minimum life in hours} = 500 \times (\text{service factor})^3$$

where

$$\text{service factor} = \frac{\text{rated capacity}}{\text{equivalent load}}$$

The rated capacity of a Type 7104 bearing at the required speed of 36,000 rpm is obtained according to AFMBA procedures from

$$\text{rating at required speed} = \text{rating at 1000 rpm} \times 3 \frac{1000 \text{ rpm}}{\text{required speed}}$$

Hence, a rated load at 36,000 rpm of 214 lb (952 N) is obtained based on a rating at 1000 rpm of 710 lb (3158 N). The equivalent load of any 7100 series bearing is obtained by selecting the maximum value from

$$E = 0.51VR + T \quad \text{or} \quad E = 1.31VR$$

where E is the equivalent load

R is the radial load

T is the thrust load

and V is 1.0 for an inner rotating race.

Using the results previously obtained and the preferred bearing preload of 60 lbf (267 N), an equivalent load of 142 lbf (632 N) is obtained. Hence, from calculated rated capacity and equivalent load, the B_{10} minimum life is 1670 hrs.

Diffuser Design

The diffuser assembly is shown in diffuser machining Drawing No. 1159-D-010. The installation of the diffuser is shown in both the turbine research package assembly Drawing No. 1159-R-002 and the turbine research package outline Drawing No. 1159-R-003. Instrumentation pads for the total pressure traverse at inlet and exit are provided in addition to static pressure taps on the outer wall and on the center body at both inlet and exit. The center body is supported axially and radially and maintained concentric with the outer contour by two sets of three aerodynamically shaped struts installed near the inlet and exit of the diffuser, as shown on the referenced drawings.

It is assumed that an external support exists and will be provided and used in the final assembly to prevent distortion of the scroll and nozzle assembly, due to the large overhung mass of the diffuser. The exhaust adapter Drawing No. 1159-D-011 was designed to interface with the existing laboratory exhaust system in both length and diameter, as specified.

Final Assembly and Installation

Copies of all detail drawings produced, plus the assembly, outline, and layout drawings are provided in Appendix III. The assembly drawing includes a complete parts list, also shown separately, with miscellaneous tools required in Table XIV. Assembly procedures are covered in the notes on appropriate drawings and all instrumentation locations are established in either the detail drawings, the assembly, or the outline drawing.

CONCLUSIONS AND RECOMMENDATIONS

Conclusions

1. A complete radial inflow turbine stage comprising an inlet scroll, a vaned nozzle row, a rotor, and an exhaust diffuser has been designed and drawings for all new parts prepared. The stage is a redesign for a BRU turbine previously tested in a turbine research package. The new design is the result of an aerodynamic optimization; although the rotor diameter has been increased and nonradial blading introduced, the increase in stress levels is mechanically acceptable because of the relatively low levels of rotor tip speed and the operating temperature. The rotor mechanical design analysis has been completed for the actual BRU operating conditions. However, the stationary parts consisting of the scroll, the nozzle row, and the diffuser have been designed for the research package and its lower operating temperatures.
2. The design-point efficiency of the redesigned stage, based on over-all total-to-static pressure ratio from scroll inlet to diffuser discharge, is predicted to be between 91 and 93 per cent representing a 2 to 4 percentage point improvement compared with the original design.
3. The uncertainty associated with the predicted stage design-point efficiency largely reflects the uncertainty in the prediction of the nozzle row loss coefficient. The low loss coefficient and high efficiency assessment is based on a loss correlation based on axial turbine stator rows which was developed for the preliminary design analysis. In this method the number of blades is optimized based on a trade-off between exit passage aspect ratio and trailing edge blockage but assumes the row will be designed with near-optimum solidity. The efficiency assessment applied to the final design standard is based on the calculation of boundary layers

with a correction based on wall-to-blade surface areas. The latter efficiency assessment indicates that the solidity of the nozzle row is considerably in excess of an optimum. However, at this time neither method of predicting nozzle row loss coefficients can be regarded as superior to the other, since there are no experimental data for nozzle rows of the type selected, that is, one in which there is a substantial contraction of axial width across the nozzle row.

4. The rotor has been designed using a tandem row configuration with 16 blades in each of the two rows. The predicted efficiency of the rotor is responsible for an approximate 1.5 per cent increase in stage efficiency compared with the original design. One disadvantage associated with the design of a two-row configuration highlighted during the final design was that a greater number of blades per row would be required in a tandem configuration compared with one with full rotor blading from inlet to exit. The selection of surface velocity distributions to avoid flow separation from the suction surface of the first row leads to a limitation on the blade loading for the first row.
5. The exhaust diffuser has been designed for a linear rate of static pressure rise following an initial section of constant static pressure immediately downstream of the rotor. The predicted improvement in over-all efficiency of the stage includes a 0.9 percentage point improvement for the redesigned diffuser.

Recommendations

The turbine stage is to be manufactured and tested. Hence, recommendations for further modification to improve stage performance will depend largely on the measured performance characteristics of the stage. Nevertheless, a critical review of the design standard and predictions based on this standard lead to the following recommendations.

1. Two or more additional nozzle vane geometries should be designed and tested. This recommendation is based on the uncertainty of current prediction techniques for nozzle rows with axial passage width contraction. Since the nozzle row can be characterized by a number of geometric variables and aerodynamic parameters, changes in the row solidity by a reduction in the number of blades and by a reduction in blade chords (by reducing the inlet-to-exit diameter ratio) are recommended.
2. Based on a review of the surface velocity distributions for the tandem row configuration with 16 blades in each row and boundary-layer calculations for the computed distributions, it would appear likely that further improvements could be made in the design-point performance of the rotor. It is recommended that a design with more blades in the first row and fewer blades in the exducer section be considered. A design with 18 or 20 blades in the first row and 9 or 10 in the second would be recommended, subject to more detailed flow analyses of design alternatives.

REFERENCES

1. Nusbaum, William J. and Kofskey, Milton G., Cold Performance Evaluation of 4.97-Inch Radial-Inflow Turbine Designed for Single-Shaft Brayton Cycle Space-Power System (NASA TN D-5090), National Aeronautics and Space Administration, March, 1969.
2. Dunn, James., Design and Fabrication of the Brayton Cycle High Performance Turbine Research Package (NASA CR-72478), National Aeronautics and Space Administration, February, 1968.
3. The Design and Performance Analysis of Radial-Inflow Turbines, Volume I - Theory and Practice of Design (NREC Report No. 1067-1), Northern Research and Engineering Corporation, Cambridge, Massachusetts, 1964.
4. The Design and Performance Analysis of Radial-Inflow Turbines, Volume II - Design Examples and Digital Computer Programs (NREC Report No. 1067-2), Northern Research and Engineering Corporation, Cambridge, Massachusetts, 1964.
5. Katsanis, Theodore, Computer Program for Calculating Velocities and Streamlines on a Blade-to-Blade Stream Surface of a Turbomachine (NASA TN D-4525), National Aeronautics and Space Administration, Washington, D. C., April, 1968.
6. Analysis of Geometry and Design Point Performance of Axial Flow Turbines, Part I - Development of the Analysis Method and the Loss Coefficient Correlation (NREC Report No. 1125-1), Northern Research and Engineering Corporation, Cambridge, Massachusetts, September 14, 1967.
7. An Investigation of Efficiency Limits for Small, Cooled Turbines (NREC Report No. 1137-1), Northern Research and Engineering Corporation, Cambridge, Massachusetts, May 8, 1970.
8. Roark, Raymond J., Formulas for Stress and Strain, McGraw-Hill, Fourth Edition, 1965.
9. Voysey, R. G., "Some Vibration Problems in Gas Turbine Engines", Proceedings of the Institute of Mechanical Engineers, vol. 152, 1945, p. 419.
10. The Design of Turbine Blading by a Prescribed Velocity Distribution Method (NREC Report No. 1104-1), Northern Research and Engineering Corporation, Cambridge, Massachusetts, June 30, 1966.
11. Rohlik, Harold E., Kofskey, Milton G., and Nusbaum, William J., Radial Inflow Turbine Performance with an Exit Diffuser Designed for Linear Static Pressure Variation (NASA TM X-52890), National Aeronautics and Space Administration, September, 1970.
12. An Engineering Research Program for Centrifugal Compressors: Compressible Turbulent Boundary Layer Development with Cross Flow, Rotation, and Normal Pressure Gradients (NREC Report No. 1143-18), Northern Research and Engineering Corporation, Cambridge, Massachusetts, June, 1970.

13. Stewart, W. L., Whitney, W. J., and Wong, R. T., 'A Study of Boundary Layer Characteristics of Turbomachine Blade Rows and Their Relation to Overall Blade Loss, J. of Basic Eng., Trans. ASME, vol. 82, 1960, p. 588.
14. Bear, M. S. and Platt, M., Computer Program for the Estimation of Root Stresses in Centrifugal Impeller Blading (NREC Report No. 900AF-1), Northern Research and Engineering Corporation, Cambridge, Massachusetts, August 26, 1970.
15. Trumpler, W. E., Jr. and Owens, H. M., "Turbine Blade Vibration and Strength", Trans. ASME, April, 1955.
16. Den Hartog, J. P., Mechanical Vibrations, McGraw-Hill Book Company, New York, 1956.
17. Eckert, B. and Schnell, E., Axial-und Radial Kompressoren, pp. 417-430.
18. The Design and Performance Analysis of Centrifugal Fluid Machines, Volume I - Theory and Practice of Design (NREC Report No. 1061-1), Northern Research and Engineering Corporation, Cambridge, Massachusetts, May, 1963.
19. A Computing System for the Design and Analysis of Radial Turbomachinery, Volume I - Bases and Capabilities of the System (NREC Report No. 1000B-1), Northern Research and Engineering Corporation, Cambridge, Massachusetts, 1967.
20. A Computing System for the Design and Analysis of Radial Turbomachinery, Volume II - Description of Computer Programs (NREC Report No. 1000B-2), Northern Research and Engineering Corporation, Cambridge, Massachusetts, 1967.
21. An Engineering Research Program for Centrifugal Compressors: Volume I - Blade-to-Blade Velocity Distribution Computer Program (NREC Report No. 1143-16), Northern Research and Engineering Corporation, Cambridge, Massachusetts, May, 1970.
22. An Engineering Research Program for Centrifugal Compressors: Volume II - Blade-to-Blade Velocity Distribution Computer Program (NREC Report No. 1143-17), Northern Research and Engineering Corporation, Cambridge, Massachusetts, May, 1970.
23. An Engineering Research Program for Centrifugal Compressors: Compressible Turbulent Boundary Layer Development with Cross Flow, Rotation, and Normal Pressure Gradients (NREC Report No. 1143-18), Northern Research and Engineering Corporation, Cambridge, Massachusetts, June, 1970.
24. Stanitz, J. D. and Prian, V. O., A Rapid Approximate Method for Determining Velocity Distribution on Impeller Blades of Centrifugal Compressors (NACA TN 2421), National Advisory Committee for Aeronautics, July, 1951.
25. Computer Program for the Analysis of Annular Combustors, Volume I - Calculation Procedures (NASA CR-72374), National Aeronautics and Space Administration, Washington, D. C., January 29, 1968.

26. Computer Program for the Analysis of Annular Combustors, Volume II - Operating Manual (NASA CR-72375), National Aeronautics and Space Administration, Washington, D. C., January 29, 1968.
27. Dussourd, J. L., et al, Aerodynamic Criteria for Optimum Design of Mixed-Flow Impellers - Experimental Results for Impellers I and IB (WADC TN 58-88), AiResearch Manufacturing Company, June, 1960.
28. von Doenhoff, A. E. and Tetervin, N., Determination of General Relations for the Behavior of Turbulent Boundary Layers (NACA Rep 772), National Advisory Committee for Aeronautics, 1943.
29. Reneau, L. R., Johnston, J. P., and Kline, S. J., Performance and Design of Straight, Two-Dimensional Diffusers (ASME Prep. 66-GE-10), American Society of Mechanical Engineers, May, 1966.
30. Sovran, G. and Klomp, E. D., Experimentally-Determined Optimum Geometries for Rectilinear Diffusers with Rectangular, Conical or Annular Cross-Section, Presented at the Symposium "Fluid Mechanics of Internal Flow", General Motors Research Laboratories, Michigan, September, 1965.
31. Horgner, Oscar J., ASME Metals Engineering Design Handbook, Chapter 6.17, 1953.
32. Timoshenko, S. and MacCullough, G. H., Elements of Strength of Materials, D. Van Nostrand Company, Inc., Princeton, New Jersey, Third Edition, June, 1949.

TABLES

TABLE 1
MAJOR DESIGN GEOMETRIC VALUES FOR DATUM TURBINES
USED IN THE PARAMETRIC INVESTIGATION

<u>Parameter</u>	<u>Subject[*]</u> <u>Turbine</u>	<u>Datum 3</u>	<u>Datum 2</u>	<u>Datum 1</u>	<u>Reference^{**}</u> <u>Turbine</u>
Nozzle Vane Inlet Diameter, in (cm)	7.654 (19.441)	7.430 (18.872)	7.144 (18.146)	6.869 (17.447)	6.656 (16.906)
Nozzle Vane Exit Diameter, in (cm)	5.426 (13.782)	5.438 (13.812)	5.438 (13.812)	5.331 (13.541)	5.118 (13.000)
Rotor Inlet Diameter, in (cm)	5.268 (13.381)	5.281 (13.414)	5.281 (13.414)	5.177 (13.149)	4.970 (12.624)
Rotor Exit Tip Diameter, in (cm)	3.460 (8.788)	3.460 (8.788)	3.460 (8.788)	3.460 (8.788)	3.460 (8.788)
Rotor Exit Hub Diameter, in (cm)	1.822 (4.628)	1.822 (4.628)	1.822 (4.628)	1.822 (4.628)	1.822 (4.628)
Nozzle Inlet Width, in (cm)	0.560 (1.422)	0.434 (1.102)	0.417 (1.059)	0.401 (1.018)	0.385 (0.978)
Nozzle Exit Width, in (cm)	0.400 (1.016)	0.400 (1.016)	0.400 (1.016)	0.385 (0.978)	0.385 (0.978)
Rotor Inlet Width, in (cm)	0.400 (1.016)	0.400 (1.016)	0.400 (1.016)	0.385 (0.978)	0.385 (0.978)
Axial Length, in (cm)	1.552 (3.942)	1.627 (4.132)	1.694 (4.303)	1.765 (4.483)	1.765 (4.483)
Number of Rotor Blades	10	11	11	11	11
Number of Splitters	10	11	11	11	11
Number of Nozzle Vanes	15	15	14	13	13

* The "subject turbine" is essentially that selected at the conclusion of the preliminary design investigation. The rotor configuration was later changed to a tandem row.

** The "reference turbine" is the AiResearch design of Reference 2.

TABLE II
SUMMARY OF STAGE PERFORMANCE AND
OPERATING CONDITIONS

Parameter	Subject Turbine (Rotor Diameter = 5.268 in) (13.381 cm)	Reference Turbine (Rotor Diameter = 4.97 in) (12.624 cm)
Total-to-Total Efficiency at Rotor Exit, η_{t4}	0.9433	0.913
Total-to-Static Efficiency at Rotor Exit, η_{s4}	0.9009	0.870
Total-to-Total Efficiency at Diffuser Exit, η_{t5}	0.9358	0.896
Total-to-Static Efficiency at Diffuser Exit, η_{s5}	0.9300	0.890
Over-All Efficiency, η_{ov}^*	0.9249	0.887
Inlet Total Temperature, T_{oo} , deg R	2060 (1144 deg K)	2060 (1144 deg K)
Inlet Total Pressure, P_{oo} , psia	25 (172 kN/m ²)	25 (172 kN/m ²)
Weight Flow, \dot{m} , lbm per sec	0.7484 (0.3395 kg/sec)	0.7484 (0.3395 kg/sec)
Shaft Work, k_w , kilowatts	18.08	17.33
Turbine Speed, N , rpm	36,000	36,000
Specific Speed, N_s , ft ^{3/4} / (min)(sec ^{1/2})	75.1 (30.8 m ^{3/4} / (min)(sec ^{1/2}))	75.9 (31.1 m ^{3/4} / (min)(sec ^{1/2}))
Turbine Inlet Total-to- Diffuser Exit Static Pres- sure Ratio, P_{oo}/P_5	1.763	1.763

* Over-all efficiency (η_{ov}) = (total-to-static efficiency at diffuser exit; - efficiency decrement due to disk friction).

TABLE III

PRELIMINARY DESIGN-POINT PERFORMANCE AND FLOW FIELD DETAILS

DESIGN OPERATING CONDITIONS

ROTATIONAL SPEED	RPM	36000.00
ABSOLUTE MASS FLOW	W	.7484
TOTAL-TO-TOTAL PRESSURE RATIO AT 4	PRT4	1.7472
TOTAL-TO-STATIC PRESSURE RATIO AT 4	PRS4	1.7997
TOTAL-TO-TOTAL PRESSURE RATIO AT 5	PRT5	1.7560
TOTAL-TO-STATIC PRESSURE RATIO AT 5	PRS5	1.7630
GAS CONSTANT	RGAS	18.4570
SPECIFIC HEAT RATIO	GAM	1.6667
TURBINE REYNOLDS NUMBER	REYT	72041
SPECIFIC SPEED	SPSD	75.10

STAGE PERFORMANCE

SHAFT WORK	WORK	18.077
OVERALL EFFICIENCY	ETA0V	.9249
TOTAL-TO-TOTAL EFFICIENCY AT 4	ETAT4	.9433
TOTAL-TO-STATIC EFFICIENCY AT 4	ETAS4	.9009
TOTAL-TO-TOTAL EFFICIENCY AT 5	ETAT5	.9358
TOTAL-TO-STATIC EFFICIENCY AT 5	ETAS5	.9300

COMPONENT EFFICIENCY DECREMENTS

NOZZLE TOTAL	DETAN	.0161
ROTOR TOTAL	DETA R	.0402
DIFFUSER TOTAL	DETAET	.0137

BREAKDOWN OF EFFICIENCY DECREMENTS

SCROLL FRICTION	DETA SC	.0026
NOZZLE VANE LOADING	DETA VB	.0082
NOZZLE ASPECT RATIO	DETA VA	.0033
NOZZLE VANE TRAILING EDGE	DETA VT	.0002
NOZZLE REYNOLDS NUMBER	DETA VR	.0009
VANELESS SPACE FRICTION	DETA VL	.0032
ROTOR FRICTION	DETA RF	.0079
ROTOR CLEARANCE	DETA RC	.0109
ROTOR DIFFUSION AND FRICTION	DETA RD	.0294
DIFFUSER	DETA DI	.0077
DISCHARGE	DETA DE	.0060
DISC FRICTION (WINDAGE)	DETA DF	.0051
NOZZLE VANE TOTAL	DETA VN	.0103

TABLE III (CONTINUED)

PRELIMINARY DESIGN-POINT PERFORMANCE AND FLOW FIELD DETAILSFLOW AND GEOMETRIC DATA AT STATION 0

ABSOLUTE TOTAL PRESSURE	P00	3600.00
ABSOLUTE TOTAL TEMPERATURE	T00	2060.00
STATIC PRESSURE	P0	3595.34
STATIC TEMPERATURE	T0	2058.93
ABSOLUTE VELOCITY	C0	36.23
ABSOLUTE MACH NUMBER	EM0	.0394
MEAN DIAMETER (SCROLL)	DOMIN	16.040
MEAN HYDRAULIC DIAMETER (SCROLL)	DHSCIN	2.546
SCROLL FRICTION COEFFICIENT	CFSC	.00531

FLOW AND GEOMETRIC DATA AT STATION 1

ABSOLUTE TOTAL PRESSURE	P01	3595.00
ABSOLUTE TOTAL TEMPERATURE	T01	2060.00
STATIC PRESSURE	P1	3561.92
STATIC TEMPERATURE	T1	2052.00
ABSOLUTE VELOCITY	C1	150.11
MERIDIONAL VELOCITY	CM1	85.02
ABSOLUTE TANGENTIAL VELOCITY	CT1	123.71
ABSOLUTE GAS ANGLE	ALF1IN	55.50
ABSOLUTE MACH NUMBER	EM1	.105
DIAMETER	D1IN	7.654
PASSAGE WIDTH	B1IN	.5600

REPRODUCIBILITY OF THE ORIGINAL PAGE IS POOR.

52

TABLE III (CONTINUED)

PRELIMINARY DESIGN-POINT PERFORMANCE AND FLOW FIELD DETAILS

FLOW AND GEOMETRIC DATA AT STATION 2

ABSOLUTE TOTAL PRESSURE	P02	3575.19
ABSOLUTE TOTAL TEMPERATURE	T02	2060.00
STATIC PRESSURE	P2	2896.63
STATIC TEMPERATURE	T2	1893.67
ABSOLUTE VELOCITY	C2	702.08
MERIDIONAL VELOCITY	CM2	184.96
ABSOLUTE TANGENTIAL VELOCITY	CT2	677.27
ABSOLUTE GAS ANGLE	ALF2IN	74.73
ABSOLUTE MACH NUMBER	EM2	.513
DIAMETER	D2IN	5.426
PASSAGE WIDTH	B2IN	.4120
NOZZLE TRAILING EDGE ANGLE	BETA2I	74.23
NOZZLE TRAILING EDGE THICKNESS	TENIN	.0100
NUMBER OF NOZZLE VANES	ZN	15
NOZZLE THROAT/HEIGHT ASPECT RATIO	AR	1.623
RATIO OF TRAILING EDGE/THROAT WIDTH	TEOTW	.033

FLOW AND GEOMETRIC DATA AT STATION 3

ABSOLUTE TOTAL PRESSURE	P03	3569.86
ABSOLUTE TOTAL TEMPERATURE	T03	2060.00
RELATIVE TOTAL PRESSURE	P03R	2925.42
RELATIVE TOTAL TEMPERATURE	T03R	1902.31
STATIC PRESSURE	P3	2852.64
STATIC TEMPERATURE	T3	1883.23
ABSOLUTE VELOCITY	C3	723.76
MERIDIONAL VELOCITY	CM3	198.15
ABSOLUTE TANGENTIAL VELOCITY	CT3	696.11
ABSOLUTE GAS ANGLE	ALF3IN	74.11
ABSOLUTE MACH NUMBER	EM3	.531
RELATIVE VELOCITY	W3	237.75
RELATIVE TANGENTIAL VELOCITY	WT3	-131.39
RELATIVE GAS ANGLE	ALF3RI	-33.55
RELATIVE MACH NUMBER	EM3R	.174
WHEELSPEED	U3	827.49
DIAMETER	D3IN	5.268
PASSAGE WIDTH	B3IN	.4000
ROTOR INLET BLADE ANGLE	BETA3I	4.78
ROTOR BLADE NUMBER	ZR3	12

REPRODUCIBILITY OF THE ORIGINAL PAGE IS POOR.

53

TABLE III (CONTINUED)

PRELIMINARY DESIGN-POINT PERFORMANCE AND FLOW FIELD DETAILS

FLOW AND GEOMETRIC DATA AT STATION 4

TOTAL ABSOLUTE PRESSURE	P04	2060.42
TOTAL ABSOLUTE TEMPERATURE	T04	1671.24
TOTAL RELATIVE PRESSURE	P04R	2244.10
TOTAL RELATIVE TEMPERATURE	T04R	1729.31
STATIC PRESSURE	P4	2000.33
STATIC TEMPERATURE	T4	1651.57
ABSOLUTE VELOCITY	C4	241.42
MERIDIONAL VELOCITY	CMM4	241.42
ABSOLUTE TANGENTIAL VELOCITY	CTM4	0.00
ABSOLUTE GAS ANGLE	ALFM4I	0.00
ABSOLUTE MACH NUMBER	EM4	.189
RELATIVE VELOCITY	W4	479.98
RELATIVE TANGENTIAL VELOCITY	WTM4	414.85
RELATIVE GAS ANGLE	ALF4RI	-59.80
RELATIVE MACH NUMBER	EM4R	.376
WHEELSPEED	UM4	414.85
DIAMETER AT HUB	DH4IN	1.822
DIAMETER AT MEAN RADIUS	DM4IN	2.041
DIAMETER AT SHROUD	DS4IN	3.460
PASSAGE WIDTH	B4IN	.8190
BLADE EXIT ANGLE AT MEAN RADIUS	BETA4I	-56.07
TRAILING EDGE THICKNESS AT MEAN RADIUS	TERIN	.0500
MEAN ROTOR BLADE PASSAGE HYDRAULIC DIA	DHRIN	.6850
ROTOR BLADE NUMBER	ZR4	12

REPRODUCIBILITY OF THE ORIGINAL PAGE IS POOR.

54

TABLE III (CONTINUED)

PRELIMINARY DESIGN-POINT PERFORMANCE AND FLOW FIELD DETAILS

FLOW AND GEOMETRIC DATA AT STATION 5

ABSOLUTE TOTAL PRESSURE	P05	2050.11
ABSOLUTE TOTAL TEMPERATURE	T05	1671.24
STATIC PRESSURE	P5	2041.97
STATIC TEMPERATURE	T5	1668.58
ABSOLUTE VELOCITY	C5	88.70
ABSOLUTE MACH NUMBER	EM5	.069
SHROUD DIAMETER	DS5IN	5.160
HUB DIAMETER	DH5IN	1.822
DIFFUSER AREA RATIO-OVERALL	ARDIF	2.69
DIFFUSER AREA RATIO-EQUIV. UPPER	ARDIFU	2.69
DIFFUSER AREA RATIO-EQUIV. LOWER	ARDIFL	2.69
DIFFUSER NORMALIZED LENGTH-GIVEN LENGTH	ELDNL	8.75
DIFFUSER NORMALIZED LENGTH-GIVEN AREA	ELDNA	11.26
DIFFUSER LENGTH-GIVEN LENGTH	ELDINL	7.165
DIFFUSER LENGTH-GIVEN AREA	ELDINA	9.241
DIFFUSER HALF ANGLE-GIVEN LENGTH (2D)	ALFDIL	5.53
DIFFUSER HALF ANGLE-GIVEN AREA (2D)	ALFDIA	4.29
DIFFUSER OVERALL EFFECTIVENESS	DIFFE	.799
DIFFUSER INLET BLOCKAGE	BLK4	.100
DIFFUSER LOSS COEFFICIENT	CLOSDA	.173
DIFFUSER AVERAGE-TO-MEAN LOSS RATIO	CLOSDR	1.000

TABLE IV
MERIDIONAL FLOW PATH SPECIFICATION
OF THE BRU ROTOR

First Blade Row

<u>Outer Contour Coordinates*</u>				<u>Hub Contour Coordinates</u>			
<u>Radius</u>		<u>Axial Distance</u>		<u>Radius</u>		<u>Axial Distance</u>	
<u>(in)</u>	<u>(cm)</u>	<u>Measured from</u>	<u>Rotor Exit</u>	<u>(in)</u>	<u>(cm)</u>	<u>Measured from</u>	<u>Rotor Exit</u>
		<u>(in)</u>	<u>(cm)</u>			<u>(in)</u>	<u>(cm)</u>
2.634	6.690	-1.152	-2.926	2.634	6.690	-1.552	-3.942
2.510	6.375	-1.141	-2.898	2.427	6.165	-1.516	-3.851
2.397	6.088	-1.119	-2.842	2.230	5.664	-1.469	-3.731
2.293	5.824	-1.085	-2.756	2.039	5.179	-1.411	-3.584
2.197	5.580	-1.041	-2.644	1.853	4.707	-1.338	-3.398
2.105	5.347	-0.983	-2.497	1.669	4.239	-1.244	-3.160
2.018	5.126	-0.913	-2.319	1.493	3.792	-1.120	-2.845
1.938	4.922	-0.830	-2.108	1.329	3.376	-0.961	-2.441
1.835	4.661	-0.678	-1.722	1.122	2.850	-0.678	-1.722

Second Blade Row

1.835	4.661	-0.678	-1.722	1.122	2.850	-0.678	-1.722
1.750	4.445	-0.451	-1.145	1.018	2.586	-0.475	-1.206
1.733	4.402	-0.313	-0.795	0.955	2.426	-0.297	-0.754
1.730	4.394	-0.198	-0.503	0.925	2.349	-0.148	-0.376
1.730	4.394	-0.059	-0.150	0.911	2.314	+0.018	+0.046

* Rotor casing coordinates are obtained with the addition of a 0.010 in (0.0254 cm) clearance.

TABLE V
FIRST BLADE ROW DEFINITION ALONG THE STREAMTUBE CENTERS

<u>Outer Casing Streamtube</u>						
<u>Radius</u>		<u>Axial Distance</u> <u>Measured from</u>		<u>Angular</u>	<u>Normal</u>	
<u>(in)</u>	<u>(cm)</u>	<u>Rotor Exit</u>		<u>Coordinate</u>	<u>Thickness</u>	
		<u>(in)</u>	<u>(cm)</u>	<u>(deg)</u>	<u>(in)</u>	<u>(cm)</u>
2.634	6.690	-1.170	-2.972	0.00	0.0500	0.1270
2.568	6.523	-1.163	-2.954	- 0.37	0.0500	0.1270
2.506	6.365	-1.155	-2.934	- 0.95	0.0500	0.1270
2.446	6.213	-1.146	-2.911	- 1.65	0.0500	0.1270
2.389	6.068	-1.134	-2.880	- 2.45	0.0500	0.1270
2.333	5.926	-1.119	-2.842	- 3.33	0.0500	0.1270
2.279	5.789	-1.102	-2.799	- 4.25	0.0500	0.1270
2.227	5.657	-1.082	-2.748	- 5.23	0.0500	0.1270
2.178	5.532	-1.056	-2.682	- 6.24	0.0500	0.1270
2.131	5.413	-1.026	-2.606	- 7.27	0.0500	0.1270
2.086	5.298	-0.993	-2.522	- 8.31	0.0500	0.1270
2.042	5.187	-0.958	-2.433	- 9.36	0.0500	0.1270
1.999	5.077	-0.920	-2.337	-10.39	0.0500	0.1270
1.958	4.973	-0.879	-2.233	-11.38	0.0499	0.1267
1.918	4.872	-0.834	-2.118	-12.33	0.0482	0.1224
1.880	4.775	-0.786	-1.996	-13.21	0.0436	0.1107
1.846	4.689	-0.733	-1.862	-14.00	0.0359	0.0912
1.815	4.610	-0.678	-1.722	-14.69	0.0250	0.0635

<u>Hub Streamtube</u>						
2.634	6.690	-1.538	-3.906	1.68	0.1000	0.2540
2.530	6.426	-1.518	-3.856	1.06	0.1016	0.2581
2.430	6.172	-1.497	-3.802	0.13	0.1031	0.2619
2.334	5.928	-1.474	-3.744	- 0.98	0.1046	0.2657
2.239	5.687	-1.449	-3.680	- 2.20	0.1061	0.2695
2.145	5.448	-1.422	-3.612	- 3.51	0.1076	0.2733
2.053	5.215	-1.393	-3.538	- 4.89	0.1091	0.2771
1.961	4.981	-1.359	-3.452	- 6.31	0.1106	0.2809
1.871	4.752	-1.321	-3.355	- 7.77	0.1121	0.2847
1.782	4.526	-1.278	-3.246	- 9.22	0.1136	0.2885
1.694	4.303	-1.228	-3.119	-10.63	0.1152	0.2926
1.610	4.089	-1.171	-2.974	-11.96	0.1167	0.2964
1.529	3.884	-1.105	-2.807	-13.16	0.1183	0.3004
1.454	3.693	-1.030	-2.616	-14.15	0.1200	0.3048
1.382	3.510	-0.949	-2.410	-14.86	0.1146	0.2911
1.316	3.343	-0.862	-2.189	-15.21	0.0970	0.2464
1.255	3.188	-0.772	-1.961	-15.16	0.0671	0.1704
1.200	3.048	-0.678	-1.722	-14.70	0.0250	0.0635

TABLE VI
SECOND BLADE ROW DEFINITION ALONG THE STREAMTUBE CENTERS

<u>Outer Casing Streamtube</u>						
<u>Radius</u>		<u>Axial Distance</u> <u>Measured from</u>		<u>Angular</u>	<u>Normal</u>	
<u>(in)</u>	<u>(cm)</u>	<u>Rotor Exit</u>		<u>Coordinate</u> *	<u>Thickness</u>	
		<u>(in)</u>	<u>(cm)</u>	<u>(deg)</u>	<u>(in)</u>	<u>(cm)</u>
1.815	4.610	-0.678	-1.722	10.255	0.020	0.051
1.785	4.534	-0.620	-1.575	9.337	0.061	0.155
1.761	4.473	-0.561	-1.425	8.114	0.071	0.180
1.741	4.422	-0.503	-1.278	6.628	0.070	0.178
1.726	4.384	-0.446	-1.133	4.806	0.068	0.173
1.715	4.356	-0.393	-0.998	2.709	0.061	0.155
1.708	4.338	-0.341	-0.866	0.399	0.056	0.142
1.705	4.331	-0.293	-0.744	- 2.096	0.048	0.122
1.703	4.326	-0.246	-0.625	- 4.710	0.044	0.112
1.701	4.321	-0.201	-0.511	- 7.400	0.043	0.109
1.700	4.318	-0.157	-0.399	-10.135	0.038	0.097
1.700	4.318	-0.115	-0.292	-12.917	0.034	0.086
1.700	4.318	-0.059	-0.150	-16.700	0.026	0.066
<u>Hub Streamtube</u>						
1.179	2.995	-0.678	-1.722	2.342*	0.025	0.064
1.150	2.921	-0.622	-1.580	2.867	0.083	0.211
1.124	2.855	-0.565	-1.435	3.315	0.122	0.310
1.099	2.791	-0.507	-1.288	3.389	0.147	0.373
1.076	2.733	-0.448	-1.138	2.989	0.154	0.391
1.056	2.682	-0.389	-0.988	2.219	0.147	0.373
1.037	2.634	-0.330	-0.838	1.136	0.131	0.333
1.020	2.591	-0.272	-0.691	- 0.338	0.115	0.292
1.006	2.555	-0.216	-0.549	- 2.384	0.096	0.244
0.996	2.530	-0.161	-0.409	- 4.833	0.076	0.193
0.989	2.512	-0.108	-0.274	- 7.565	0.056	0.142
0.984	2.499	-0.057	-0.145	-10.554	0.039	0.099
0.978	2.484	-0.008	-0.020	-14.849	0.025	0.064

* Angular coordinates are measured with reference to the stacking point of the second blade row axial blade sections.

TABLE VII
NOZZLE VANE GEOMETRY SPECIFICATION

<u>Radius</u>		<u>Angular Coordinate</u> <u>(deg)</u>	<u>Tangential Thickness</u>	
<u>(in)</u>	<u>(cm)</u>		<u>(in)</u>	<u>(cm)</u>
3.827	9.720	0.00	0.0102	0.0259
3.774	9.586	1.09	0.1300	0.3302
3.720	9.449	2.20	0.1769	0.4493
3.665	9.309	3.31	0.2082	0.5288
3.610	9.169	4.43	0.2312	0.5872
3.555	9.030	5.56	0.2482	0.6304
3.499	8.887	6.72	0.2615	0.6642
3.445	8.750	7.91	0.2715	0.6896
3.392	8.616	9.13	0.2786	0.7076
3.341	8.486	10.39	0.2834	0.7198
3.292	8.362	11.70	0.2871	0.7292
3.246	8.245	13.06	0.2894	0.7351
3.204	8.138	14.47	0.2896	0.7356
3.163	8.034	15.92	0.2875	0.7302
3.126	7.940	17.42	0.2822	0.7168
3.091	7.851	18.95	0.2735	0.6947
3.057	7.765	20.51	0.2611	0.6632
3.026	7.686	22.10	0.2452	0.6228
2.996	7.610	23.72	0.2263	0.5748
2.967	7.536	25.36	0.2045	0.5194
2.939	7.465	27.02	0.1818	0.4618
2.912	7.396	28.70	0.1603	0.4072
2.885	7.328	30.40	0.1405	0.3569
2.859	7.262	32.13	0.1224	0.3109
2.834	7.198	33.87	0.1063	0.2700
2.809	7.135	35.63	0.0924	0.2347
2.784	7.071	37.40	0.0806	0.2047
2.760	7.010	39.20	0.0710	0.1803
2.737	6.952	41.01	0.0634	0.1610
2.713	6.891	42.84	0.0577	0.1465

TABLE VIII
DIFFUSER SPECIFICATION

<u>Axial Distance</u> <u>from Rotor Exit</u>		<u>Casing Radius</u>		
<u>(in)</u>	<u>(cm)</u>	<u>(in)</u>	<u>(cm)</u>	
0.00	0.00	1.730	4.394	
1.00	2.54	1.736	4.409	
1.25	3.17	1.740	4.420	
2.00	5.08	1.766	4.486	
3.00	7.62	1.815	4.610	
4.00	10.16	1.875	4.762	Hub Radius is Constant for the Entire Length = 0.911 in (2.314 cm)
5.00	12.70	1.950	4.953	
6.00	15.24	2.047	5.200	
7.00	17.78	2.202	5.593	
8.25	20.95	2.500	6.350	
9.25	23.49	2.580	6.553	

Note: Area schedule is based on an assumed constant static pressure between 0 and 1.0 in (2.54 cm), linear static pressure rise between 1.0 in (2.54 cm) and 8.25 in (20.95 cm), and a linear drop of total pressure with axial distance from 0 to 8.25 in (20.95 cm).

TABLE IX
TURBINE INLET SCROLL GEOMETRY SPECIFICATION

Maximum Radius of the Cross Section, R_M		Azimuth Angle Measured from Scroll Inlet (deg)	Area of the Cross Section		Radius of the Cross Section, R		R_{OR}		R_{OL}	
(in)	(cm)		(sq in)	(sq cm)	(in)	(cm)	(in)	(cm)	(in)	(cm)
8.427	21.404	0.0	14.209	91.671	2.050	5.207				
8.301	21.084	20.0	13.372	86.271	1.987	5.047				
8.171	20.754	40.0	12.537	80.884	1.922	4.882				
8.038	20.416	60.0	11.704	75.510	1.855	4.712				
7.899	20.063	80.0	10.875	70.161	1.786	4.536				
7.756	19.700	100.0	10.049	64.832	1.715	4.356				
7.608	19.324	120.0	9.226	59.522	1.641	4.168				
7.453	18.930	140.0	8.408	54.245	1.563	3.970				
7.291	18.519	160.0	7.594	48.993	1.482	3.764				
7.120	18.085	180.0	6.785	43.774	1.397	3.548				
6.940	17.628	200.0	5.983	38.600	1.307	3.320				
6.747	17.137	220.0	5.186	33.458	1.211	3.076				
6.536	16.601	240.0	4.395	28.355	1.108	2.814				
6.301	16.004	260.0	3.611	23.297	0.998	2.535				
6.033	15.324	280.0	2.838	18.310	0.876	2.225				
5.718	14.524	300.0	2.079	13.413	0.741	1.882				
5.326	13.528	320.0	1.341	8.651	0.587	1.491				
4.784	12.151	340.0	0.638	4.116	0.408	1.036				
4.394	11.161	350.0	0.306	1.974	0.315	0.800				
4.301	10.924	352.0	0.242	1.561	0.300	0.762				
4.203	10.676	354.0	0.180	1.161	0.287	0.729				
4.152	10.546	355.0	0.149	0.961	0.282	0.716				
4.084	10.373	356.0	0.119	0.768			0.227	0.576	0.258	0.655
4.006	10.175	357.0	0.089	0.574			0.158	0.401	0.179	0.455
3.940	10.008	358.0	0.059	0.381			0.100	0.254	0.113	0.287
3.881	9.858	359.0	0.029	0.187			0.048	0.122	0.054	0.137
3.827	9.720	360.0	0.000	0.000			0.000	0.000	0.000	0.000

Note: The nomenclature of the cross sections is defined in Figure 22.

TABLE X
ROTOR ADIABATIC WALL TEMPERATURE AND BIOT NUMBER
DISTRIBUTION ASSUMED FOR ROTOR TEMPERATURE
AND STRESS CALCULATIONS

<u>Front Face of Disk</u>				<u>Back Face of Disk</u>		
<u>Radius</u> [*] <u>Ratio</u>	<u>Region</u> ^{**}	<u>Temperature</u> ^{***} <u>Ratio</u>	<u>Biot</u> <u>Number</u>	<u>Region</u>	<u>Temperature</u> <u>Ratio</u>	<u>Biot</u> <u>Number</u>
0.000	EF	0.8032	0.000	AB	0.3906	1.505
0.076		0.8030	0.065		0.3906	1.505
0.114		0.8025	0.084	BC	0.9631	0.084
0.190		0.8013	0.113		0.9636	0.113
0.266		0.7995	0.139		0.9642	0.139
0.304		0.7983	0.150		0.9646	0.150
0.342		0.7971	0.161		0.9651	0.161
0.346	DE	0.8203	3.500		0.9656	0.162
0.418		0.8369	2.040		0.9667	0.182
0.494		0.8476	1.320		0.9674	0.201
0.570		0.8579	1.180		0.9689	0.219
0.646		0.8682	1.050		0.9706	0.237
0.661		0.8706	1.040		0.9714	0.240
0.677		0.8725	1.040		0.9714	0.243
0.692		0.8735	1.050	BC	0.9716	0.245
0.722		0.8784	1.070		0.9726	0.253
0.798		0.8901	1.110		0.9747	0.268
0.874		0.9028	1.060		0.9772	0.283
0.950		0.916	1.200		0.9797	0.298
1.000	CD	1.000	0.307	CD	1.0000	0.307

* Radii are ratioed to the rotor inlet radius of 2.634 in (6.690 cm).

** For definitions of regions, see Figure 35.

*** Temperatures are normalized to the rotor inlet disk face temperature of 2048 deg R (1140 deg K).

TABLE XI

PHYSICAL PROPERTIES OF HIGH TEMPERATURE ALLOYS

<u>Alloy</u> <u>Name</u>	<u>Test</u> <u>Tem-</u> <u>pera-</u> <u>ture</u> <u>(deg F)</u>	<u>Stress</u> <u>Rupture</u> <u>(50,000</u> <u>hrs)</u>	<u>Creep</u> <u>0.4x10⁻⁵</u> <u>Per</u> <u>Cent/hr</u> <u>Minimum</u> <u>Creep Rate</u>	<u>Endur-</u> <u>ance</u> <u>Limit</u> <u>(10⁸</u> <u>Cycles)</u>	<u>Ultimate</u> <u>Strength</u>	<u>Yield</u> <u>2 Per</u> <u>Cent</u> <u>Offset</u>	<u>Per</u> <u>Cent</u> <u>Weight</u> <u>Change</u> <u>(200 hrs)</u>	<u>Per</u> <u>Cent</u> <u>Elonga-</u> <u>tion</u>	<u>Per</u> <u>Cent</u> <u>Reduc-</u> <u>tion</u> <u>in Area</u>	<u>Endur-</u> <u>ance</u> <u>Limit</u> <u>Stress/</u> <u>Rupture</u> <u>Strength</u>	<u>Remarks</u>
<u>Casting</u> <u>Alloys</u>											
713C	1400 (1033 deg K)	40,000	27,000	26,000	135,000	109,000	-0.05	6	10	0.65	Developed to combine good stress-rupture properties with excellent room temperature, ductility, and strength; for use with integrally cast turbine wheels
713LC	1400 (1033 deg K)	43,000	22,000	25,500	138,000	110,000	-0.10	10	19	0.59	Developed to optimize stress rupture and room temperature, ductility, and strength
IN100	1400 (1033 deg K)	50,000	35,000	11,000	155,000	125,000	-0.80	6	7.2	0.22	Good strength to density characteristics, long-time embrittlement problem

TABLE XI (CONTINUED)

PHYSICAL PROPERTIES OF HIGH TEMPERATURE ALLOYS

Alloy Name	Test Temperature (deg F)	Stress Rupture (50,000 hrs)	Creep 0.4×10^{-5} Per Cent/hr Minimum Creep Rate	Endurance Limit (10^8 Cycles)	Ultimate Strength	Yield 2 Per Cent Offset	Per Cent Weight Change (200 hrs)	Per Cent Elongation	Per Cent Reduction in Area	Endurance Limit Stress/Rupture Strength	Remarks
UDIMET 500	1400 (1033 deg K)	33,000	25,000	10,000	120,000	105,000	-0.15	21	24	0.30	Good oxidation resistance, relatively low strength
MAR-M 200	1400 (1033 deg K)	30,000	-	25,000	135,000	122,000	-0.10	3.5	-	0.83	Lacks ductility at lower temperatures as needed for integrally cast turbine wheels
<u>Wrought Alloys</u>											
UDIMET 700	1400 (1033 deg K)	43,700	-	26,000	145,000	120,000	-	8	10	-	Difficult and expensive to forge
WASPALLOY	1400 (1033 deg K)	24,300	-	18,000*	120,000	100,000	-	22	30	-	Properties not as good as casting alloy at 1400 deg F (1033 deg K)
RENE 41	1400 (1033 deg K)	26,800	-	15,000*	100,000	82,000	-	7	15	-	Properties not as good as casting alloy at 1400 deg F (1033 deg K)

* Assumes $\sigma_e / \sigma_u = 0.15$.

TABLE XI (CONTINUED)

PHYSICAL PROPERTIES OF HIGH TEMPERATURE ALLOYS

Alloy Name	Test Tem- pera- ture (deg F)	Stress Rupture (50,000 hrs)	Creep 0.4x10 ⁻⁵ Per Cent/hr Minimum Creep Rate	Endur- ance Limit (10 ⁸ Cycles)	Ultimate Strength	Yield 2 Per Cent Offset	Per Cent Weight Change (200 hrs)	Per Cent Elonga- tion	Per Cent Reduc- tion in Area	Endur- ance Limit Stress/ Rupture Strength	Remarks
INCONEL 718	1400 (1033 deg K)	20,000	-	12,000*	80,000	62,000	-	10	25	-	Insufficient strength at 1400 deg F (1033 deg K) difficult to machine

* Assumes $\sigma_e / \sigma_u = 0.15$.

TABLE XII

SUMMARY OF DISK STRESSES AND DEFLECTIONS

<u>Property</u>	<u>Steel (Cold)</u>	<u>Steel (Hot)</u>			<u>Aluminum (Cold)</u>
	<u>120 Per Cent Speed</u>	<u>100 Per Cent Speed</u>	<u>120 Per Cent Speed</u>	<u>140 Per Cent Speed</u>	<u>150 Per Cent Speed</u>
Average Tangential Stress (psi)	12,717	12,258	18,448	25,757	4,861
(kN/m ²)	87,680	84,516	127,194	177,588	33,515
Axial Deflection at Tip (in)	+0.0008	0.0016	0.0019	0.0023	0.0005
(cm)	0.0020	0.0041	0.0048	0.0058	0.0013
Radial Deflection at Tip (in)	+0.0013	0.0398	0.0402	0.0407	0.0007
(cm)	0.0033	0.1011	0.1021	0.1034	0.0018

TABLE XIII

SUMMARY OF BLADE FREQUENCY AND VIBRATORY STRESS RESULTS

Blade Row	Location	Method	f (cps)	X (E)	K	α	σ_b (psi)	σ_v^* (psi)
1	L.E.	Flat Beam (1)	13,450	22.4	1.3	2.5	110	358
1	T.E.	Voysey (2)	31,800	53.0	1.3	2.5	0	0
2	L.E.	Cantilever Plate (3)	3,940	6.8	1.2	6.0	1485	10,620
2	T.E.	Cantilever Plate (3)	3,940	6.8	1.2	6.0	1260	9,090

- (1) Mechanical Design and System Handbook - Rothbart - pp. 6-58

$$f_n = C_n \frac{V}{L^2} \times 10^4 K_m \quad \text{for Flat Beam, } C_n = 11.30$$

- (2) Some Vibration Problems in Gas Turbine Engines - Voysey

$$f_n = \frac{1.8 A t_n}{4\pi L^2} \left[\frac{E g_0}{38} \right] \quad \text{for Trailing Edge Panel}$$

Where L = Diagonal Length at $\angle = 35$ degrees from Reference Through Blade Tip Parallel to Center Line

- (3) Mechanical Design and System Handbook - Rothbart - pp. 6-59

$$f_n = C_n \frac{h}{a^2} \times 10^4 \times K_m \quad \text{for Cantilever Plate, } C_n = 3.31$$

where for $n = 1$, h = Blade Thickness = t_n
 a = Blade Height = L
 b = Blade Width
 K_m = Material Constant = 1.0 for Steel
 r = Radius of Gyration = $\sqrt{I/A}$ in
 E = Young's Modulus, psi
 ρ = Material Density, lb/in³
 A = Constant (a Function of Taper Ratio)

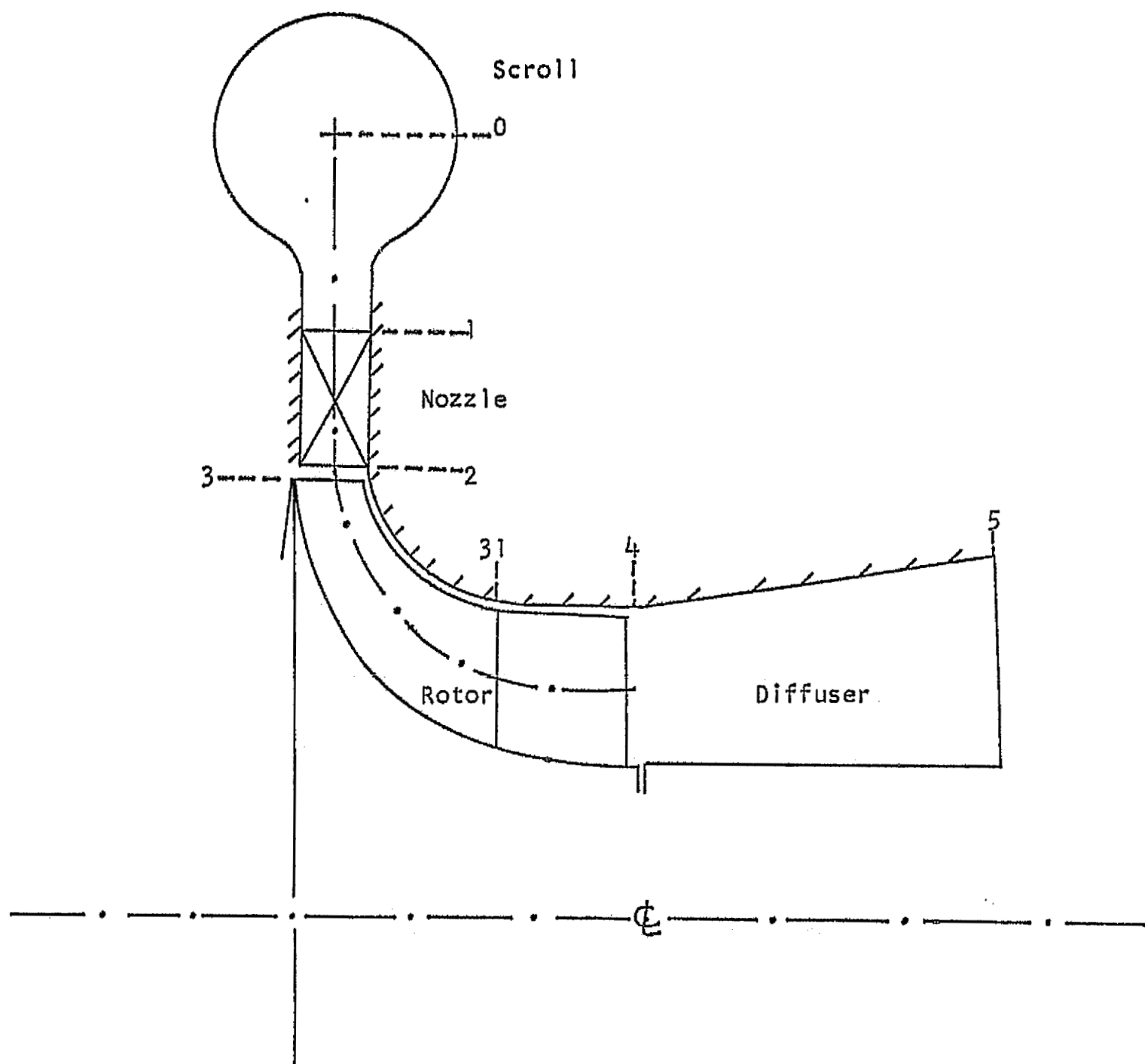
* The vibratory stress is calculated from the equation $\sigma_v = \sigma_b K \alpha$ where σ_b = bending stress, K = stress concentration factor, and α = amplification factor (Ref 15) given in the above table.

TABLE XIV
TURBINE RESEARCH PACKAGE ASSEMBLY AND TOOL LIST

<u>Part Number</u>	<u>Description</u>	<u>Quantity</u>
1159-D004	Wheel Turbine	1
1159-E005	Wheel Assembly Turbine	1
1159-R006	Scroll Fabrication Assembly	1
1159-R007	Scroll Machining Assembly	1
1159-R008	Nozzle Machining Assembly	1
1159-D009	Shroud Machining	1
1159-D010	Diffuser Machining	1
1159-D011	Exhaust Adapter	1
1159-C012	Rotor Back Shield	1
1159-B013	Pin Cap	5
1159-A014	Pin, Locating	5
1159-D015	Shim, Sealing Spacer	1
1159-A016	Ring, Retaining	1
Precision No. 010-12137	Packing "O" Ring	3
Precision No. 161-12137	Packing "O" Ring	2
Precision No. 012-12137	Packing "O" Ring	2
Precision No. 168-12137	Packing "O" Ring	3
Precision No. 253-12137	Packing "O" Ring	1
Waldes No. N5000-775-S	Retaining Ring	1
Waldes No. 6900	Pliers	1
	Screw, Cap Socket Head, No. 10-32 x 1 in Long Stainless Steel	23
	Tube (0.0625 O.D. x 0.010 Wall), Stainless Steel	As Required
100-1-1	Fitting (0.0625 Tube x 0.0625 Pipe), Swagelok	2
100-1-2	Fitting (0.0625 Tube x 0.125 Pipe), Swagelok	2

For all other components of turbine, see turbine research package assembly,
Drawing No. 699801 of Reference 2.

FIGURES



Station Nomenclature

0	Scroll Inlet
1	Nozzle Inlet
2	Nozzle Exit
3	Rotor Inlet (First Blade Row Inlet)
31	Intermediate Station (Second Blade Row Inlet)
4	Rotor Exit
5	Diffuser Exit

FIGURE 1 - SCHEMATIC PICTURE OF RADIAL INFLOW TURBINE STAGE

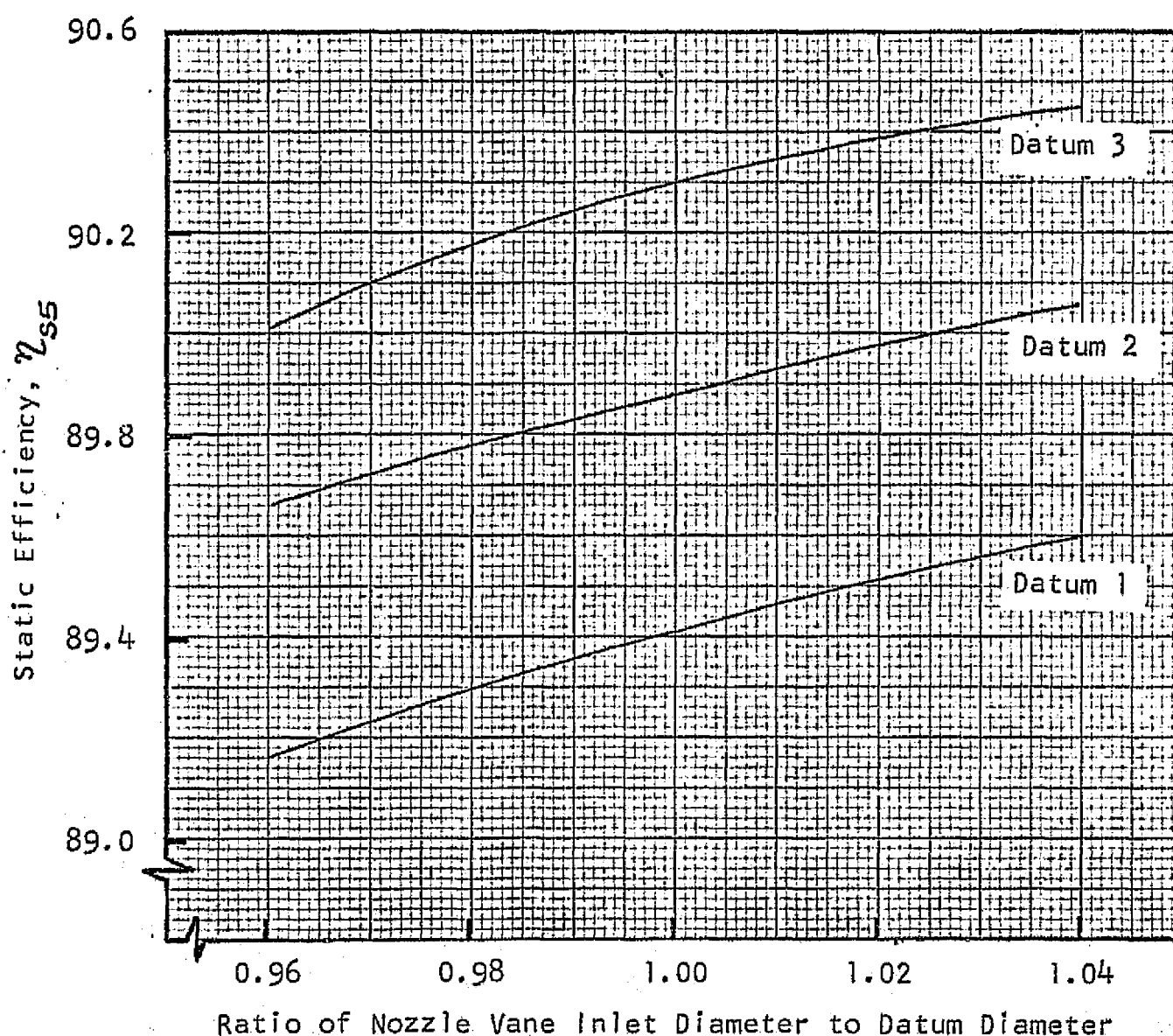
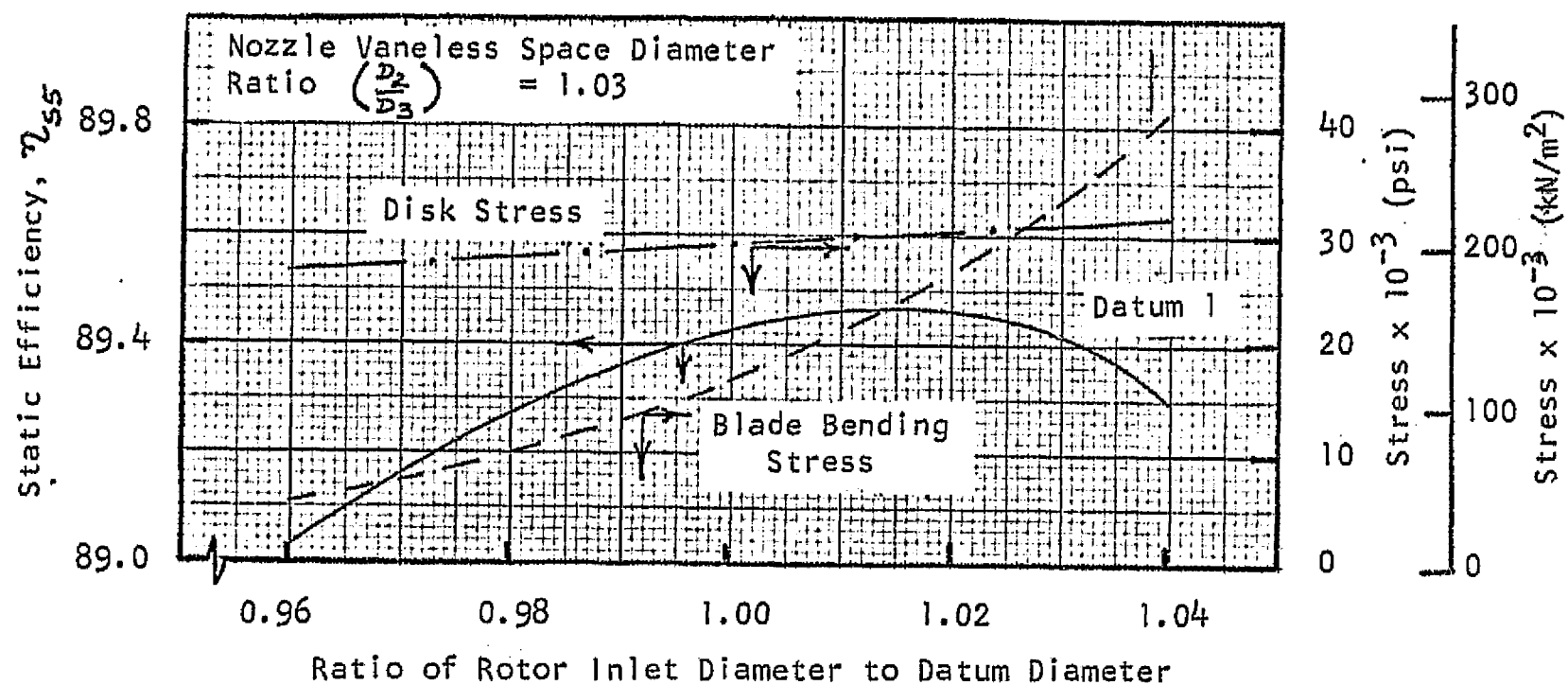


FIGURE 2 - STATIC EFFICIENCY VARIATION WITH NOZZLE INLET DIAMETERS FOR THREE DATUM DESIGNS AND VARIATION OF STATIC EFFICIENCY, DISK, AND BENDING STRESSES WITH ROTOR INLET DIAMETERS FOR DATUM 1 DESIGN

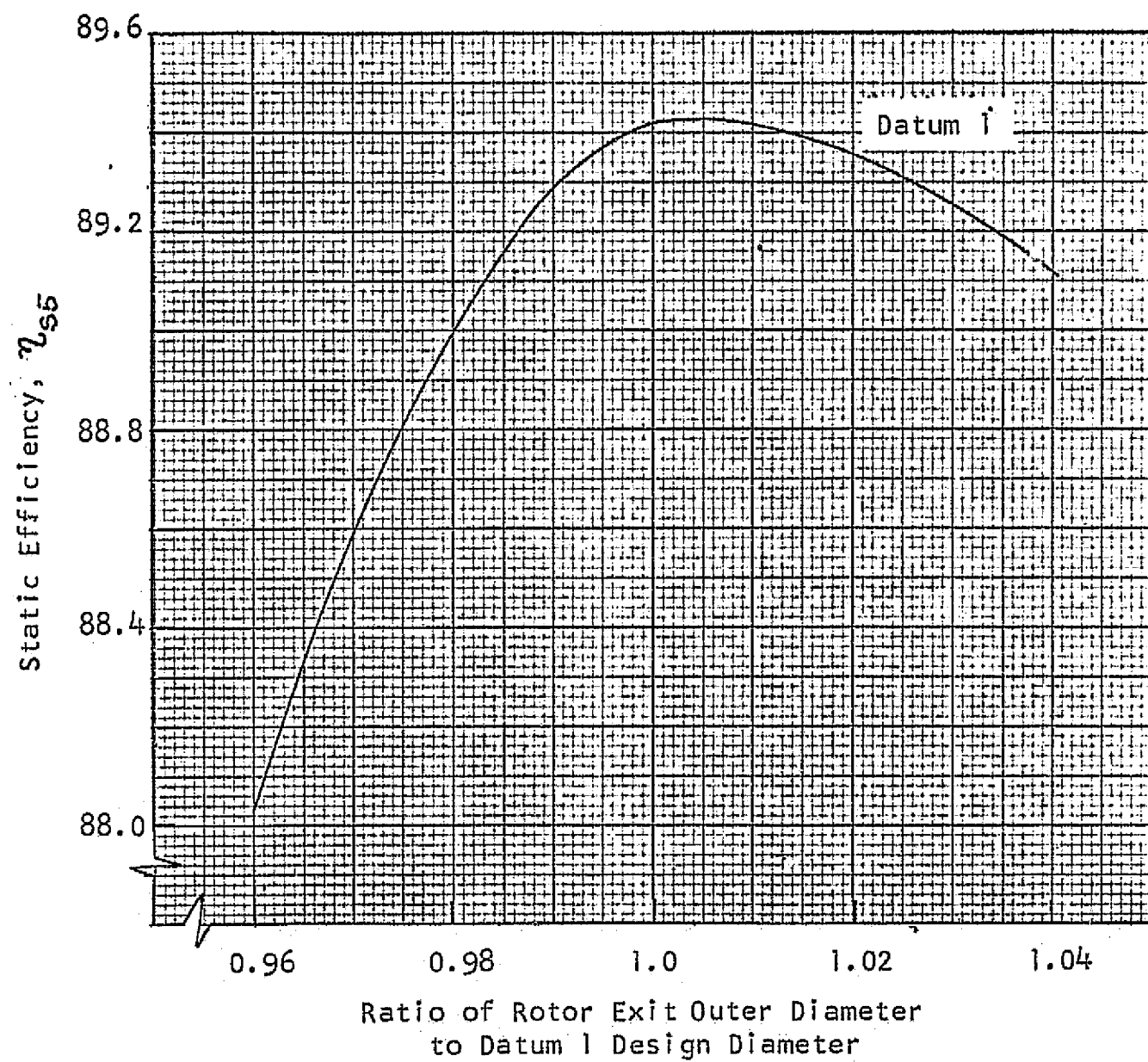
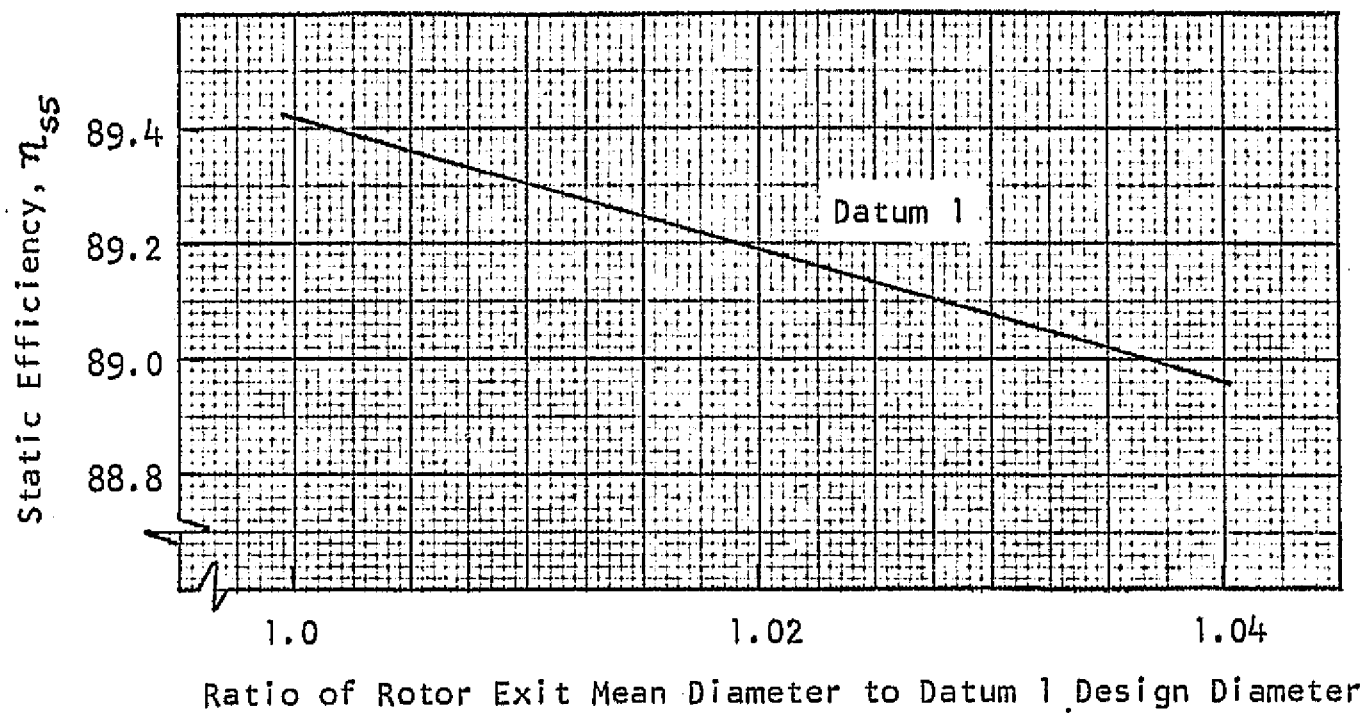


FIGURE 3 - VARIATION OF STATIC EFFICIENCY WITH OUTER DIAMETER
AND MEAN DIAMETER AT ROTOR DISCHARGE

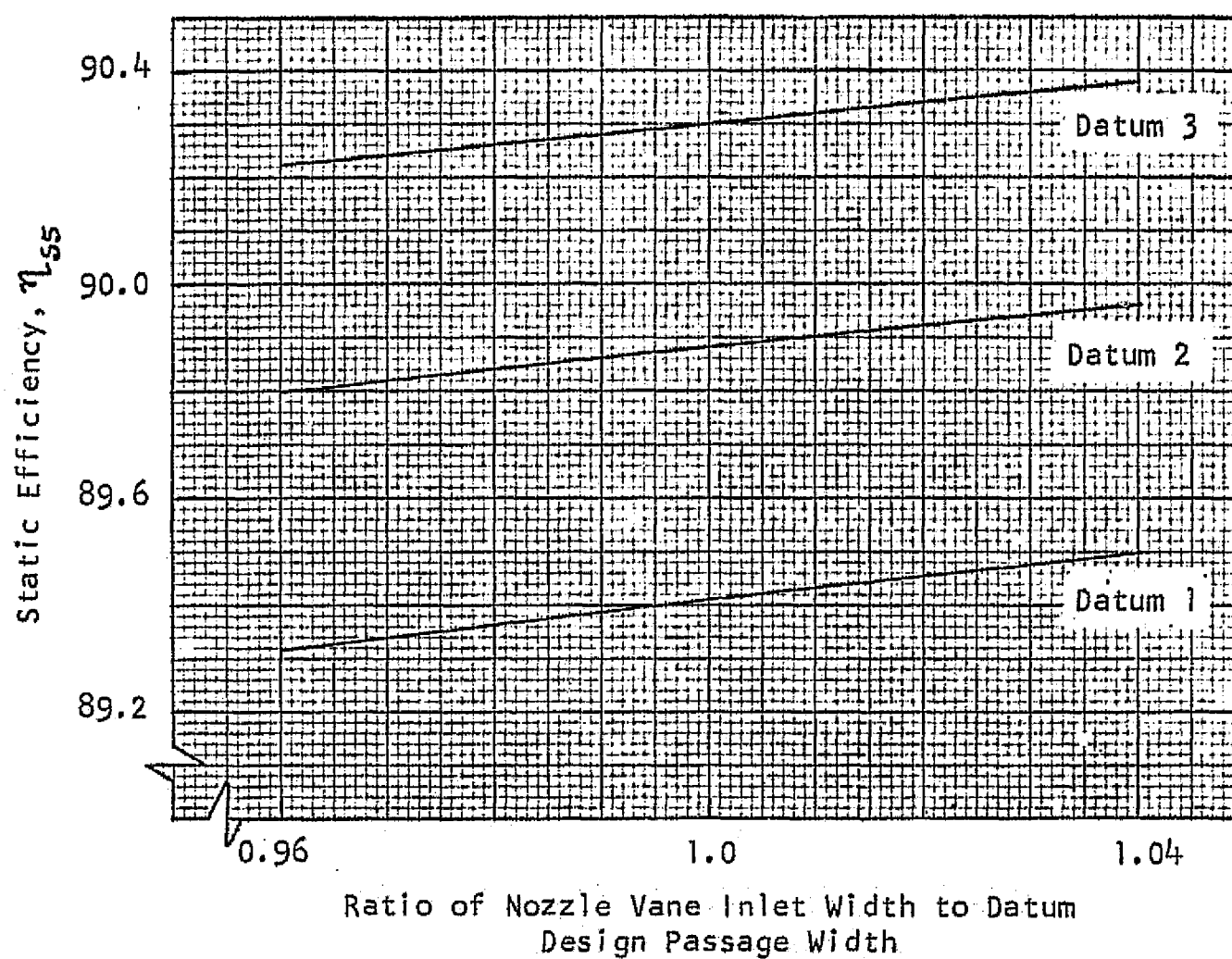
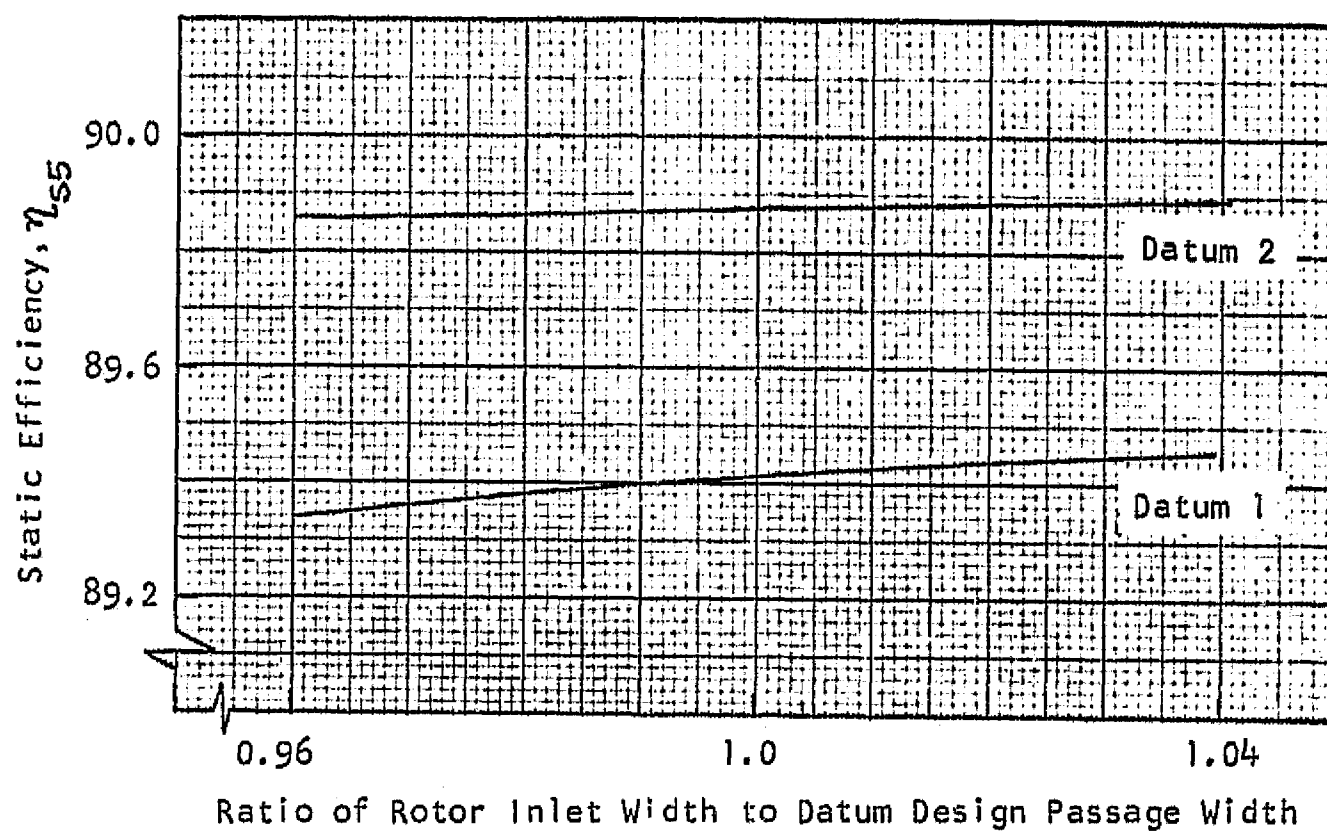


FIGURE 4 - VARIATION OF STATIC EFFICIENCY WITH PASSAGE WIDTH AT NOZZLE INLET AND ROTOR INLET

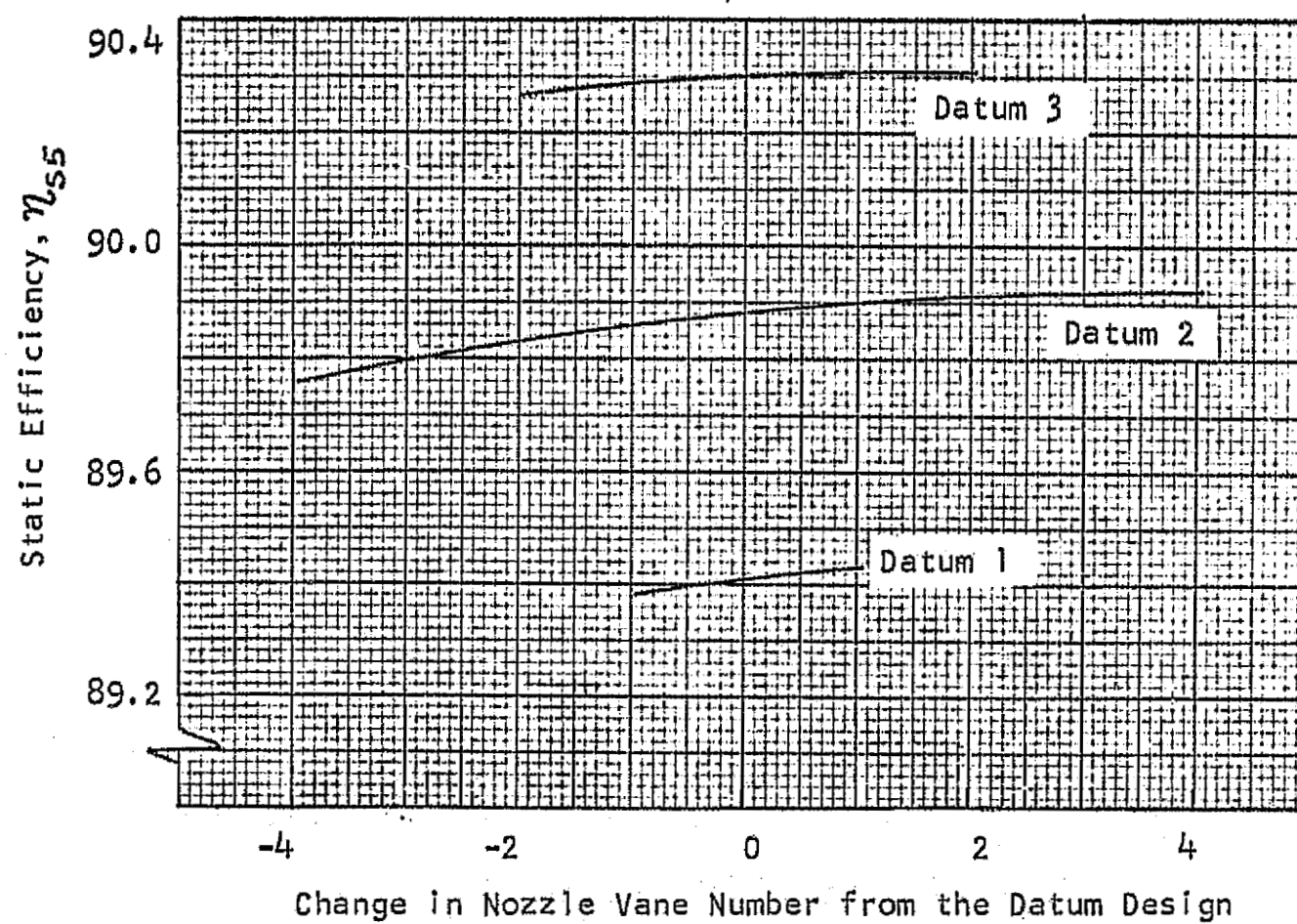
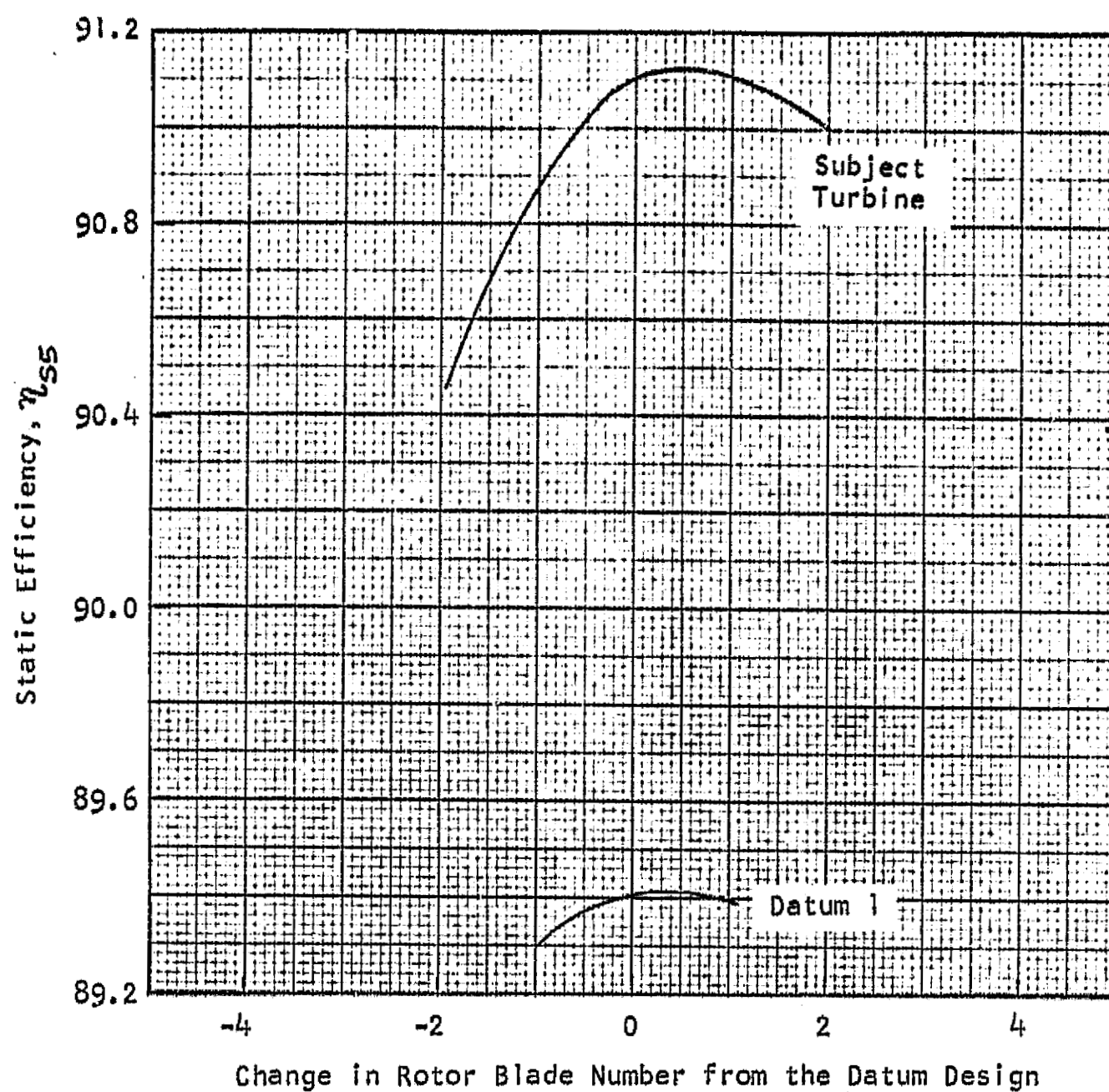


FIGURE 5 - VARIATION OF STATIC EFFICIENCY WITH ROTOR BLADE NUMBER AND STATOR VANE NUMBER

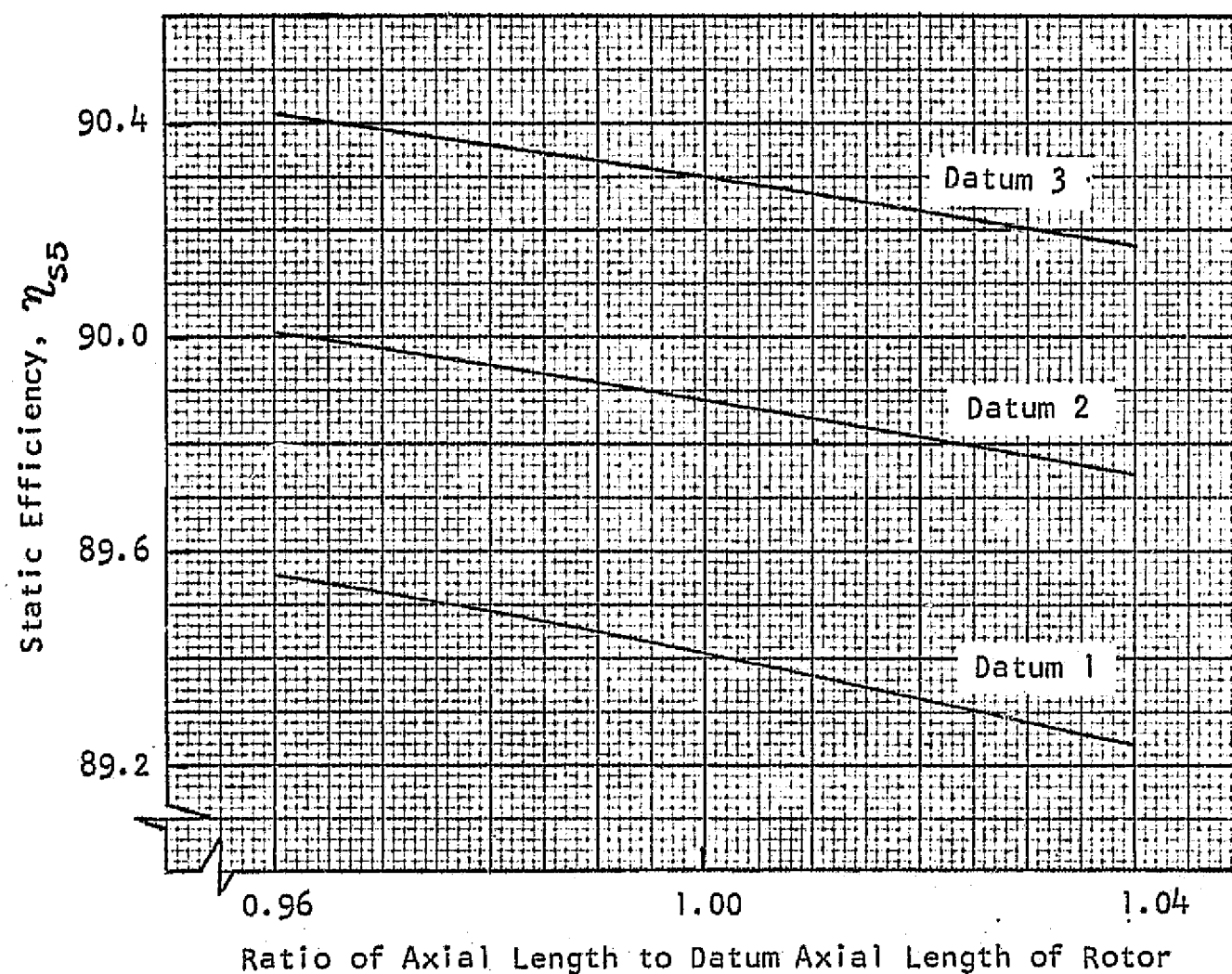
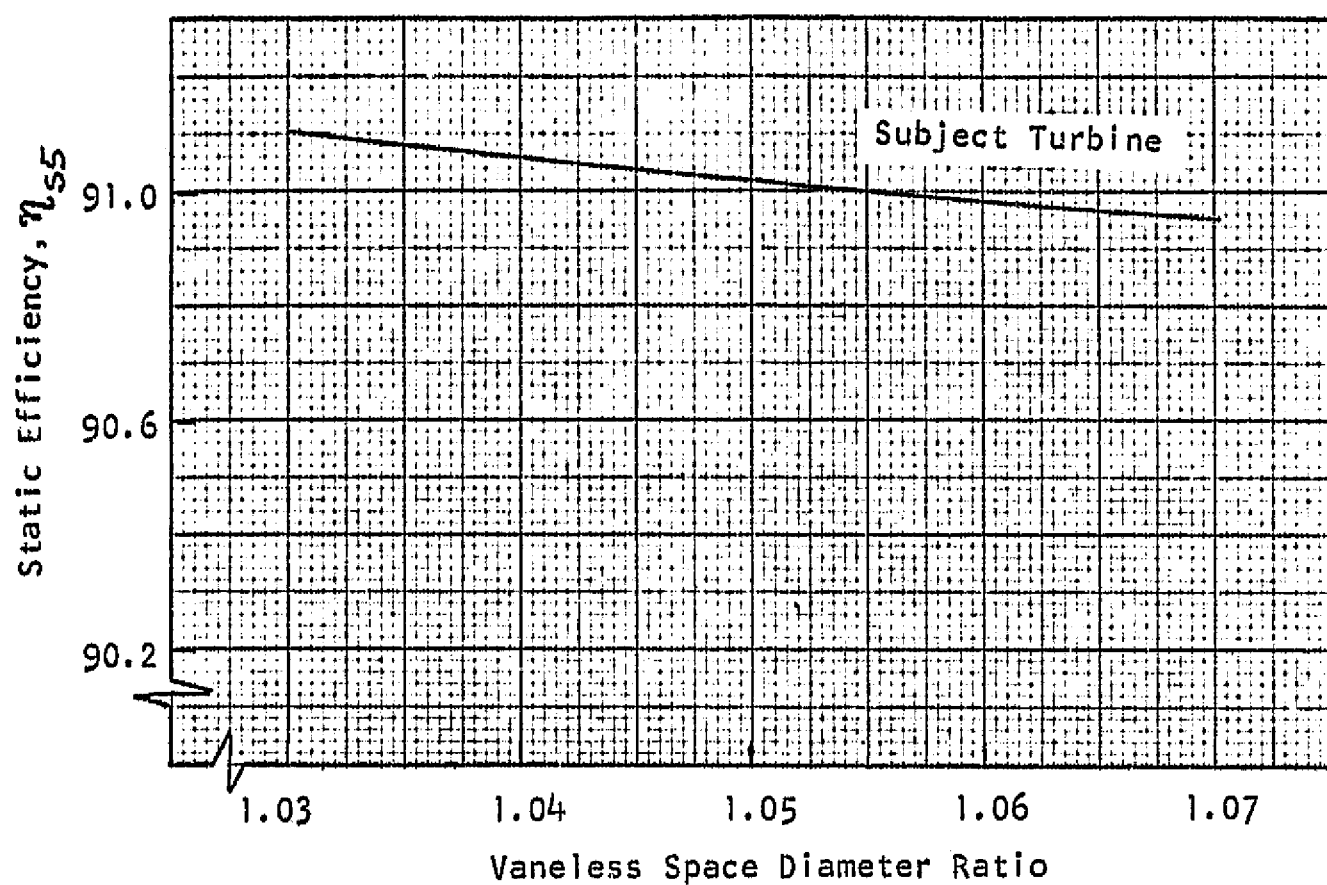


FIGURE 6 - VARIATION OF STATIC EFFICIENCY WITH ROTOR AXIAL LENGTH AND VANELESS SPACE DIAMETER RATIO

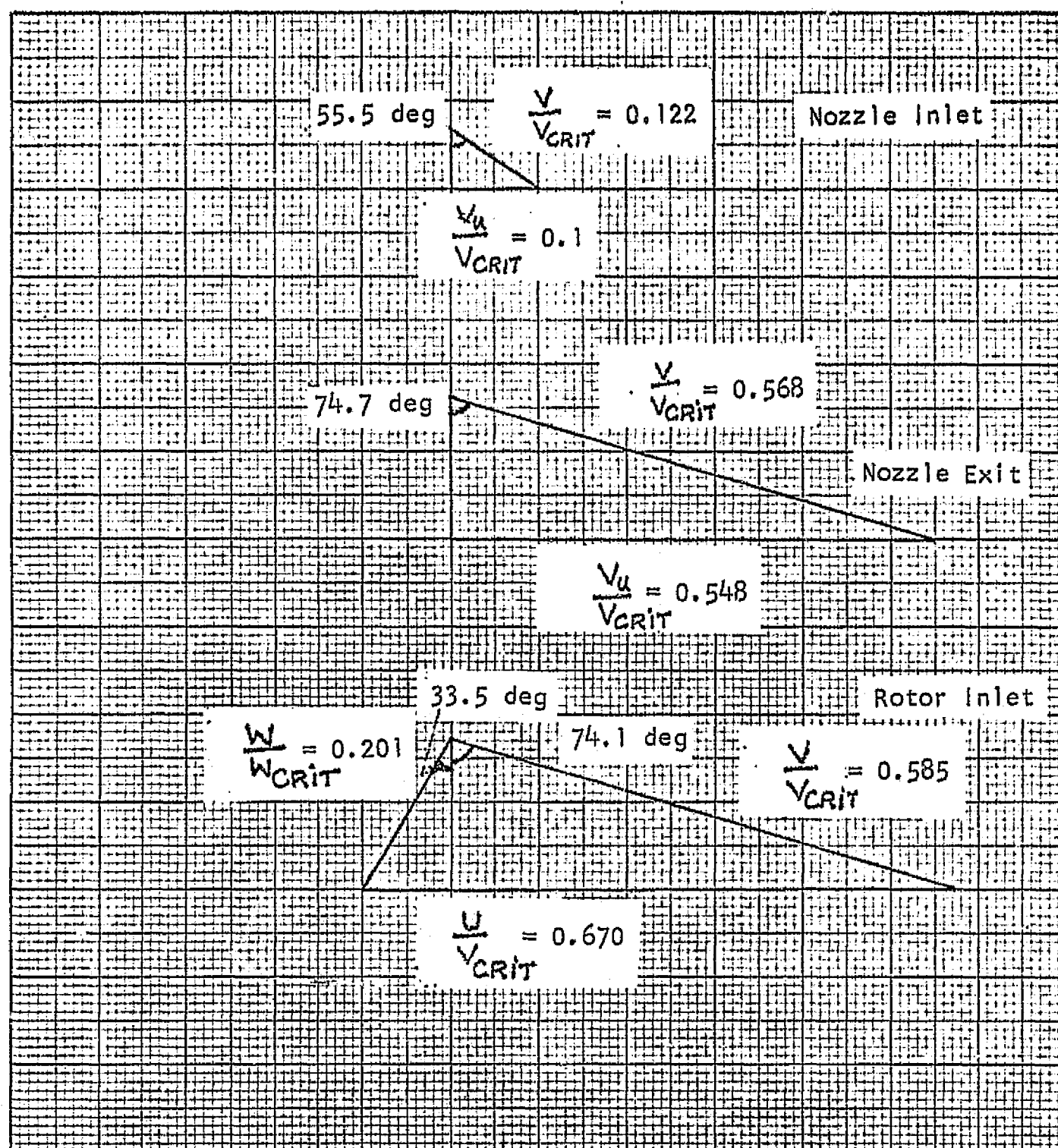


FIGURE 7 - DESIGN VELOCITY DIAGRAMS FOR THE VANED NOZZLE AND THE ROTOR INLET STATION

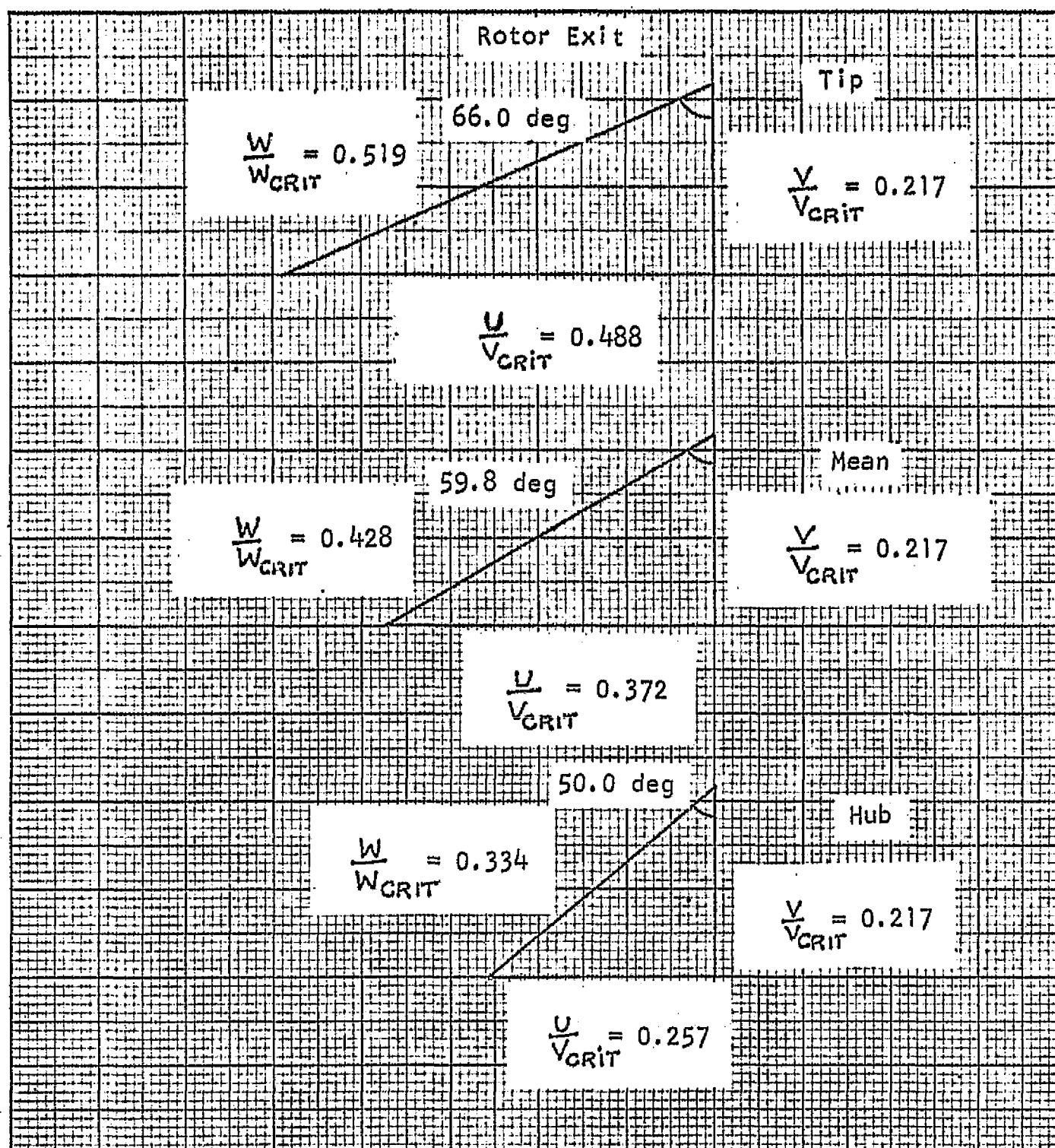


FIGURE 8 - DESIGN VELOCITY DIAGRAMS AT THE ROTOR DISCHARGE STATION

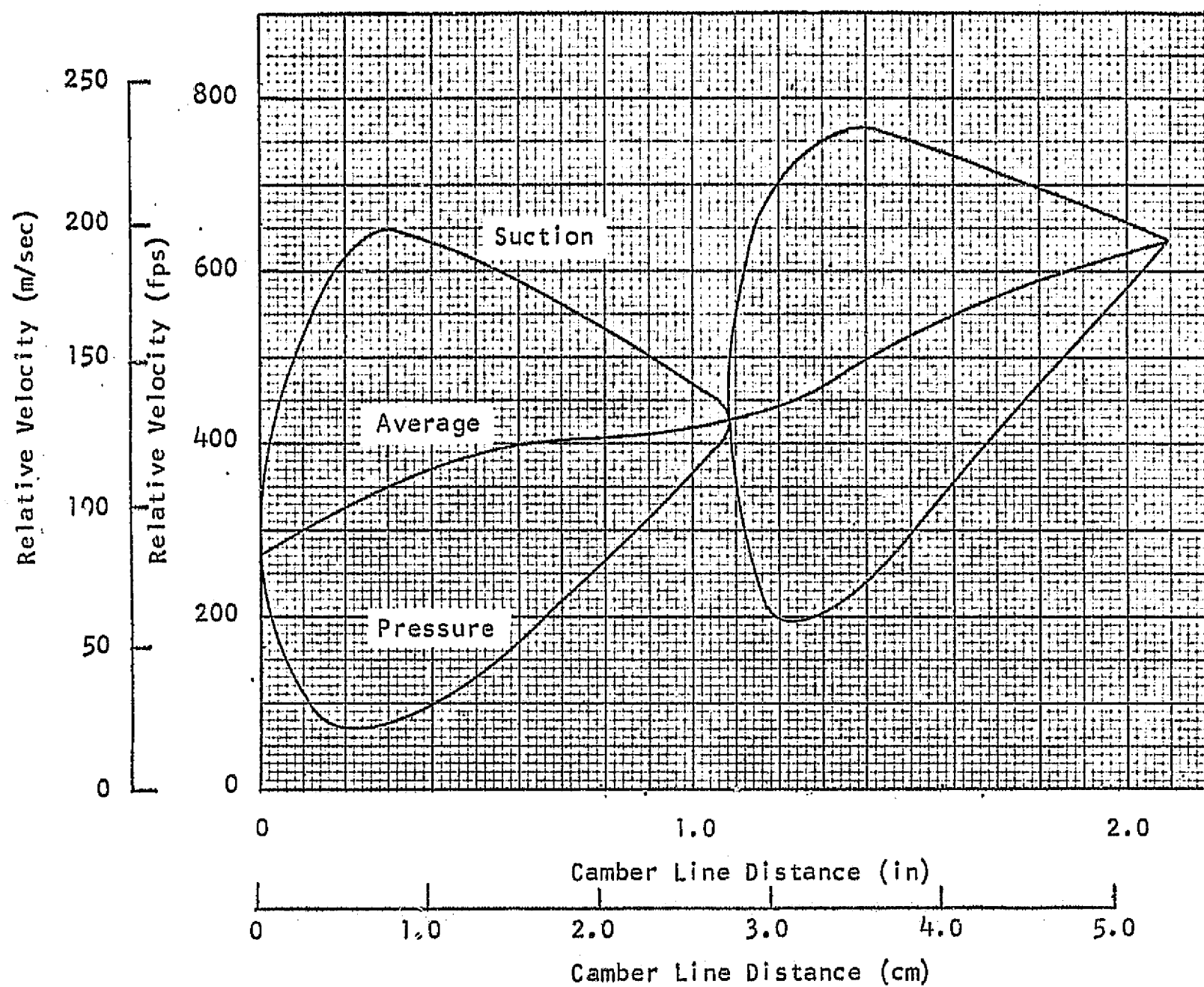


FIGURE 9 - THE BLADE LOADING OBJECTIVE FOR THE OUTER CASING
STREAMTUBE OF THE REDESIGNED TURBINE (16 BLADES IN EACH
ROW OF A TANDEM ROW CONFIGURATION)

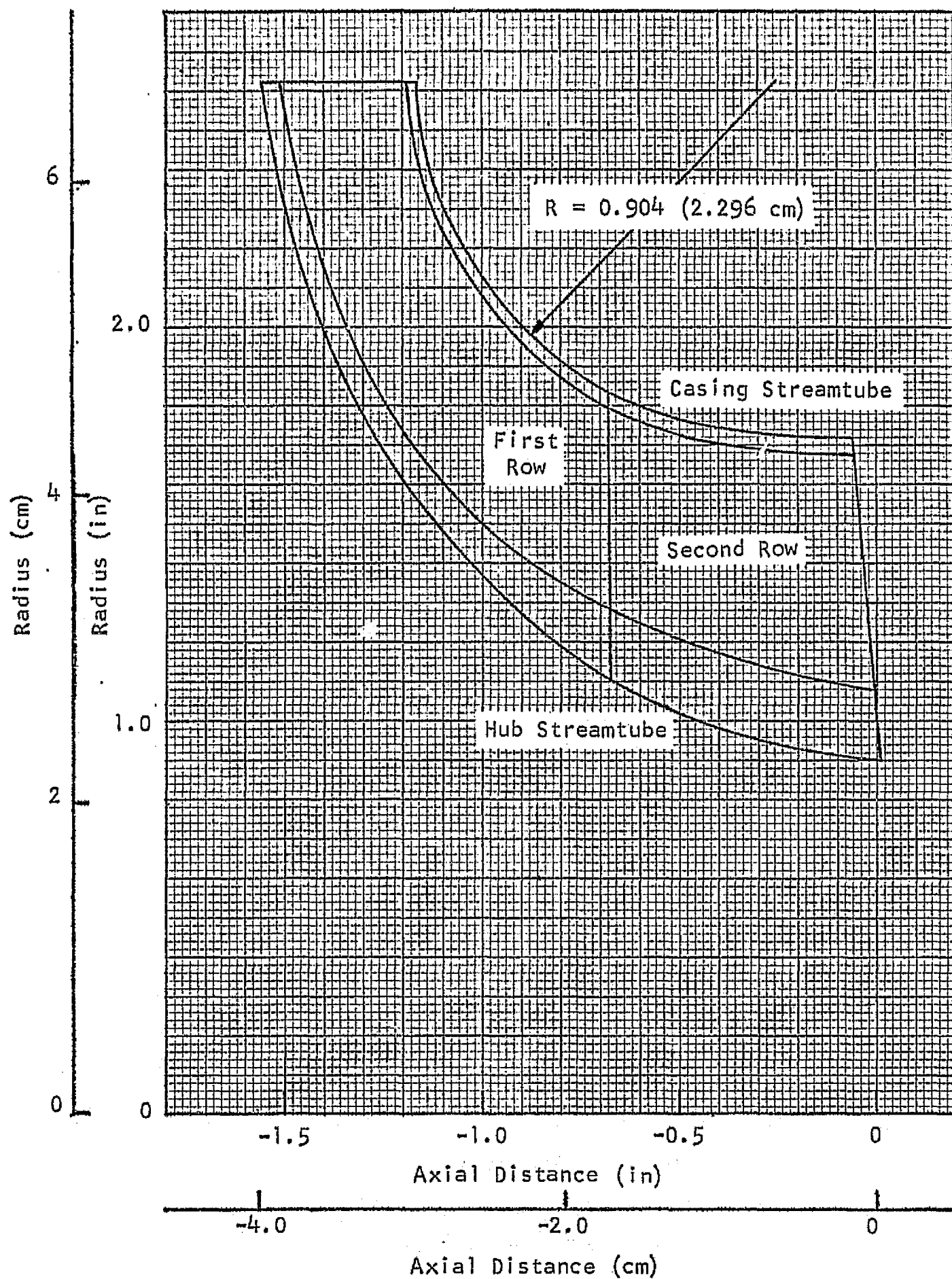


FIGURE 10 - FINAL MERIDIONAL FLOW PATH OF THE BRU TURBINE ROTOR

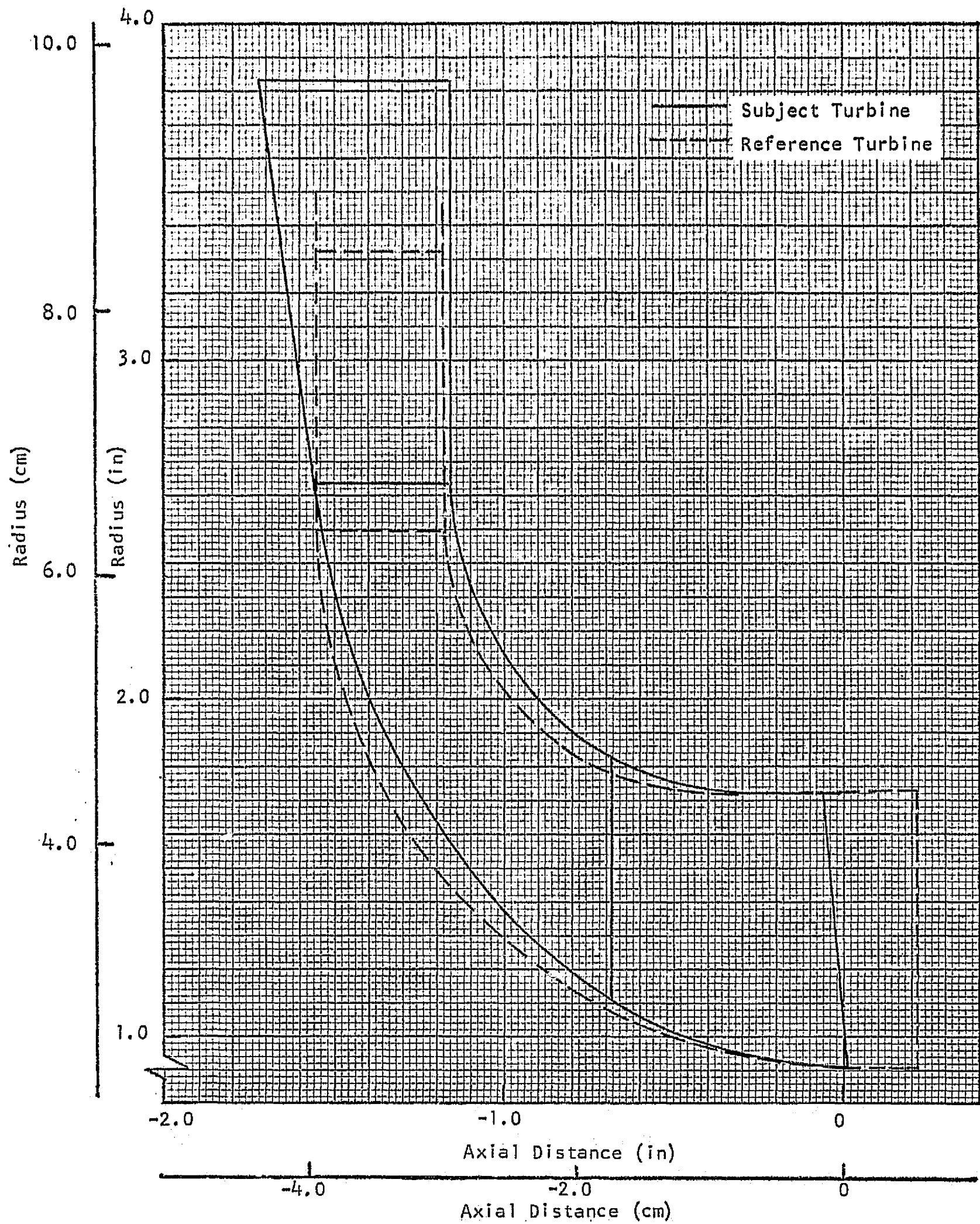


FIGURE 11 - COMPARISON OF THE ORIGINAL AND REDESIGNED TURBINE
MERIDIONAL FLOW PATHS

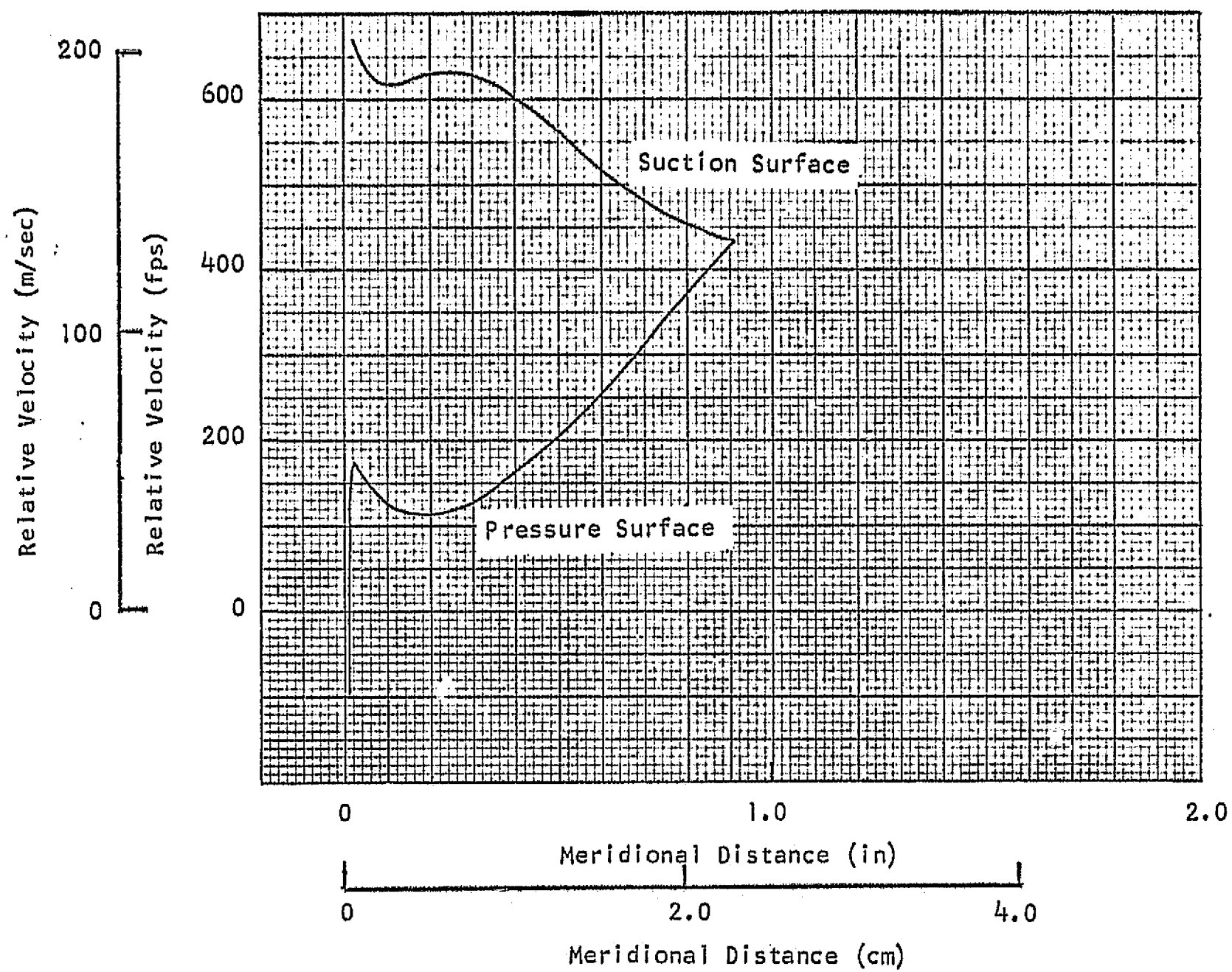


FIGURE 12 - FIRST BLADE ROW SURFACE VELOCITY DISTRIBUTION
(CASING STREAMTUBE)

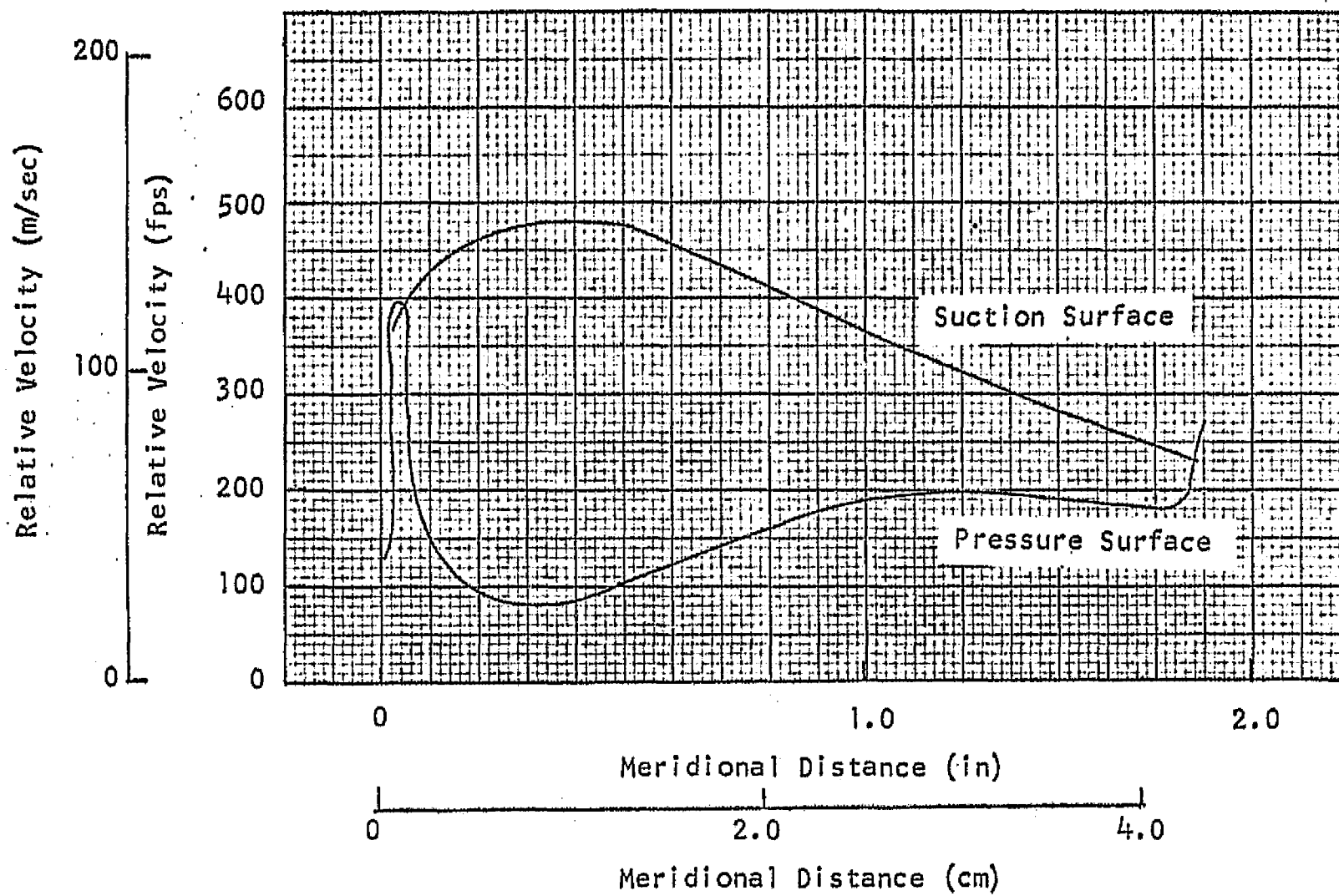


FIGURE 13 - FIRST BLADE ROW SURFACE VELOCITY DISTRIBUTION
(HUB STREAMTUBE)

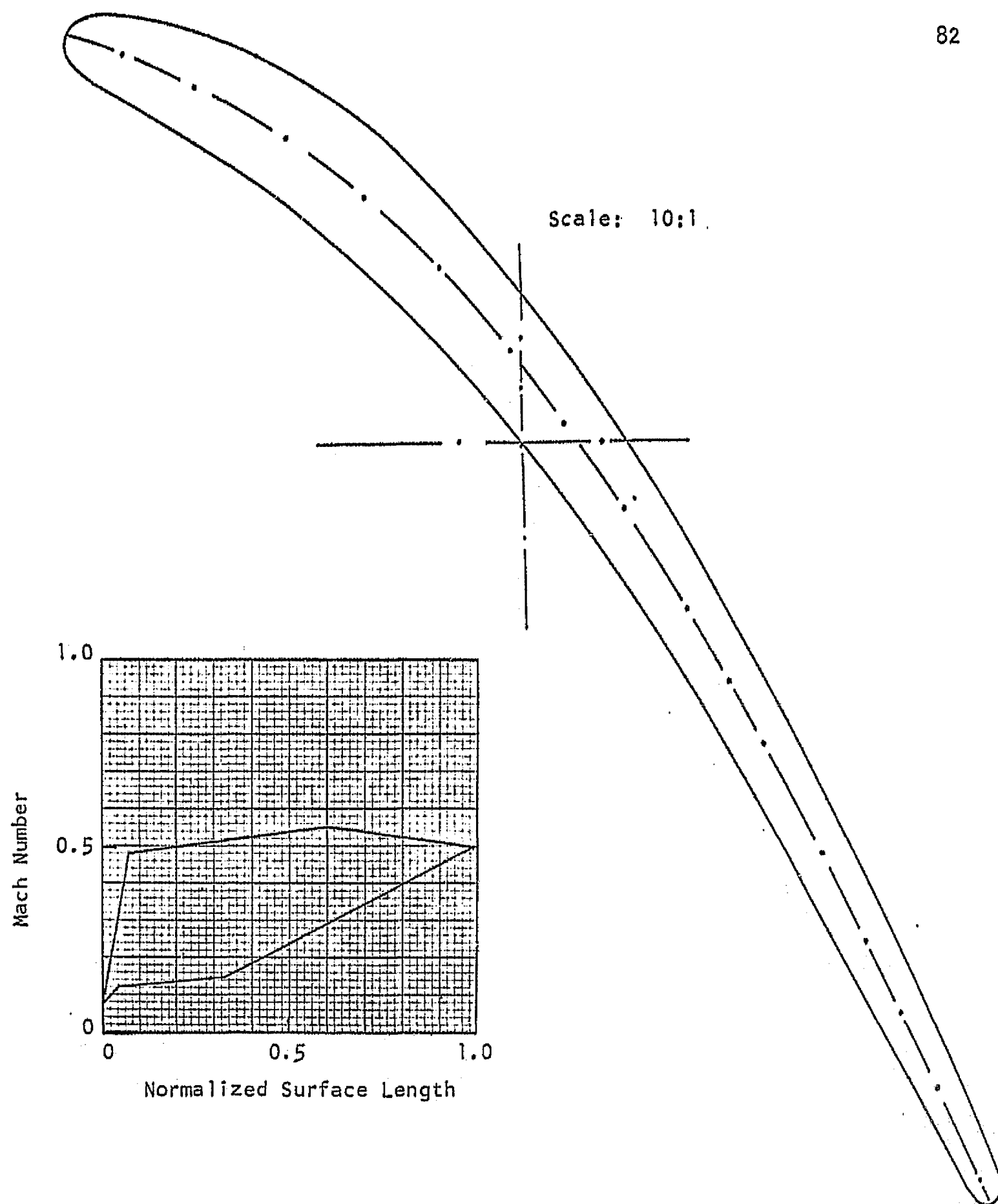


FIGURE 14 - SECOND BLADE ROW SURFACE MACH NUMBER DISTRIBUTION AND
CORRESPONDING BLADE SHAPE AT A RADIUS OF 1.70 INCHES
(NEAR THE OUTER CONTOUR)

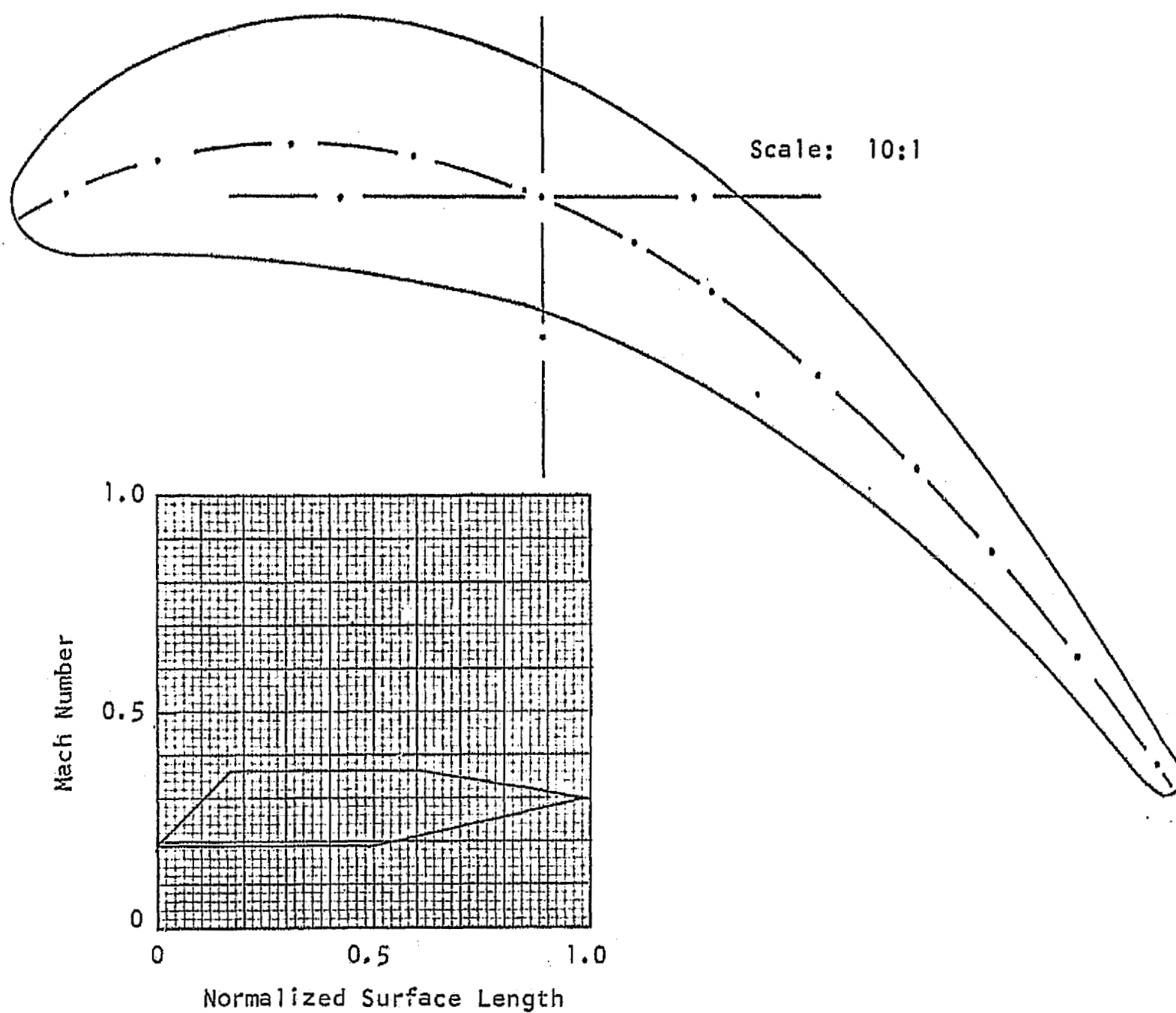


FIGURE 15 - SECOND BLADE ROW SURFACE MACH NUMBER DISTRIBUTION AND
CORRESPONDING BLADE SHAPE AT A RADIUS OF 1.125 INCHES
(NEAR THE HUB)

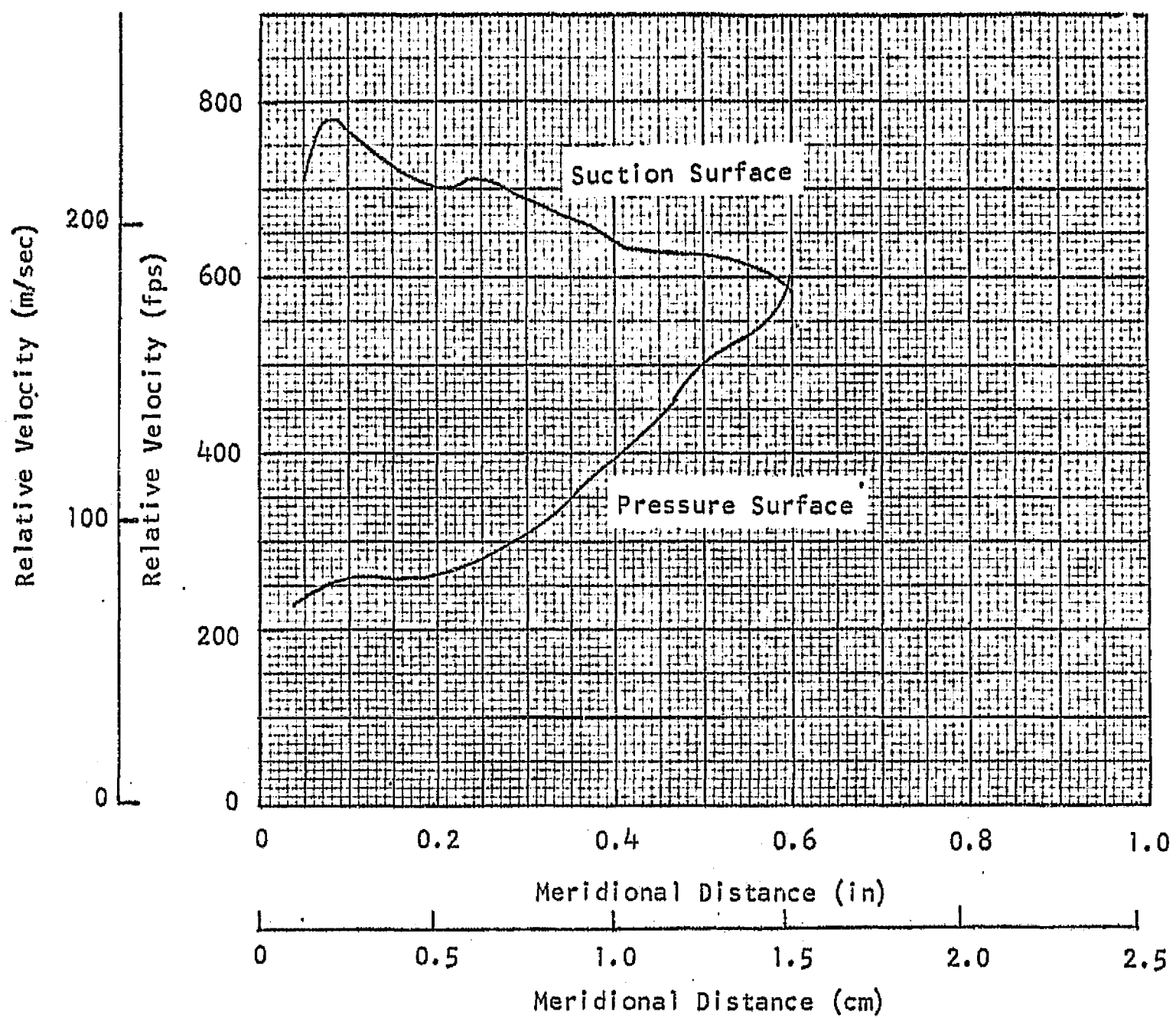


FIGURE 16 - SECOND BLADE ROW SURFACE VELOCITY DISTRIBUTION
(CASING STREAMTUBE)

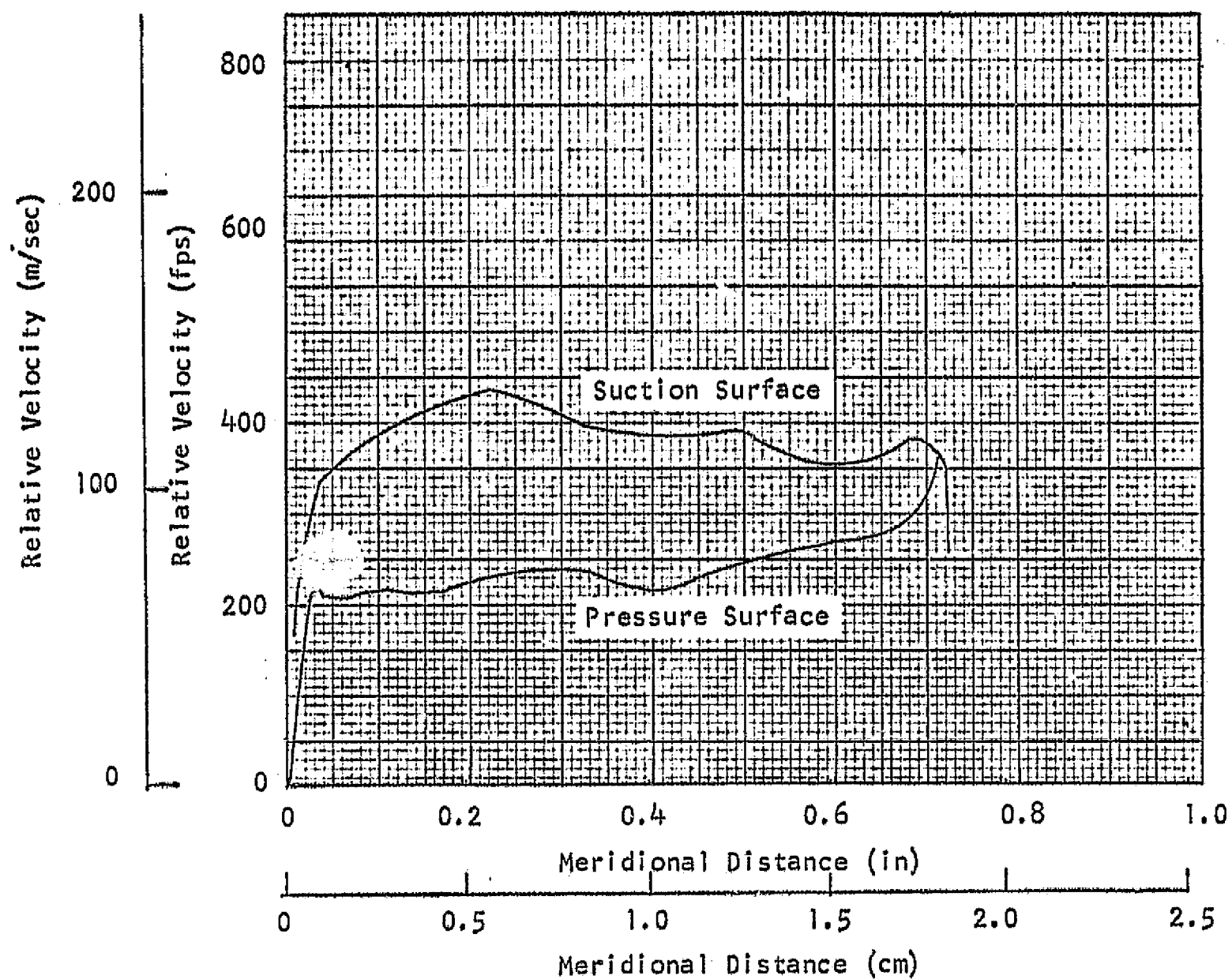


FIGURE 17 - SECOND BLADE ROW SURFACE VELOCITY DISTRIBUTION (HUB STREAMTUBE)

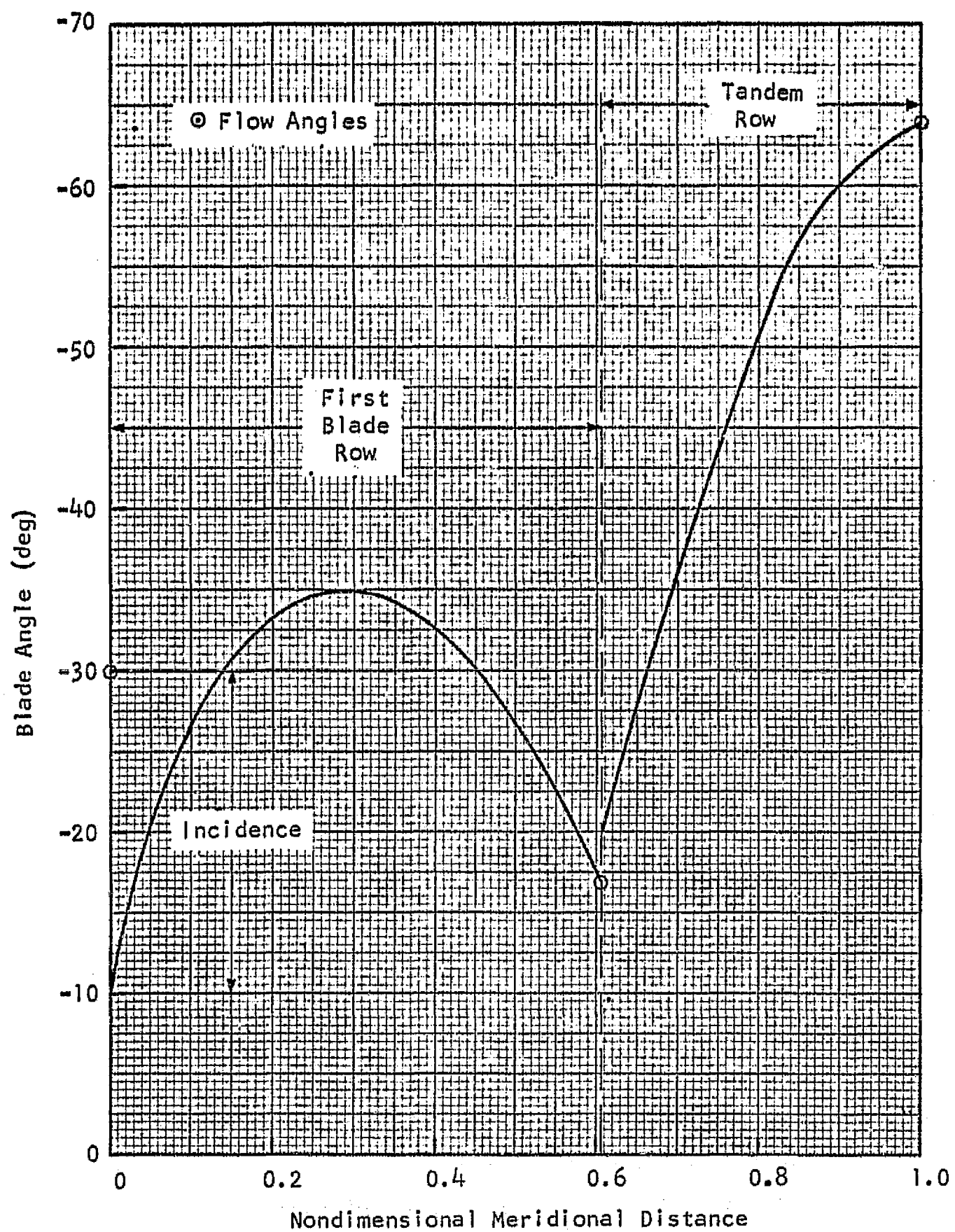


FIGURE 18 - BLADE ANGLE VARIATION ALONG THE STREAMLINE NEAR THE OUTER CASING
(CASING STREAMTUBE CENTERS)

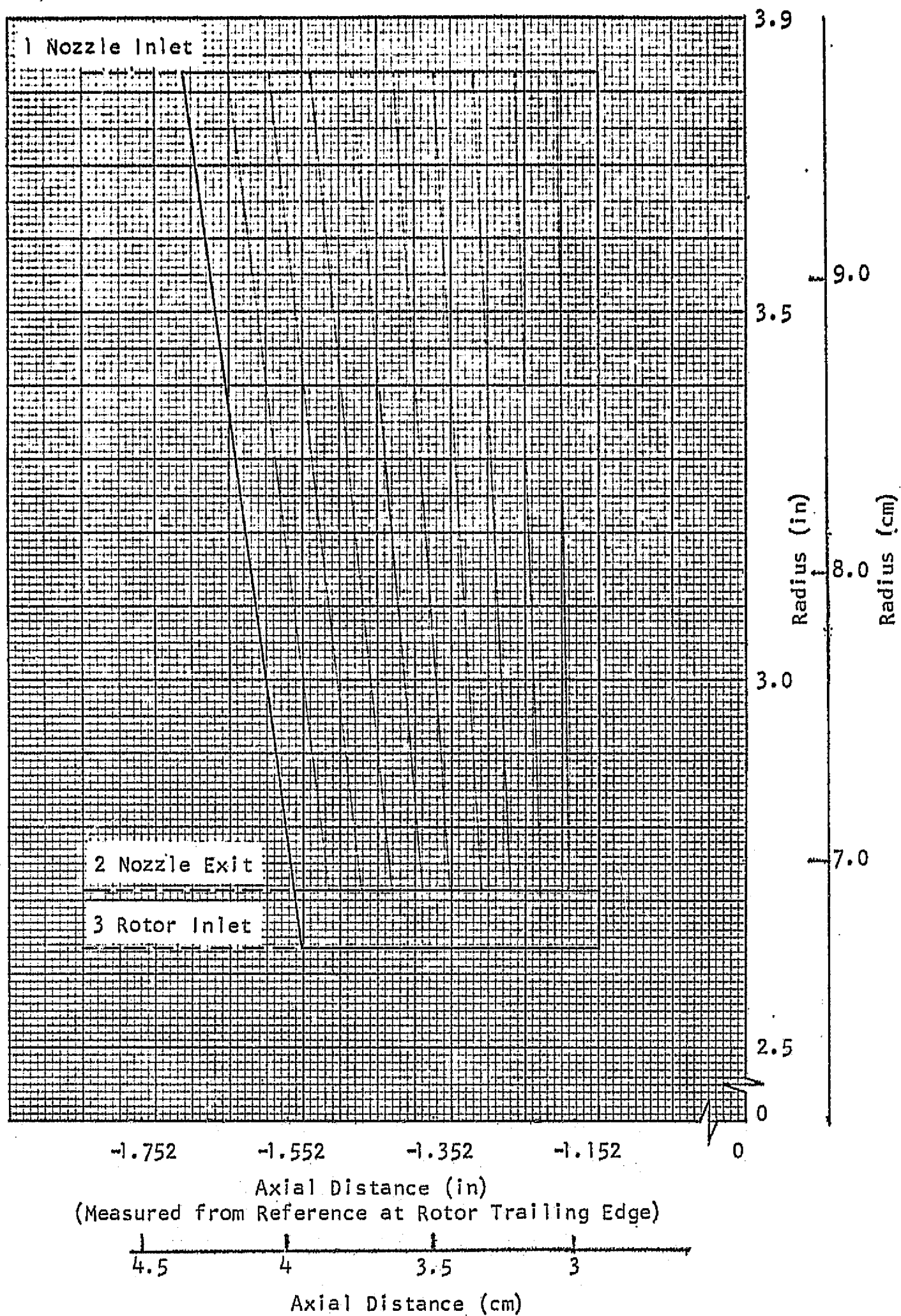


FIGURE 19 - MERIDIONAL FLOW PATH OF THE NOZZLE

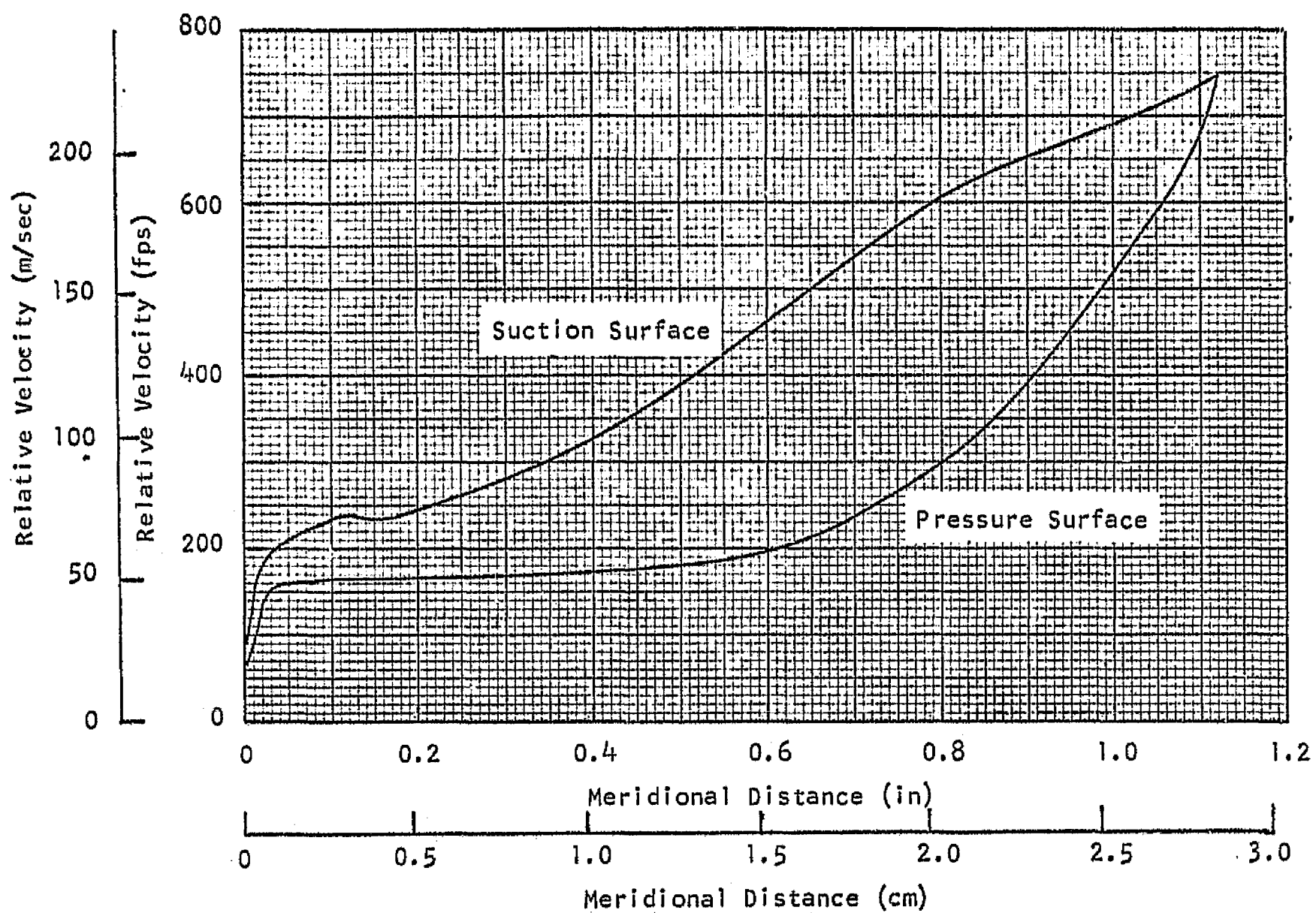


FIGURE 20 - SURFACE VELOCITY DISTRIBUTION OF THE NOZZLE VANE

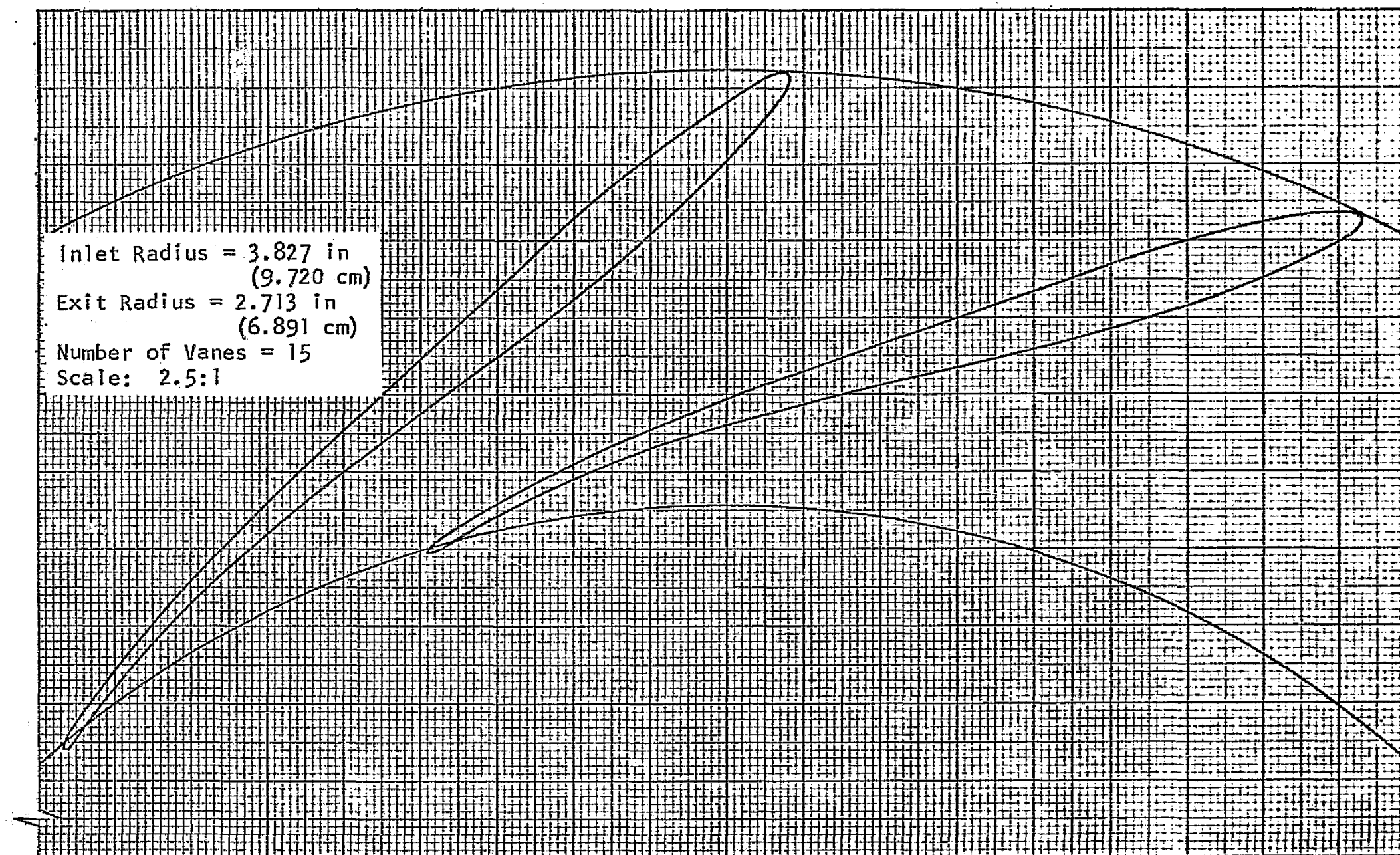


FIGURE 21 - NOZZLE VANE GEOMETRY SELECTED FOR THE FINAL DESIGN

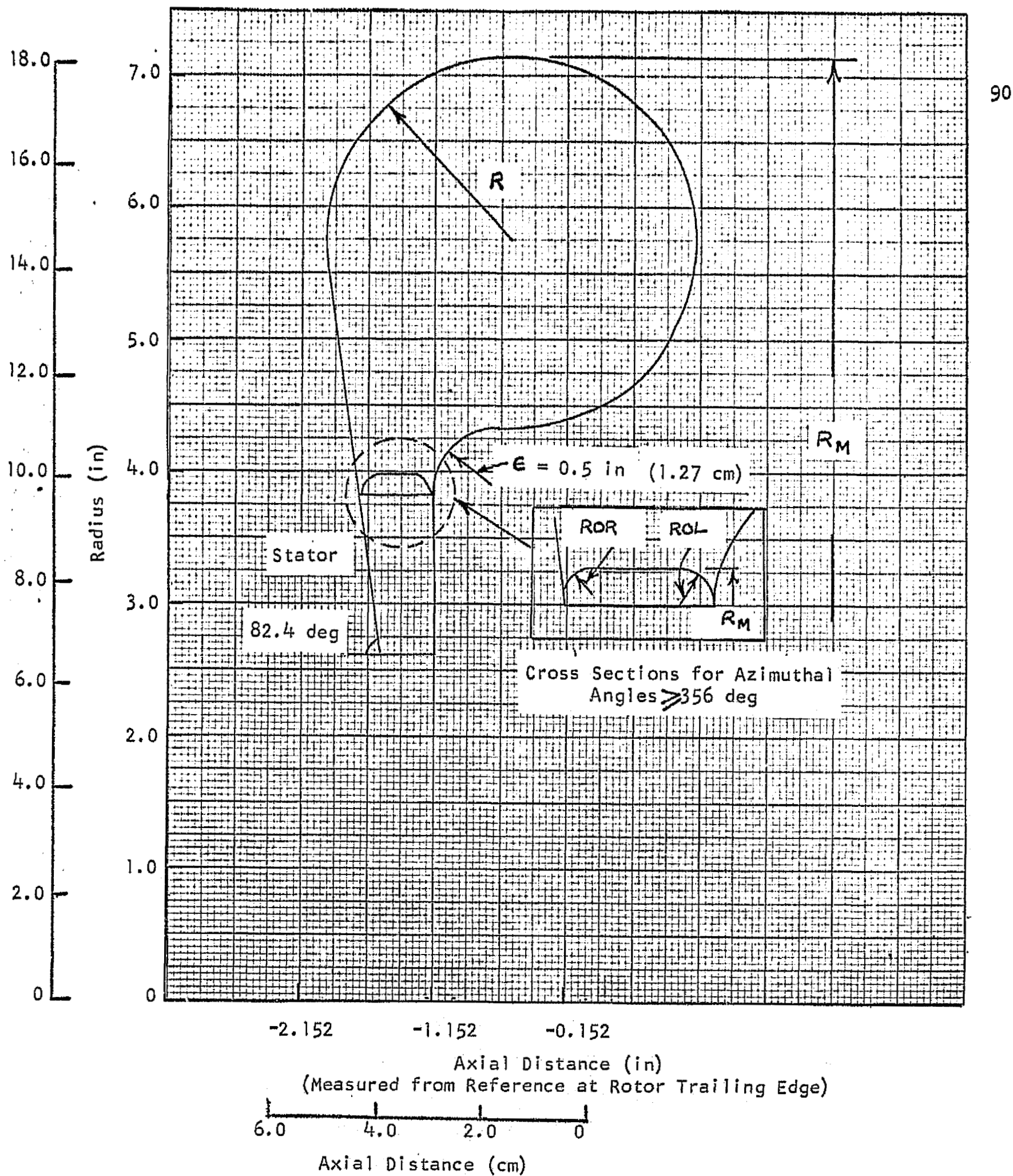


FIGURE 22 - TURBINE INLET SCROLL GEOMETRY

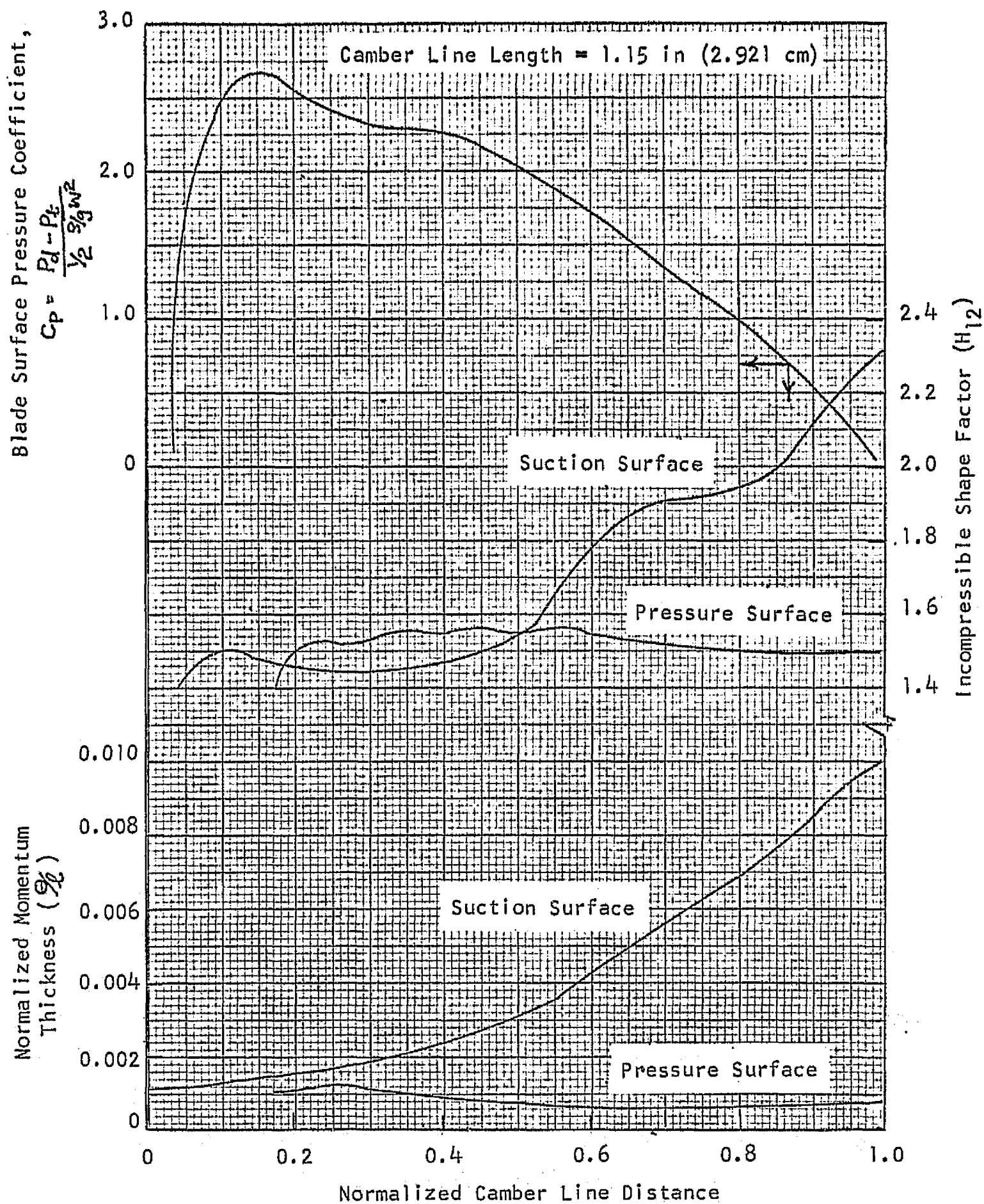


FIGURE 23 - TWO-DIMENSIONAL BOUNDARY-LAYER PARAMETERS AND SECONDARY FLOW
 PARAMETER C_p OF THE FIRST BLADE ROW (CASING STREAMTUBE)

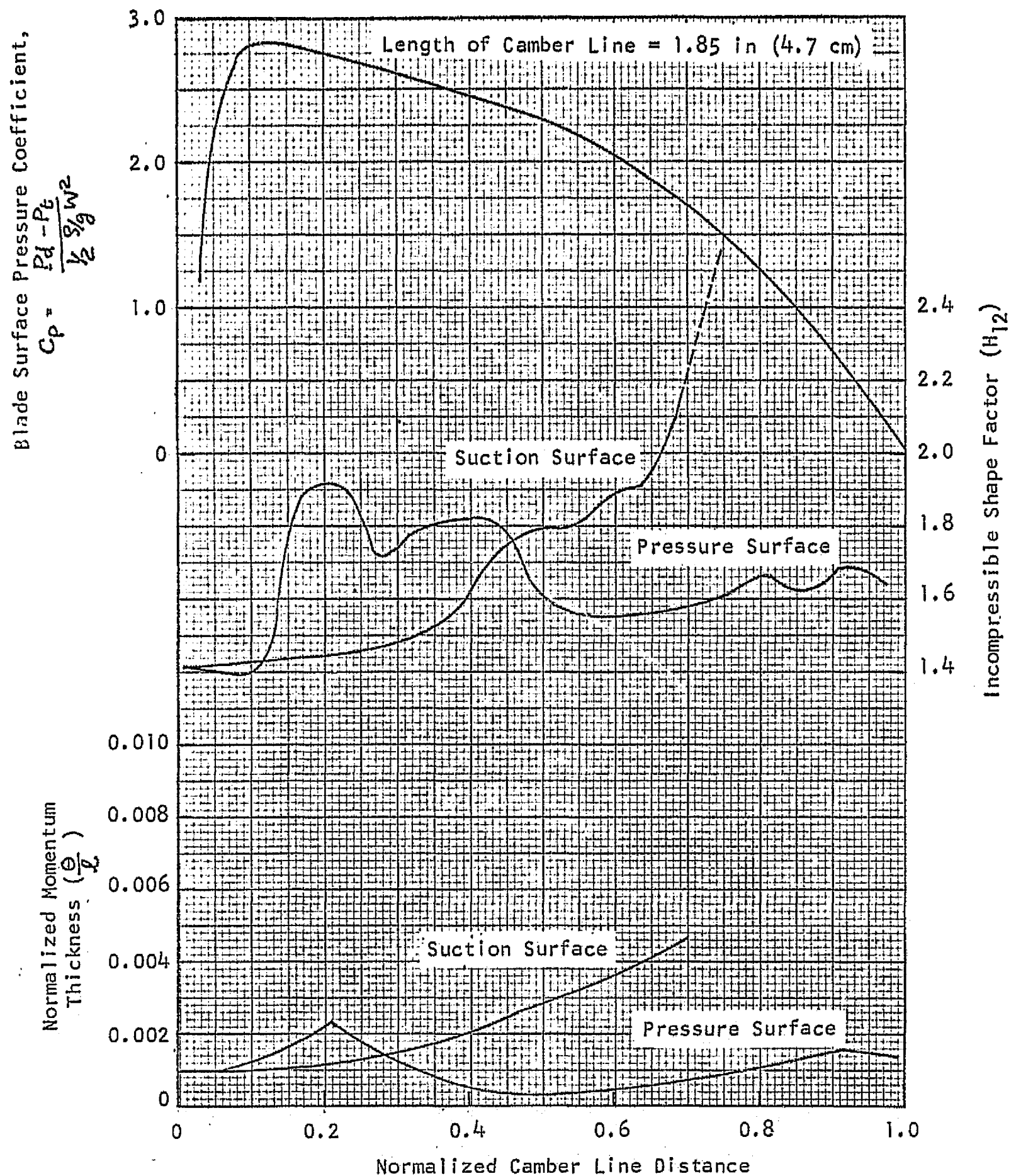


FIGURE 24 - TWO-DIMENSIONAL BOUNDARY-LAYER PARAMETERS AND SECONDARY FLOW
 PARAMETER C_p OF THE FIRST BLADE ROW (HUB STREAMTUBE)

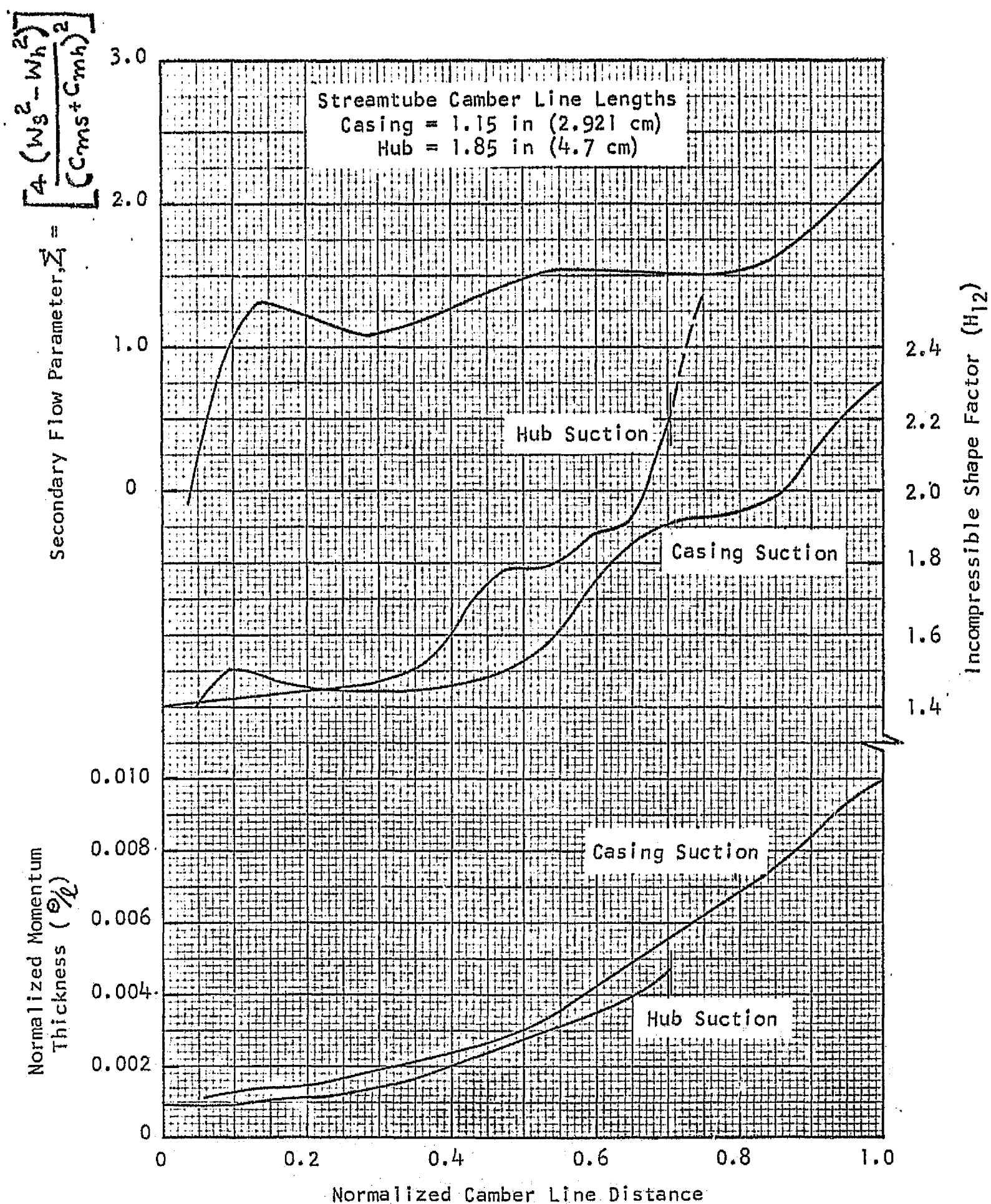


FIGURE 25 - TWO-DIMENSIONAL BOUNDARY-LAYER PARAMETERS AND SECONDARY FLOW PARAMETER Z_1 FROM HUB TO CASING OF THE FIRST BLADE ROW (SUCTION SURFACE)

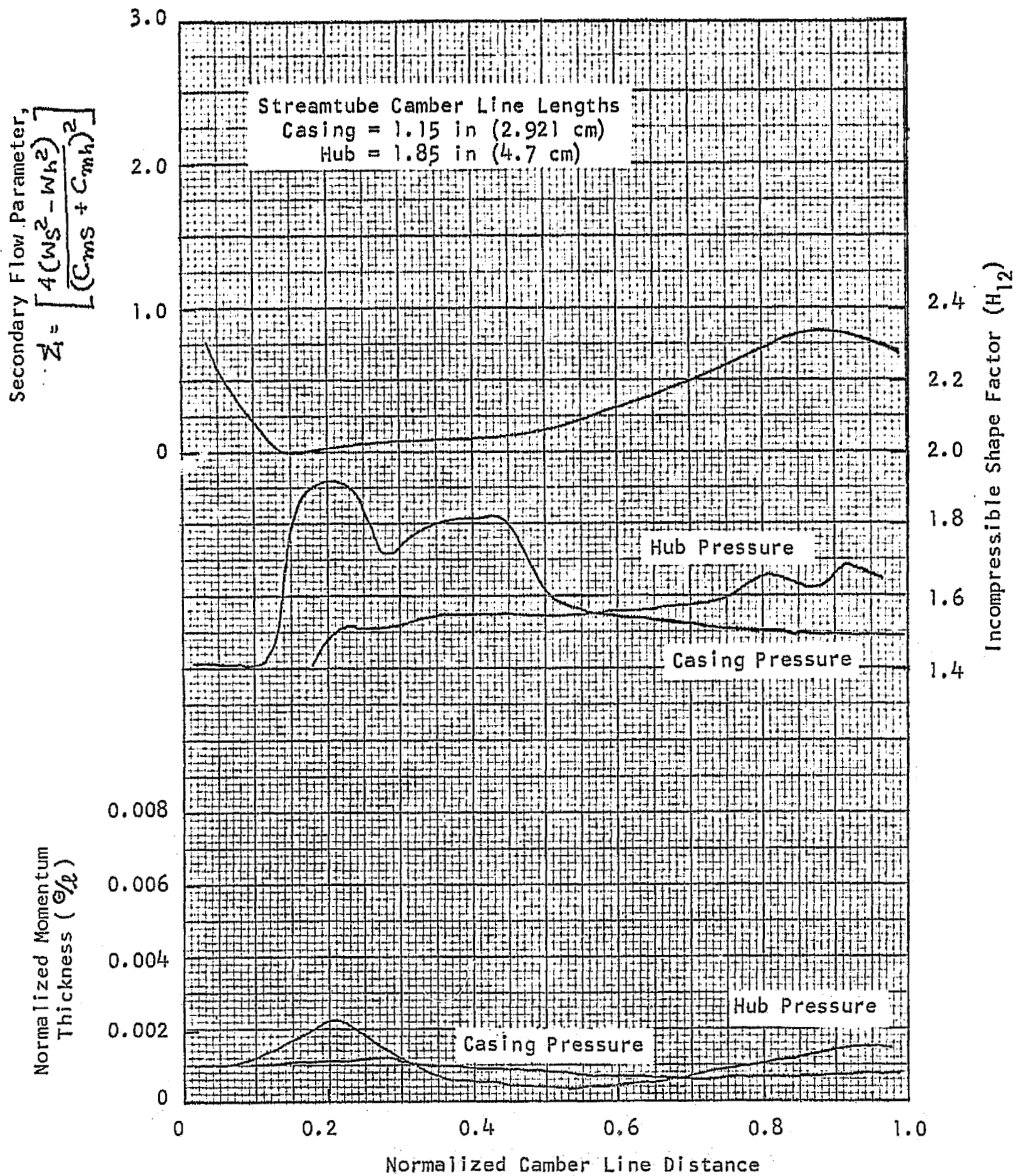


FIGURE 26 - TWO-DIMENSIONAL BOUNDARY-LAYER PARAMETERS AND SECONDARY FLOW PARAMETER Z_1 FROM HUB TO CASING OF THE FIRST BLADE ROW (PRESSURE SURFACE)

Blade Surface Pressure Coefficient,

$$C_p = \frac{P_d - P_t}{\frac{1}{2} \rho V^2}$$

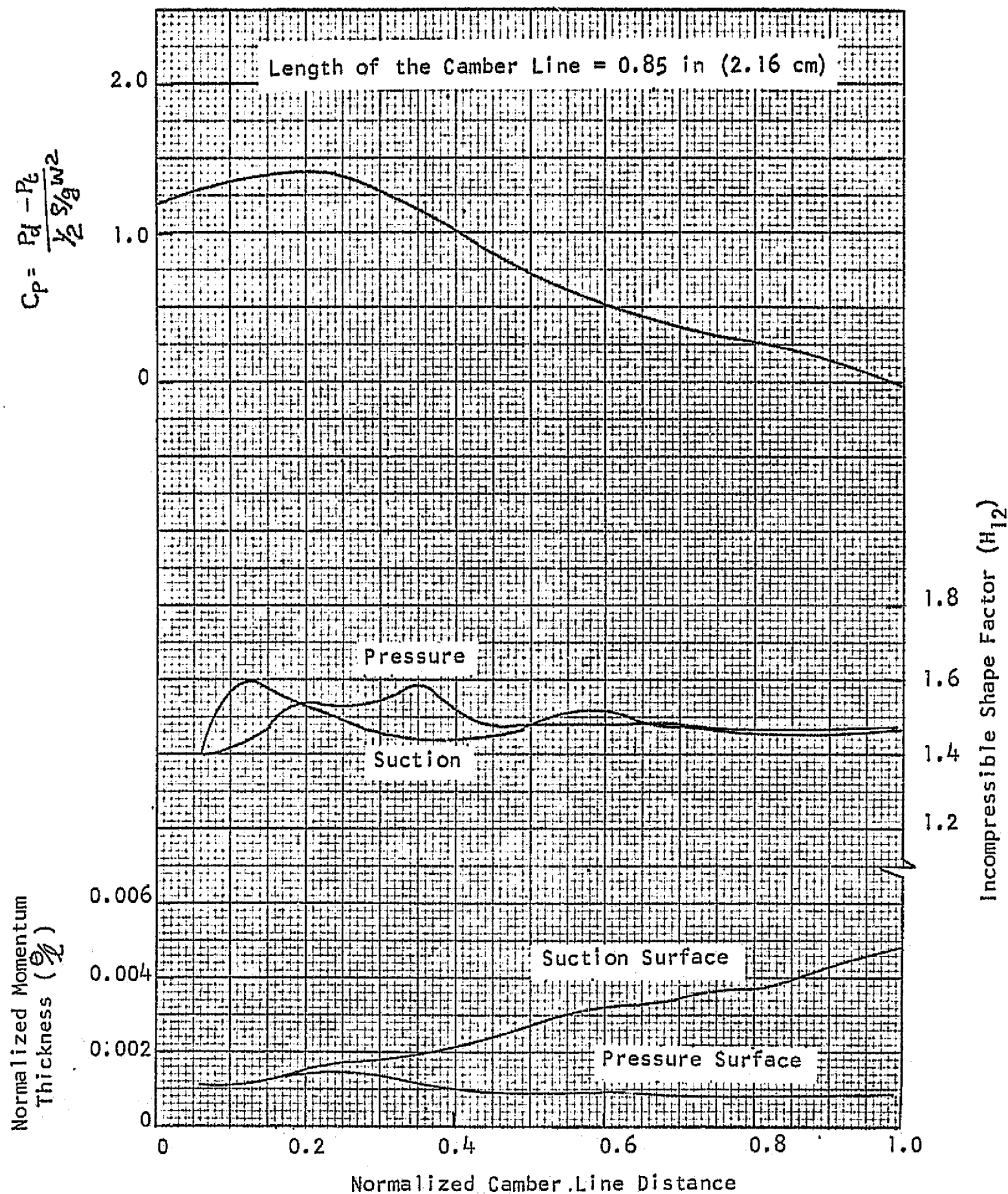


FIGURE 27 - TWO-DIMENSIONAL BOUNDARY-LAYER PARAMETERS AND SECONDARY FLOW
PARAMETER C_p OF THE SECOND BLADE ROW (CASING STREAMTUBE)

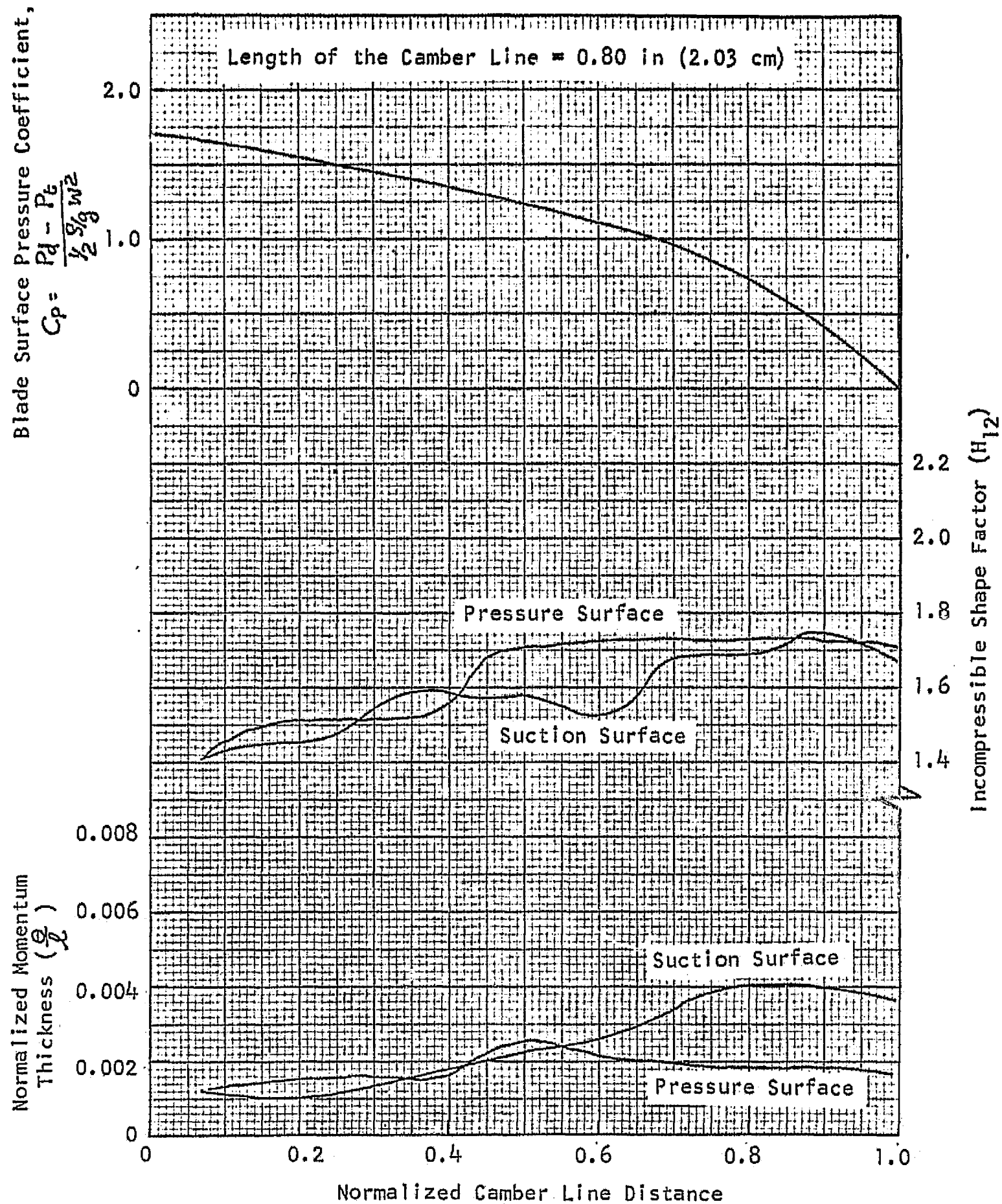


FIGURE 28 - TWO-DIMENSIONAL BOUNDARY-LAYER PARAMETERS AND SECONDARY FLOW PARAMETER C_p OF THE SECOND BLADE ROW (HUB STREAMTUBE)

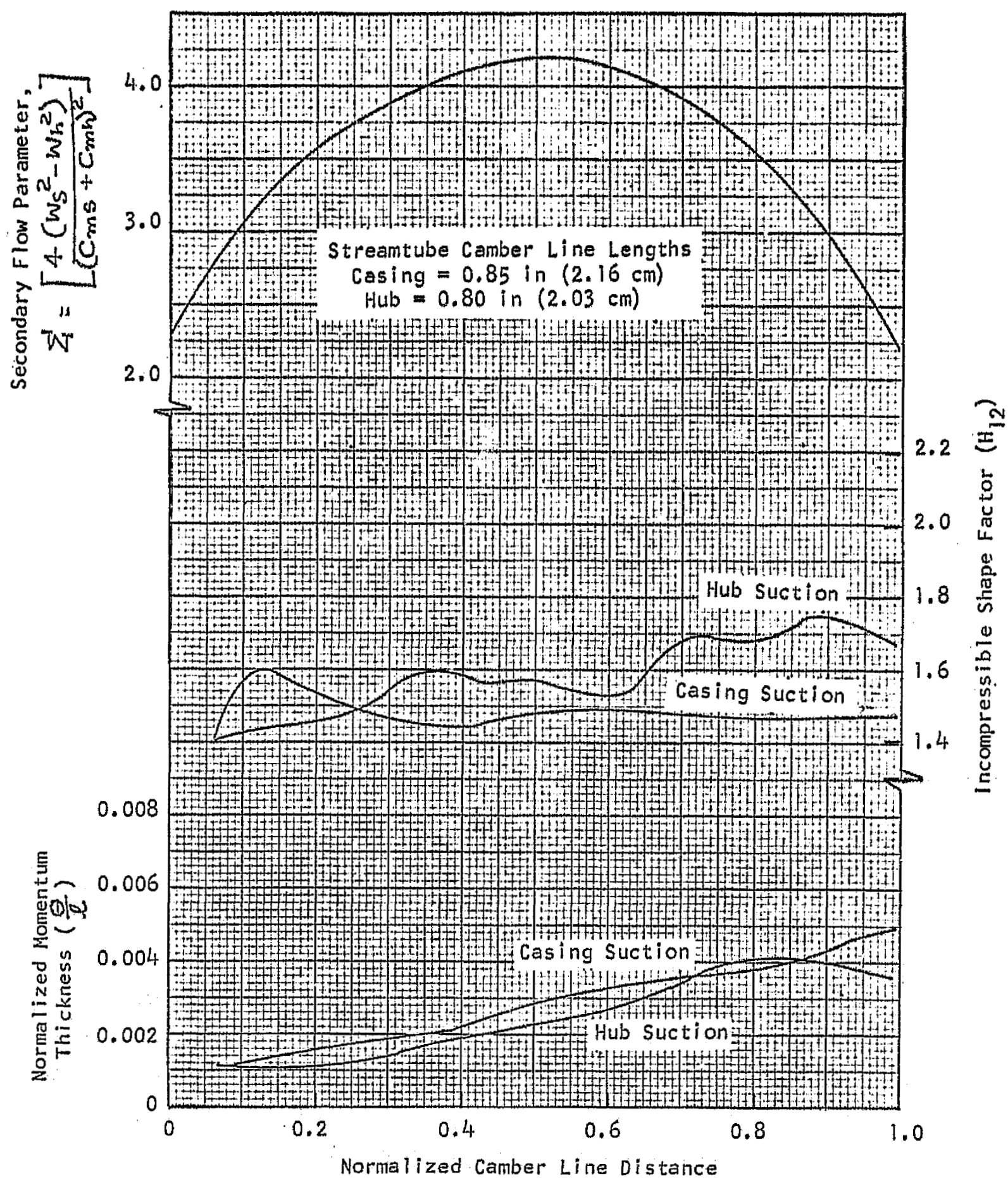


FIGURE 29 - TWO-DIMENSIONAL BOUNDARY-LAYER PARAMETERS AND SECONDARY FLOW
 PARAMETER Σ_1 FROM HUB TO CASING OF THE SECOND
 BLADE ROW (SUCTION SURFACE)

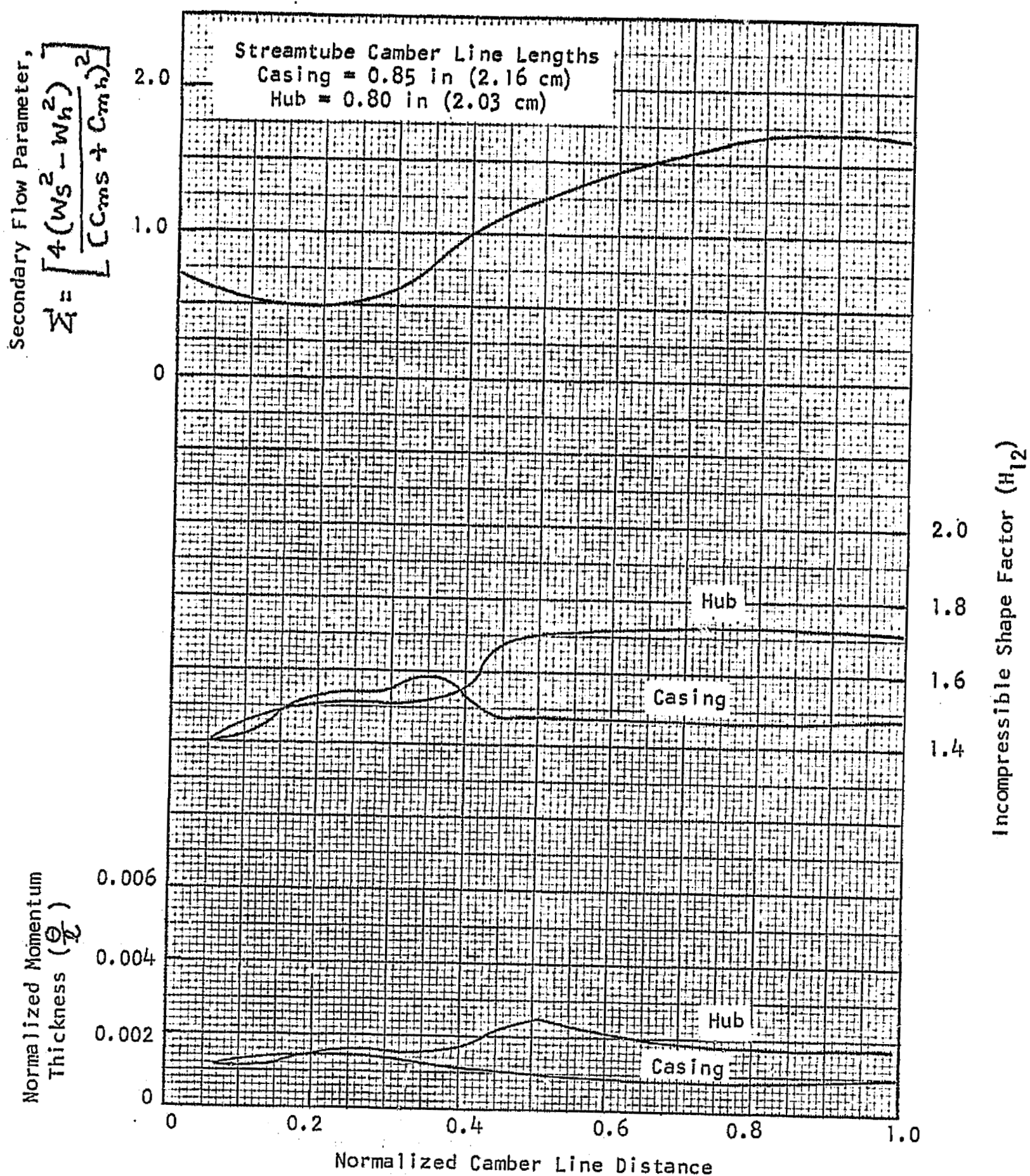


FIGURE 30 - TWO-DIMENSIONAL BOUNDARY-LAYER PARAMETERS AND SECONDARY FLOW
 PARAMETER Σ_1 FROM HUB TO CASING OF THE SECOND
 BLADE ROW (PRESSURE SURFACE)

Blade Surface Pressure Coefficient,

$$C_p = \frac{P_t - P_t}{\frac{1}{2} \rho V^2}$$

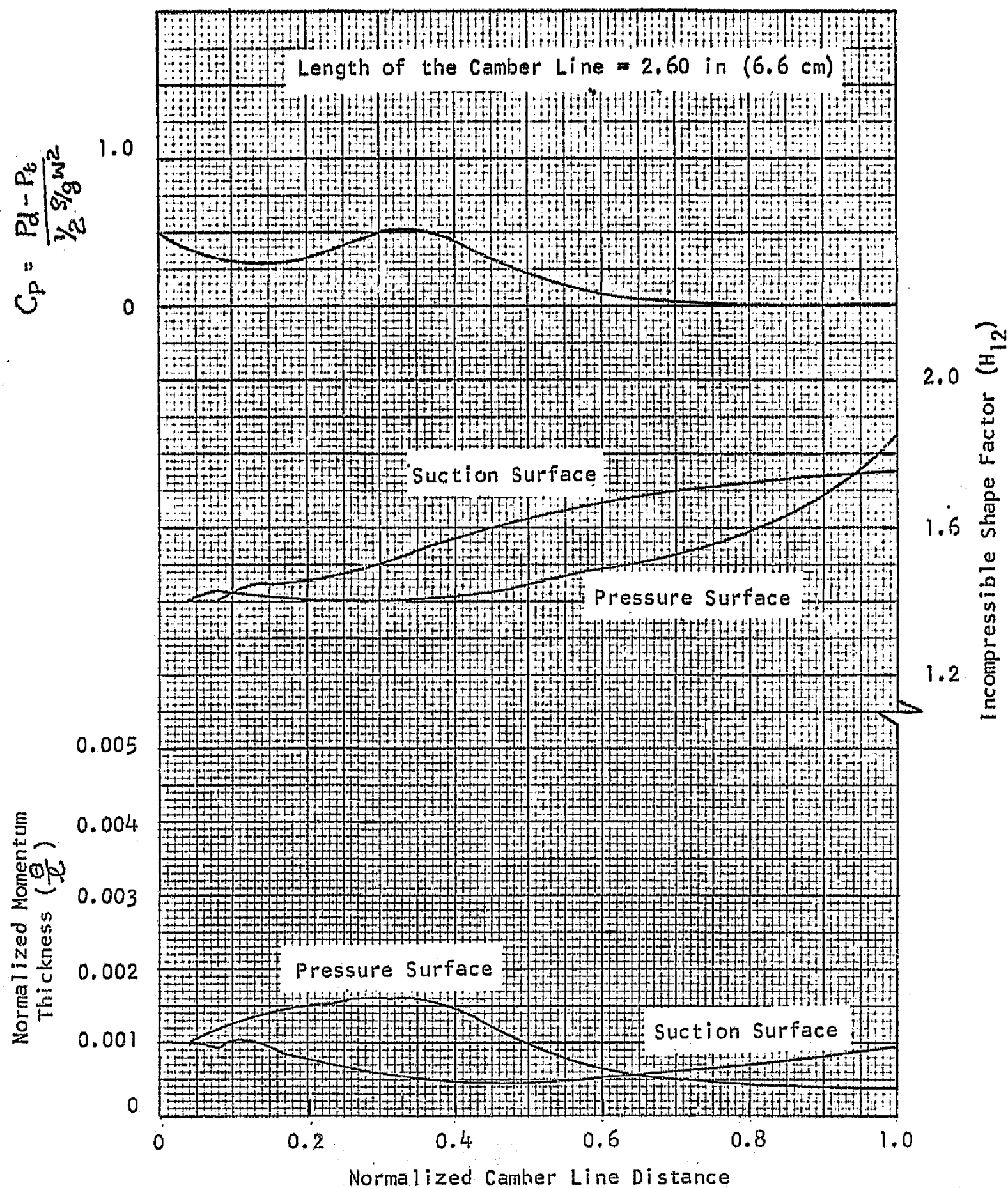


FIGURE 31 - TWO-DIMENSIONAL BOUNDARY-LAYER PARAMETERS AND SECONDARY FLOW
PARAMETER C_p FROM PRESSURE TO THE SUCTION SURFACE OF THE NOZZLE VANE

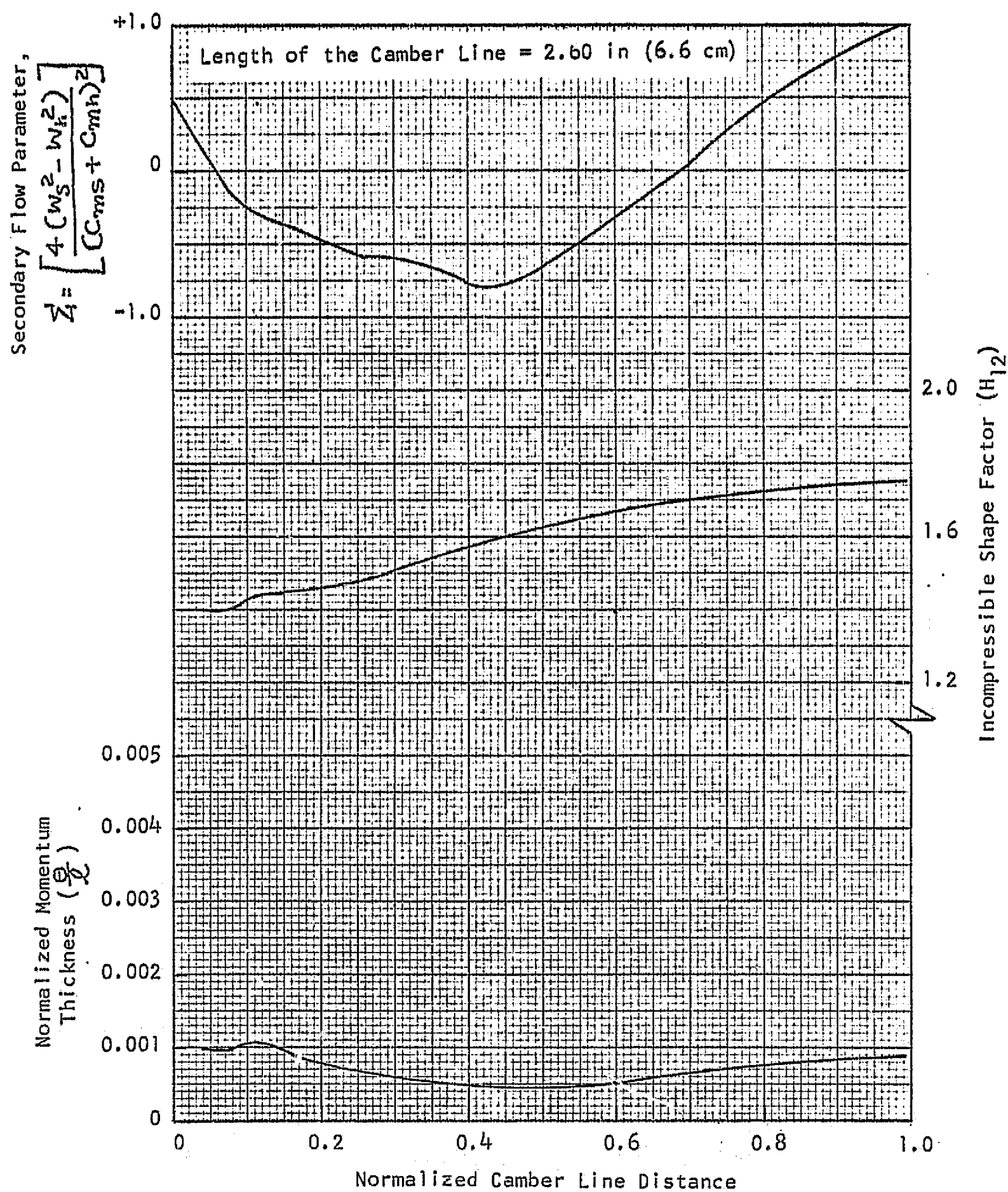


FIGURE 32 - TWO-DIMENSIONAL BOUNDARY-LAYER PARAMETERS AND SECONDARY FLOW
 PARAMETER Σ FROM CASING TO HUB ALONG THE SUCTION SURFACE
 OF THE NOZZLE VANE

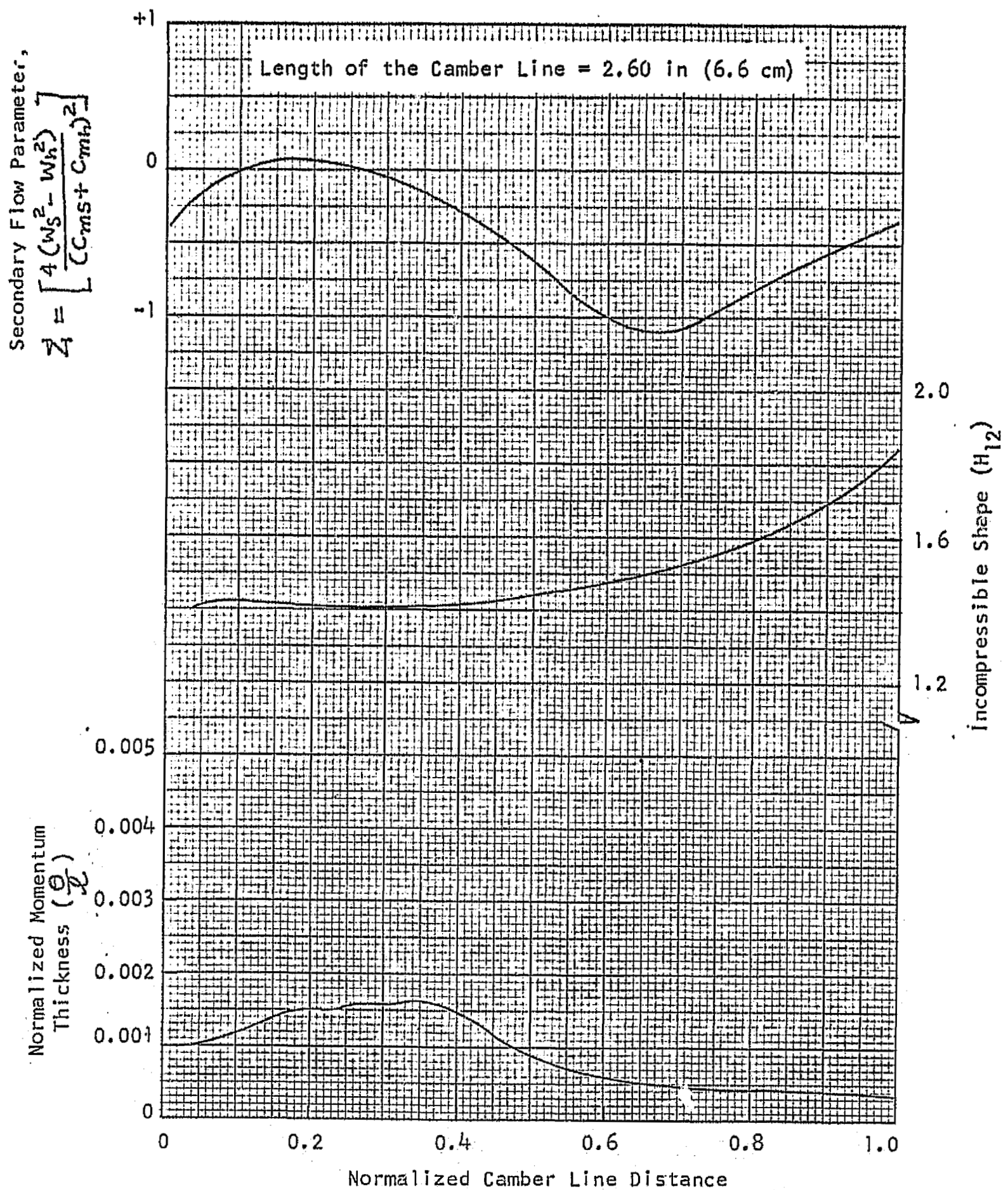


FIGURE 33 - TWO-DIMENSIONAL BOUNDARY-LAYER PARAMETERS AND SECONDARY FLOW
 PARAMETER Z_1 FROM CASING TO HUB ALONG THE PRESSURE
 SURFACE OF THE NOZZLE VANE

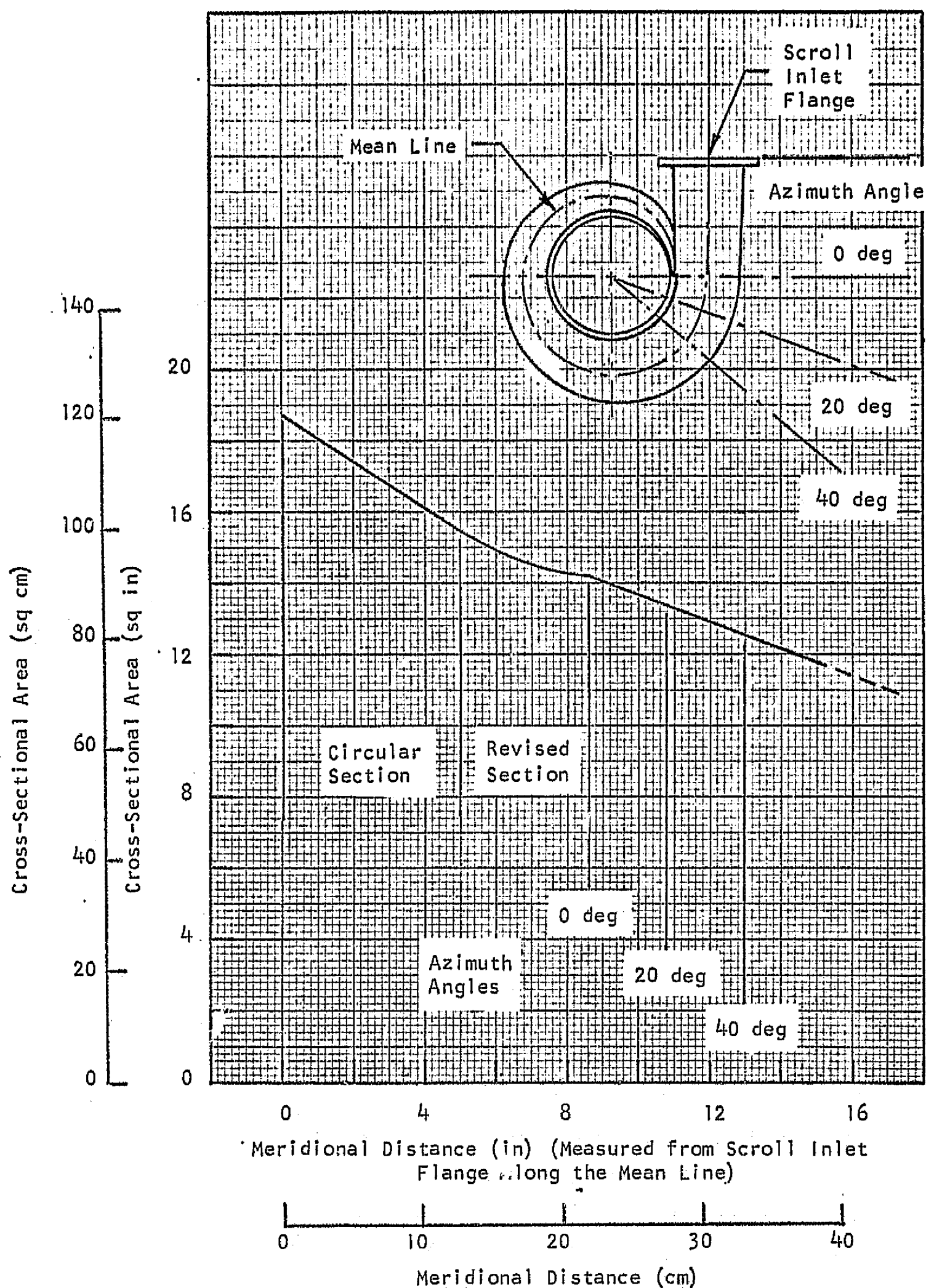


FIGURE 34 - VARIATION IN CROSS SECTION OF THE TURBINE INLET SCROLL TRANSITION PIECE (FROM SCROLL INLET FLANGE TO ZERO DEGREES AZIMUTHAL ANGLE)

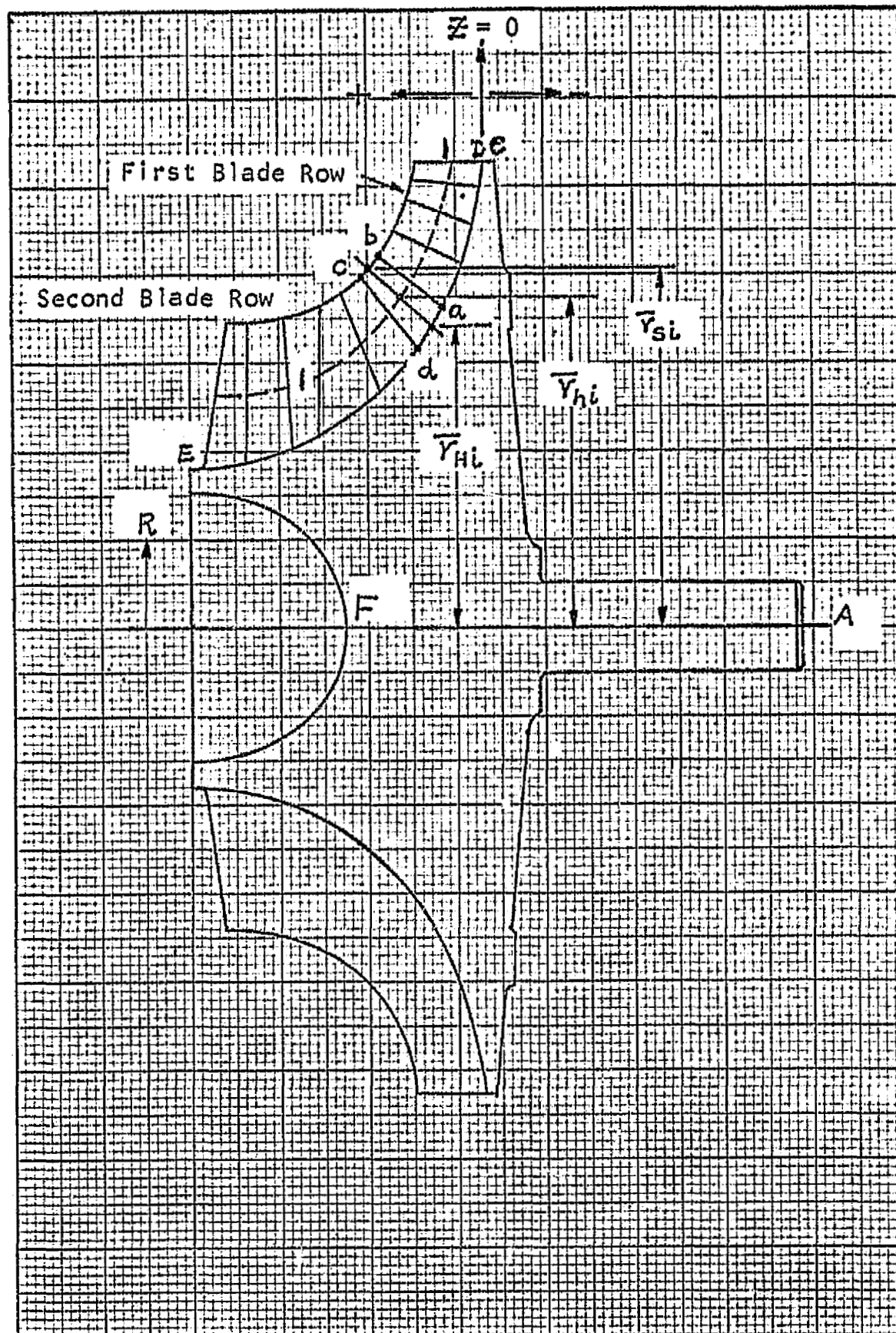


FIGURE 35 - MERIDIONAL VIEW OF ROTOR SHOWING HEAT TRANSFER AREAS,
BLADE PANELS, AND REFERENCE SURFACE

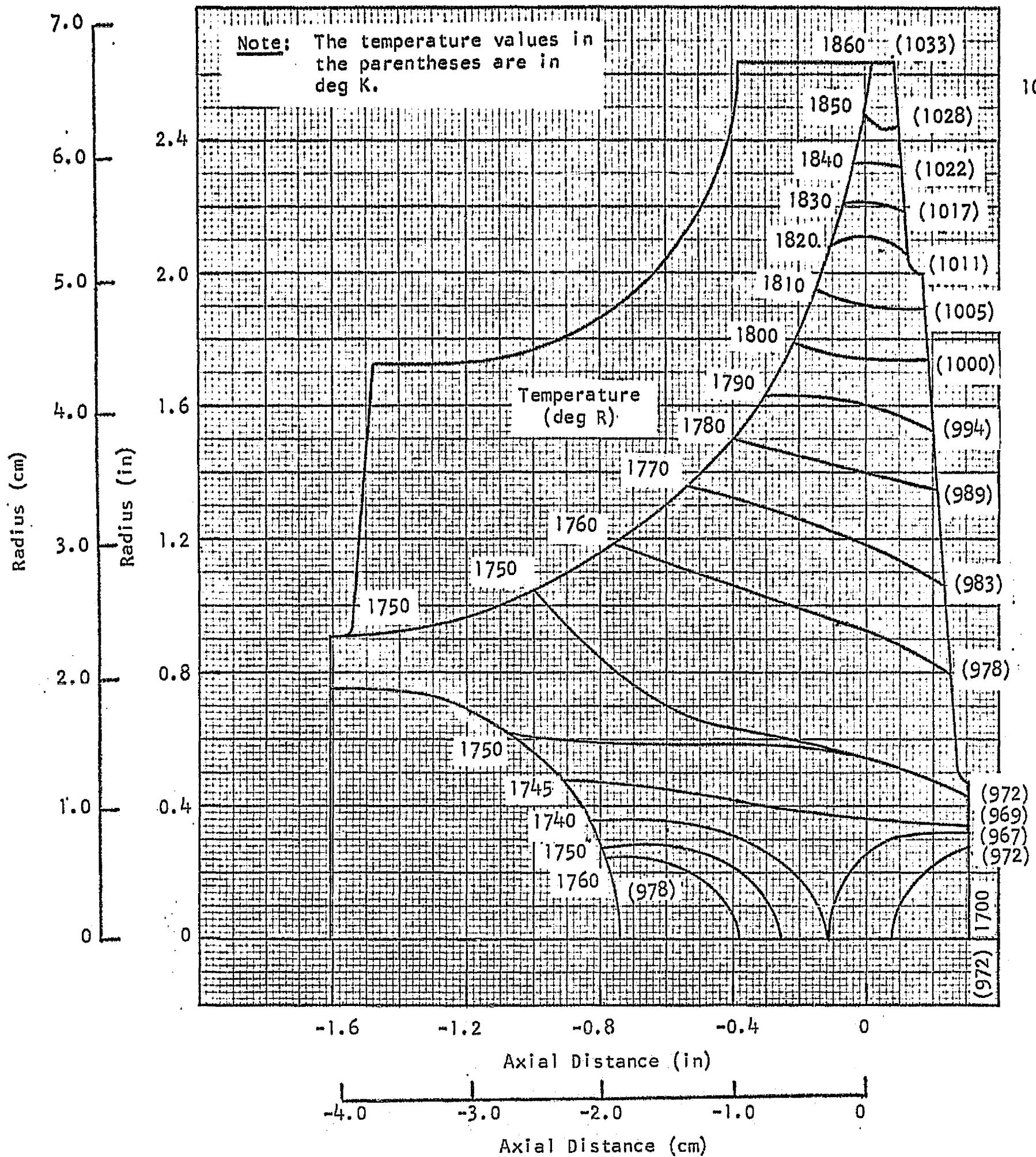


FIGURE 36 - ROTOR TEMPERATURE DISTRIBUTION AT 100 PER CENT SPEED

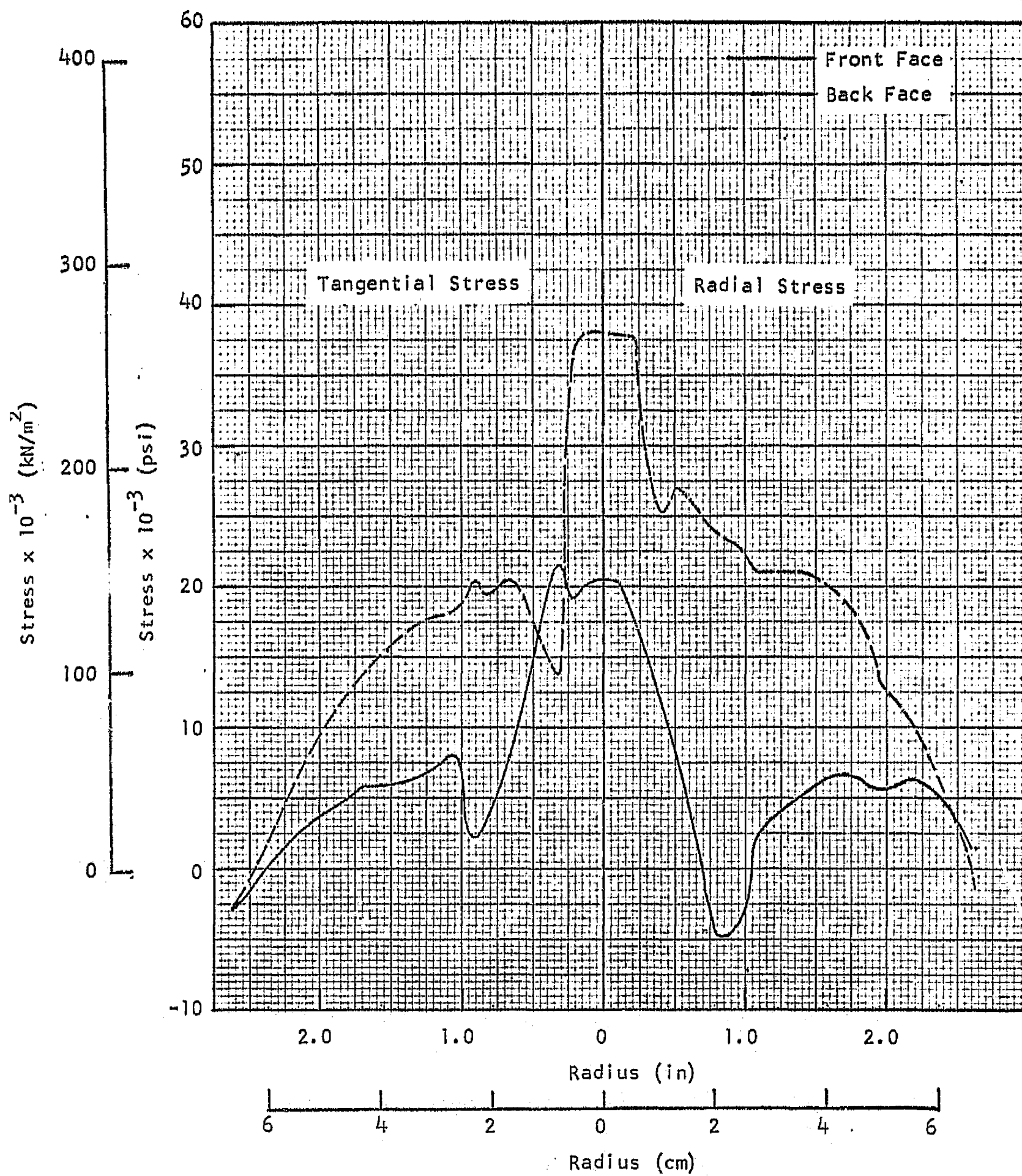


FIGURE 37 - RADIAL VARIATION OF THE DISK STRESSES AT DESIGN TEMPERATURE
OPERATING AT 100 PER CENT SPEED

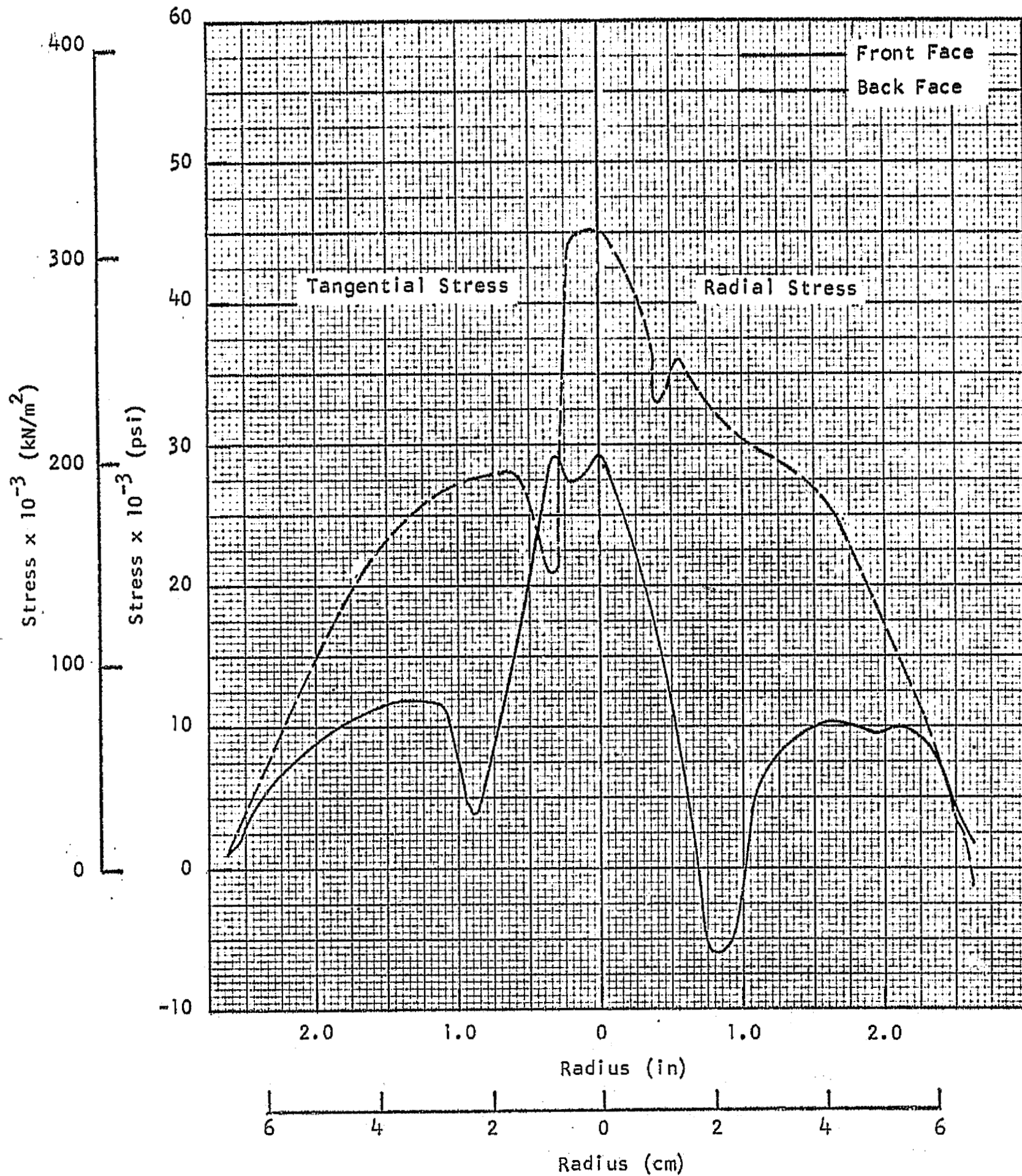


FIGURE 38 - RADIAL VARIATION OF DISK STRESSES AT DESIGN TEMPERATURE
OPERATING AT 120 PER CENT SPEED

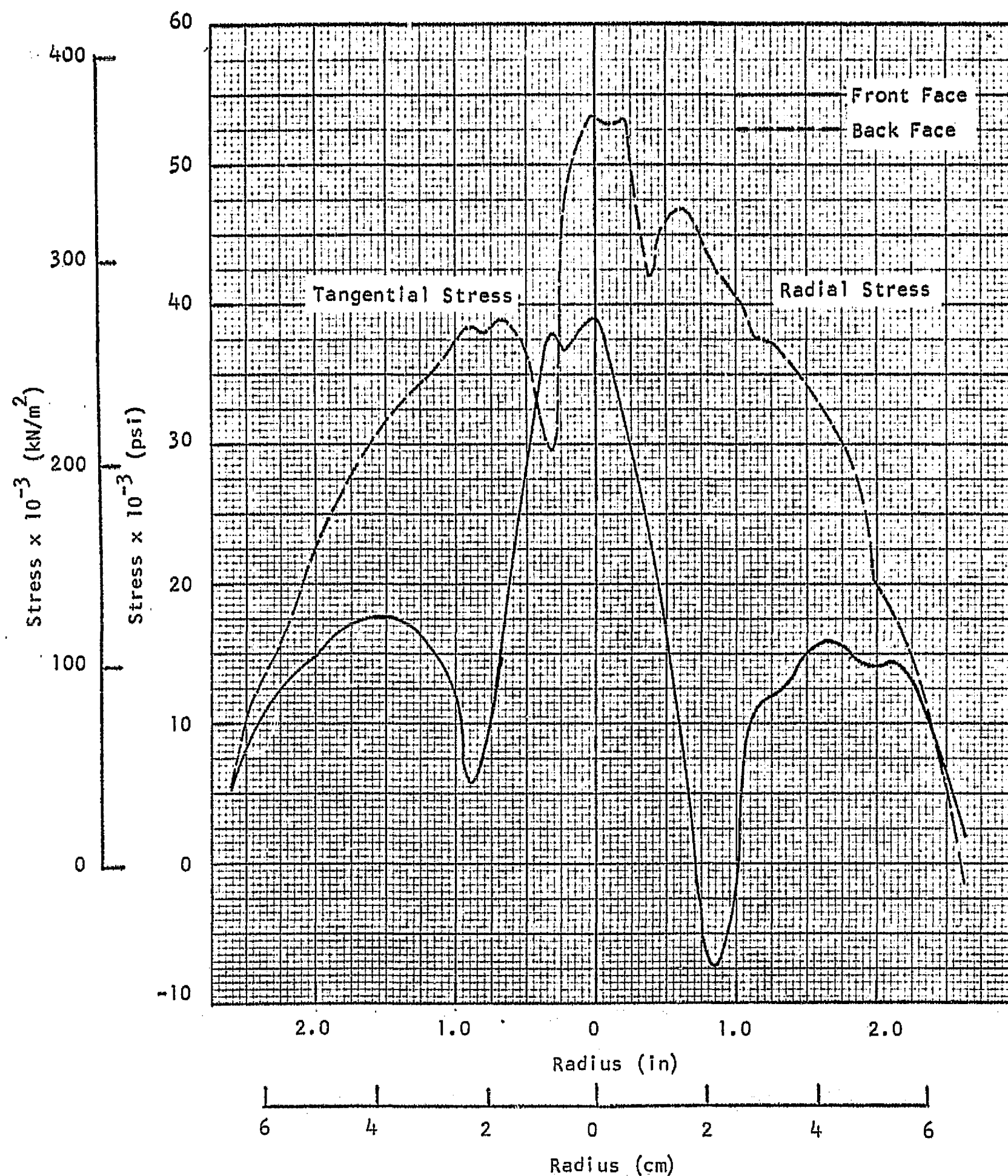


FIGURE 39 - RADIAL VARIATION OF DISK STRESSES AT DESIGN TEMPERATURE
OPERATING AT 140 PER CENT SPEED

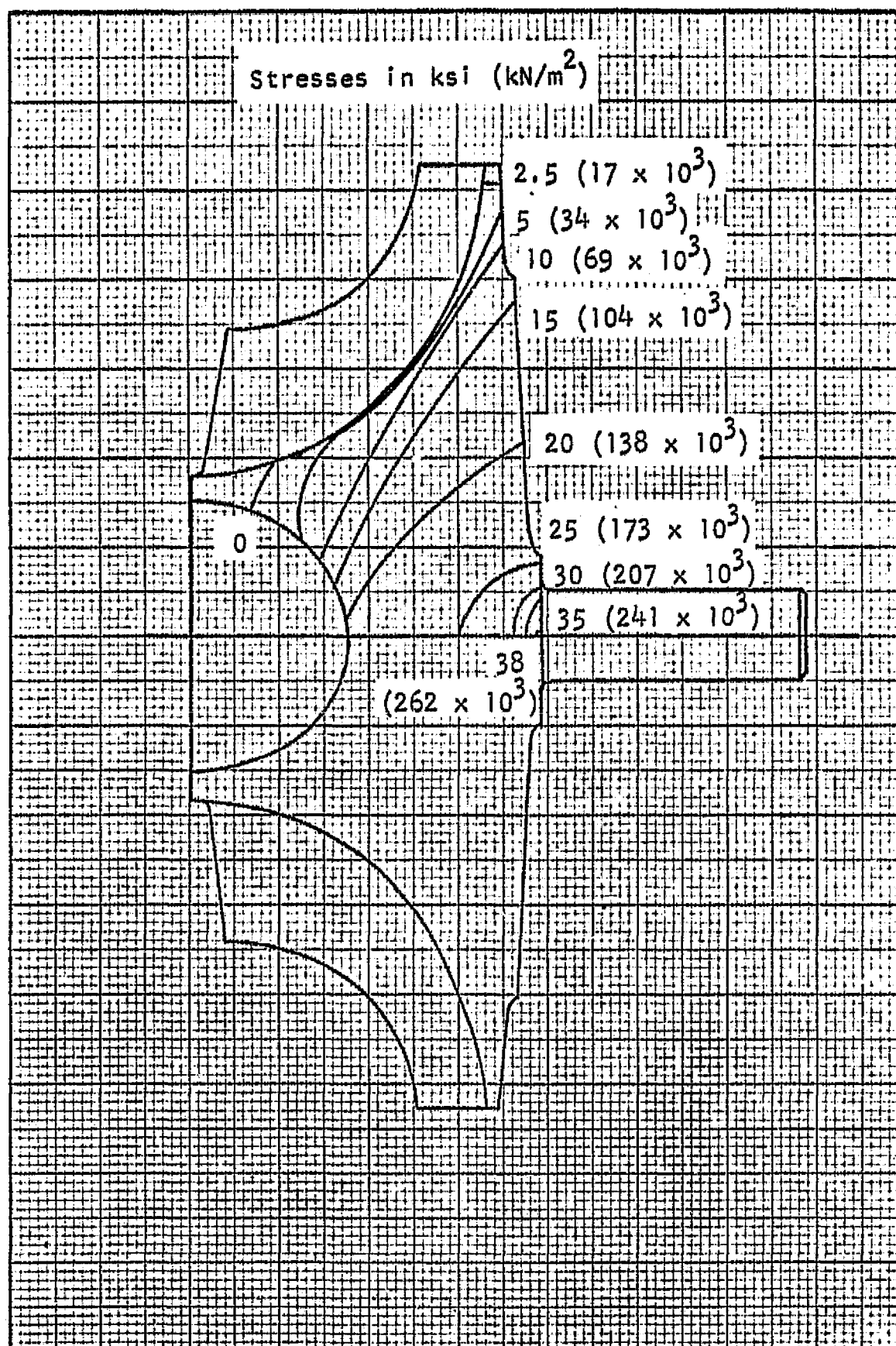


FIGURE 40 - RADIAL STRESS DISTRIBUTION AT DESIGN TEMPERATURE
OPERATING AT 100 PER CENT SPEED

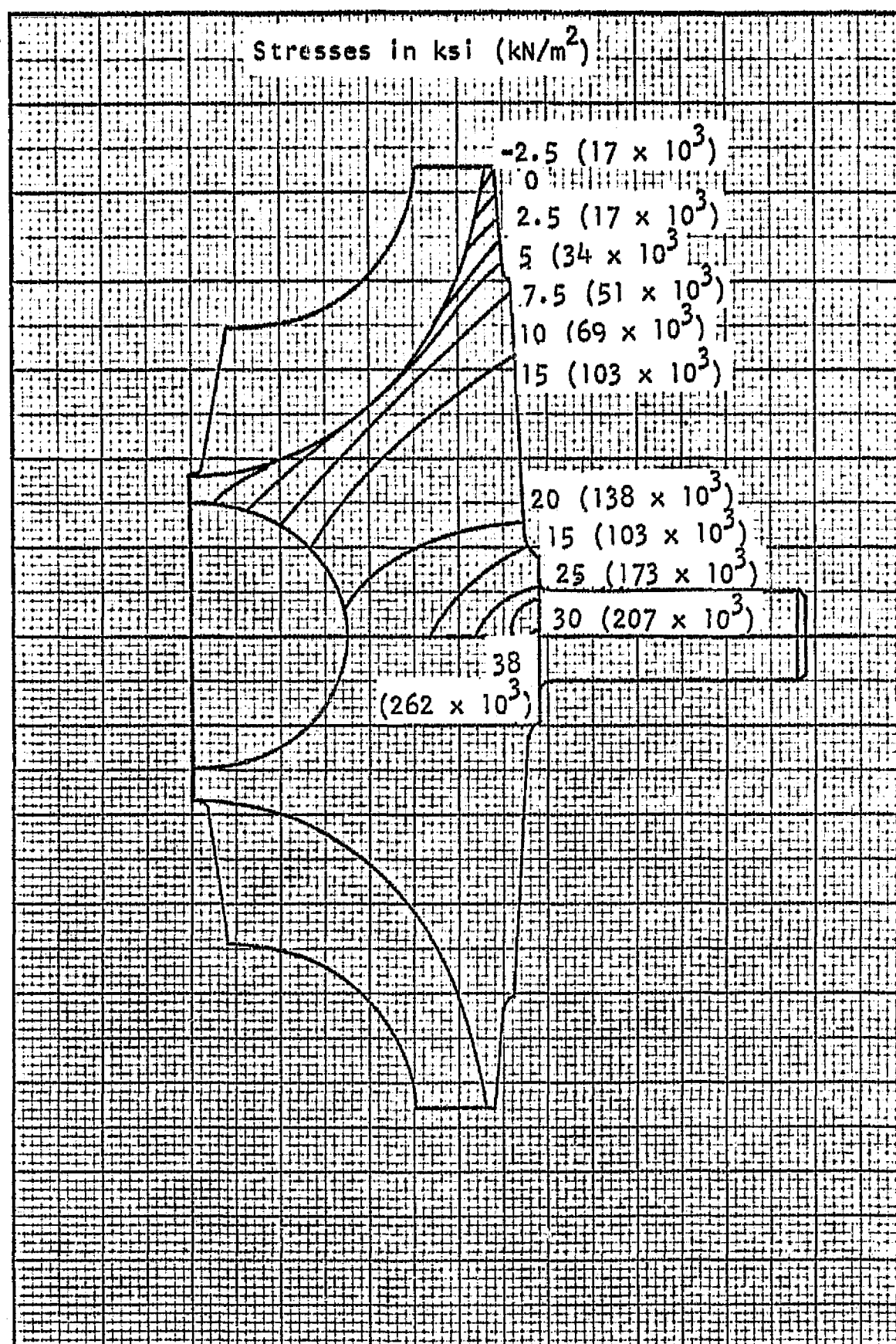


FIGURE 41 - TANGENTIAL STRESS DISTRIBUTION AT DESIGN TEMPERATURE
OPERATING AT 100 PER CENT SPEED

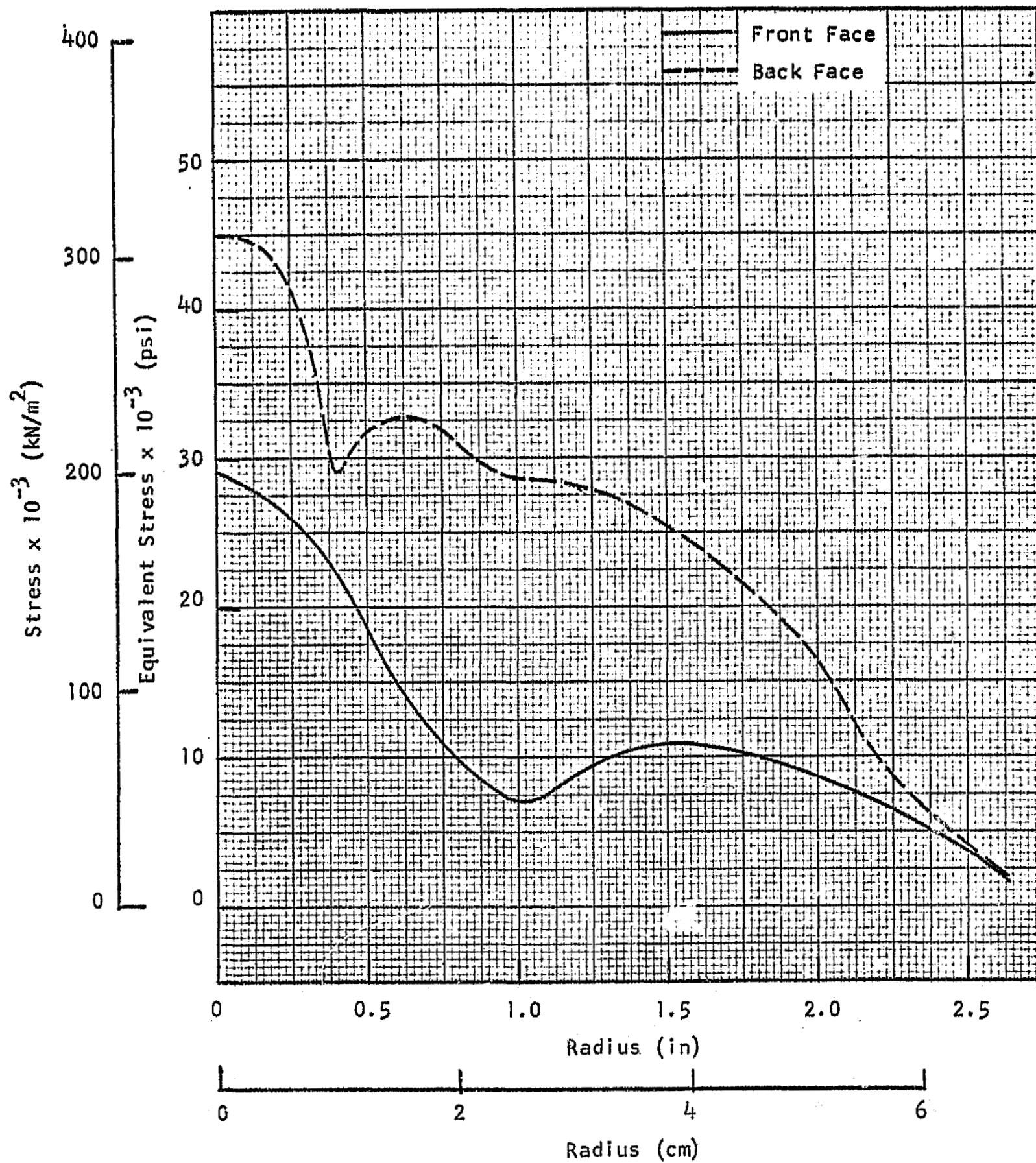


FIGURE 42 - RADIAL VARIATION OF EQUIVALENT STRESS AT DESIGN TEMPERATURE
OPERATING AT 120 PER CENT SPEED

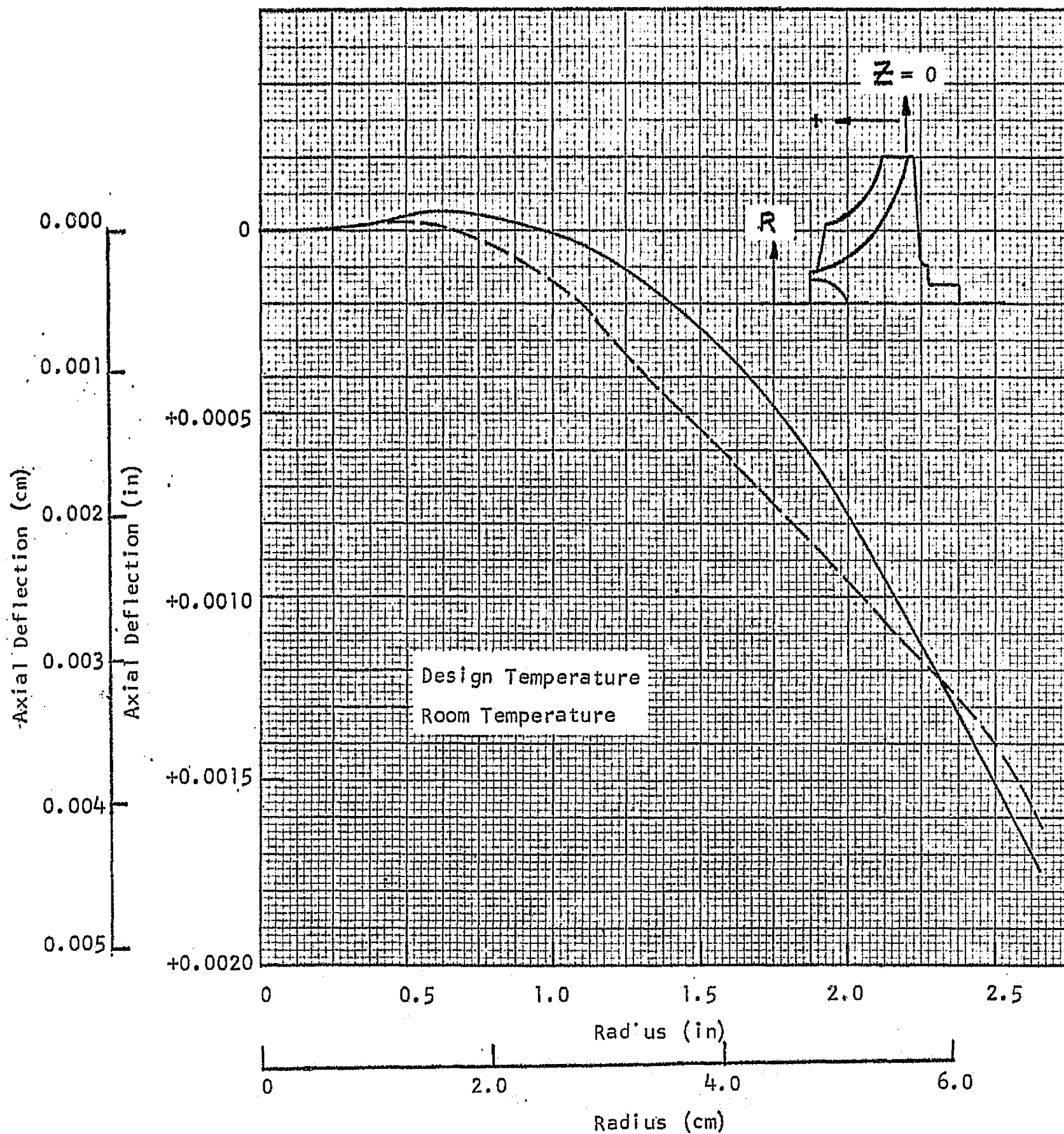


FIGURE 43 - RADIAL VARIATION OF AXIAL DEFLECTION AT DESIGN AND ROOM TEMPERATURES (REFERENCE AT $Z = 0$)

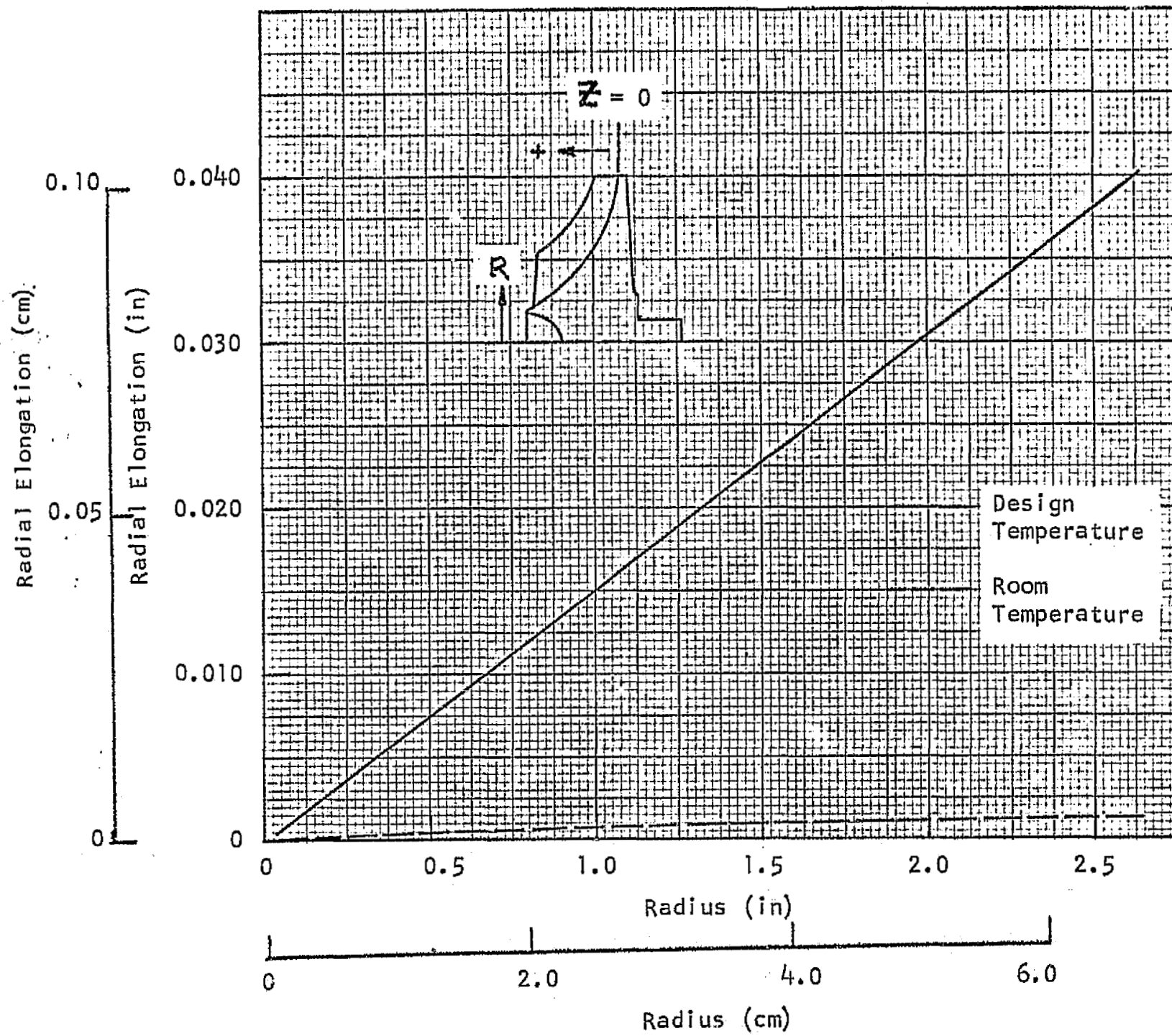


FIGURE 44 - VARIATION OF RADIAL ELONGATION WITH RADIUS
AT DESIGN AND ROOM TEMPERATURES

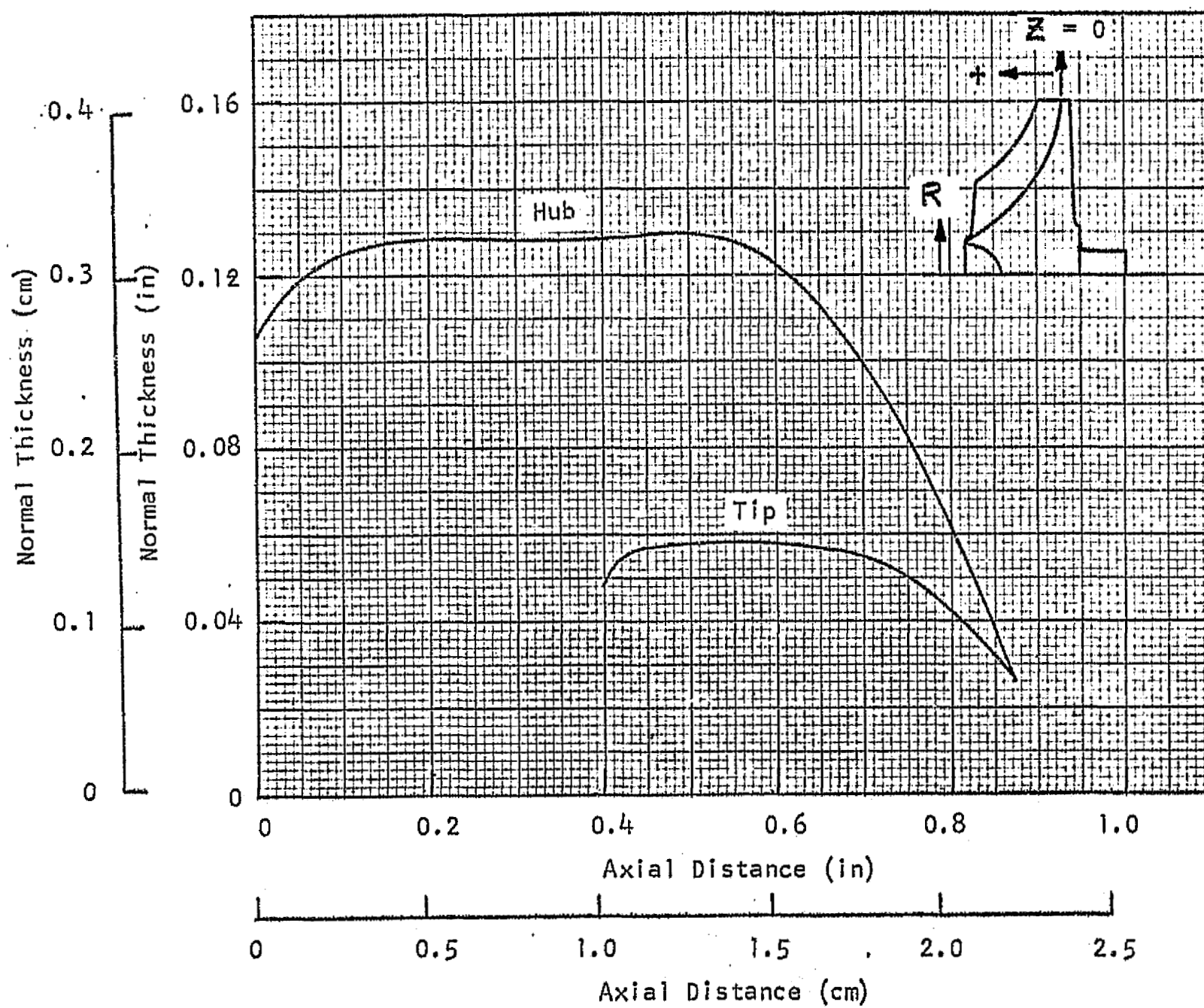


FIGURE 45 - NORMAL THICKNESS DISTRIBUTION ALONG THE HUB AND
OUTER CONTOUR (FIRST BLADE ROW)

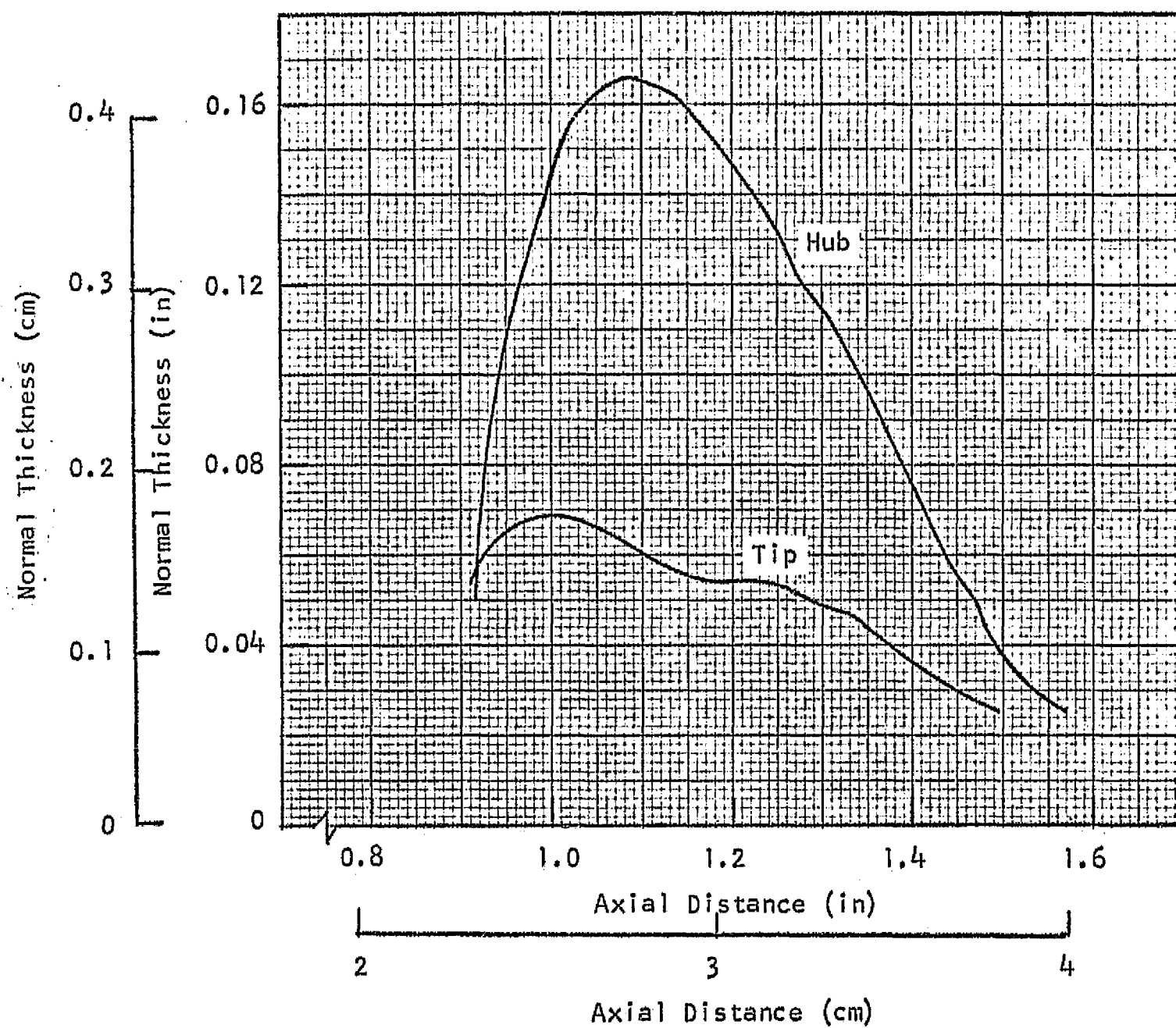


FIGURE 46 - NORMAL THICKNESS DISTRIBUTION ALONG THE HUB AND
OUTER CONTOUR (SECOND BLADE ROW)

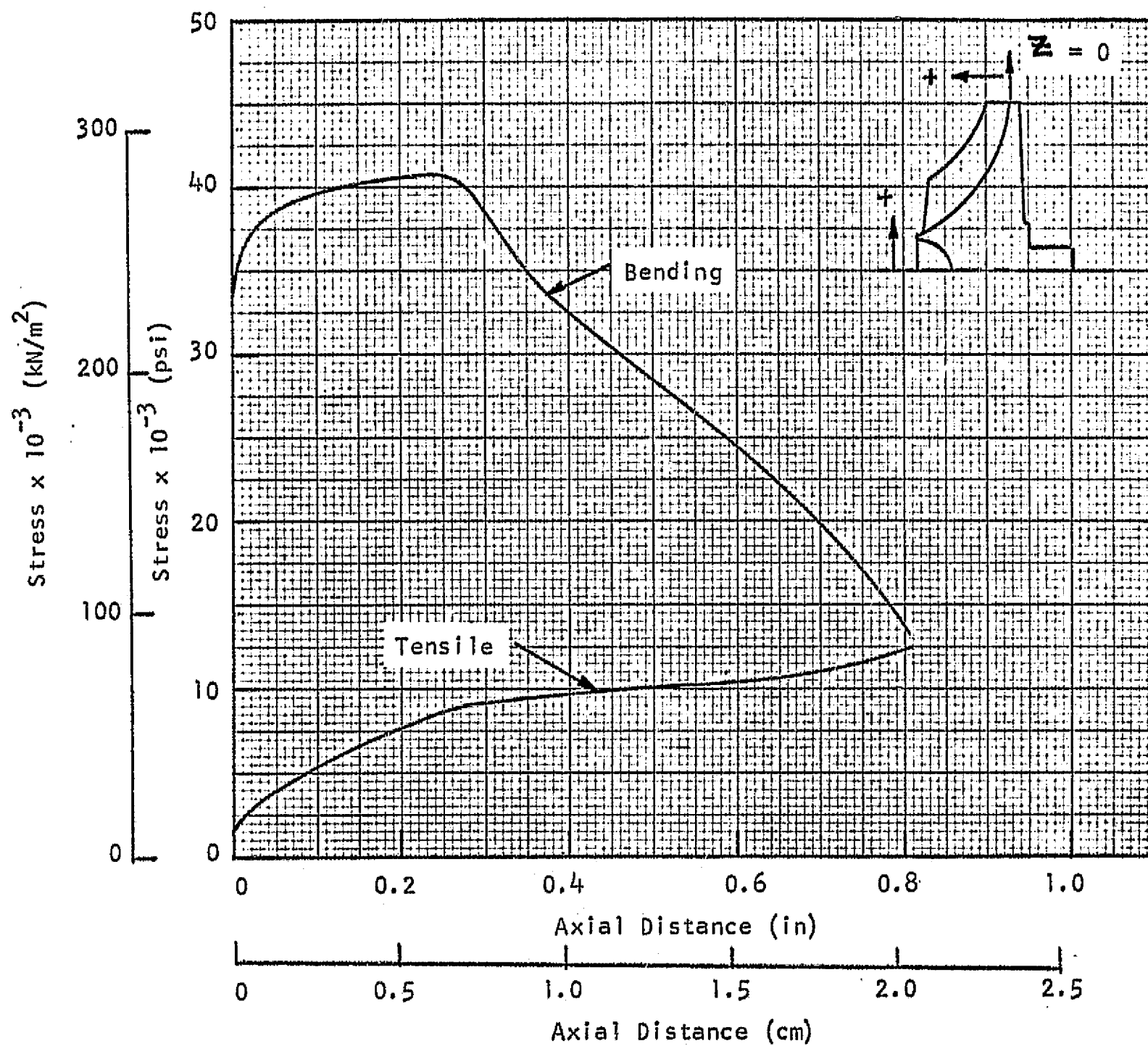


FIGURE 47 - BLADE ROOT BENDING AND TENSILE STRESSES AT
120 PER CENT SPEED (FIRST BLADE ROW)

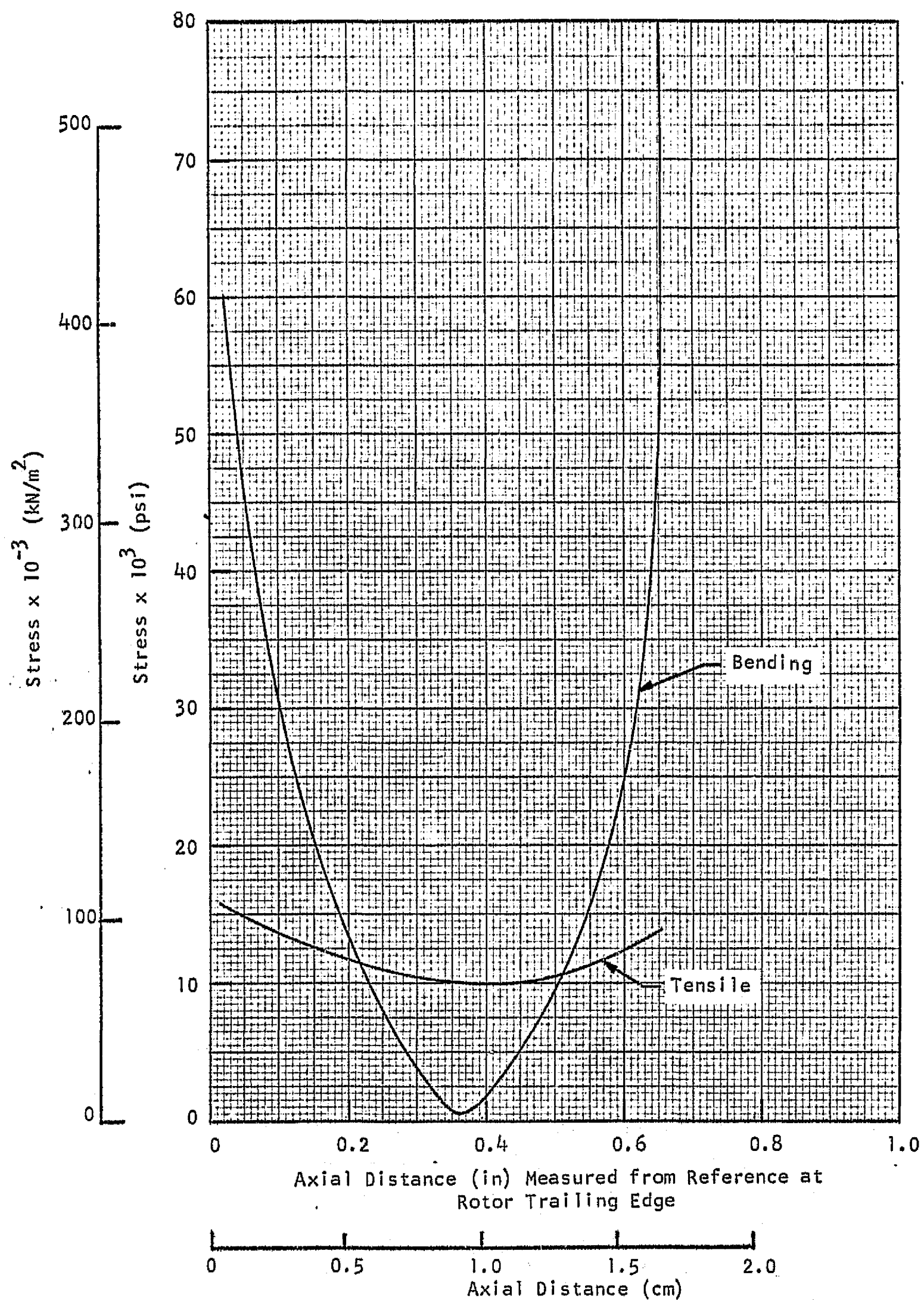


FIGURE 48 - BLADE ROOT BENDING AND TENSILE STRESSES AT
120 PER CENT SPEED (SECOND BLADE ROW)

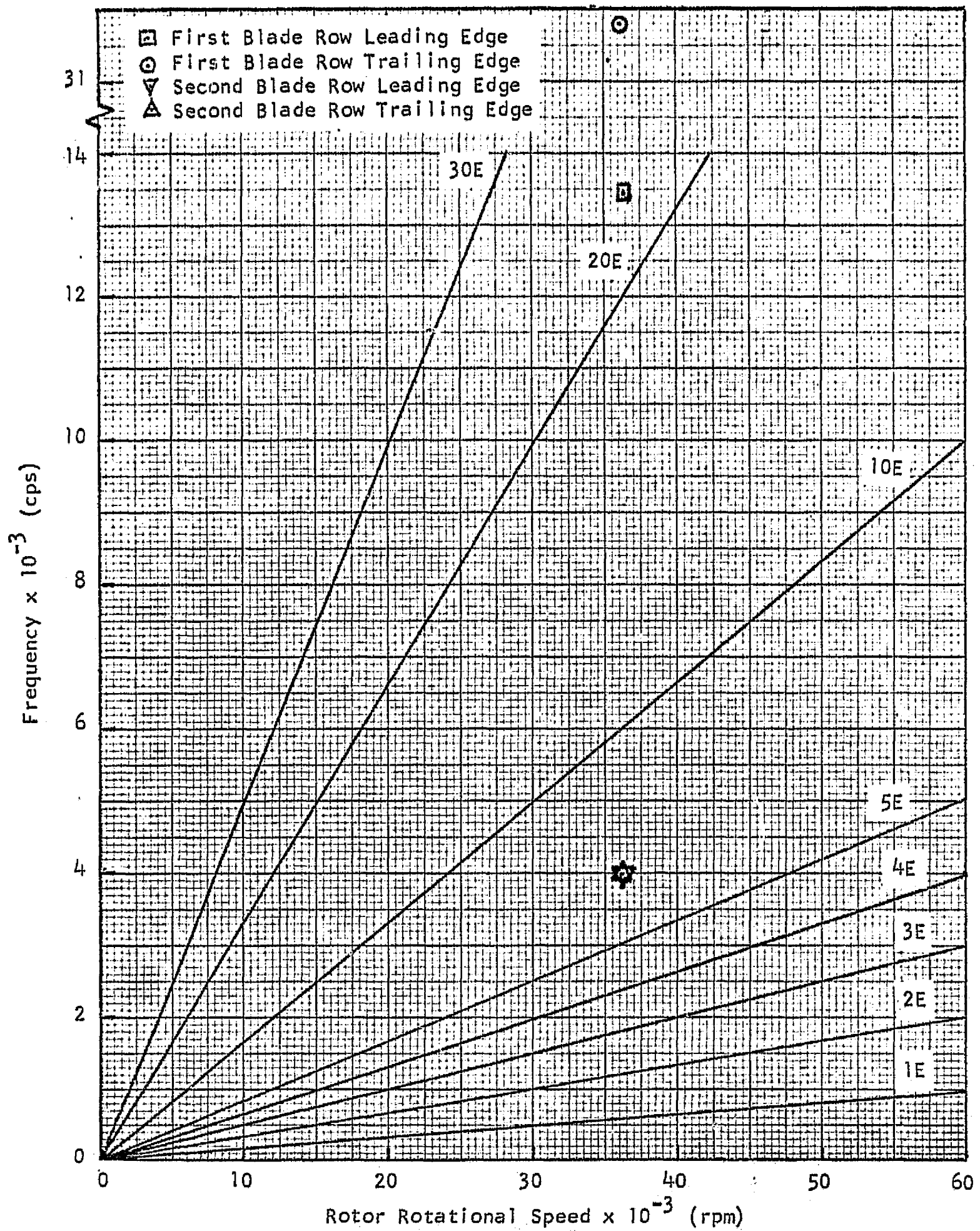


FIGURE 49 - CAMPBELL DIAGRAM FOR THE ROTOR

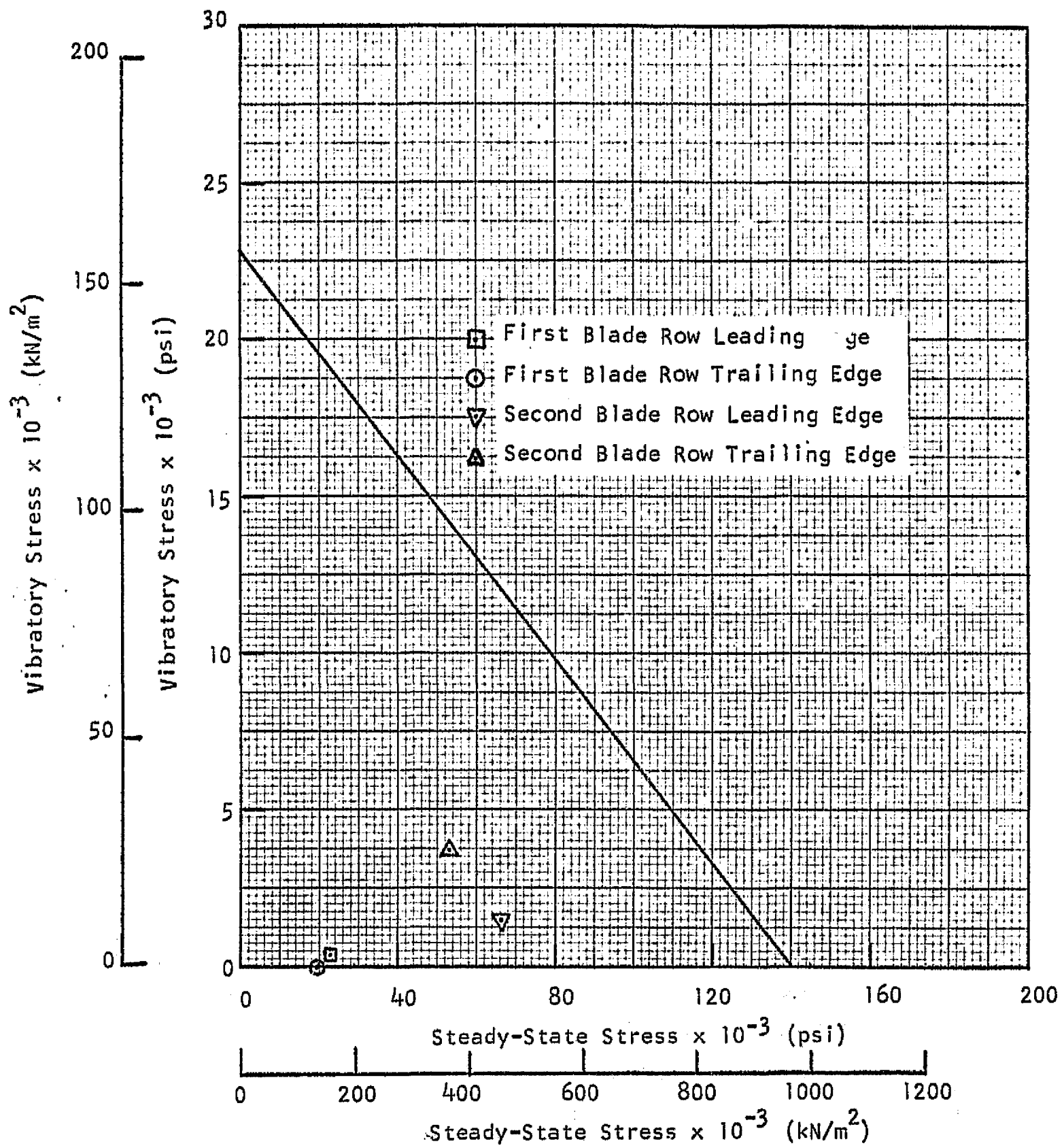
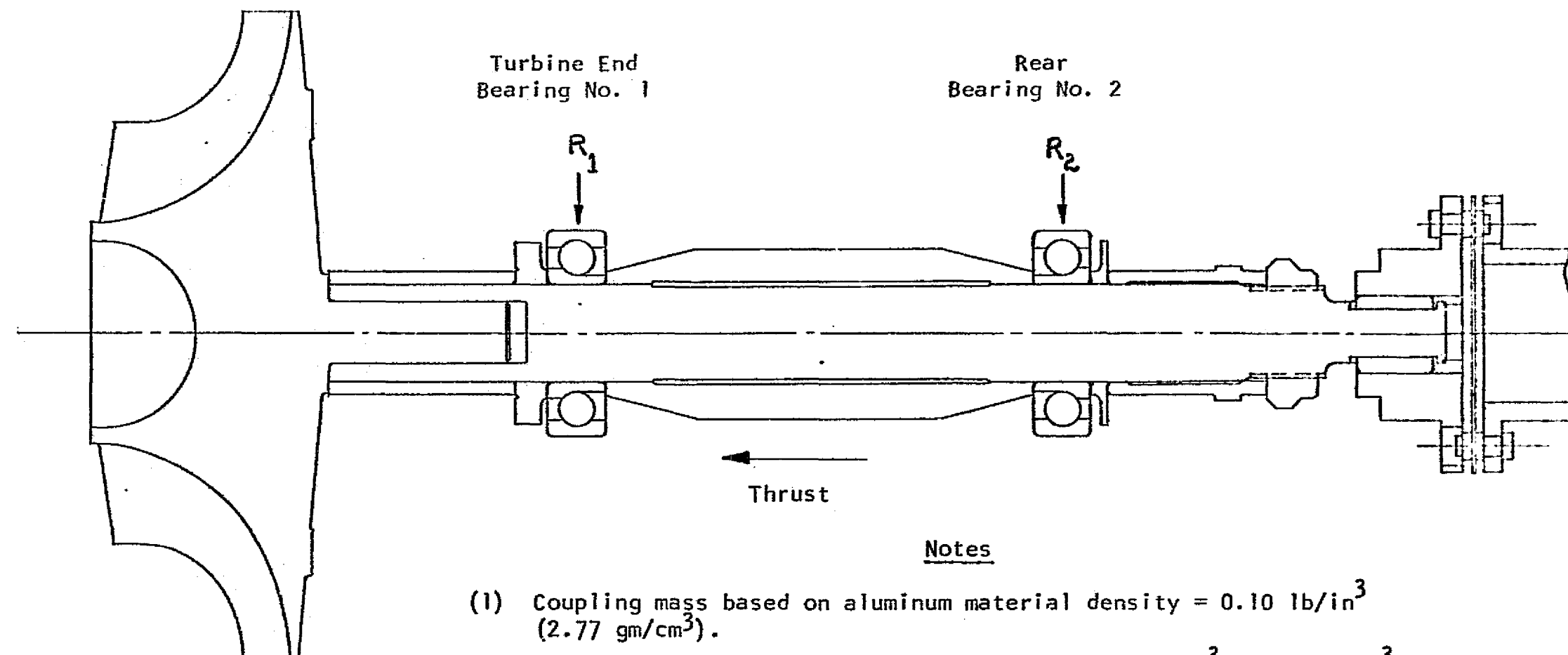


FIGURE 50 - GOODMAN DIAGRAM FOR THE ROTOR



Turbine Wheel

Mass	3.8679 (1.7544 kg)
I_p	7.7269 lb-in ² (22.61 kgcm ²)
I_D	4.5647 lb-in ² (13.36 kgcm ²)

Notes

- (1) Coupling mass based on aluminum material density = 0.10 lb/in³ (2.77 gm/cm³).
- (2) Rotor and shaft mass based on density = 0.29 lb/in³ (8.03 gm/cm³).
- (3) The moment transmitted through the wafers was assumed negligible. In essence, a pinned point was assumed at each end of the flexible coupling.

- (4) Rear bearing spring rate assumed constant, $K = 2.5 \times 10^5$ lb/in (4.38 N/cm).

- (5) Bearing 2 takes thrust load in direction shown.

- (6) Bearing loads calculated as follows:
- | R_1 (lbs) | R_2 (lbs) | Thrust (lbs) |
|-------------|-------------|--------------|
| 11.1 | 13.2 | 75 |
| (49.4 N) | (58.7 N) | (333.6 N) |

FIGURE 51 - TURBINE ROTOR SYSTEM CHARACTERISTICS

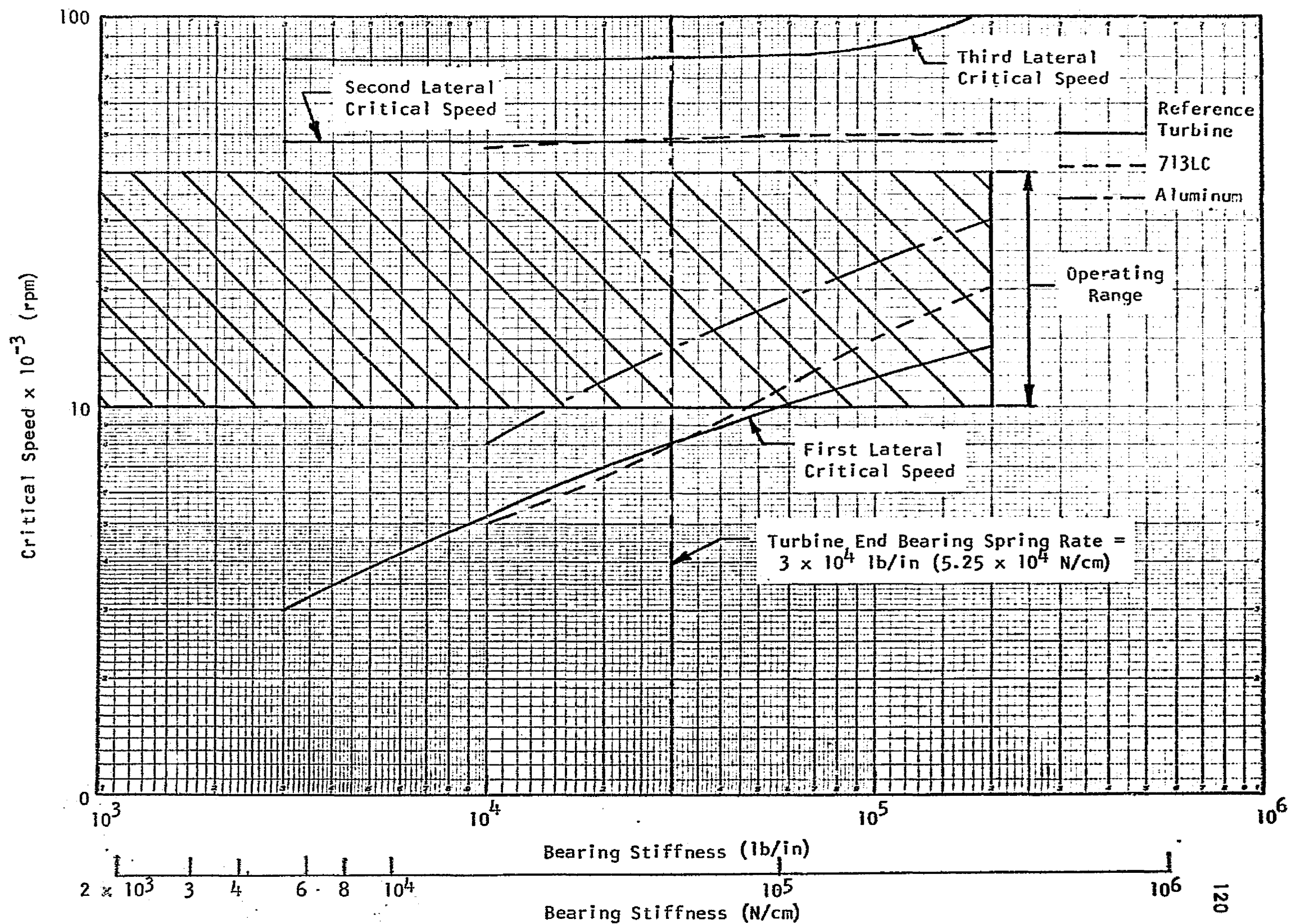


FIGURE 52 - VARIATION OF CRITICAL SPEED WITH BEARING STIFFNESS

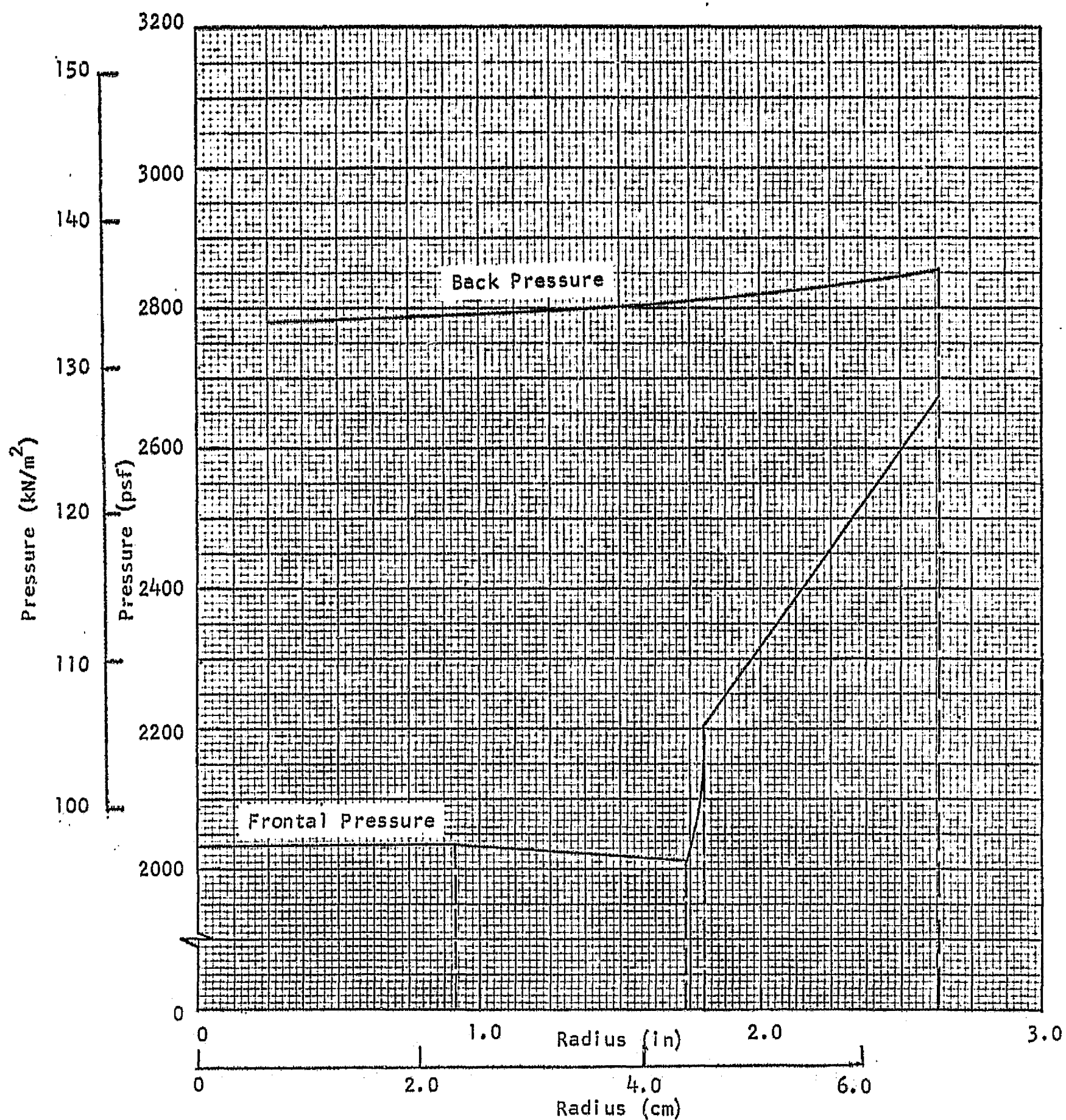


FIGURE 53 - RADIAL VARIATION OF FRONTAL AND BACK PRESSURES
ON THE TURBINE WHEEL

NOMENCLATURE

<u>Symbols</u>	<u>Description</u>	<u>Units</u>
A	Area	sq ft (sq cm)
b	Passage width	in (cm)
Bi	Biot number	--
C_f	Skin friction coefficient	--
C_m	Meridional velocity	fps (m/sec)
C_p	Specific heat at constant pressure	Btu/lbm deg R
D	Diameter	in (cm)
D_h	Hydraulic diameter	in (cm)
D_w	Diffusion parameter (Equation 2)	--
f	Frequency	cycles per sec
g_o	Gravitational constant	lbm ft/lbf sec ²
R	Heat transfer coefficient	Btu/hr sq ft deg F
H_{12}	Incompressible shape factor, $\frac{S}{D}$	--
J	Energy conversion factor	ft lbf/Btu
L_z	Axial length	in (cm)
ℓ	Length	in (cm)
\dot{m}	Mass flow	lbm/sec (kg/sec)
N	Rotational speed	rpm
N_s	Specific speed, $\frac{N\sqrt{Q}}{\Delta H^{3/4}}$	$\frac{\text{ft}^{3/4}}{(\text{min})^{1/2}} \frac{(\text{m}^{3/4}}{(\text{sec})^{1/2}}$
P	Pressure	psia (kN/m ²)
Pr	Prandtl number	--
Q	Volume flow rate	cu ft/sec
Re	Reynolds number,	--
r	Radius	ft (cm)
S	Blade spacing	in (cm)

<u>Symbols</u>	<u>Description</u>	<u>Units</u>
T	Temperature	deg R (deg K)
t_e	Trailing edge thickness	in (cm)
U	Wheel speed	fps (m/sec)
V	Absolute velocity	fps (m/sec)
W	Relative velocity	fps (m/sec)
Z	Number of blades	--
α	Absolute flow angle from axial direction	deg
δ	Displacement thickness	in (cm)
ΔH	Isentropic head on total pressure ratio	ft (m)
μ	Dynamic viscosity	lbm/ft sec (kg/m sec)
ρ	Density	lbm/ft ³ (g/cm ³)
ω	Angular velocity	rad/sec
θ	Momentum thickness	in (cm)
η	Efficiency	--
C_p	Secondary flow parameter, $\frac{P_d - P_e}{\frac{1}{2} \rho W^2}$	--
M	Secondary flow parameter, $\frac{4(W_s^2 - W_h^2)}{(C_{ms} + C_{mh})^2}$	--

<u>Subscripts</u>	<u>Description</u>
b	Back
Cylt	Conditions corresponding to Mach number of 1.0
d	Driving surface
f	Frontal
R	Hub
m	Mean
n	Nozzle
o	Total conditions
ov	Over-all
Ref	Reference
r	Rotor

<u>Subscripts</u>	<u>Description</u>
S	Shroud
S	Static
t	Trailing surface
W	Wall
0	Station at scroll inlet
1	Station at nozzle inlet
2	Station at nozzle exit
3	Station at rotor inlet
3i	Intermediate station
4	Station at rotor exit
5	Station at diffuser exit

APPENDICES

APPENDIX I

AERODYNAMIC DESIGN PROCEDURES

Stator Aerodynamic Design Method

Scroll Design Procedure

The method used for the detailed design of the scroll is based on Reference 17 and may be used for arbitrary cross-sectional shapes. The method determines the cross-sectional area of a scroll, as a function of the azimuth angle, that is necessary to obtain uniform static pressure distribution around the circumference.

Assumptions and Limitations

The method basically solves the continuity equation and angular momentum equation with the following assumptions:

1. Flow is incompressible.
2. Free vortex flow.
3. Flow is one-dimensional.
4. No secondary flow effects.

The cross section of the scroll is calculated in two stages.

1. Calculation of area at a specified azimuth angle with the above assumptions.
2. Correction of the above area to allow for frictional effects.

The method is limited to cases of low Mach numbers with uniform flows.

Input and Output Description

The following are the input requirements in addition to the specification of type of cross section and any dimensional restrictions in the radial direction:

1. Azimuth angle at scroll inlet.
2. Stator inlet flow width.

3. Stator inlet flow angle.
4. Stator inlet radius.
5. Friction factor.

The output values at a given azimuth angle consist of:

1. Mean radius of the cross section.
2. Corrected area of the cross section.
3. Height of the cross section.
4. Head loss.

Nozzle Aerodynamic Design Procedure

The method employed in the aerodynamic design of the rotor applies here in essence. An important simplification in stator design is introduced by the use of two-dimensional blades, which may be specified directly in terms of camber line angle instead of indirectly by prescribed loading. The method reduces to an analysis of the flow field and boundary layers for specified passage geometry, which is systematically modified until satisfactory performance is indicated. A description of the relevant design tools, their capabilities and limitations and the required input and resulting output are presented in the discussion of rotor design method.

Vaneless Space Design Procedure

The flow analysis of the vaneless space is based on one-dimensional compressible flow equations in an axisymmetric radial duct as described in Reference 18. The angular momentum and continuity equations are solved with the aid of an empirical expression for the friction coefficient as a function of Reynolds and Mach numbers. An iterative integration of these equations has been chosen as the method most applicable to digital computer computations and a corresponding routine (Program VLS) is available. The chief limitation of this method is the assumption of one-dimensional flow.

Input data are the axial channel width as a function of radius, the viscosity of the fluid and its variation with temperature, and inlet conditions consisting of the stagnation state, inlet Mach number, and flow

angle. The output comprises the flow conditions and the static and total state at specified radial stations.

Rotor Aerodynamic Design Method

Design Procedure

The detailed aerodynamic design of the turbine rotor involves the following steps:

1. Generation of a blade surface from prescribed loading distribution and imposed geometrical constraints.
2. Quasi-three-dimensional analysis of the inviscid flow field in the turbine blade passages.
3. Detailed three-dimensional flow analysis in the blade row inlet and discharge regions.
4. Compressible turbulent boundary-layer analysis on the walls of the blade passage and evaluation of discharge losses.

The initial blade loading specifications may be related to the rotor performance and systematically revised by repeating the above series of steps in order to produce an optimum design. Concurrently, the geometric constraints imposed on the design of the blade surface must be evaluated or modified in terms of permissible blade root bending stresses and manufacturing feasibility.

NREC has developed computing routines for this design process which include the following:

1. Program DESIGN to generate detailed blade geometry from given blade loading, flow path, and geometrical specifications. The theoretical basis for this method has been reported in Reference 19 and the computer program in Reference 20.
2. Program ANALS to analyze the three-dimensional inviscid flow in a rotor blade passage of specified geometry. This method is also described in detail in References 19 and 20.

3. Program BL2BL to analyze in detail the inviscid flow field of the blade end regions. This method has been reported in References 21 and 22.
4. Program BIANCA to compute compressible turbulent boundary-layer characteristics. This method is described in Reference 23.

Basis, Capabilities, and Limitations of Design Methods

The basis of NREC's current impeller blade design method is the assumption that the flow can be analyzed in axisymmetric streamtubes. This amounts to ignoring the effects of viscous and inviscid secondary flow and represents a limitation.

The determination of the blade shape is based on the relation between blade surface velocities, streamline shape, and streamwise distribution of angular momentum (or loading) as expressed by the momentum equation. The prescribed distribution of loading along any streamline defines for a known meridional flow field, the geometry of that streamline. When corrections are applied to that geometry to account for incidence and deviation near the blade end regions, the corresponding camber line is found. This process may be repeated for one or two additional streamlines in the flow passage. A geometrical constraint is imposed on the loading of additional streamlines by the requirement that in order to define a practical blade shape, the several camber lines must be aligned on specified leading or trailing edges. The remainder of the blade surface is then determined by the specification of straight-line generatrices. Such straight-line elements are uniquely determined by three camber lines. An alternate blade element specification, which is frequently used, is to prescribe along one camber line the element orientation relative to the axis and the meridional plane.

The limitations of this method are evidently the restriction to straight-line elements and certain approximations in the use of the momentum equation and in the assumed streamwise variation of deviation between flow angle and blade camber line angle inside the blade passage.

The flow field analysis in the blade passages determines the positions of the axisymmetric streamtubes in the blade passage by application of the momentum, continuity, and energy equations. This result is achieved by an iterative procedure in which the positions of the streamlines which define the streamtubes of specified mass flow increments are initially estimated and subsequently revised by the flow field solution corresponding to their geometric properties of slope and curvature. When successive streamline estimates agree to within a specified tolerance, the solution has converged. In a second step this axisymmetric solution is extended in circumferential direction to the blade driving and trailing surfaces by using approximations to the momentum equation first applied in Reference 27.

The limitations of this method lie chiefly in the latter approximations which preclude the determination of the deviation between mean flow angle and blade camber line angle. In the major part of the blade passage this deviation may be negligible. Near the blade end region the computed blade surface conditions are certainly inaccurate. A thorough analysis of the flow field in these areas is accomplished by the following method which is designed to calculate the compressible flow field within an infinitesimal axisymmetric streamtube of variable thickness, as calculated by the foregoing method. The approach here is to solve the two-dimensional stream function equations by a relaxation method; NREC's computer program (BL2BL) is based on the method developed by T. Katsanis of NASA LeRC (Ref 5). A limitation of the method is the restriction to subsonic flows.

The analysis of the compressible turbulent boundary layers along the passages of the blade surface is based on an explicit integral theory, which is characterized by the initial integration of the governing equations across the boundary layer and the computation of integrated parameters from the resulting ordinary differential equations. The essence of the method is the solution of the momentum and kinetic energy equations integrated across the boundary layer. These basic relations are supplemented by semi-empirical relations for the wall shear stress coefficient and the dissipation coefficient.

Input Requirements

The input information required for the blade design (Program DESIGN) consists of hub and shroud and blade edge contours in the meridional plane, the normal blade thicknesses along the hub and shroud, the blade element orientation at leading and trailing edges, inlet flow conditions consisting of total pressure, temperature and angular momentum, an average polytropic efficiency, the total mass flow, the operating speed, and the specification of incidence and the angular momentum at discharge.

The flow analysis input data (Program ANALS) consists of the inlet flow conditions and operating conditions (as above) and the specification of the flow path and blade shape. The description of the blade surface is in the form of a grid of points defined by the cylindrical point coordinates and local tangential blade thickness. Additional data are the incidence factor (defined like the slip factor), the location along the blade camber lines where the flow deviation ceases, and a polytropic efficiency.

Input data for detailed flow analysis in the blade end region (Program BL2BL) are streamtube and blade section geometry, fluid properties and flow conditions, the distribution of losses along the flow path, and the spatial domain and finite difference mesh geometry. Flow conditions are specified by the absolute total temperature, total pressure, entropy and swirl upstream of the blade, and the streamtube mass flow or upstream flow angle.

Input data for the compressible boundary-layer analysis (Program BIANCA) consists of streamline geometry on the passage surface, fluid properties, and initial and boundary conditions. The geometric information consists of the definition of the free streamlines along which boundary-layer properties are to be computed, including radius and orientation of the normal with respect to the axis of rotation as a function of streamline distance, and the width of the streamtubes (measured on the surface) for which the streamlines are representative. Fluid property information required includes the gas constant, specific heat and specific

heat ratio, and fluid viscosity at standard temperature. Boundary conditions required are, in general, the free stream velocity and static pressure distribution along the streamlines and the rotational speed of the surface.

Output

1. Full specification of flow path and blade geometry.
2. Free stream flow conditions on the blade surfaces.
3. Boundary-layer characteristics along representative streamlines of the blade passage and passage discharge losses.

Diffuser Aerodynamic Design Method

Design Procedure

The detailed design of annular diffusers of optimized over-all dimensions reduces to the proper selection of cross-sectional area as a function of diffuser length. The basis for this choice is an adequate description of the internal flow field and of the boundary layers. NREC has formulated a procedure to compute diffuser effectiveness and the point of separation for two-dimensional and annular diffusers. The method was designed to allow for the effect of a distorted velocity profile at inlet, but not for curvature terms and tangential swirl. A comparison with experimental results shows that the method can predict diffuser effectiveness with fair accuracy for diffusers with uniform flow at inlet, and also predict the development of a shear profile, if the inlet profile is in equilibrium.

The method involves a streamtube analysis to calculate the development of the velocity field. The output from this calculation is used to obtain the characteristics of the boundary layer, and hence the point of flow separation. The following steps may be identified:

1. Calculate the stagnation properties of a specified number of streamtubes at diffuser inlet.

2. Make a first estimate of the boundary-layer displacement thickness to give the effective diffuser wall position.
3. Proceed downstream in steps, calculating the pressure and velocity profile at each axial station.
4. Using the pressure distribution thus obtained, make new estimates of the boundary-layer displacement thickness and, hence, the displaced wall coordinates.
5. Steps 3 and 4 are repeated until the solution converges.

A computer routine is available to automate this procedure and is described in References 25 and 26.

Step 4 in the above procedure merits further comment here. A key parameter is the shape factor, H , which is the ratio of the displacement thickness to the momentum thickness

$$H = \delta^*/\theta$$

Using the velocity distribution obtained in Step 3, the momentum thickness is obtained by solving a form of the momentum integral equation for compressible flow. A simple empirical relation suggested by Dussourd (Ref 27) from work on diffusers is used to find the shape factor. These two relations are presented in Appendix I of Reference 25. The new displacement thickness is then obtained directly.

The separation criterion is expressed in terms of the shape factor, H . Separation occurs when H reaches a critical value, H_{SEP} . Doenhoff and Tetervin (Ref 28) measured H_{SEP} on NACA-65 aerofoils at moderate incidence angles and found values in the range 1.8 to 2.2.

To use the streamtube method, a value of $H_{SEP} = 1.9$ is recommended. This value was selected to give the best correlation between the streamtube method and the experimental results of Reneau, Johnston, and Kline (Ref 29) for two-dimensional diffusers, and Sovran and Klomp (Ref 30) for annular diffusers.

Basis, Assumptions, and Limitations

1. There is no radial pressure gradient or tangential swirl.

2. The flow may be represented by a number of streamtubes. The flow in each streamtube is uniform and isentropic, and no mixing occurs between adjacent streamtubes. The fluid obeys the perfect gas law.
3. The boundary layer is identical to that on a flat plate with the same pressure gradient that exists in the diffuser. The effect of the boundary layer is to produce an effective displacement of the diffuser wall. When the flow separates, no further pressure rise occurs.
4. There is a linear variation of streamline slope from one wall to the other at any axial station. At the first station there is zero streamline slope.

A limitation of the procedure is that the inviscid flow calculation does not allow for curvature terms and tangential swirl.

Input Requirements

The input conditions at the inlet station are:

1. Weight mean total pressure.
2. Uniform stagnation temperature.
3. Mass flow rate.
4. A velocity profile given by

$$\frac{u}{U} = f(\eta)$$

where U = an arbitrary velocity

$f(\eta)$ a tabulated function of $\frac{u}{U}$ against η .

5. The boundary-layer displacement thickness.
6. The boundary-layer shape factor.

Output

Output data at intermediate and final stations are:

1. The velocity profile.
2. The boundary-layer displacement thickness.
3. The boundary-layer shape factor.

APPENDIX II
MECHANICAL DESIGN PROCEDURES

Rotor Mechanical Design Methods

Rotor Steady-State Heat Transfer Coefficients

In order to predict the temperature distribution in the rotor, it is necessary to compute the surface temperature of the metal. These temperatures depend upon the gas and adiabatic wall temperatures as well as on the heat transfer coefficients. Both heat transfer coefficients and Biot numbers are calculated. For the disk surface, the heat transfer coefficient may be calculated by standard methods. It will in general depend upon the Reynolds and Prandtl numbers and is computed by equations derived empirically for high velocity flow. For the areas where blades exist, the surface is treated as a finned surface. The additional heat transfer is accounted for by correction of the standard heat transfer coefficients derived above.

Limitations

The major limitation of this process is in the selection of the formula for calculation of the heat transfer coefficient. The experimental conditions leading to the equation should be as similar to flow in the impeller as possible.

Input Requirements

1. Impeller geometry.
2. Gas properties.
3. Gas temperatures, velocity, and pressure distribution.

Output

1. Heat transfer coefficient distribution.

2. Biot number distribution.
3. Adiabatic wall temperature distribution.

Calculation of Temperature Distribution in Rotor

The calculation of the rotor temperature distribution is accomplished when the Biot number and adiabatic wall temperature distribution are known. It is desired to determine the metal surface temperature distribution. This is accomplished by NREC Program STRESS (Refs 3 and 4) which uses an "energy-integral" temperature analysis procedure. The impeller is divided into a series of concentric cylinders for the analysis. A typical annular cylindrical element will have heat flow in or out of its four surfaces. All elements are then solved simultaneously with the boundary conditions included.

Limitations

The axial temperature distribution is an approximation and its accuracy depends upon the selection of appropriate constants. The method also depends upon the initial calculation of Biot numbers and temperature distributions.

Input Requirements

1. Biot number distribution.
2. Adiabatic wall temperature distribution.
3. Rotor geometry.
4. Rotor material properties.

Output

Rotor surface temperature distribution.

Thermal and Mechanical Disk Stress

Impeller disk stresses are calculated using NREC Program STRESS.

(Ref 4). Both thermal and centrifugal loadings are considered. The basic method employed in the analysis is that of Schilhansl. To use the method, the rotor geometry, rotor face temperature distribution, and material properties must be known. The computer program uses a series of concentric cylinders to determine centrifugal and thermal distributions and loadings. The disk back and front face stress as well as radial and axial disk deformations are computed.

For burst considerations the average tangential stress at the worst location will be computed by an area integration method.

Limitations

The approximation itself and the assumption of linear cylindrical deformations is the major limitation of the method. The procedure is thus not good for the axial portions of long rotors. The results will show a low stress due to centrifugal loading at the impeller eye.

Input Requirements

1. Impeller geometry and operating conditions.
2. Impeller face temperature distribution.
3. Material properties.

Output

1. Radial and tangential disk stresses for the impeller back and front face.
2. Radial disk deformation at the axial plane of the turbine inlet.
3. Axial disk deformation at the axial plane of the turbine inlet.
4. Average tangential stress at 140 per cent speed.

Blade Root Stresses

To predict the blade root stress due to centrifugal loading,

NREC Program BLDR0T (Ref 14) is used. The method employed by the program is a rectangular beam approximation. That is, the continuous blade is approximated by a series of beams of rectangular cross section. The beams are pinned at the shroud line to adjacent beams in a direction normal to the blade. Motions other than normal are thus unrestrained and lead to conservative results.

Limitations

The beam approximation method itself is a limitation. It is, however, not a severe limitation as it has been found that the magnitude of the stress computed is as would be expected. The location of the stress, however, particularly near the boundaries is not accurate.

Another limitation is that the stresses calculated by the program are at present limited to bending and tensile. This is generally sufficient, particularly where nonradial blade elements are considered as these stresses will predominate. In radial blades, if radial beam elements are used, a conservative estimate of stress will be obtained since the radial direction would be unrestrained.

Input Requirements

1. Geometric definition of blades.
2. Operating speeds.
3. Material properties.

Output

1. Blade root tensile stress distribution.
2. Blade root bending stress distribution.

Blade Natural Frequency

Impeller blade natural frequencies, in general, are much higher than operating speeds. Where this is the case, relatively crude methods may be used to estimate natural frequencies. The methods used employ

plate theory. A section of the blade may be thought of as a plate, clamped on two sides which would represent its attachment to the hub and the adjacent blade section. The eye of the impeller is generally the area of lowest frequency. This is treated separately by a method due to Voysey (Ref 9). This method is also a plate oriented method but considers taper in a more rigorous fashion and has been checked experimentally. It includes the experimental factor derived to bring the analytical results into agreement with the empirical.

Limitations

The major limitation of the method discussed is that segments of the blade are treated separately. In this manner, interaction effects with the remainder of the blade are either ignored or approximated.

If a blade frequency is in the range of an operating or fundamental frequency, it will be necessary to perform a more sophisticated analysis using finite element techniques. In this manner a continuous blade analysis may be performed.

Input Requirements

1. Blade geometry.
2. Material property.
3. Operating speed.

Output

Impeller blade first natural frequency.

Blade Vibratory Stress Levels

The vibratory blade stresses, or those caused by pulsating aerodynamic loads are, in general, quite small when compared with the centrifugal loading. They do become important, however, when operation occurs near a natural blade resonance. To estimate these stresses, it is necessary to know actual blade aerodynamic loading. This may be

doubled since the worst variation will be from zero to twice the steady-state loading. To determine an amplification factor the method of Trumpler and Owens (Ref 15) may be used. They give an amplification factor to be applied to the stress result based on a comparison of the frequency of the disturbance with that of the fundamental mode.

In general, the target value for maximum vibratory stress is 10,000 psi or less.

Limitations

The limitation of the method is that the amplification factor is a statistically derived number based on experimental results. A lot depends upon the manufacturing quality; that is, the existence of stress risers and the like. In addition, the fundamental frequencies themselves are not that well known. These limitations are not significant where resonance and operation are widely separated.

Input Requirements

1. Gas blade loading magnitude.
2. Natural frequencies of interest of the blade.
3. Disturbance frequencies.

Output

Estimate of vibratory stresses at the blade root.

Flexural Vibrations (Critical Speeds)

Flexural vibrations in the nature of critical speed and relative mode shapes will be computed for the turbine rotor system. The system to be considered consists of the rotor and shaft in two bearings. The method employed is a modified "Holzer" technique (Ref 16) using the NREC computer Program HOLZER.

The program uses a stiffness approach using finite elements. The finite elements are lump masses joined to massless bars. The rotor

assembly is thus approximated by a system of masses and bars. The bars will support both bending and shear. The lump masses may contain both mass and gyroscopic inertia. The two bearing stations may contain pre-specified spring gradients, a different gradient at each bearing. The cross section of the massless bars is arbitrary, since only moment of inertia need be known.

Limitations

One limitation of the method is that it is basically an approximation. Lump masses are used to approximate a distributed mass system. This is not considered a severe limitation as the approximation is quite good. Another limitation is the fact that damping at the bearings is not considered. Depending upon the bearing system, this may or may not be a severe limitation. In the bearing system considered for this application, damping is low such that the limitation is not severe.

Input Requirements

1. Approximate system dimensions.
2. Masses.
3. Shear stiffness.
4. Bending stiffness.
5. Impeller gyroscopic inertia.

Output

1. Natural frequencies for a practical range of impeller end spring constants for the final shaft impeller geometry.
2. Mode shapes for the lower frequencies having the greatest effect on the operating speeds.

Shaft Attachment Methods

Design Procedure

The shaft attachment method considered at present is a press fit. The impeller will have a stub shaft and the shaft will have a cavity to receive it. Those parameters needing calculation are the torque transmission capability under centrifugal load and the impeller and shaft stress under no external load. The procedure to be followed is detailed in Reference 31.

Limitations

The major limitation in calculations such as this is that of accurately estimating the friction coefficient for torque transmission. This can be overcome by using a reasonably conservative estimate for friction coefficients in addition to insuring that the joint is not overstressed. A reasonable target maximum figure is $3/4$ yield strength of the material as the maximum joint stress.

Input Requirements

1. Torque transmission requirements.
2. Shaft size.
3. Material stress limits.

Output

1. The design and drawings of the impeller shaft assembly.
2. Results of calculations for torque transmission capability of the joint.
3. Results of calculations for static joint stress conditions.

Bearing Selection and Analysis

Prior to ball bearing selection and analysis, a calculation of the anticipated thrust load variation will be made. The thrust loads are

computed by integrating the expected static pressure distribution along the front face and back face of the impeller to determine the resultant thrust force. On the back face, any anticipated pumping is considered. Having the expected thrust and radial loads, the bearings may be selected on the basis of B_{10} life expectancies. The method of calculating the bearing life estimate is based on the method established by the Anti-Friction Bearing Manufacturers Association (AFBMA). After these calculations have been made, there is to be a comparison made with the existing bearing set. If major differences in B_{10} life are found and it is possible to do so, the bearings will be reselected.

Limitations

The only major limitation is that in computing B_{10} life a small percentage of the bearings fail, perhaps well in advance of the estimated life. In addition, care must be taken in assembly with regard to such factors as alignment, preload, and lubrication system to ensure that the calculations are valid.

Input Requirements

1. Results of critical speed calculations.
2. Design data for existing system.
3. Static pressure distributions at maximum and minimum expected thrust loads.
4. Dynamic and static radial loads.

Output

1. A specification for the bearings.
2. Rotor thrust load predictions.
3. B_{10} life predictions for the bearings.

Turbine Scroll, Nozzle, and Diffuser Design Methods

Design Procedure

The mechanical design of the stationary parts of the stage involved the calculation of the following items as a minimum requirement for a satisfactory end product:

1. Surface temperatures at certain critical locations from the inlet to the outlet flanges.
2. Stress and/or deflection at corresponding critical locations from the inlet to the outlet flanges, as a function of local temperature.

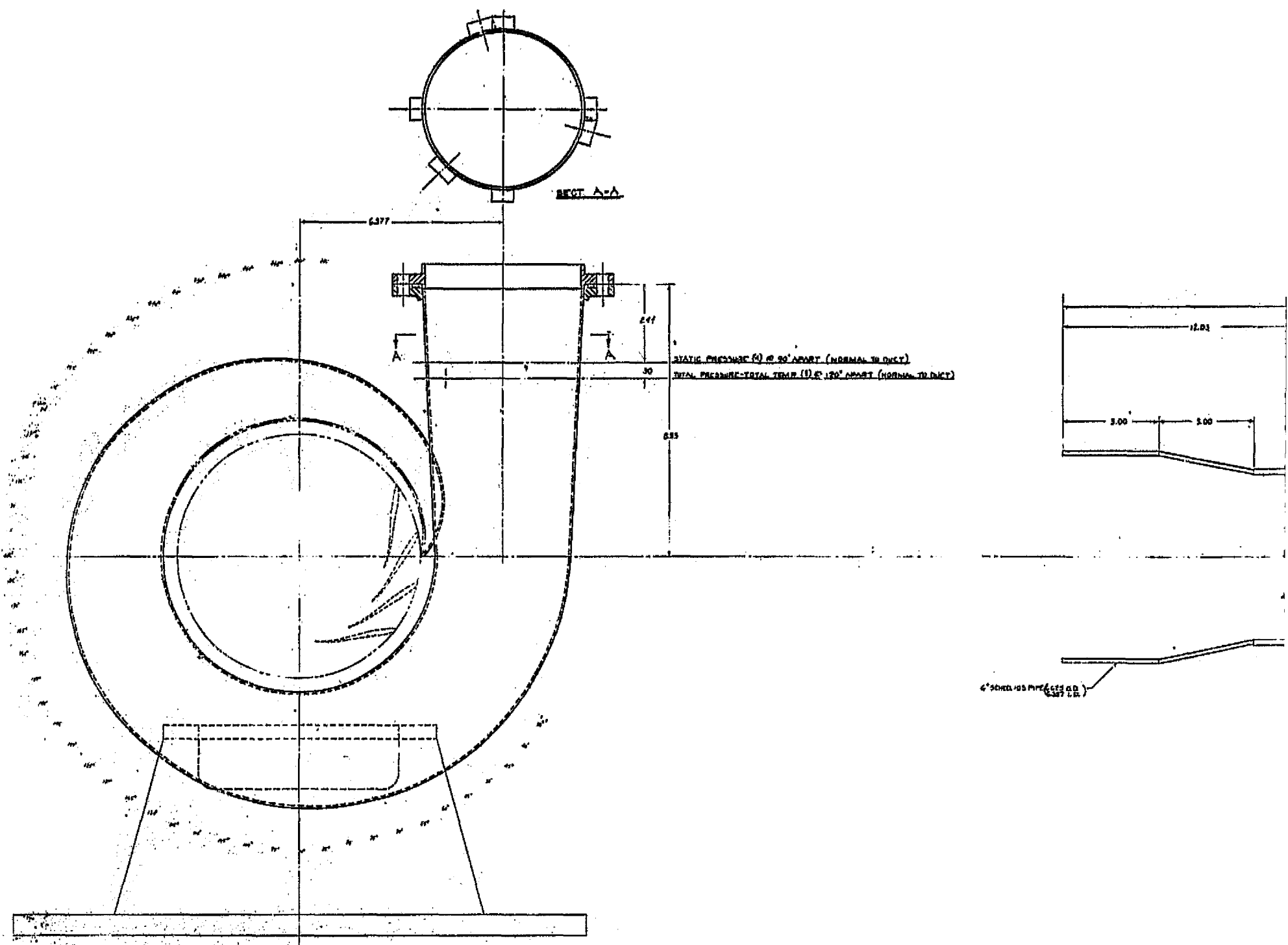
All temperatures will be based upon steady-state conditions. The procedures used for stationary parts such as the inlet scroll, the nozzle row, and the exhaust diffuser are relatively standard practice. The detailed methods of analysis are largely based on the standard textbooks of References 8 and 32. In the present design, the stationary parts have been designed for the turbine research package rather than the BRU operating at high temperatures and high pressure differentials. Hence, relatively little effort is needed to be devoted to the mechanical analyses of the stationary parts. Rather, the emphasis was placed on designing a research vehicle which provided ease of assembly and modification of design standard.

APPENDIX III
REPRODUCTIONS OF THE MANUFACTURING DRAWINGS

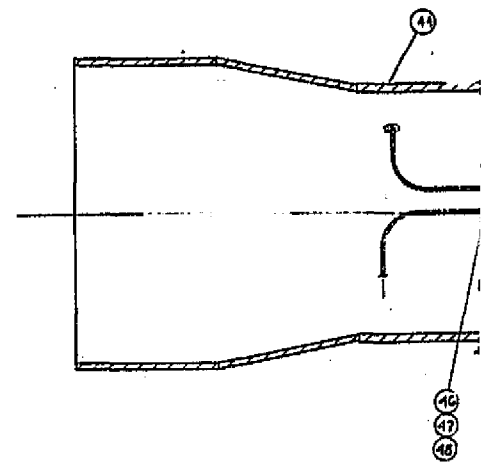
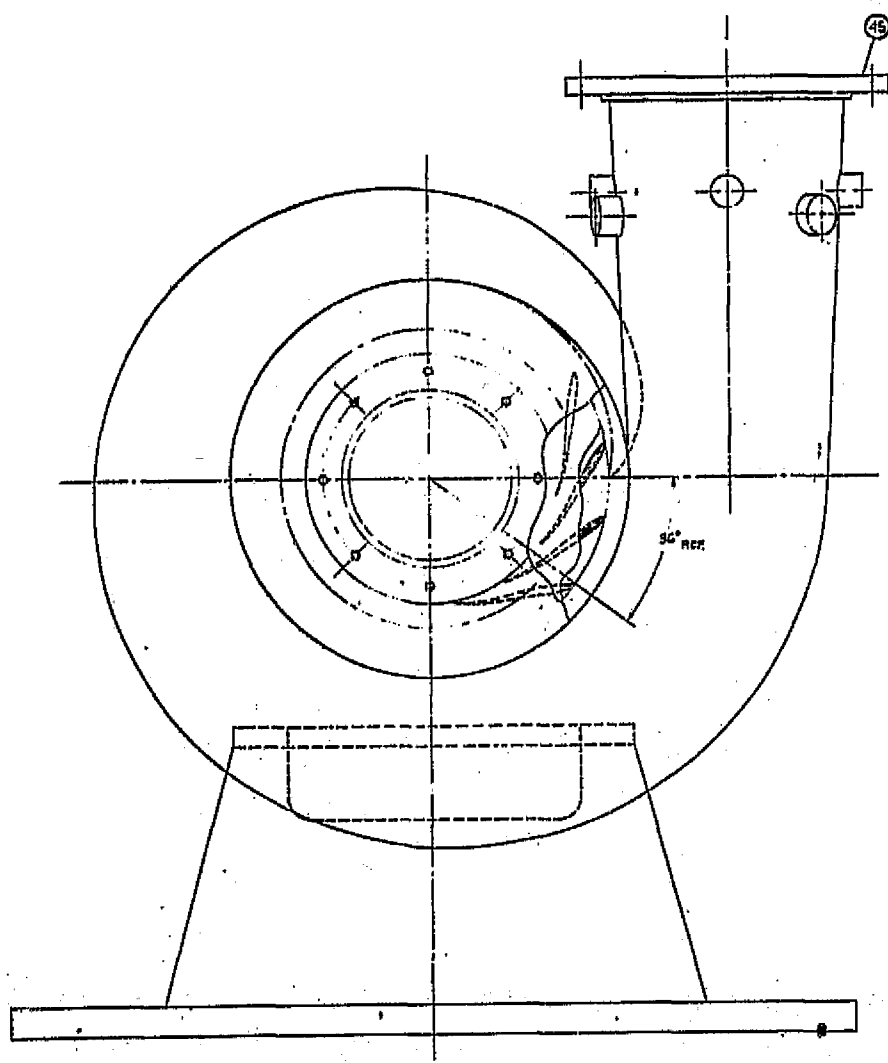
The following pages contain reproductions of the drawings produced for the new turbine stage. These drawings have been reduced by arbitrarily selected scaling factors for inclusion in this report. The following is a list of drawing numbers, drawing titles, and the page on which the drawing is reproduced.

<u>Drawing No.</u>	<u>Title</u>	<u>Page No.</u>
1159-R001	Research Package Layout	146
1159-R002	Research Package Assembly, Turbine	147
1159-R003	Research Package Outline, Turbine	148
1159-D004	Wheel Turbine	149
1159-E005	Wheel Assembly, Turbine	151
1159-R006	Scroll Fabrication Assembly	152
1159-R007	Scroll Machining Assembly	153
1159-R008	Nozzle Maching Assembly	154
1159-D009	Shroud Machining	155
1159-D010	Diffuser Machining	156
1159-D011	Exhaust Adapter	157
1159-C012	Rotor Back Shield	158
1159-B013	Pin Cap	159
1159-A014	Pin, Locating	160
1159-D015	Shim, Sealing Spacer	161
1159-A016	Retaining Ring	162

FOLDOUT FRAME 1



FOLDOUT FRAME 1

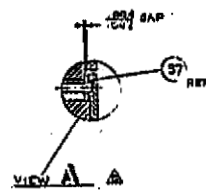
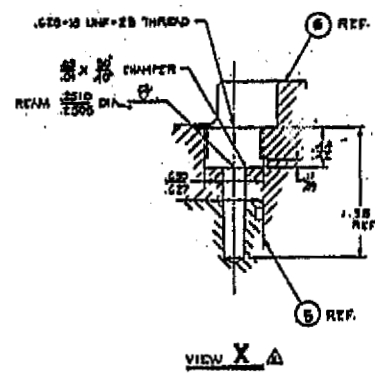
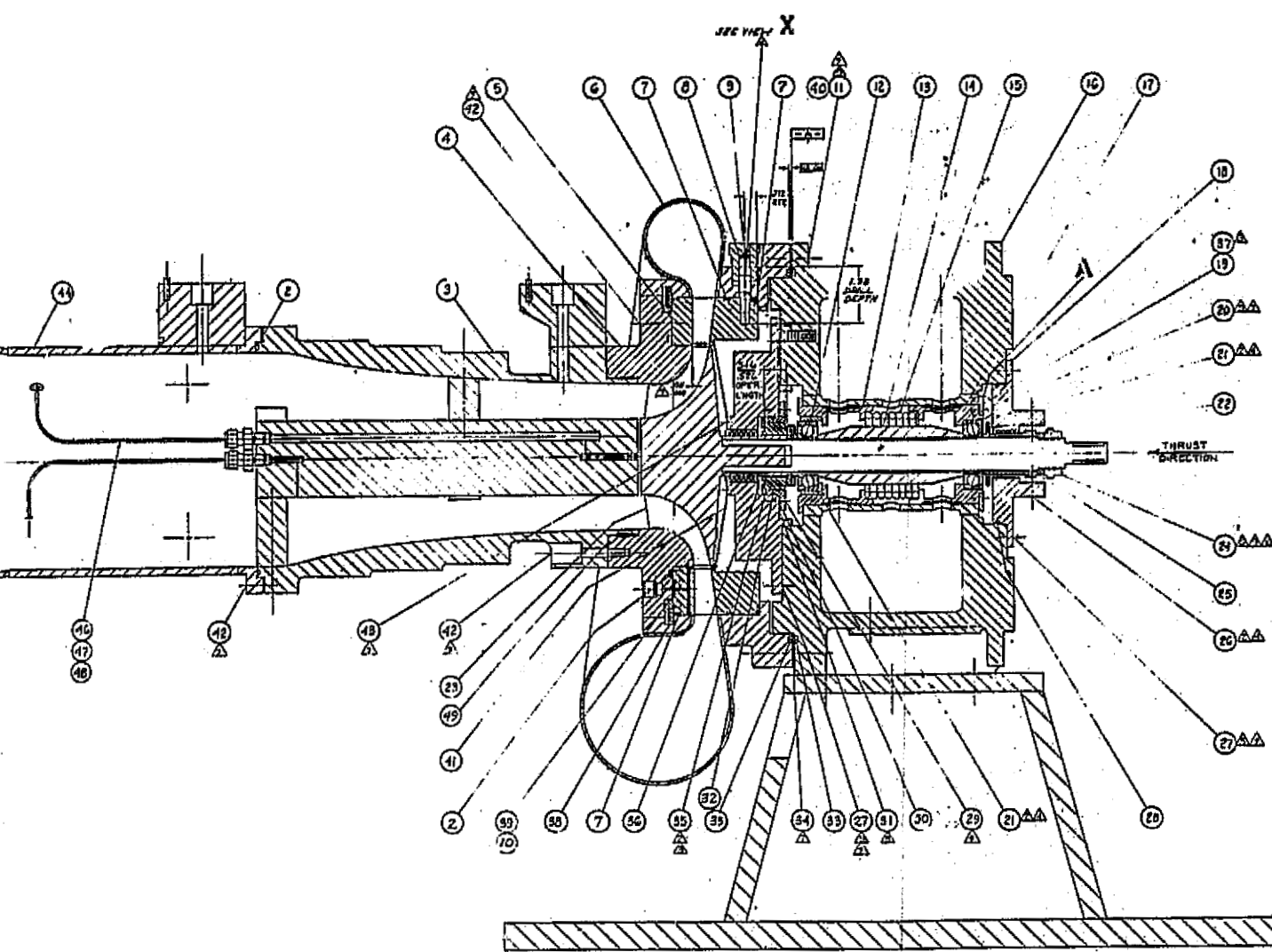


Note: Notes and parts list provided on original drawing.

NRED DRAWING NO. 1159-R002 - RESEARCH PACKAGE

FOLDOUT. FRAME 2

147

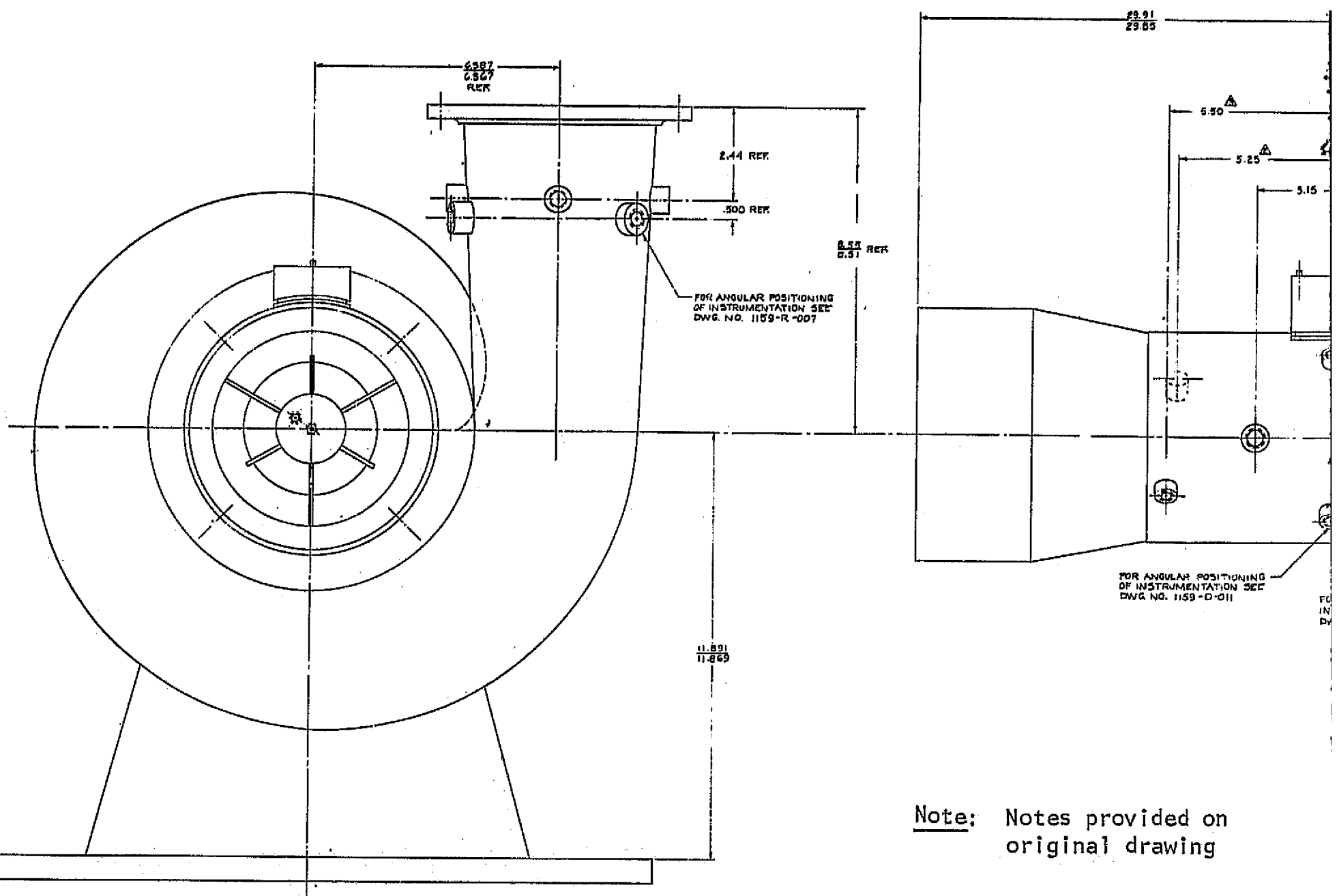


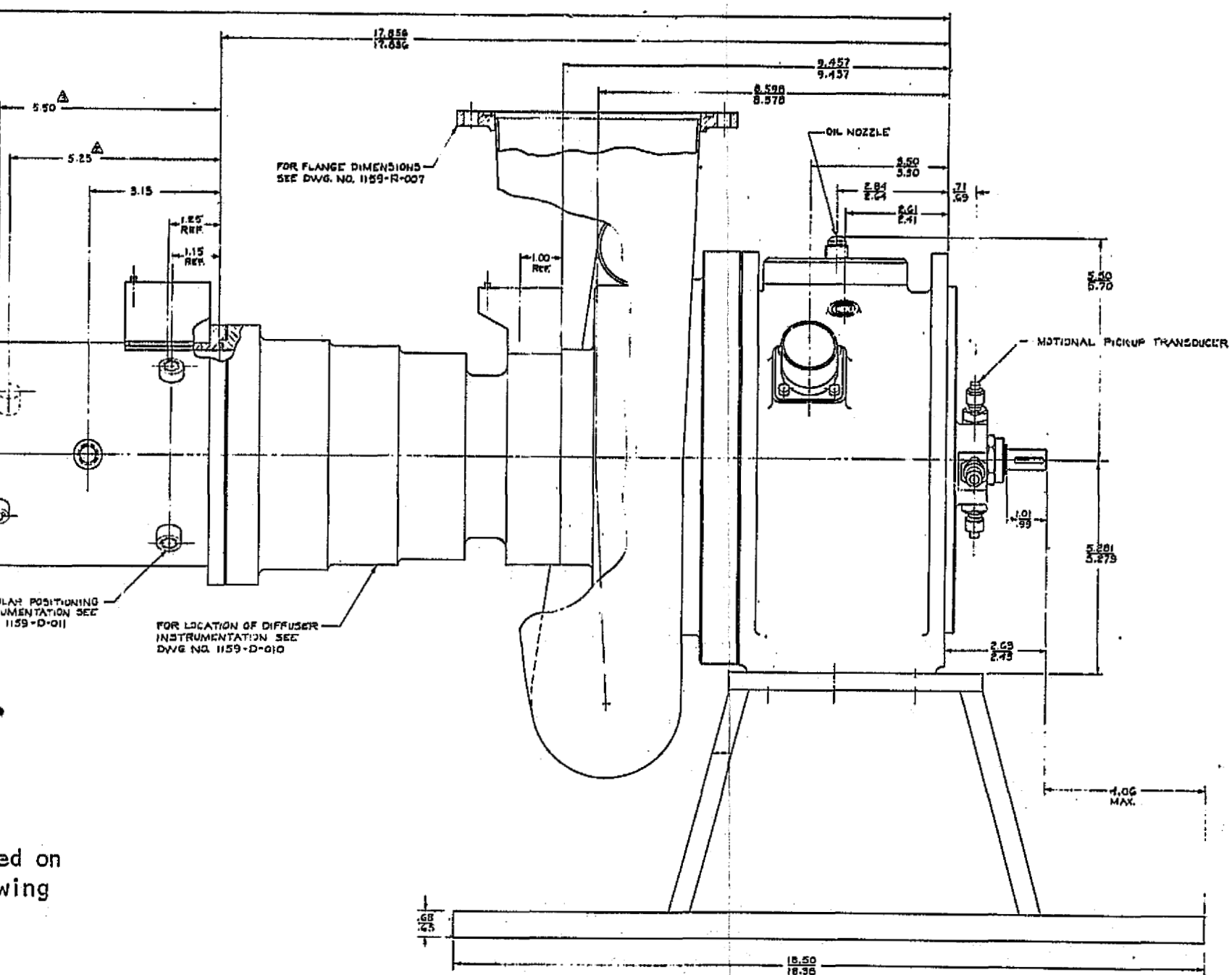
① ASSEMBLY

vided

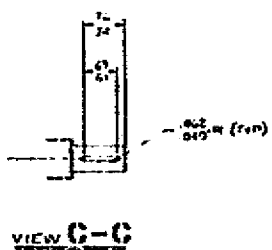
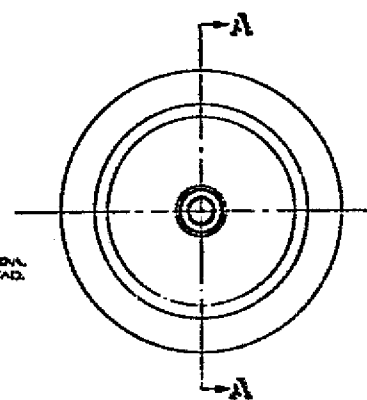
PACKAGE ASSEMBLY, TURBINE

FOLDOUT FRAME/

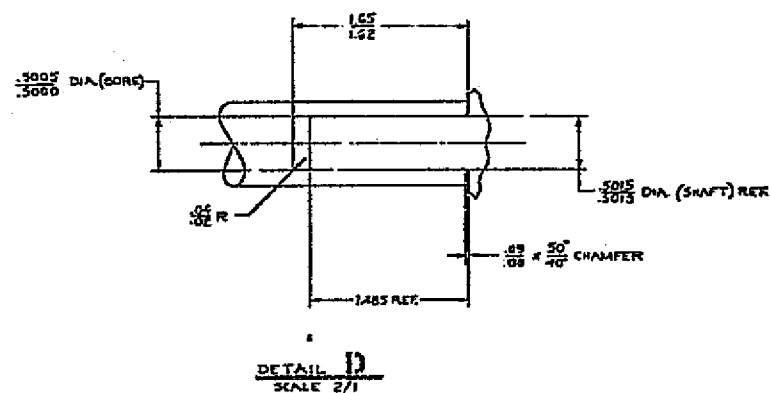




FIRST BLADE ROW INTERPOLATE								FIRST BLADE ROW INTERPOLATE								FIRST BLADE ROW INTERPOLATE					SECOND BLADE ROW INTERPOLATE				
No.	X (in.)	Y (in.)	Z (in.)	R ₁ (in.)	R ₂ (in.)	T ₁ (deg.)	T ₂ (deg.)	No.	X (in.)	Y (in.)	Z (in.)	R ₁ (in.)	R ₂ (in.)	T ₁ (deg.)	T ₂ (deg.)	No.	X (in.)	Y (in.)	Z (in.)	R ₁ (in.)	No.	X (in.)	Y (in.)	Z (in.)	R ₁ (in.)
1	-0.006	2.634	.400	2.634	- .002	.048	.059	1	0.080	2.633	.000	2.634	+ 1.749	.102	.105	1	29.793	31.885	3.880	.509	2	.000	-14.813	.000	1.750
2	-0.0197	2.570	.404	2.571	- .039	.048	.051	2	0.050	2.578	.012	2.579	+ 1.117	.104	.111	2	27.666	30.064	4.058	.375	3	.245	-12.692	- .190	.761
3	-0.044	2.509	.411	2.510	- .099	.048	.053	3	0.000	2.527	.037	2.527	+ .192	.106	.116	3	27.400	2.445	4.304	.381	4	1.401	-11.072	.309	.733
4	-0.072	2.457	.420	2.452	- 1.127	.048	.055	4	-0.038	2.337	.058	2.328	- .930	.108	.120	4	27.015	4.593	4.491	.384	5	1.947	- 9.294	1.811	.728
5	-0.101	2.394	.433	2.396	- 2.470	.047	.056	5	-0.085	2.228	.083	2.230	- 2.185	.110	.124	5	26.547	1.629	4.596	.388	6	2.798	- 7.461	2.796	.716
6	-0.136	2.340	.449	2.344	- 3.322	.047	.057	6	-0.131	2.130	.110	2.134	- 3.526	.111	.116	6	26.111	- 0.095	4.619	.399	7	2.233	- 6.167	3.557	.720
7	-0.169	2.287	.467	2.293	- 4.226	.047	.057	7	-0.175	2.032	.141	2.039	- 4.935	.113	.127	7	25.681	- 3.490	4.578	.404	8	1.866	- 5.019	4.128	.725
8	-0.202	2.235	.487	2.244	- 5.173	.046	.057	8	-0.217	1.933	.175	1.945	- 6.294	.114	.128	8	25.265	- 5.472	4.547	.404	9	1.516	- 4.038	4.118	.726
9	-0.236	2.184	.511	2.197	- 6.164	.046	.058	9	-0.254	1.835	.214	1.851	- 7.884	.116	.129	9	24.867	- 6.940	4.502	.409	10	1.111	- 3.046	4.063	.728
10	-0.269	2.133	.539	2.150	- 7.188	.047	.058	10	-0.287	1.738	.258	1.761	- 9.349	.118	.129	10	24.475	- 9.335	4.471	.405	11	.637	- 2.116	3.791	.733
11	-0.301	2.083	.569	2.105	- 8.232	.047	.058	11	-0.313	1.640	.308	1.669	-10.811	.120	.130	11	24.087	- 12.426	4.423	.415	12	.075	- 1.158	3.481	.735
12	-0.332	2.034	.603	2.061	- 9.277	.047	.058	12	-0.334	1.544	.366	1.580	-12.204	.122	.129	12	23.703	- 15.511	4.364	.414	13	-0.593	- 0.184	3.196	.736
13	-0.361	1.986	.639	2.018	-10.308	.048	.057	13	-0.367	1.452	.432	1.493	-13.456	.124	.129	13	23.326	- 18.525	4.316	.416	14	-1.134	0.796	2.906	.737
14	-0.388	1.939	.679	1.977	-11.308	.048	.056	14	-0.383	1.364	.508	1.409	-14.503	.127	.130	14	22.959	- 21.566	4.261	.401	15	-1.666	1.818	2.613	.738
15	-0.412	1.894	.722	1.938	-12.264	.046	.055	15	-0.399	1.282	.591	1.339	-15.232	.122	.126	15	22.607	- 24.604	4.211	.409	16	-2.162	3.133	2.315	.739
16	-0.433	1.851	.769	1.901	-13.162	.042	.047	16	-0.416	1.209	.681	1.255	-15.938	.103	.104	16	22.277	- 27.636	4.166	.405	17	-2.577	3.741	1.915	.740
17	-0.457	1.811	.810	1.867	-14.001	.035	.038	17	-0.434	1.144	.775	1.186	-16.569	.071	.072	17	21.977	- 30.661	4.124	.403	18	-2.934	4.444	1.507	.741
18	-0.466	1.775	.874	1.835	-14.696	.025	.027	18	-0.485	1.086	.874	1.122	-16.707	.025	.026	18	21.700	- 33.687	4.082	.402	19	-3.248	5.142	1.110	.742
SECOND BLADE ROW INTERPOLATE								SECOND BLADE ROW INTERPOLATE								SECOND BLADE ROW INTERPOLATE					SECOND BLADE ROW INTERPOLATE				
No.	X (in.)	Y (in.)	Z (in.)	R ₁ (in.)	R ₂ (in.)	T ₁ (deg.)	T ₂ (deg.)	No.	X (in.)	Y (in.)	Z (in.)	R ₁ (in.)	R ₂ (in.)	T ₁ (deg.)	T ₂ (deg.)	No.	X (in.)	Y (in.)	Z (in.)	R ₁ (in.)	No.	X (in.)	Y (in.)	Z (in.)	R ₁ (in.)
1	-0.301	1.555	.874	1.815	-17.500	.002	.000	1	-0.592	.954	.874	1.727	-17.211	.000	.000	1	-0.592	.954	.874	1.727	2	-0.719	1.570	.912	1.816
2	-0.319	1.570	.912	1.816	-17.125	.004	.002	2	-0.579	.942	.902	1.705	-17.572	.000	.007	2	-0.579	.942	.902	1.705	3	-0.737	1.646	.948	1.800
3	-0.337	1.646	.948	1.800	-17.828	.005	.005	3	-0.545	.921	.830	1.689	-17.256	.006	.008	3	-0.545	.921	.830	1.689	4	-0.762	1.624	.983	1.786
4	-0.362	1.624	.983	1.786	-17.558	.008	.002	4	-0.531	.922	.758	1.674	-17.840	.016	.029	4	-0.531	.922	.758	1.674	5	-0.790	1.601	1.015	1.774
5	-0.390	1.601	1.015	1.774	-17.371	.008	.008	5	-0.537	.913	.687	1.659	-18.434	.037	.046	5	-0.537	.913	.687	1.659	6	-0.790	1.583	1.045	1.765
6	-0.390	1.583	1.045	1.765	-17.230	.006	.003	6	-0.526	.903	1.617	1.645	-19.030	.055	.059	6	-0.526	.903	1.617	1.645	7	-0.801	1.564	1.074	1.757
7	-0.401	1.564	1.074	1.757	-17.122	.004	.009	7	-0.517	.892	1.647	1.631	-19.627	.072	.074	7	-0.517	.892	1.647	1.631	8	-0.821	1.545	1.101	1.751
8	-0.421	1.545	1.101	1.751	-17.046	.004	.007	8	-0.510	.880	1.677	1.618	-20.225	.086	.087	8	-0.510	.880	1.677	1.618	9	-0.846	1.527	1.127	1.746
9	-0.446	1.527	1.127	1.746	-16.977	.007	.006	9	-0.504	.869	1.708	1.606	-20.824	.104	.104	9	-0.504	.869	1.708	1.606	10	-0.870	1.508	1.152	1.741
10	-0.470	1.508	1.152	1.741	-16.922	.015	.006	10	-0.503	.857	1.738	1.595	-21.424	.122	.122	10	-0.503	.857	1.738	1.595	11	-0.895	1.490	1.176	1.738
11	-0.495	1.490	1.176	1.738	-16.876	.024	.000	11	-0.502	.845	1.768	1.583	-22.024	.139	.139	11	-0.502	.845	1.768	1.583	12	-0.910	1.471	1.199	1.735
12	-0.510	1.471	1.199	1.735	-16.834	.034	.008	12	-0.503	.833	1.798	1.570	-22.624	.157	.157	12	-0.503	.833	1.798	1.570	13	-0.927	1.452	1.219	1.734
13	-0.527	1.452	1.219	1.734	-16.795	.044	.012	13	-0.505	.820	1.827	1.556	-23.224	.173	.173	13	-0.505	.820	1.827	1.556	14	-0.944	1.433	1.240	1.733
14	-0.544	1.433	1.240	1.733	-16.759	.054	.018	14	-0.510	.808	1.855	1.543	-23.824	.189	.189	14	-0.510	.808	1.855	1.543	15	-0.960	1.414	1.259	1.732
15	-0.560	1.414	1.259	1.732	-16.726	.063	.023	15	-0.516	.796	1.882	1.530	-24.424	.205	.205	15	-0.516	.796	1.882	1.530	16	-0.977	1.395	1.279	1.732
16	-0.577	1.395	1.279	1.732	-16.694	.071	.028	16	-0.523	.784	1.909	1.517	-25.024	.221	.221	16	-0.523	.784	1.909	1.517	17	-0.993	1.376	1.298	1.731
17	-0.593	1.376	1.298	1.731	-16.664	.079	.030	17	-0.532	.771	1.934	1.504	-25.624	.237	.237	17	-0.532	.771	1.934	1.504	18	-1.009	1.357	1.317	1.730
18	-0.609	1.357	1.317	1.730	-16.636	.086	.035	18	-0.542	.758	1.958	1.491	-26.224	.252	.252	18	-0.542	.758	1.958	1.491	19	-1.025	1.338	1.336	1.730
19	-0.625	1.338	1.336	1.730	-16.609	.094	.039	19	-0.554	.745	1.982	1.478	-26.824	.267	.267	19	-0.554	.745	1.982	1.478	20	-1.041	1.319	1.355	1.730
20	-0.641	1.319	1.355	1.730	-16.584	.102	.043	20	-0.566	.732	1.994	1.465	-27.424	.282	.282	20	-0.566	.732	1.994	1.465	21	-1.057	1.299	1.374	1.730
21	-0.657	1.299	1.374	1.730	-16.559	.110	.047	21	-0.578	.719	2.006	1.452	-28.024	.297	.297	21	-0.578	.719	2.006	1.452	22	-1.073	1.279	1.393	1.730
22	-0.673	1.279	1.393	1.730	-16.536	.118	.051	22	-0.590	.706	2.018	1.439	-28.624	.312	.312	22	-0.590	.706	2.018	1.439	23	-1.089	1.259	1.412	1.730
23	-0.689	1.259	1.412	1.730	-16.514	.126	.055	23	-0.604	.693	2.029	1.426	-29.224	.327	.327	23	-0.604	.693	2.029	1.426	24	-1.105	1.239	1.431	1.730
24	-0.705	1.239	1.431	1.730	-16.493	.134	.059	24	-0.617	.679	2.039	1.413	-29.824	.342	.342	24	-0.617	.679	2.039	1.413	25	-1.121	1.219	1.450	1.730
25	-0.721	1.219	1.450	1.730	-16.473	.142	.063	25	-0.630	.666	2.049	1.400	-30.424	.357	.357	25	-0.630	.666	2.049	1.400	26	-1.137	1.199	1.469	1.730
26	-0.737	1.199	1.469	1.730	-16.454	.150	.067	26	-0.644	.653	2.059	1.387	-31.024	.372	.372	26	-0.644	.653	2.059	1.387	27	-1.153	1.179	1.488	1.730
27	-0.753	1.179	1.488	1.730	-16.436	.158	.071	27	-0.658	.640	2.069	1.374	-31.624	.387	.387	27	-0.658	.640	2.069	1.374	28	-1.169	1.159	1.507	1.730
28	-0.769	1.159	1.507	1.730	-16.419	.166	.075	28	-0.671	.626	2.079	1.361	-32.224	.402	.402	28	-0.671	.626	2.079	1.361					

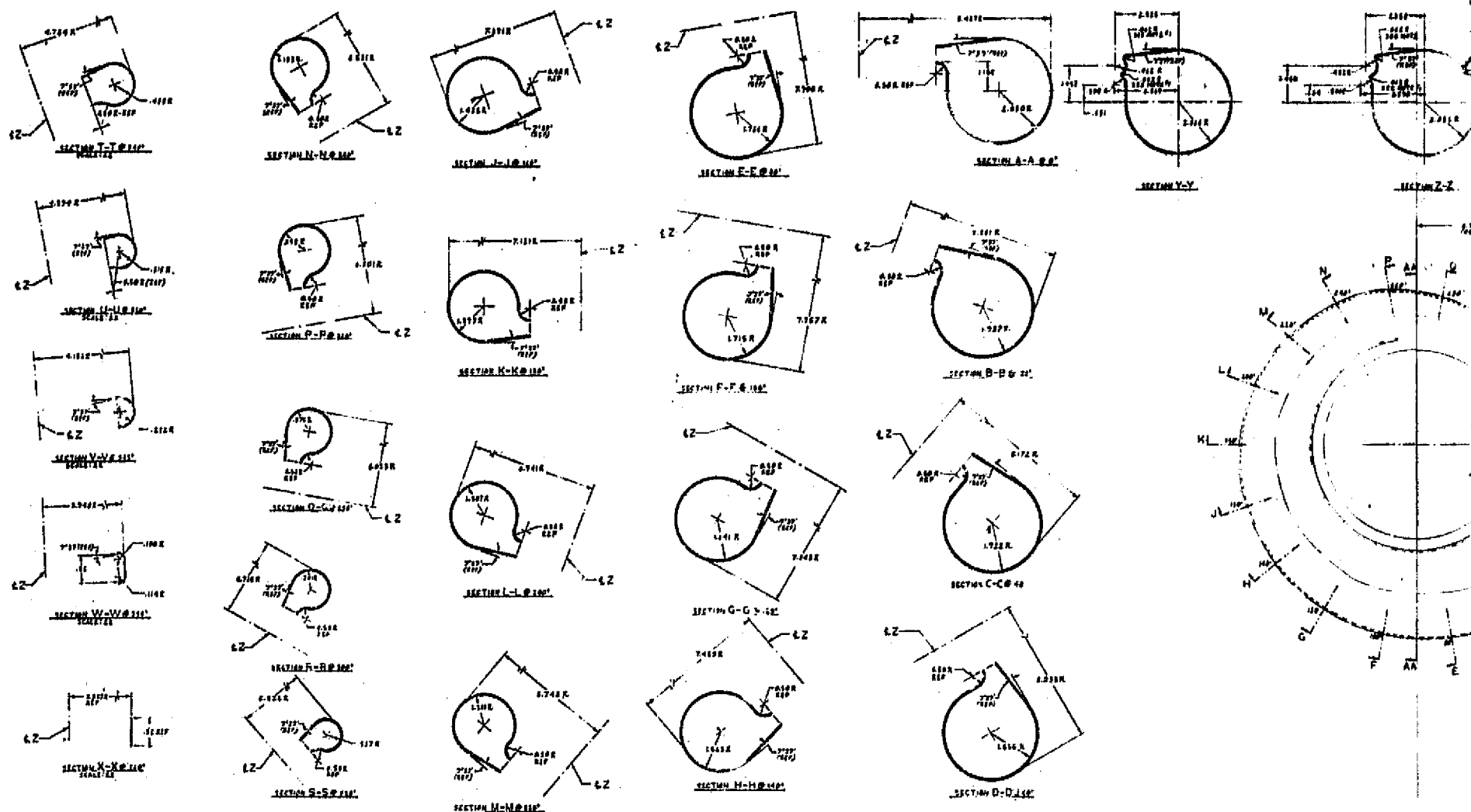
[illegible]

⑦ ASSY



2. ASSEMBLE ITEM 2 BY CHILLING TO -300° F. IN LIQUID N₂.
3. HEATING ITEM 2 TO 700° F. IN OVEN.
4. DILUTION MINERAL AT 1800° F. - ABC HARDEN AT 100° F. 1150° F.
5. REMOVE ALL BURNS.
6. MATERIAL MAY BE REMOVED FROM THIS AREA, FOR BALANCING, TO A MAX. DEPTH OF .06 AND MUST BLEND SMOOTHLY WITH SURROUNDING SURFACES.
7. OVERSPEED TEST AT 45,000 RPM FOR ONE MINUTE.
8. DYNAMIC BALANCE TO A MASS CENTER LOCATION OF 10.10 IN. - BALANCING AXIS TO BE DEFINED BY MID SPIN DIAS OF POINTS 0 & C.
9. FLUORESCENT PENETRANT INSPECT AFTER SPIN TESTING.
10. UNLESS OTHERWISE SPECIFIED.

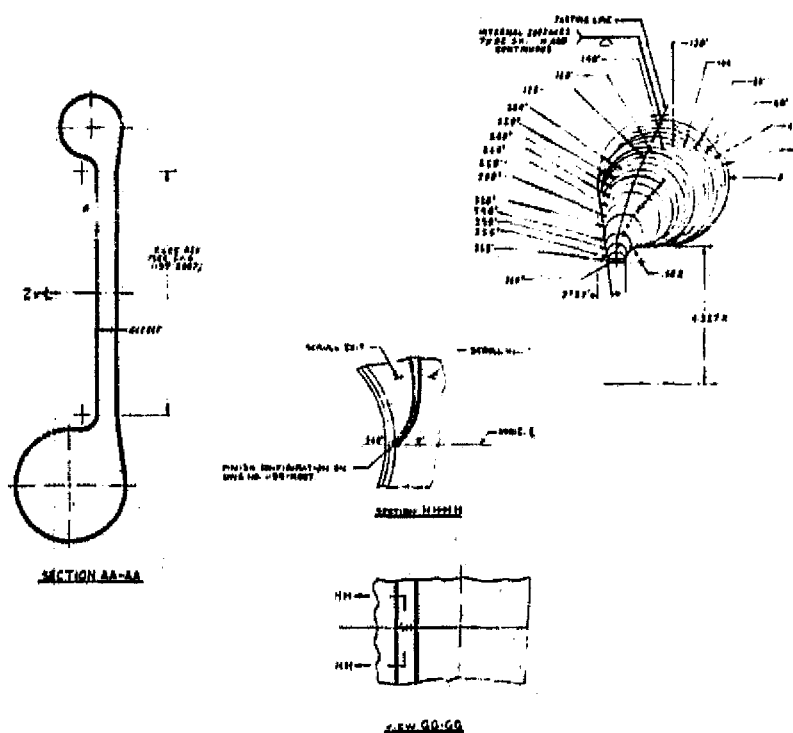
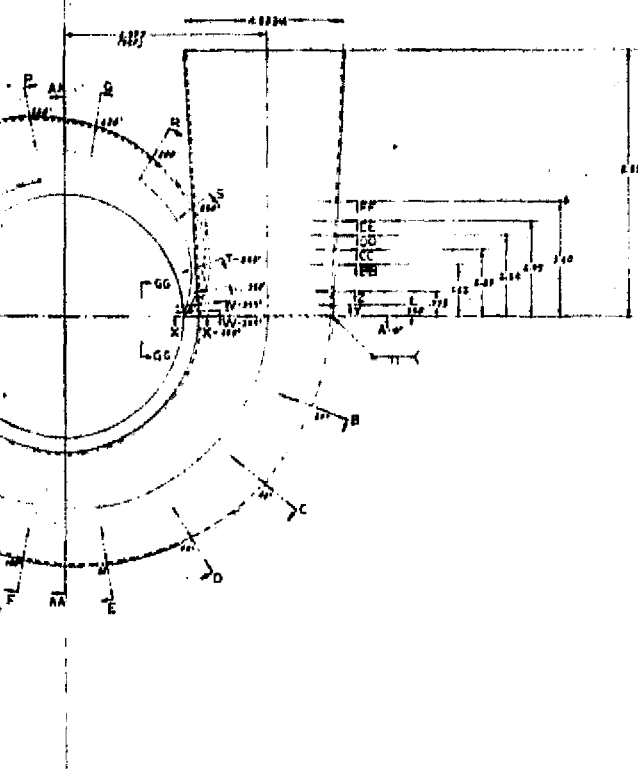
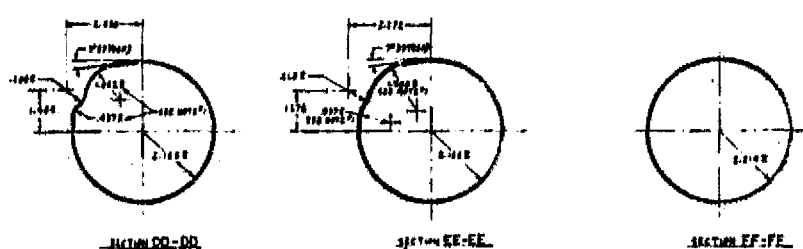
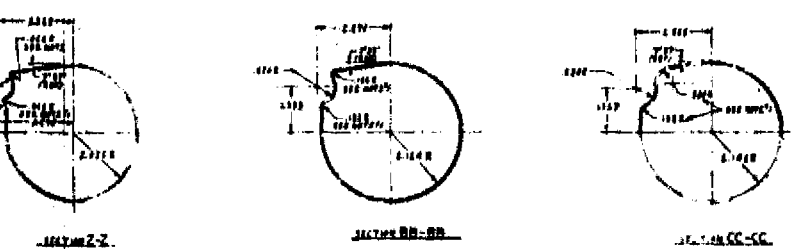
EOLDOUT. FRAME!



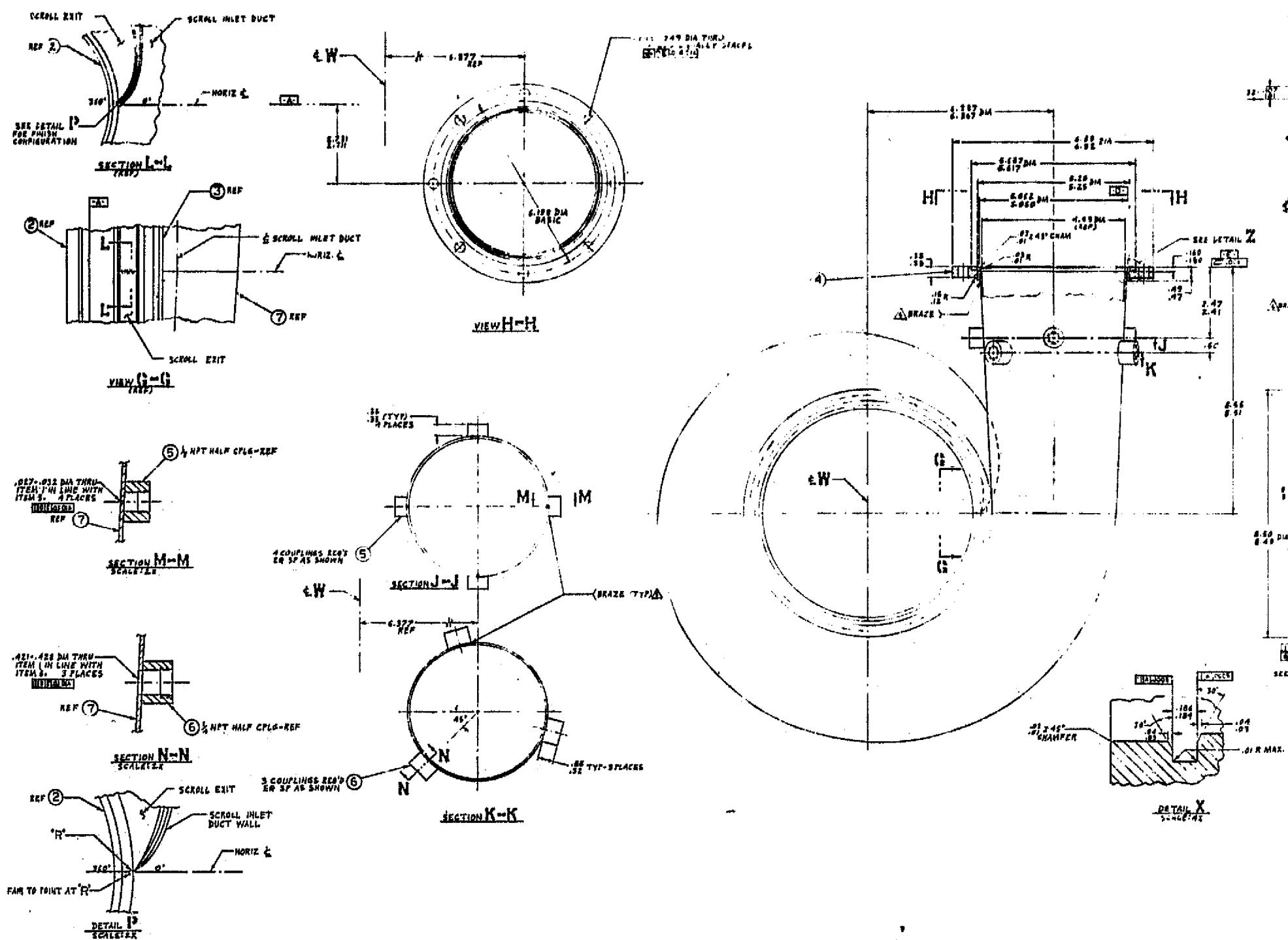
Note: Notes provided on original drawing

FOLDOUT. FRAME 2

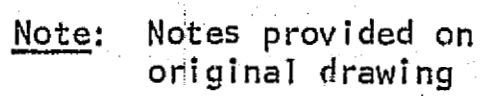
152



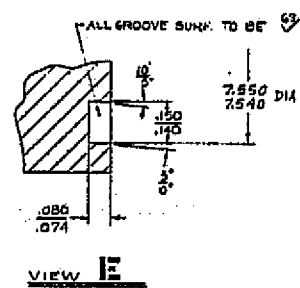
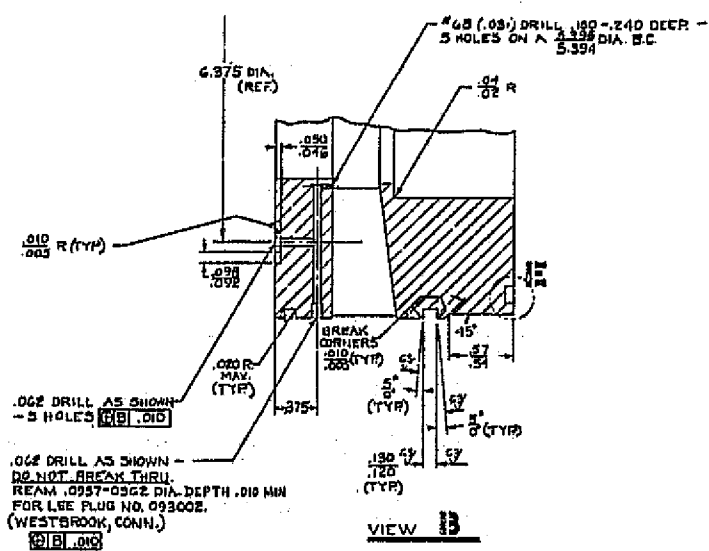
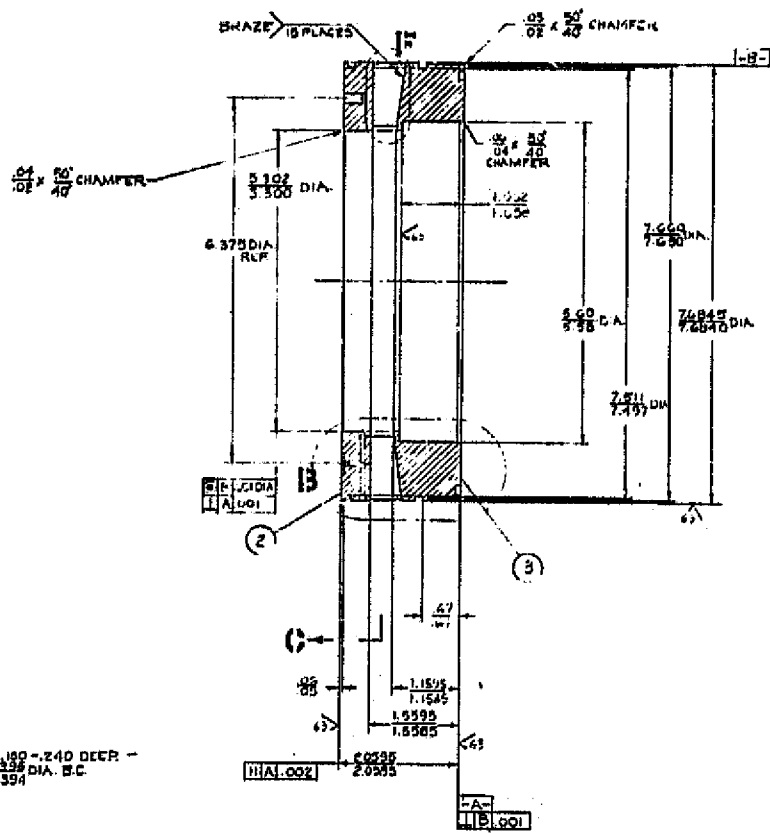
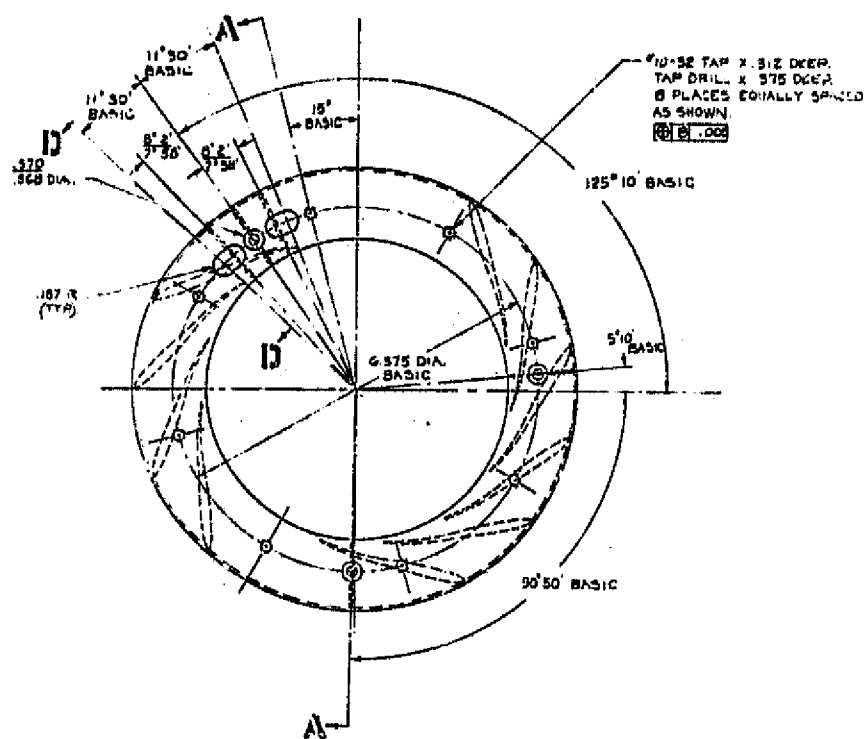
FOLDOUT FRAME 1



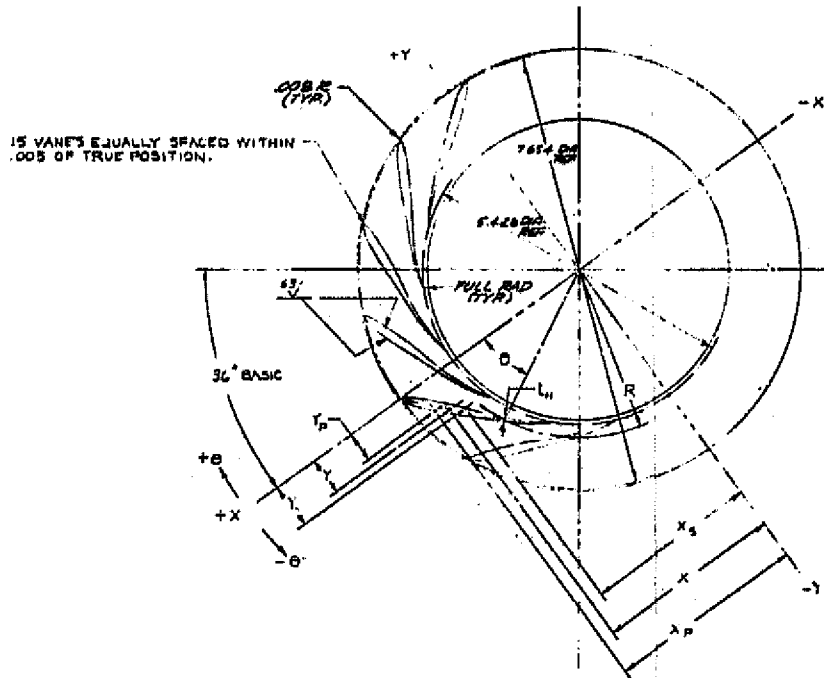
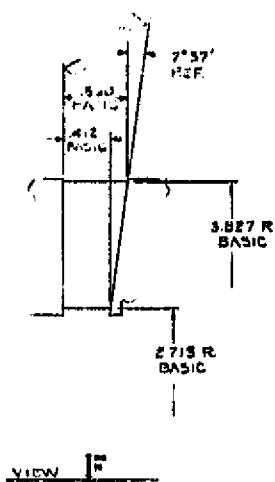
153



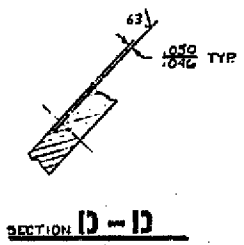
FOLDOUT FRAME /



EOLDOUT FRAME 2 154



SECTION C-C



SECTION D-D

1. BREAK ALL SHARP EDGES .010 R.
2. TOLERANCE PERMITTED ON VANE COORDINATES X, Y (OR R & Θ) IS ±.002 FROM TRUE CONTOUR.
3. UNLESS OTHERWISE SPECIFIED.

STAMP DATA (IN INCHES)			
NO.	STAMP DATA	STAMP DATA	STAMP DATA
1	1.017	0.000	0.000
2	1.017	0.000	0.000
3	1.017	0.000	0.000
4	1.017	0.000	0.000
5	1.017	0.000	0.000
6	1.017	0.000	0.000
7	1.017	0.000	0.000
8	1.017	0.000	0.000
9	1.017	0.000	0.000
10	1.017	0.000	0.000
11	1.017	0.000	0.000
12	1.017	0.000	0.000
13	1.017	0.000	0.000
14	1.017	0.000	0.000
15	1.017	0.000	0.000
16	1.017	0.000	0.000
17	1.017	0.000	0.000
18	1.017	0.000	0.000
19	1.017	0.000	0.000
20	1.017	0.000	0.000
21	1.017	0.000	0.000
22	1.017	0.000	0.000
23	1.017	0.000	0.000
24	1.017	0.000	0.000
25	1.017	0.000	0.000
26	1.017	0.000	0.000
27	1.017	0.000	0.000
28	1.017	0.000	0.000
29	1.017	0.000	0.000
30	1.017	0.000	0.000
31	1.017	0.000	0.000

STAMP DATA (IN INCHES)						
NO.	CAMBER		SECTION SURFACE		PRESSURE SURFACE	
	X	Y	X ₁	Y ₁	X ₂	Y ₂
1	1.017	0.000	1.017	0.000	1.017	0.000
2	1.017	0.000	1.017	0.000	1.017	0.000
3	1.017	0.000	1.017	0.000	1.017	0.000
4	1.017	0.000	1.017	0.000	1.017	0.000
5	1.017	0.000	1.017	0.000	1.017	0.000
6	1.017	0.000	1.017	0.000	1.017	0.000
7	1.017	0.000	1.017	0.000	1.017	0.000
8	1.017	0.000	1.017	0.000	1.017	0.000
9	1.017	0.000	1.017	0.000	1.017	0.000
10	1.017	0.000	1.017	0.000	1.017	0.000
11	1.017	0.000	1.017	0.000	1.017	0.000
12	1.017	0.000	1.017	0.000	1.017	0.000
13	1.017	0.000	1.017	0.000	1.017	0.000
14	1.017	0.000	1.017	0.000	1.017	0.000
15	1.017	0.000	1.017	0.000	1.017	0.000
16	1.017	0.000	1.017	0.000	1.017	0.000
17	1.017	0.000	1.017	0.000	1.017	0.000
18	1.017	0.000	1.017	0.000	1.017	0.000
19	1.017	0.000	1.017	0.000	1.017	0.000
20	1.017	0.000	1.017	0.000	1.017	0.000
21	1.017	0.000	1.017	0.000	1.017	0.000
22	1.017	0.000	1.017	0.000	1.017	0.000
23	1.017	0.000	1.017	0.000	1.017	0.000
24	1.017	0.000	1.017	0.000	1.017	0.000
25	1.017	0.000	1.017	0.000	1.017	0.000
26	1.017	0.000	1.017	0.000	1.017	0.000
27	1.017	0.000	1.017	0.000	1.017	0.000
28	1.017	0.000	1.017	0.000	1.017	0.000
29	1.017	0.000	1.017	0.000	1.017	0.000
30	1.017	0.000	1.017	0.000	1.017	0.000
31	1.017	0.000	1.017	0.000	1.017	0.000

Note: Notes provided on original drawing

10-32 UNF .38 DP
TAP DRILL .62 DP MAX.
7 HOLES EQ SP ON THE
BASIS OF 8 HOLES.
OMIT HOLE AT TOP ϕ

12.13 DIA THRU
2 HOLES EQ SP AS SHOWN

12.5" 10°
BASIC

5.10"
BASIC

9.0" 50°
BASIC

1.25" 27 NPT .31 DP MIN
TAP DRILL .44 DP MAX.
.094 DIA THRU.
5 HOLES SPACED AS SHOWN.

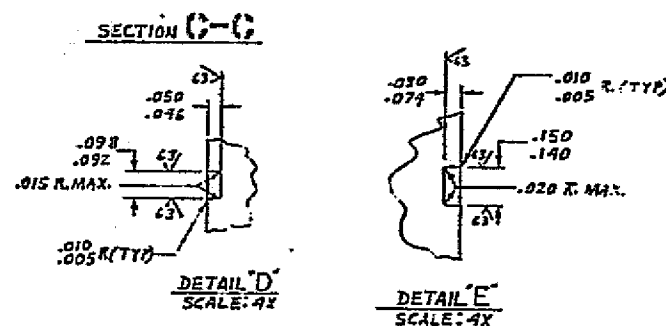
6.375
BASIC

4.625 DIA
BASIC

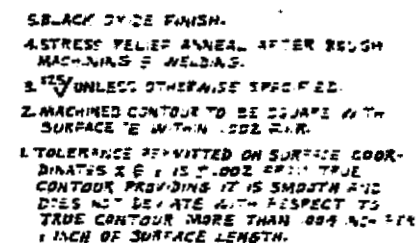
11" 30°

15"
BASIC

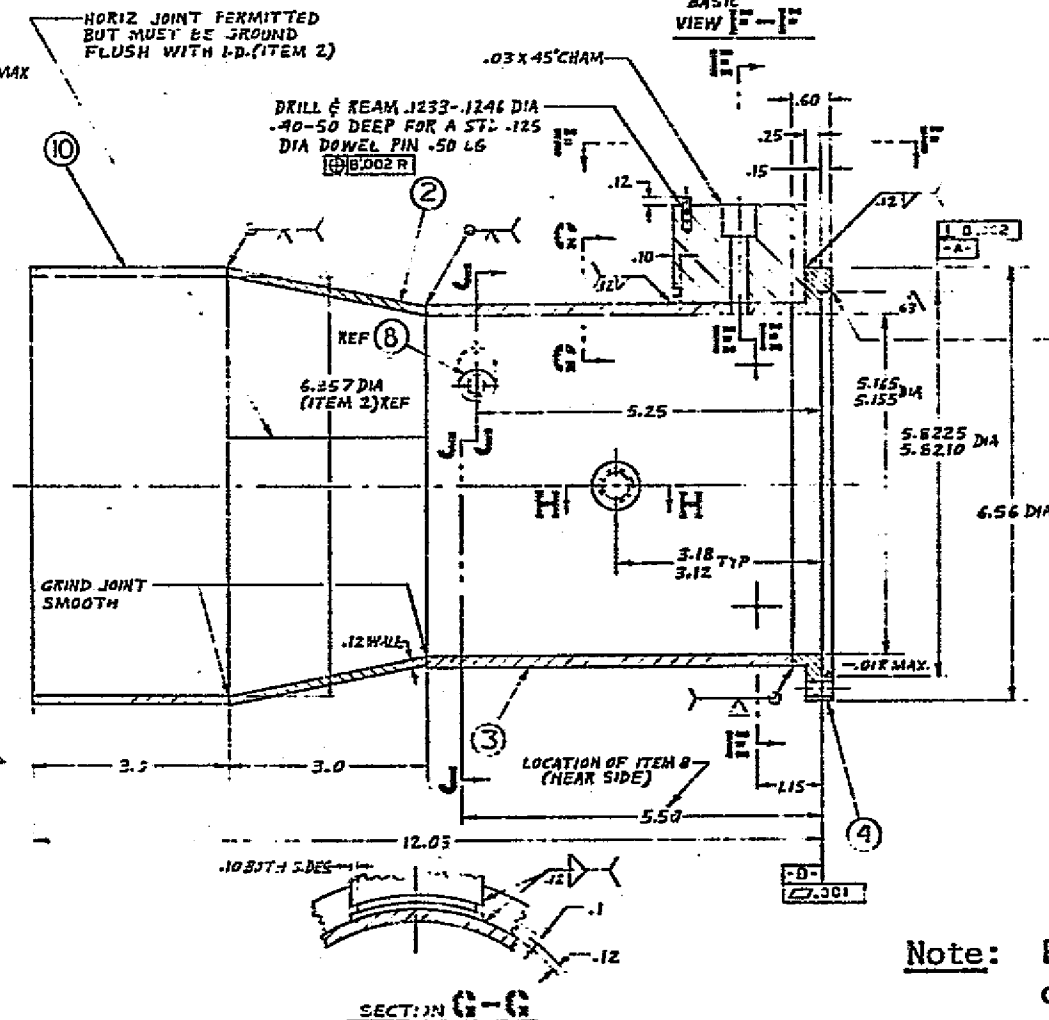
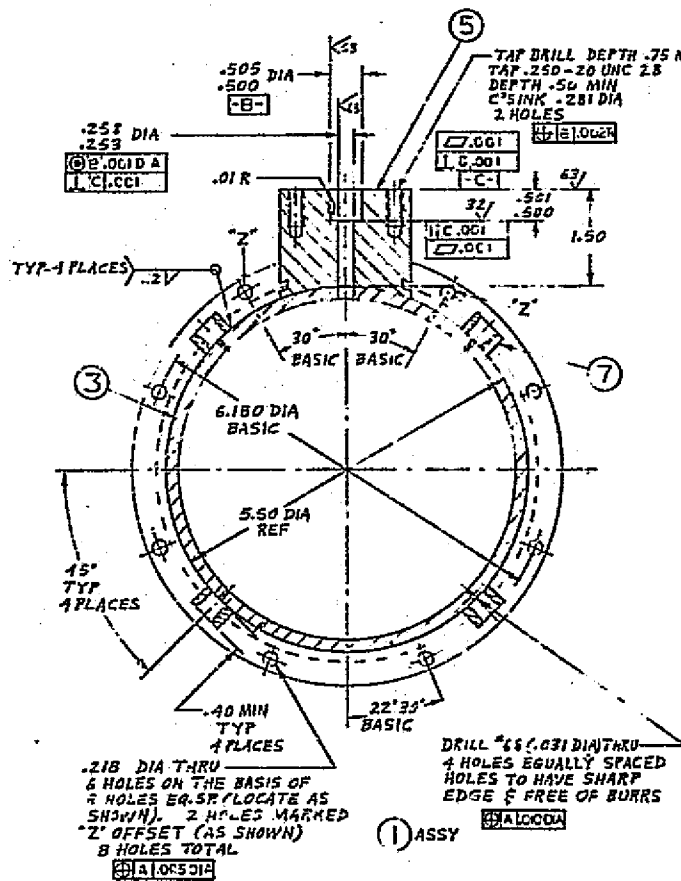
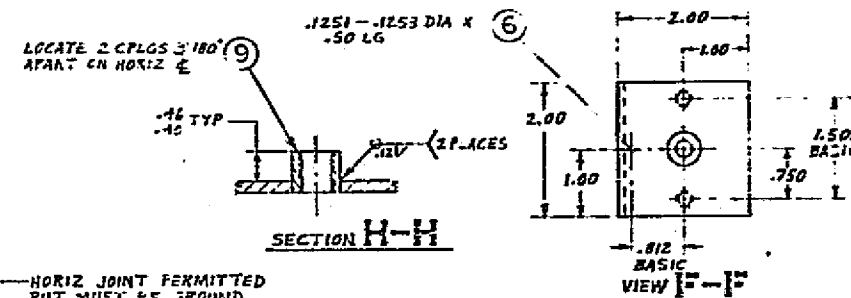
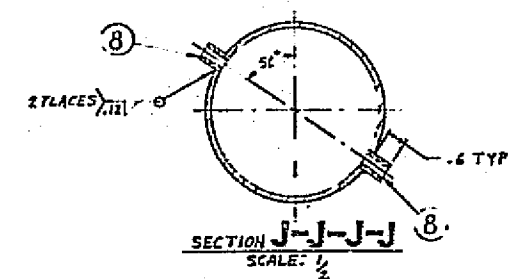
BASIC



4. BREAK SHARP EDGES .012 MAX.
.005
3. TOLERANCE PERMITTED ON SURFACE COORDINATES
"K E" IS $\pm .002$ FROM TRUE CONTOUR TRACING
IT IS SMOOTH.
2. PASSIVATE AFTER FINISH MACHINING.
1. $\frac{1}{2}$ UNLESS OTHERWISE SPECIFIED.



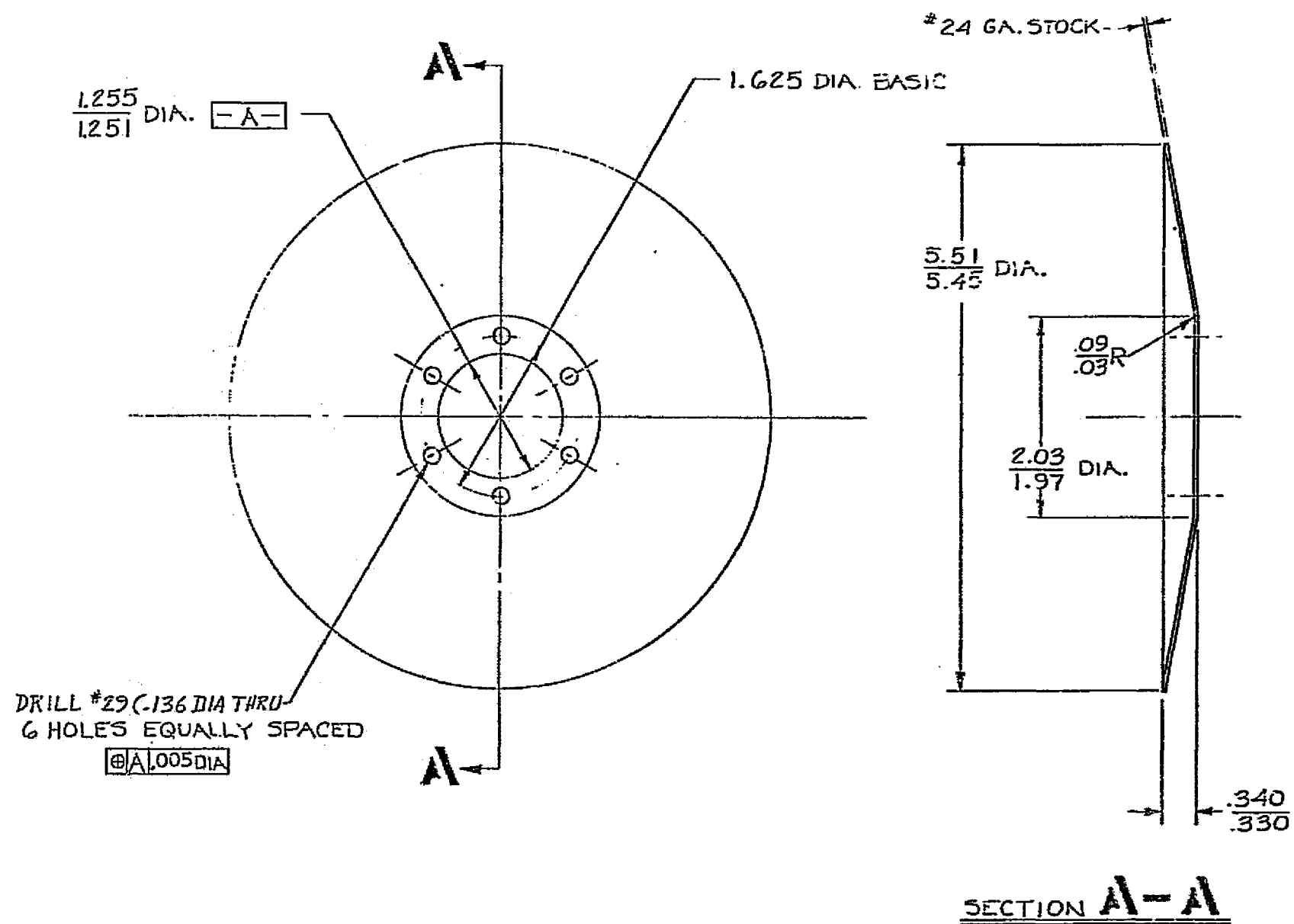
NREC DRAWING NO. 1159-D010 - DIFFUSER MACHINING



2. BLACK OXIDE FINISH
2. STRESS RELIEF ANNEAL AFTER MACHINING
1.125 UNLESS OTHERWISE SPECIFIED.

Note: Parts list provided on original drawing

NREC DRAWING NO. 1159-DO11 - EXHAUST ADAPTER

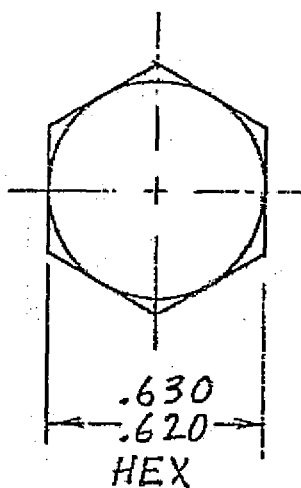


①

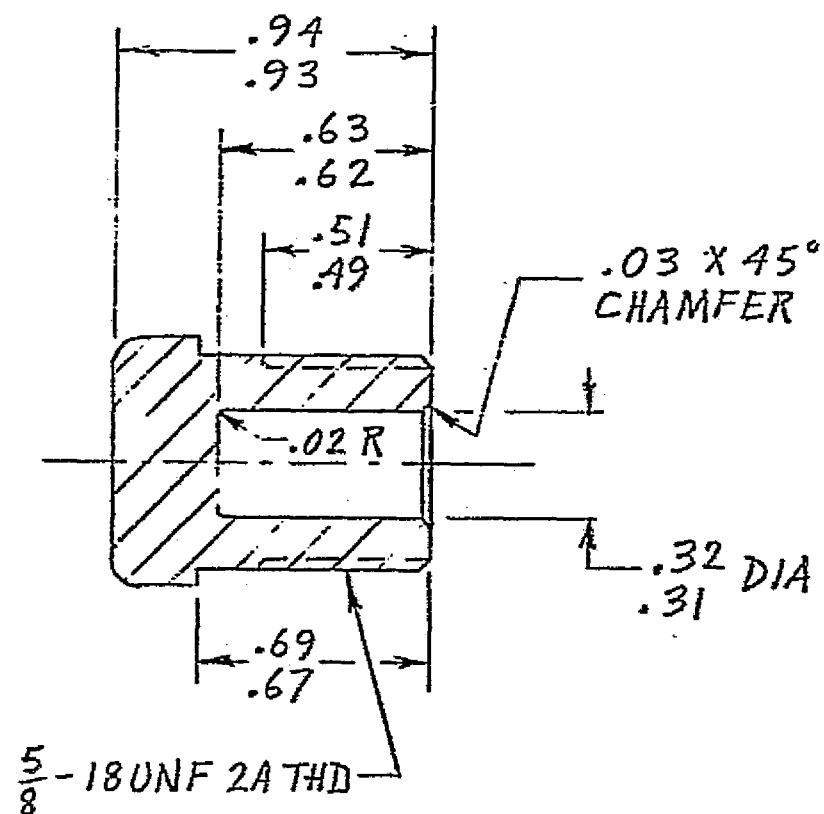
1. REMOVE ALL BURRS

NREC DRAWING NO. 1159-C012 - ROTOR BACK SHIELD

158



①



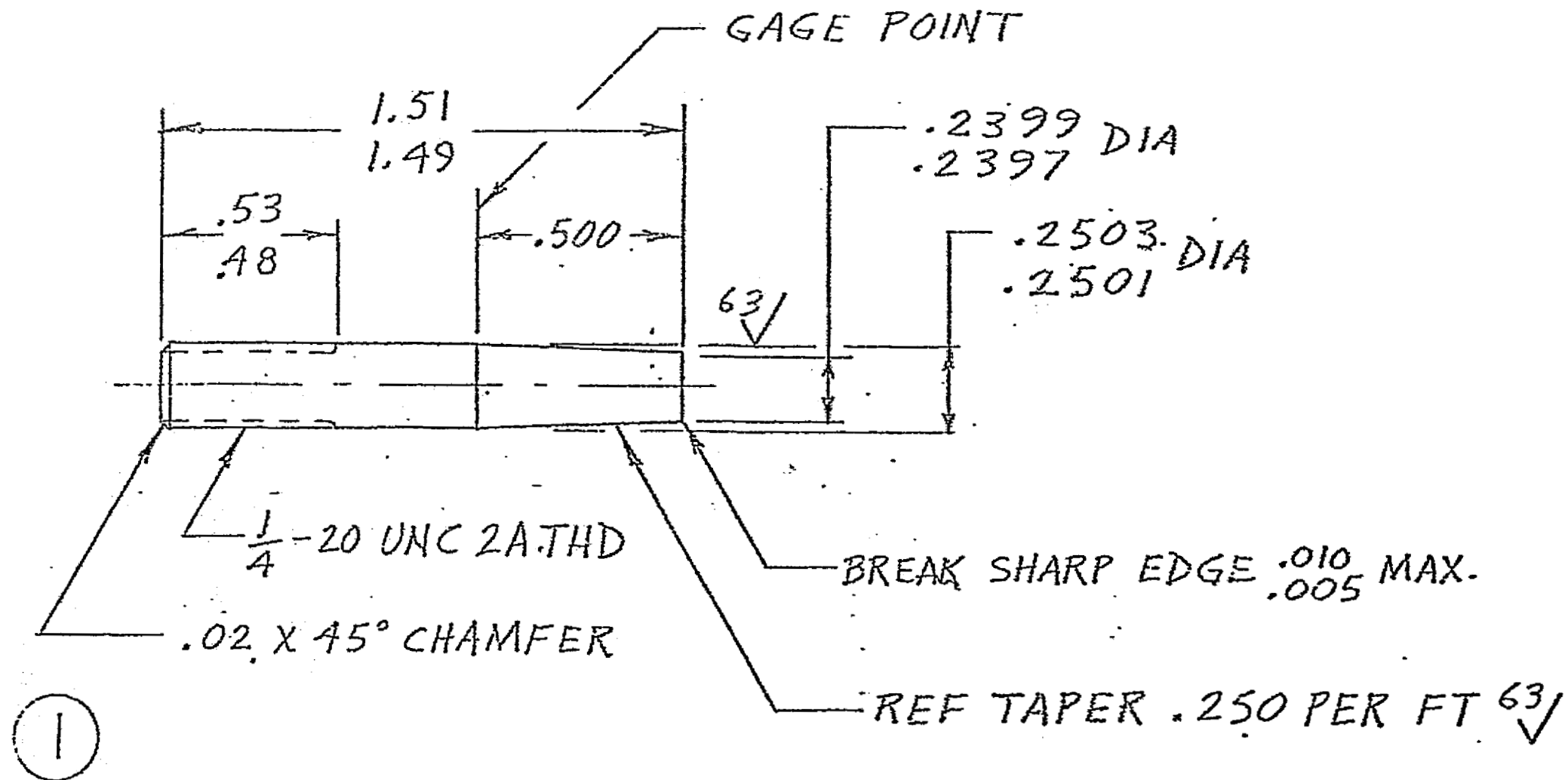
NOTES:

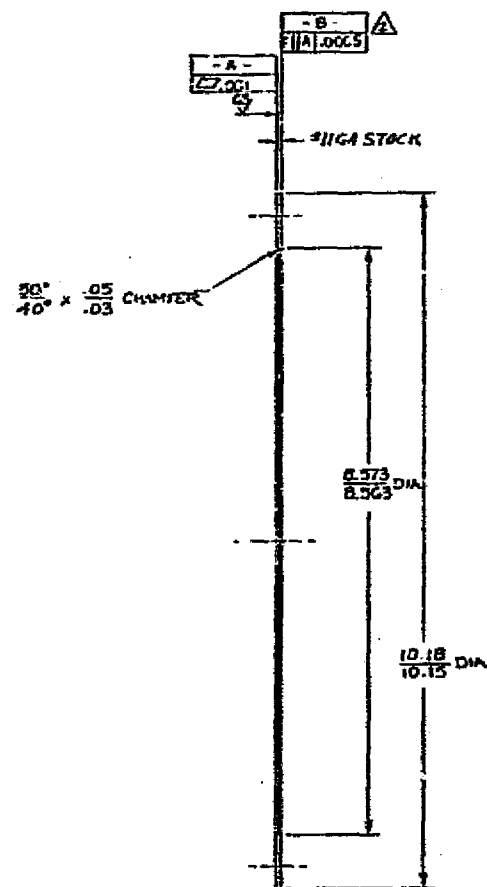
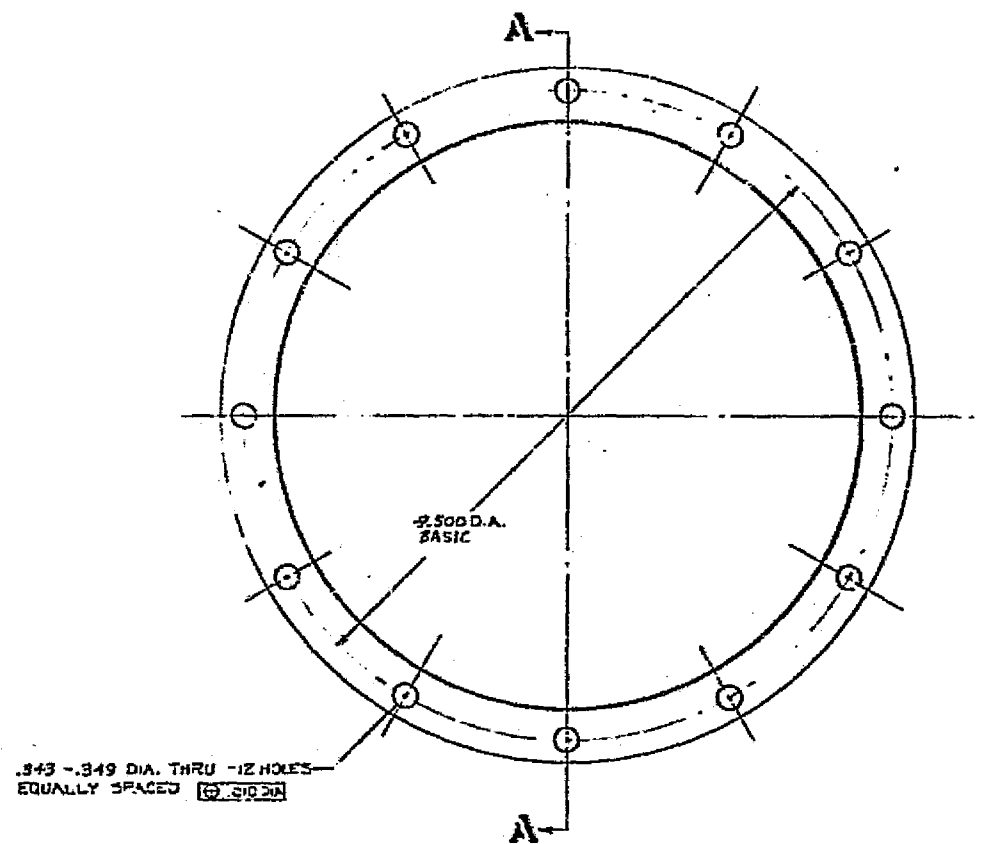
1. ALL SURFACES 125/
2. PASSIVATE AFTER FINISH MACHINING
3. BREAK SHARP EDGES .012
.015

NREC DRAWING NO. 1159-B013 - PIN CAP

NOTE:

1. $\sqrt[125]{}$ UNLESS OTHERWISE SPECIFIED





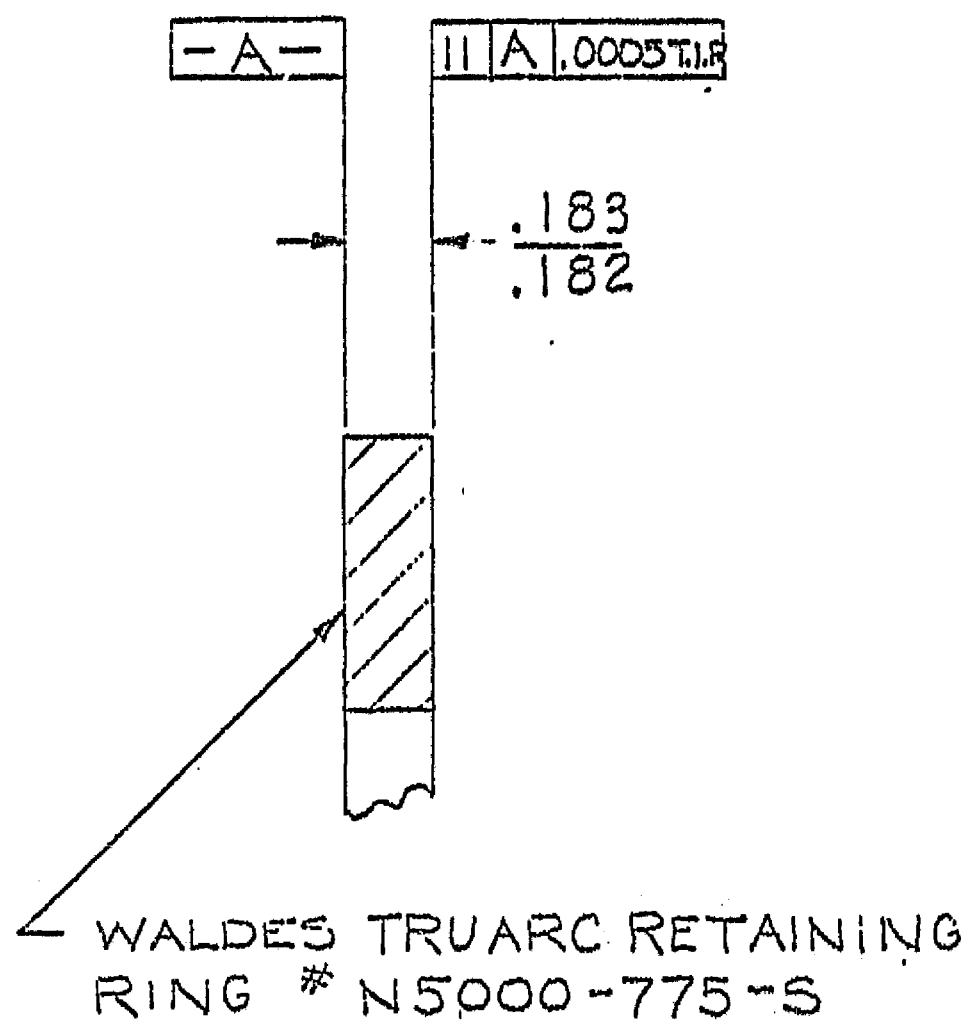
SECTION A-A

①

MACHINE THIS SURFACE 'B' TO THICKNESS ESTABLISHED AT FINAL ASSEMBLY.

✓ ALL FINISHED SURFACES.

NREC DRAWING NO. 1159-D015 - SHIM, SEALING SPACER



①

2. $\sqrt{63}$ GROUND SURFACE (OPP. **-A-**)
1. GRIND RING TO DIM. SHOWN.

DISTRIBUTION LIST

1. National Aeronautics and Space Administration
Washington, D. C. 20546
Attention: P. R. Miller Code NS-1 1
2. National Aeronautics and Space Administration
Lewis Research Center
21000 Brookpark Road
Cleveland, Ohio 44135
Attention: J. E. Dilley MS 500-201 1
Dr. B. Lubarsky MS 500-201 1
D. G. Beremand MS 500-201 1
D. C. Guentert MS 500-201 1
D. T. Bernatowicz MS 500-201 1
J. L. Klann MS 500-201 1
J. A. Heller MS 500-201 1
W. L. Stewart MS 500-316 1
H. E. Rohlik MS 500-316 1
S. M. Futral MS 500-316 1
W. J. Nusbaum MS 500-316 1
J. L. Means MS 500-316 1
M. G. Kofskey MS 500-316 10
D. W. Drier MS 21-4 1
D. R. Packe MS 500-201 7
3. NASA Ames Research Center
Moffett Field, California 94035
Attention: Library 1
4. NASA Flight Research Center
P. O. Box 273, Edwards, California 93523
Attention: Library 1
5. NASA Goddard Space Flight Center
Greenbelt, Maryland 20771
Attention: Library 1
6. NASA Langley Research Center
Langley Station, Hampton, Virginia 23365
Attention: Library 1
7. NASA Manned Spacecraft Center
Houston, Texas 77058
Attention: Library 1
8. NASA Marshall Space Flight Center
Huntsville, Alabama 35812
Attention: Library 1
9. NASA Western Operations Office
150 Pico Boulevard
Santa Monica, California 90406
Attention: Library 1

10. NASA Jet Propulsion Laboratory
4800 Oak Grove Drive
Pasadena, California 91103
Attention: Library 1
11. National Aeronautics and Space Administration
Scientific & Technical Information Facility
P. O. Box 33, College Park, Maryland 20740
Attention: Acquisitions Branch, SQT-34054 1
12. U.S. Army Engineer R&D Laboratories
Gas Turbine Test Facility
Fort Belvoir, Virginia 22060
Attention: W. Crim 1
13. Office of Naval Research
Department of the Navy
Washington, D. C. 20025
Attention: Dr. Ralph Roberts 1
14. Bureau of Naval Weapons
Department of the Navy
Washington, D. C. 20025
Attention: Code RAPP 1
15. Bureau of Ships
Department of the Navy
Washington, D. C. 20025
Attention: G. L. Graves 1
16. Air Force Systems Command
Aeronautical Systems Division
Wright-Patterson Air Force Base, Ohio 45433
Attention: Library 1
17. Institute for Defense Analyses
400 Army - Navy Drive
Arlington, Virginia 22202
Attention: Library 1
18. University of Pennsylvania
Power Information Center
Moore School Building
200 South 33rd Street
Philadelphia Pennsylvania 19104 1
19. Massachusetts Institute of Technology
Cambridge, Massachusetts 02139
Attention: Library 1
20. Aerojet General Corporation
Azusa, California 91703
Attention: Library 1
21. AiResearch Manufacturing Company
The Garrett Corporation
402 South 36th Street
Phoenix, Arizona 85034
Attention: R. O. Bullock 1
Library 1

22. AiResearch Manufacturing Company
The Garrett Corporation
9851 Sepulveda Boulevard
Los Angeles, California 90009
Attention: Library 1
23. Bendix Research Laboratories Division
Southfield (Detroit), Michigan 48232
Attention: Library 1
24. The Boeing Company
Aero-Space Division
Box 3707
Seattle, Washington 98124
Attention: Library 1
25. Borg-Warner Corporation
Pesco Products Division
24700 North Miles Road
Bedford, Ohio 44014
Attention: Library 1
26. Continental Aviation & Engineering Corporation
12700 Kercheval Avenue
Detroit, Michigan 48215
Attention: Library 1
27. Curtiss-Wright Corporation
Wright Aero Division
Main and Passaic Streets
Woodridge, New Jersey 07075
Attention: Library 1
28. Douglas Aircraft Company
3000 Ocean Park Boulevard
Santa Monica, California 90406
Attention: Library 1
29. General Dynamics Corporation
16501 Brookpark Road
Cleveland, Ohio 44142
Attention: Library 1
30. General Electric Company
Flight Propulsion Laboratory Division
Cincinnati, Ohio 45215
Attention: Library 1
31. General Electric Company
Lynn, Massachusetts 01905
Attention: Library 1
32. General Electric Company
Missile & Space Vehicle Department
3198 Chestnut Street
Philadelphia, Pennsylvania 19104
Attention: Library 1

33. General Motors Corporation
Indianapolis, Indiana 46206
Attention: Library 1
34. Lear Siegler, Incorporated
3171 S. Bundy Drive
Santa Monica, California 90406
Attention: Library 1
35. Lockheed Missiles & Space Company
P. O. Box 504
Sunnyvale, California 94088
Attention: Library 1
36. Mechanical Technology Incorporated
968 Albany - Shaker Road
Latham, New York 12110
Attention: Library 1
37. North American Aviation, Incorporated
Space and Information Systems Division
Downey, California 90241 1
38. Solar Division of International Harvester
2200 Pacific Highway
San Diego, California 92112
Attention: Library 1
39. Space Technology Laboratories, Incorporated
One Space Park
Redondo Beach, California 90278
Attention: Library 1
40. Sunstrand Denver
2480 West 70th Avenue
Denver, Colorado 80221
Attention: Library 1
41. Thompson-Ramo-Woolridge Accessories Division
23555 Euclid Avenue
Cleveland, Ohio 44117
Attention: Library 1
42. Union Carbide Corporation
Linde Division
P. O. Box 44, Tonawanda, New York 14152
Attention: Library 1
43. United Aircraft Research Laboratory
East Hartford, Connecticut 06108
Attention: Library 1
44. Westinghouse Electric Corporation
Astronuclear Laboratory
P. O. Box 10864, Pittsburgh, Pennsylvania
Attention: Library 1

45. Williams Research
Walled Lake, Michigan 48088
Attention: Library 1
46. United Aircraft Corporation
Pratt & Whitney Aircraft Division
S. Windsor Engineering Facilities
Governors Highway
S. Windsor, Connecticut 06074
Attention: Library 1
47. NASA Scientific and Technical Information Facility
P. O. Box 33
College Park, Maryland 20740
Attention: Acquisitions Branch 2